

Université de Paris

thèse de doctorat

Pour obtenir le grade de

DOCTEUR EN SCIENCES

Spécialité :

Physique de l'univers

Ecole doctorale des Sciences de la Terre et de l'Environnement et Physique de l'Univers, Paris

STEP'UP ED-560

Laboratoire de physique nucléaire et de hautes énergies, Paris

Mise à jour du trajectographe d'ATLAS en préparation de la phase à haute luminosité du CERN LHC : étalonnage et caractérisation de modules à pixels du détecteur de traces actuel et futur d'ATLAS

présentée par

Reem H. Taibah

Soutenue le 17^{ème} Septembre 2021 devant le jury composé de:

DR	LEDROIT Fabienne	(LPSC)	Rapporteuse
Prof.	BAUDOT Jérôme	(IPHC)	Rapporteur
Prof.	KOUCHNER Antoine	(APC)	président de jury
IR	JURAMY GILLES Claire	(UMR)	Examinatrice
MCU	MATEA Iolanda	(IJCLAB)	Examinatrice
Prof.	BUTTAR Craig	(Univ. of Glasgow)	Examinateur

Supervisé par

MCU Marco BOMBEN

Dr. Francesco CRESCIOLI



Université
de Paris



Université de Paris

PhD Thesis

Submitted in fulfillment of the requirements for the degree of

DOCTOR OF SCIENCES

Specialty :

Physics of the Universe

Doctoral school of Geo and Environment Sciences and of Physics of the Universe

STEP'UP ED-560

Laboratoire de physique nucléaire et de hautes énergies, Paris

Upgrade of the ATLAS tracking detector in preparation for the High-Luminosity phase of the LHC : Planar pixel module characterisation and calibration for the current and future ATLAS inner tracker

written by

Reem H. Taibah

Defended on 17th September 2021 in front of the jury:

DR	LEDROIT Fabienne	(LPSC)	Referee
Prof.	BAUDOT Jérôme	(IPHC)	Referee
Prof.	KOUCHNER Antoine	(APC)	President of the jury
IR	JURAMY GILLES Claire	(UMR)	Member of the jury
MCU	MATEA Iolanda	(IJCLAB)	Member of the jury
Prof.	BUTTAR Craig	(Univ. of Glasgow)	Member of the jury

Supervised by

MCU Marco BOMBEN

Dr. Francesco CRESCIOLI

Abstract

by Reem H. TAIBAH

The LHC reached its original design in 2015 delivering center of mass energies of 13 TeV of proton collisions with instantaneous luminosity $1 \times 10^{34} \text{ cm}^{-2} \text{ s}^{-1}$. To maintain scientific progress and exploit the machine's full capacity, the LHC plans to upgrade the luminosity about 7 times higher than its design value transforming the LHC into the High-Luminosity LHC (HL-LHC). In preparation for the HL-LHC phase in 2026 the experiments will have to be upgraded to maintain the same performance with the increase of the luminosity. The thesis focuses on the upgrade of the ATLAS pixel detector into an all-silicon Inner Tracker (ITk). The ITk will cover a high range of pseudorapidity $2.4 < |\eta| < 4$. The ITk pixel sensors utilize the n-in-p technology assembled with the RD53A readout chip. The pixel modules will host $100 - 150 \mu\text{m}$ thick sensors with a pixel geometry of $50 \times 50 \mu\text{m}^2$ and $25 \times 100 \mu\text{m}^2$. The performance of the ITk prototype pixel module is characterised with a particle beam to study the hit efficiency and position resolution of the sensor. To comply with ITk requirements the pixel module must achieve hit efficiency of at least 98% before irradiation and 97% after irradiation up to fluence of $\phi = 5 \times 10^{15} \text{ n}_{\text{eq}}/\text{cm}^2$. Pixel modules that agree with these requirements are qualified for the production of the ITk detector. The investigated modules produced from FBK foundry show efficiency performance in well agreement with the ITk requirements for the pixel detector to operate in the HL-LHC phase of the LHC. The foundries participating in the production of the ITk pixel detector are qualified based on the performance of the sensors characterised in the Market Survey testbeam campaign. The methodology of characterising a pixel module with a particle beam and analysing the results is discussed in detail to guide the reader to the concluded results of qualified modules for the ITk pixel detector. In parallel I present simulated performance of the ITk pixel sensors with the RD53A readout chip in the testbeam setup to study the impacts of multiple scattering in the setup. Results of residuals from simulated tracks are compared with testbeam data to show the compatibility between the simulation and the testbeam setup for the ITk pixel module. The results show the effects of multiple scattering on the performance of the pixel module. The simulation setup is prepared in allpix-squared framework and could be used by other users to simulate and predict the performance of the future ITk pixel modules. The work for this thesis also branched to investigate the calibration of the FE-I4B readout chip for the current IBL detector. It was found that a discrepancy of charge collection in the IBL module rises from a local threshold asymmetry when tuning the threshold of the FE-I4B chip using the charge injection circuit. The investigation led to the introduction of the novel threshold baseline tuning method to solve this local threshold asymmetry in the FE-I4B chip. The threshold baseline tuning method depends solely on counting hits and thus tunes the local threshold without using the charge injection circuit. The new tuning method indeed proves effective and therefore having a symmetrical charge collection throughout the IBL module. As the tuning algorithm is now implemented in the ATLAS pixel DAQ system, we are able to tune one module but the algorithm must be further improved to tune to complete detector. It is one step forward towards achieving higher quality of data for Run3.

Keywords: LHC – ATLAS - ITk - PIXELS - DETECTORS - TRACKER - INSTRUMENTATION

Abstract

by Reem H. TAIBAH

Le collisionneur des protons Large Hadron Collider (LHC) du CERN a atteint ses valeurs de dessin en 2015, avec une énergie dans le centre de masse de 13 TeV et une luminosité instantanée de $1 \times 10^{34} \text{cm}^{-2}\text{s}^{-1}$. Pour continuer à faire avancer les connaissances dans le domaine de la physique des particules et exploiter au maximum le potentiel de l'accélérateur le CERN a préparé un plan de mises à jour pour transformer le LHC dans une machine à haute luminosité (HL-LHC), avec une augmentation de 5 à 7 de la luminosité instantanée. En vue du HL-LHC en 2026, les expériences auprès du LHC ' comme ATLAS ' seront aussi mises à niveau, afin de maintenir le même niveau de performances ' voir l'améliorer ' même dans les conditions très contraignantes ' augmentation du niveau de radiation et du taux d'occupation - de la phase à haute luminosité. La thèse porte sur la mise à jour du trajectographe d'ATLAS qui va à devenir un détecteur basé entièrement sur des capteurs silicium le Inner Tracker (ITk). Le ITk sera composé de détecteurs à pixels dans la partie la plus interne et à microbandes pour le reste, avec une couverture plus étendue en pseudo-rapacité "eta" qu'avant (jusqu'à $|\eta| = 4$). Le ITk pixel detector sera instrumenté avec des modules hybrides avec capteurs n-in-p et puce de lecture ITkPixV2. Les capteurs auront une épaisseur de $100 - 150 \mu\text{m}$ avec un pas de $50 \times 50 \mu\text{m}^2$ ou $25 \times 100 \mu\text{m}^2$. Des prototypes de modules hybrides à pixels ont été préalablement testés avec des faisceaux de particules de hautes énergies pour mesurer leurs performances et valider les dessins proposés. En particulier les modules devaient assurer une efficacité de reconstruction de hit supérieure à 97% même après irradiation à un niveau comparable à celui attendu pendant la prise de donné. Les capteurs à pixels en technologie planaire que j'ai étudié pendant ma thèse ont été produits par la fonderie FBK et ont montré une efficacité de 97% ce qui a permis à FBK de se qualifier pour la production de capteurs à pixels pour ATLAS ITk Pixels. Les techniques de mesures et analyse de données de faisceaux tests, ainsi que les résultats, qui ont conduit à la qualification sont présentées dans la thèse et elles sont au coeur de mon travail. En parallèle j'ai travaillé à des simulations numériques des performances des capteurs à pixels pour l'ITk lorsqu'ils sont mesurés en faisceau test, en utilisant le logiciel «allpix-squared». Ce travail m'a permis de mieux comprendre la résolution spatiale des détecteurs pour ITk et plus particulièrement l'impact de la diffusion multiple sur la précision de reconstruction des hits. L'accord entre simulations et données est acceptable et mon travail servira aussi de base pour des études futurs. Pendant la thèse j'ai aussi investigué une nouvelle méthode de calibration du seuil pour les pixels dans la couche la plus interne (IBL) du trajectographe actuel d'ATLAS. Ce sous-détecteur est équipé avec une puce de lecture (FE-I4B) qui a montré une non-uniformité importante dans la collection de charge; cela est dû à un problème du système d'injection de charge de la puce même. La nouvelle méthode proposée repose sur le comptage de hits dus aux bruits ; le seuil est ajusté jusqu'à quand le taux d'occupation souhaité est atteint. Les résultats avec la nouvelle méthode montrent une bonne uniformité dans la récolte de charge et l'algorithme est maintenant disponible dans le système d'acquisition d'ATLAS.

Keywords: LHC – ATLAS - ITk - PIXELS - DETECTORS - TRACKER - INSTRUMENTATION

Contents

Abstract	iii
1 Introduction	5
1.1 The Standard Model	5
1.2 Beyond the Standard Model	9
1.3 Experimental state of the art	10
1.4 The Large Hadron Collider	12
1.5 The LHC upgrade Plan	14
1.6 The physics potential of HL-LHC	15
1.7 The ATLAS detector	17
1.8 ATLAS Inner Tracker	22
1.9 Status and deficiencies of the current Inner Detector	25
2 Silicon sensors for High Energy Physics	29
2.1 Working principle of silicon sensors	29
2.1.1 Charge carriers concentration	30
2.1.2 The pn junction	31
2.2 Charge generation and signal formation	33
2.3 Pixel detector technology	36
2.3.1 Manufacture and layout	38
2.3.2 Pixel sensor geometry	39
2.3.2.1 Planar pixel sensors	39
2.3.2.2 3D pixel sensors	42
2.3.2.3 Hybrid pixel sensors	43
2.3.2.4 Monolithic pixel sensors	43
2.4 Radiation damage	43
2.4.1 Bulk damage	44
2.4.1.1 Non Ionizing Energy Loss	44
2.4.1.2 Impacts of defects on silicon sensors	45
2.4.2 Surface damage	49
3 Planar pixel modules for the ATLAS detector	53
3.1 IBL pixel module	53
3.1.1 IBL sensors	54
3.1.2 FE-I4B readout chip	57
3.2 ITk pixel module	60
3.2.1 ITk pixel sensors	61
3.2.2 RD53A readout chip	63
3.2.3 ITkPixV1	65

3.3	Hybrid module assembly	68
3.3.1	Interconnection technology	70
3.3.2	Gluing	70
3.3.3	Wire bonding	72
3.3.4	ITk pixel module preparation	72
4	Pixel module calibration	77
4.1	Tuning setup	77
4.1.1	PyBAR	78
4.1.2	BDAQ53	78
4.1.3	Yarr	80
4.2	Charge calibration and chip tuning	80
4.2.1	Charge injection calibration	81
4.2.1.1	FE-I4B readout chip	81
4.2.1.2	RD53A readout chip	84
4.2.2	Chip tuning	85
4.2.2.1	Digital test	85
4.2.2.2	Analog test	85
4.2.2.3	Threshold tuning	85
4.2.2.4	Time over Threshold tuning	88
4.2.2.5	Noise occupancy scan	90
4.3	Threshold investigation in FE-I4B modules	90
4.3.1	Threshold discrepancy	91
4.3.2	Threshold baseline tuning algorithm	92
4.3.3	Threshold baseline tuning investigation	93
4.3.3.1	Tunings	94
4.3.3.2	Source scans	97
4.3.4	Implementation of threshold baseline tuning algorithm	100
5	Characterisation tools for ITk pixel modules	105
5.1	Electrical characterisation	106
5.2	EUDET beam telescopes	106
5.2.1	Data Acquisition software	108
5.3	Particle beam lines	109
5.3.1	CERN SPS	110
5.3.2	DESY	111
5.4	Reconstruction and analysis	112
5.4.1	Eutelescope	112
5.4.1.1	Converter	114
5.4.1.2	Clustering	114
5.4.1.3	Hitmaker	115
5.4.1.4	GBL-Align	116
5.4.1.5	GBL-fit	117
5.4.2	Tbmon2	118
5.4.3	Residuals	120
5.4.4	Multiple scattering	122

6	Performance of planar pixel modules	125
6.1	Electrical characterisation	126
6.1.1	ITk R&D pixel module	126
6.1.2	Thin pixel modules	127
6.2	Performance of planar pixel modules	130
6.2.1	R&D ITk planar pixel production	135
6.2.1.1	Hit efficiency for unirradiated modules	135
6.2.1.2	Hit efficiency of irradiated modules	136
6.2.1.3	Impact of threshold on hit efficiency	142
6.2.2	ITk pixel sensors Market Survey production	145
6.2.3	Future thin sensors production	153
6.3	Effect of thickness for planar pixel sensors	156
7	Simulated performance of ITk pixel modules	163
7.1	Allpix ²	163
7.2	Simulation setup	164
7.3	Simulation-based study on ITk pixel modules	165
7.3.1	Validation from telescope planes	166
7.3.2	Multiple scattering and pixel geometry	170
7.3.3	Multiple scattering and material budget	171
7.3.4	Multiple scattering and beam energy	176
7.4	Conclusions and outlook	177
A	Module assembly	185
B	Pixel DAQ infrastructure and algorithm integration	187
B.1	Implementation of the algorithm in PixelDAQ	188
B.2	Tuning procedure in SR1	190
C	Irradiation centers	193
C.1	Karlsruhe irradiation center	193
C.2	University of Birmingham	193
C.3	CERN Irrad facility	195
C.4	CYRIC	196
	Bibliography	201

List of Abbreviations

ACB	Analog Chip Bottom
ADC	Analog-Digital Converter
ATLAS	A Toroidal LHC Apparatus
APS	ATLAS Pixel Sensors
CCE	Charge Collection Efficiency
CMOS	Complementary Metal Oxide Semiconductor
CSA	Charge Sensitive Amplifier
DAQ	Data Acquisition
DCB	Digital Chip Bottom
DC	Double Column
DUT	Device Under Test
FCC	Future Circular Collider
FE	Front-End
GDAC	Global DAC
GRs	Guard Rings
HEP	High Energy Physics
IBL	Insertable Beta Layer
ID	Inner Detector
IP	Interaction Point
ITk	Inner Tracker
INL	Integrated NonLinearity
LPNHE	Laboratoire de Physique Nucléaire et des Hautes Énergies
MIP	Minimal Ionizing Particle
MPV	Most Probable value
MS	Market Survey
NIEL	Non Ionizing Energy Loss
PCB	Printed Circuit Board
PDR	Pixel Digital Region
PT	Punch-Through dot mechanism
PDF	Probability Density Function
SNR	Signal-Noise Ratio
TDAC	Threshold DAC
ToT	Time over Threshold
TLU	Trigger Logic Unit
TM	Temporary Metal
UBM	Under Bump Metalization

To my family.

Foreword

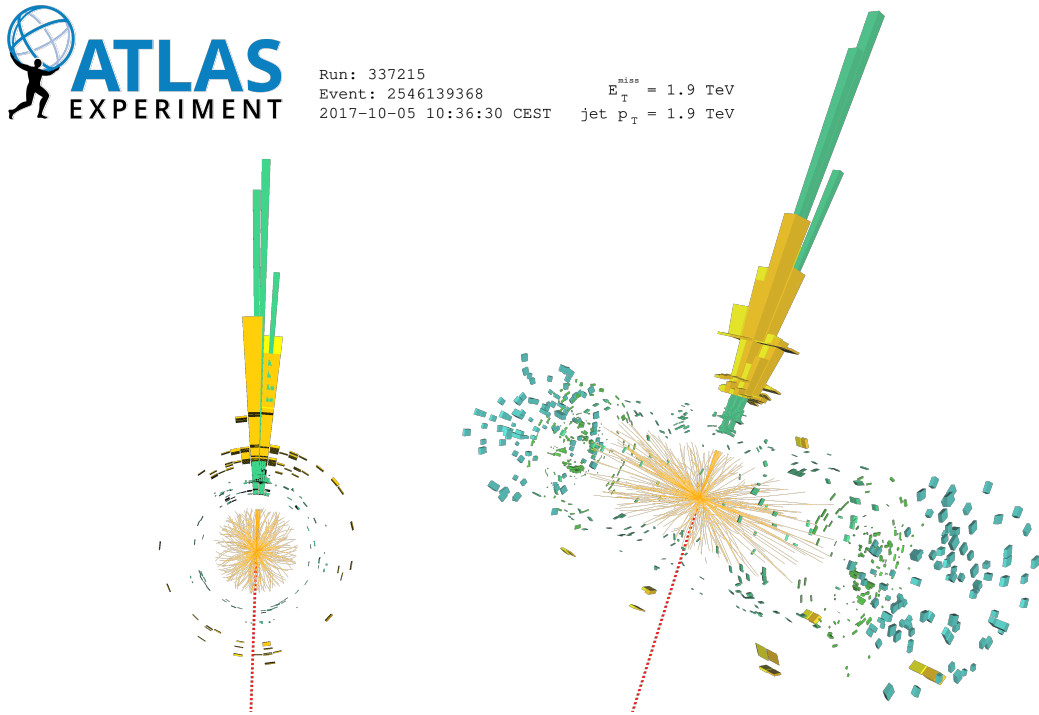


FIGURE 1: An ATLAS event recording of monojets collected in 2017 with a single jet. The green bars show energy deposit in the electromagnetic calorimeter, the yellow bar in the hadronic calorimeter, and the red line is the missing transverse momentum [1].

Within the past decade, our understanding of the universe has only gotten better and more precise. Particle physicists are interested in exploring the building blocks and fundamental laws of the universe. This exploration is a continuous human effort over the years beginning with the discovery of the positron in a bubble chamber to the most advanced detecting technologies available today that allow us to track hadrons at high energies as shown in figure 1. In particle physics the experimental and technological advances of the last 50 years are summarised in the Standard Model (SM) theory [2]. The SM describes particles and their interaction with the three fundamental forces of nature: the electromagnetic force, the weak force, and the strong force. The true movers and shakers of the universe. The SM theory classifies all the elementary particles in a model that predicted the completion of the theory. The last piece of the puzzle in the SM, the Higgs boson, which describes how the particles acquire mass, was observed 2012 by ATLAS and CMS collaborations at the Large Hadron Collider (LHC) [3, 4]. Now, we are extending the physics search to discover what is beyond the SM.

After several discoveries and precise measurements at the LHC in the last two decades, the discovery rate declined. Theoretical predictions beyond the SM include the observation of Super Symmetrical (SUSY) particles [5] and Dark Matter [6]. Yet, these predictions have not been experimentally observed. To discover new physics we will push the LHC design limits by increasing the luminosity ~ 7 times

greater than the original design goal of the machine. The increase of the luminosity will allow us to see rare interactions pointing to new physics, but it will also create a harsh environment for the current installed detectors at the LHC. Therefore, an upgrade of the detectors themselves will be necessary for operation at higher luminosity.

My contribution in this thesis revolved around the upgrade of the ATLAS trackers and branched into two parts focusing on pixel modules. I start in chapter 4 with the calibration methodology to operate the pixel module, introducing a novel tuning algorithm for the FE-I4B readout chip of the current IBL detector. The novel tuning method solves the local threshold asymmetry bias that rise from the standard calibration procedure using the charge injection circuit internal to the chip. The novel tuning method is independent of the injection circuit, it depends solely on the pixel occupancy and shows to eliminate the local threshold bias. My second contribution and core of the thesis presented in chapter 6 is the characterisation and analysis of the performance of the future Inner Tracker (ITk) planar pixel modules. The presented R&D for the ITk pixel modules plays a major role in qualifying sensors for the production of the ITk pixel detector. Complementing the performance results in chapter 7 I include simulation studies on their performance to further understand the physics behind the results and set expectations for the performance of the ITk pixel modules. This research work is crucial to understand how the detector will operate and the efficiency of its operation at the high luminosity phase.

For this thesis I introduce my work motivated by the reasons for upgrading the current ATLAS detector to reach high precision measurements and new physics. In the first chapter, chapter 1 I introduce the theoretical predictions and experimental consistency of the SM that the ATLAS and CMS experiments validate, and current status and deficiencies for the ATLAS experiment. I also introduce the LHC upgrades, the ATLAS experiment bridging the current pixel detector with the new ITk detector. In chapter 2 I remind the reader with the basic principles of silicon sensors. These principles are the fundamental layer for understanding pixel sensors and for the instrumentation upgrade and design of the ITk. In chapter 3 I introduce the pixel modules for both the current IBL detector and the ITk pixel detector. In this chapter I detail the sensor's designs along with the dedicated readout chips used in the development. To operate the pixel module, it must be calibrated. In chapter 4 I focus on the tuning and calibration of the pixel module. This chapter overviews tuning details for two different readout chips, for both the current IBL modules and for future ITk modules. I also present my conclusive study investigating the threshold tuning technique on the current IBL modules to solve a local asymmetry issue discovered during Run2. In chapter 5 I introduce the tools and methodology to characterise pixel modules with a particle beam. Testbeam experiments allows us to test the devices under conditions closer to real high luminosity LHC conditions. This chapter includes the description of the laboratory setup, testbeam setup, and the required softwares for track reconstruction and analysis to obtain the performance results of the modules. In chapter 6 I present the results and analysis of the performance of ITk pixel modules and also of thin modules for future detectors. I also present the results from the Market Survey campaign for ITk planar pixel modules that are considered in the Final Design Review. Performance results presented in this chapter helped qualify ITk pixel modules for the production phase. Finally, in chapter 7 I extend my work to simulate the testbeam experiments. The simulation study helped quantify and gain a conclusive understanding of multiple scattering effects in the testbeam data trying to optimize the experimental methodology in characterising pixel modules, and to provide future expectations for the performance of ITk modules. In conclusion of the thesis, a summary of the ITk pixel detector results and plans are presented with an outlook of future activities in the domain of ITk module construction plan.

64 *"Those who are inspired by a model other than nature, labor in vain. "*

65 Leonardo Da Vinci

Chapter 1

Introduction

1.1 The Standard Model

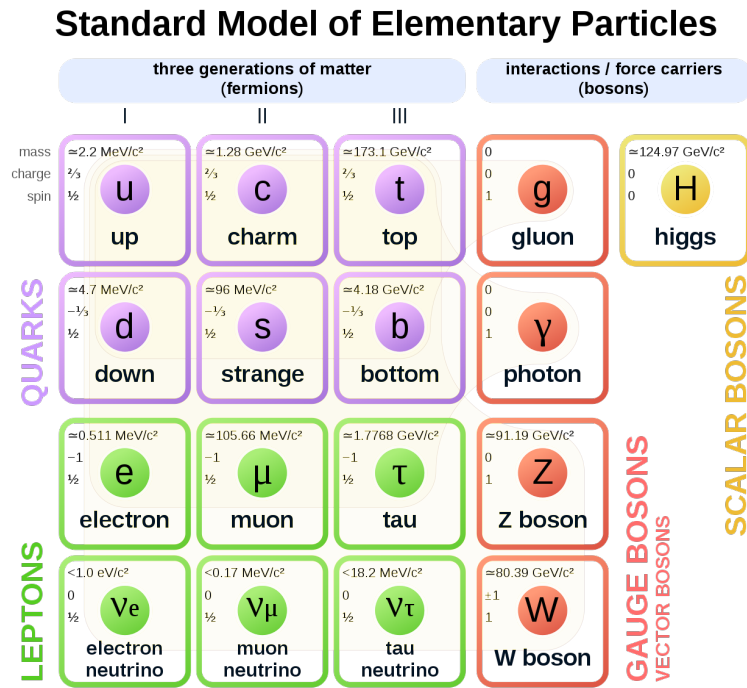


FIGURE 1.1: The Standard Model theory classification of fundamental particles [7].

The Standard Model (SM) [2] is a theoretical framework founded on the principles of Quantum Field Theory to describe elementary particles and their interactions [8]. The SM theory has gained solid experimental confirmation over the years interpreting observables and making precise predictions verified in experiments. Particles that have been experimentally observed from the SM theory are shown in figure 1.1. The SM classifies fundamental particles into two categories, fermions and bosons as presented in figure 1.1. Fermions, which have a half-integer spin and behave according to the Fermi-Dirac statistics are massive particles that can interact with the natural forces. Bosons, which have an integer spin and behave according to the Bose-Einstein statistics are particles that are classified as force mediators. Fermions that are sensitive only to the electromagnetic force and the weak force are called leptons; they do not interact with the strong force and therefore have null color charge. Fermions that are sensitive to the strong force are called quarks and they carry a color charge. There exist 6 lepton types as shown in figure 1.1 in their classifications, (electron, muon, tau and their associated neutrino) and 6 quarks (up,

down, charm, strange, top, bottom (beauty)) as fundamental fermions in total. Leptons and quarks are further classified by the SM into three "generation" families. The first generation consists of two of the lightest leptons (e and ν_e) and quarks (u and d), which are stable and make up "matter". The second and third generations appear to have identical properties (gauge interactions), they only differ by their mass and their flavour quantum number [2]. The generational pairing of leptons and quarks (doublets) is related to the $SU(2)$ group symmetry nature of the weak interaction. A group symmetry theory (such as $SU(2)$) provides the natural mathematical language to formulate symmetry principles and to derive their consequences in physics. The relation between symmetries and conservation laws is expressed by Emmy Neother's theorem [9], one of my personal favorite physicists and female icon. An example that illustrates how fundamental interaction rise as consequence of a local symmetry is the conservation of electric charge in Quantum ElectroDynamic theory (QED). The most stringent QED test comes from the high-precision measurements of the e and μ anomalous magnetic moments [10–12]. While the former has validated the predictions of QED to a very high accuracy, recent tensions in the measurement of the latter [13] could be a hint of physics beyond the SM.

Gauge theory is a promising theory because it can reduce the full spectrum of physical interactions to those who are invariant under a continuous group of local transformations [14]. Two particles interact with each other in a gauge field via the exchange of a quanta called the gauge boson. Each of the natural forces is associated with a gauge boson. Thus, the bosons are the mediators of the three natural forces, the photon γ is the mediator of the electromagnetic force, the W^\pm and Z bosons are the mediators of the weak force, and the gluons are the mediators of the strong force. While the Higgs boson is not known to be associated with a force mediator, it is responsible for the EW symmetry breaking mechanism that will be discussed later on.

The concept of gauge theory can be generalized as a tool to gauge the interactions of all three natural forces. The electromagnetic force and weak force interactions were unified to the so called Electroweak theory (EW). EW transformation is invariant under local group symmetry $SU(2)_L \times U(1)_Y$. The SM including the strong force is a gauge theory based on the symmetry group $SU(3)_c \times SU(2)_L \times U(1)_Y$. The symmetry group $SU(3)_c$ describe the strong interactions, which corresponds to the Quantum Chromodynamics theory (QCD) of the SM. As QCD is a non-Abelian theory, it leads to self coupling of gluons, which are the force mediators. For the SM Lagrangian to be invariant under the $SU(3)_c$ group, the Gell-Mann matrices are introduced to be the group generators.

The gauge bosons of the $SU(3)_c$ group are massless particles, while this is also true for the photon field, the physical W^\pm and Z bosons have been predicted and measured to be heavy objects. Therefore, the gauge symmetry is broken at the vacuum value, which triggers the Spontaneous Symmetry Breaking (SSB) of the electroweak group to the electromagnetic subgroup. The SSB mechanism generates the masses of the weak gauge bosons, and gives rise to the physical scalar particle, the so-called Higgs boson [15].

In order to generate masses, we need to break the gauge symmetry in a way to get non-symmetric results from a symmetric Lagrangian. The physical Higgs field H interacts with itself generating both self-interaction terms and mass. These terms arise from the Higgs potential in the perturbative expansion of the Higgs complex scalar doublet, ϕ [16]. Consider the potential $V(\phi)$ is the Higgs potential,

$$V(\phi) = \mu^2 \phi^\dagger \phi + h(\phi^\dagger \phi)^2. \quad (1.1)$$

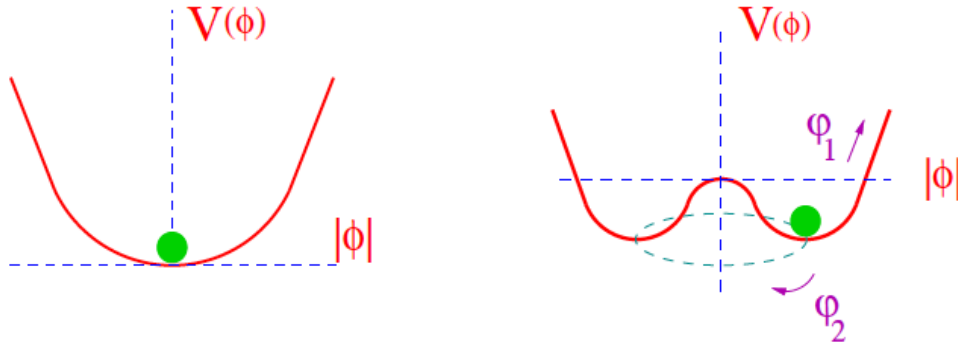


FIGURE 1.2: Shape of the scalar potential for $\mu^2 > 0$ (left) and $\mu^2 < 0$ (right). In the second case there is a continuous set of degenerate vacuum, corresponding to different phases θ , connected through a massless field excitation ϕ_2 [2].

Where the Vacuum Expectation Value (VEV) from the Higgs potential is $v = \sqrt{-\mu^2/h}$. The series expansion of the Higgs doublet around the expectation value v is equal to

$$hv^2H^2 + hvH^3 + \frac{h}{4}H^4. \quad (1.2)$$

The first term in the expansion describes the mass of the Higgs boson $m_H = \sqrt{2hv^2}$. The second and third terms describe the tri-linear and quartic self-interaction of the Higgs boson with their coupling strength h . To have a ground state in the potential $V(\phi)$ there are two possibilities:

1. $\mu^2 > 0$: there's only a trivial minimum at $\phi = 0$. It describes a massive scalar particle with a single ground state.
2. $\mu^2 < 0$: there's an infinite number of degenerate states of minimum energy at $\phi_0(x) = \frac{v}{\sqrt{2}}\exp(i\theta)$, responsible for about 20% of the energy content of the universe. By choosing a solution for θ as the ground state, the symmetry gets spontaneously broken describing the excitation around a flat direction in the potential.

Both potentials are shown in figure 1.2 for visualization. Since the latter excitations at $\mu^2 < 0$ do not cost energy, they correspond to a massless state. The fact that there are massless excitations in the SSB mechanism is a completely general result, known as the Goldstone theorem [17]. The gauged scalar Lagrangian is invariant under $SU(2)_L \times U(1)_Y$ transformation. Once we choose a particular ground state the symmetry gets spontaneously broken to the electromagnetic subgroup $U(1)_{QED}$, which remains a true symmetry of the vacuum. According to the Goldstone theorem, three massless states should then appear. The vacuum expectation value of the neutral scalar of the Lagrangian then generates a new quadratic term for the W^\pm and the Z bosons, i.e., those gauge bosons have acquired mass.

It is forbidden to directly add the fermion mass in the $SU(2)_L \times U(1)_Y$ symmetry, since it would imply mixing of left- and right-handed components. However, the Higgs doublets allows the expression of fermion masses in a Yukawa Lagrangian where the quarks and leptons are left-handed doublets for one generation mix with their corresponding right-handed fermion singlets. The mass of the fermions can then be expressed as

$$m_f = y_f \frac{v}{\sqrt{2}} \quad (1.3)$$

where y_f are the Yukawa coupling free parameters in the SM. Therefore, the masses of fermions cannot be predicted theoretically; instead, their estimation is an experimental endeavour.

The discovery of the Higgs boson particle in 2012 by the ATLAS and CMS Collaboration [18] confirmed the SM prediction of the existence of a quantum field associated to it, which is responsible for the generation of masses of fundamental particles. After the observation, a number of measurements have been performed to quantify the properties of this particle, such as: mass, spin and parity quantum numbers, and couplings. The ATLAS and CMS collaboration excluded several hypothesis for the spin and parity of the Higgs in favour of the SM hypothesis at more than 99.9% confidence level. Measurements of the Higgs, not just the self-interactions, but the trilinear and quartic interaction, is equivalent to the measurement of each term in the Higgs Lagrangian, which would fully determine the shape of the Higgs potential. Measurements of the strength of the Higgs boson self-interactions and their comparison to SM predictions are necessary to verify the electroweak symmetry breaking mechanism of the SM. Hence, precision measurements of the electroweak observables are of great importance.

Higgs production modes

The Higgs boson couples to all massive particles and to itself. The Higgs bosons' couplings to fermions are proportional to the mass of the particles with which it is interacting. The Higgs bosons' couplings to bosons are proportional to the square of the mass of the boson. Hence, it preferentially interacts with the heaviest particles in the SM: top-quarks, Z , W^\pm , and b-quarks. The coupling behaviour determines the way in which the Higgs bosons are produced. One of the main production mode that is relevant to the high luminosity phase of the LHC (HL-LHC) is the Vector Boson Fusion (VBF). The VBF production is a pair of vector bosons (either ZZ or W^+W^-) that radiate from quarks in the colliding beams as shown in the Feynman diagram of figure 1.3(a). These pair of massive bosons fuse to produce the Higgs boson.

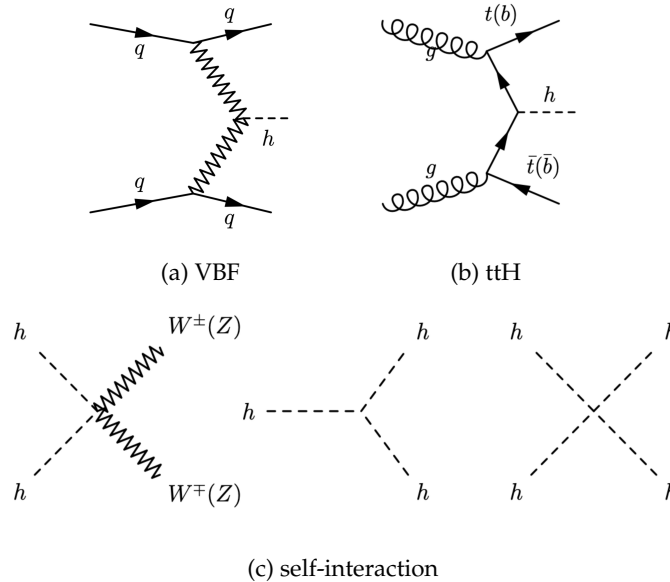


FIGURE 1.3: Feynman diagrams (top) for VBF Higgs production, (bottom) trilinear and quartic Higgs coupling.

Another Higgs production mode that is mainly expected to improve on the HL-LHC are the ttH and bbH. The Feynman diagram of this production is shown in figure 1.3(b). They are the rarest Higgs productions from top-quarks or bottom-quarks fusion that should be accessible with the increase of

luminosity. Moreover, the Feynman diagrams of Higgs self interactions are shown in figure 1.3(c.) The measurement of the strength of the trilinear Higgs coupling is one of the goals of the HL-LHC physics [19]. The trilinear Higgs couplings is expected to be in reach with 3000 fb^{-1} at $\sqrt{s} = 14 \text{ TeV}$, while the quartic Higgs coupling may only be accessible in future colliders [20].

1.2 Beyond the Standard Model

In all of the great achievements of the SM, it does fail to explain open issues such as, the origin of Dark Matter (DM) [21], the matter/antimatter asymmetry in the universe [22], the hierarchy problem [5], and the unification of gravity as a fundamental force. These problems lead to the idea that the SM may only be an effective theory, which works very well at the energies tested until now, but needs to be extended to describe the particle interactions at a higher energy scale. Perspectives Beyond the Standard Model (BSM) are the key reasons to pursue the hadron collider physics program. For example, the hierarchy problem is one of main motivation to expect new physics close to the electroweak scale. It refers to radiative corrections to the Higgs mass parameter, which can receive contribution from new physics at ultraviolet scale. One example is the scale at which gravity becomes strongly coupled, usually identified with Planck scale. Symmetry-based solutions to the hierarchy problem of the Higgs boson requires the existence of TeV-scale particles. This is the basis for theories like the Supersymmetry (SUSY) theory as well as extra-dimensional models that can naturally give rise to such TeV-scale particles and solve the hierarchy problem. Also, some SUSY particles are promising Dark Matter candidates [23].

Dark Matter is one of the big puzzles of fundamental physics. While there is stunning evidence from cosmology for its existence, there is no particular indication on what it actually is. It could be made of particles, but it is not the only option. However, if Dark Matter is made of weakly interacting massive particles (WIMPs), then what is observed can only be reproduced for a relatively small window in its mass/coupling parameter space, which makes it relevant for collider experiments. Several theoretical constructions addressing the hierarchy problem also predict a WIMP as Dark Matter candidate [20, 24].

Another big mystery of the SM is flavour [25]. Why are there such hierarchies among fermion masses?, and how neutrino masses arise?. These are two compelling questions of fundamental physics. The generation of the flavour structure in the SM by the Yukawa couplings may be correlated to a scale much above the electroweak scale. Thus, precision flavour observables are sensitive to ultraviolet physics. The observation of extremely rare flavour transitions would allow us to set constraints on new physics corresponding to scales of hundreds or thousands of TeV, which are completely inaccessible to direct searches.

In parallel to accessing rare particles by increasing their luminosity, current colliders could extend the new physics searches by looking for particles that are long-lived rather than promptly decaying. Particles with macroscopic decay length beyond the collider time scale can elude detection because of triggers designated for prompt decays, or complicated backgrounds. Long-Lived Particles (LLP) [26] models are theoretically motivated to result in stable states in the SM theory and equally well beyond the SM. New detector upgrades will enable the search in the LLP regime with new trigger strategies.

All the extensions of the SM mentioned above share the prediction of new physics close to the electroweak scale i.e. few hundreds of GeV.

1.3 Experimental state of the art

It is a remarkable era for cosmology, astrophysics and High Energy Physics (HEP). The Large Hadron Collider (LHC) is at the forefront of attempts to understand the fundamental nature of the universe. The predictions of the SM have been tested and confirmed by several experiments and the results have been nearly always in good agreement up to an energy scale of 1 TeV. The experimental results for all the fundamental particles are presented in the review of Particle Data Group [27]. Table 1.1 shows the measured particles mass and charge for fermions and table 1.2 for bosons. Global fits of the SM have combined the accurate theoretical predictions with the electroweak precision observables to constrain the masses of the top-quark and the Higgs boson [28]. These observables become sensitive probes of new physics limited in part by the accuracy of the theoretical calculations.

TABLE 1.1: Measurements of mass and charge for fermions. Adapted from [27].

Fermions (spin 1/2)				
	Quarks		Leptons	
Generation 1	u	d	e	ν_e
Mass (MeV)	$2.2^{+0.6}_{-0.4}$	$4.7^{+0.5}_{-0.4}$	0.511	$<2\text{eV}$
Charge (e)	$+2/3$	$-1/3$	-1	0
Generation 2	c	s	μ	ν_μ
Mass (MeV)	1280 ± 30	96^{+8}_{-4}	105.6	$<2\text{eV}$
Charge (e)	$+2/3$	$-1/3$	-1	0
Generation 3	b	t	τ	ν_τ
Mass (GeV)	$4.18^{+0.04}_{-0.03}$	173.1 ± 0.6	1.776	$<2\text{eV}$
Charge (e)	$+2/3$	$-1/3$	-1	0

TABLE 1.2: Measurements of mass and charge for bosons. Adapted from [27].

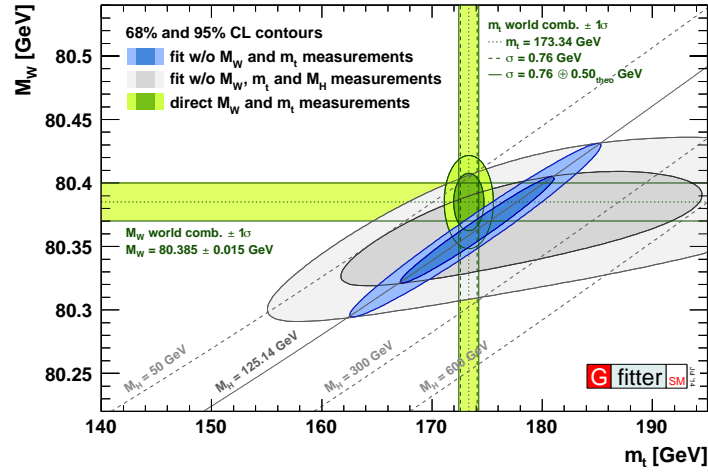
Type	W^+, W^-	Z	γ	gluon	Higgs boson
Interaction	Weak		Electromagnetism	strong	-
Charge (q)	± 1		0	0	0
Mass (GeV)	80.399	91.188	$< 10^{-24}$	0	125.3
Spin	+1		+1	+1	0
Interactions with	quarks, leptons and Higgs boson		charged leptons and quarks	quarks	massive particles

The discovery of the Higgs boson by ATLAS and CMS Collaborations confirmed the SM prediction of the existence of a quantum field that is responsible for the generation of mass of the fundamental particles. A number of measurements on the Higgs boson is performed to quantify the properties of the particle. The mass of the Higgs measured by ATLAS and CMS collaboration yields a combined value of $m_H = 125.09 \pm 0.21(\text{stat}) \pm 0.11(\text{sys}) \text{ GeV}$ [18]. The spin-parity of the observed particle agrees with the SM hypothesis. It is found that couplings to vector bosons are compatible with SM expectation within $\sim 10\%$ uncertainty, while for heavier fermions (top- and bottom-quark, and τ) the uncertainty is in the order of $15 - 20\%$ [16]. Thanks to the recent observation of the $t\bar{t}H$ production and $H \rightarrow b\bar{b}$ by ATLAS and CMS collaborations the uncertainty has improved [29].

Global fits of the SM have traditionally combined electroweak precision observables with accurate theoretical predictions to constrain the top quark and Higgs boson masses [30]. Some of the fit results of observables used in the global electroweak fit are summarised in table 1.3. The table shows the results of the full fit including all the experimental data. Assuming the measured boson to be the SM Higgs boson,

TABLE 1.3: Fit results for the observables used in the global electroweak fit including all experimental data. Adapted from [31].

Parameter	Free in fit	Fit result
M_H [GeV]	yes	125.1 ± 0.2
M_W [GeV]	-	80.359 ± 0.006
Γ_W [GeV]	-	2.091 ± 0.001
M_Z [GeV]	yes	91.1882 ± 0.0020
Γ_Z [GeV]	-	2.4947 ± 0.0014
$\sin^2\theta_{eff}^l$ (Tevt.)	-	0.23152 ± 0.00006
m_t [GeV]	yes	172.83 ± 0.65

FIGURE 1.4: Contours of 68% and 95% confidence level obtained from scans of fits with fixed variable pairs M_W vs. m_t . The narrower blue and larger grey allowed regions are the results of the fit including and excluding the M_H measurement, respectively. The horizontal/vertical bands indicate the 1σ regions of the M_W and m_t measurements respectively [31].

by inserting the measured mass into a global fit of the SM theory it constrains the electroweak sector of the SM. Electroweak observables such as the W boson mass, M_W , and the effective weak mixing angle, $\sin^2\theta_{eff}$, can be predicted with precision exceeding that of the direct measurements [30].

An important consistency test of the SM is the simultaneous indirect determination of top-quark mass, m_t and W boson mass, M_W . Figure 1.4 shows the confidence level profile between them. The figure shows contours estimated by Gfitter for the SM model [32]. It shows the fit model scenarios with direct M_H included (blue), or not included (grey). Both contours are in agreement with the direct measurements (in green) at 68% and 95% confidence level. Measurements to be performed at future colliders will increase the experimental precision of these and other electroweak observables. The direct measurement result of the Higgs mass is shown explicitly in figure 1.5 with weighted data points with errors, and the result of the simultaneous fit to all categories [33]. The fitted parameters of interest for the signal are the Higgs boson mass and the signal strength, defined as the yield normalized to the SM prediction and applied to all production modes.

The progress of the SM theory is based on the efforts of many experiments. Results of figure 1.5 are the global fit of the electroweak sector of the SM using the latest experimental data and theoretical input [31]. The fit confirms the consistency of the SM and slightly improves the precision of the indirect determination of the key observable of the electroweak sector. To match the experimental precision significant theoretical progress is required to improve the uncertainties related to the prediction of the M_W

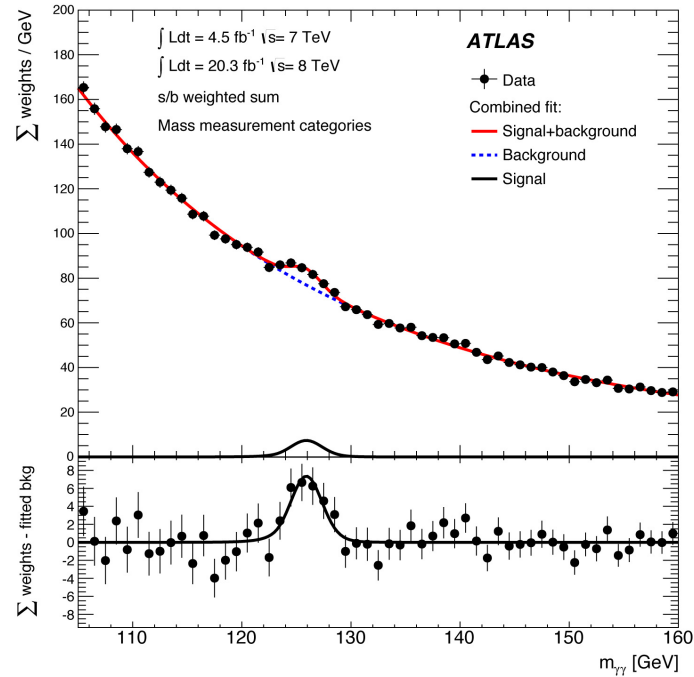


FIGURE 1.5: Invariant mass distribution in the $H \rightarrow \gamma\gamma$ analysis for data (7 TeV and 8 TeV samples combined), The fitted signal plus background is shown along with the background-only component of this fit. The bottom plot shows the difference between the summed weights and the background component of the fit.[33]

and $\sin^2\theta_{eff}$, which are dominantly affecting the fit results. The outstanding performance of the LHC experiments has inspired a diverse research program to extend the reach of the hadronic spectroscopy. The legacy of the LHC is therefore in confidence to push the reach for precision and sensitivity beyond what was originally assumed possible. These studies underscore the importance of collecting a dataset with larger integrated luminosity to give access to the rarest phenomena that can critically reduce systematics or bypass limitations with new analyses leading to measurement with unanticipated precision. It will provide the relevant sensitivity to sectors beyond the SM and ultimately allow us to get closer to answering the big questions of our field.

1.4 The Large Hadron Collider

The Large Hadron Collider (LHC) [34] in the European organization for nuclear research (CERN) [1] beneath the France-Switzerland border is the current most powerful particle accelerator to study the fundamentals of particle physics. The LHC is a circular collider with two counter-circulating particle beams that accelerates and collides protons. The circular concept is preferred so particles can pass the acceleration chain several times to gain energy and increase the probability that particles participate in a collision due to multiple passes. The current CERN accelerator complex shown in figure 1.6 includes many accelerators which are used to boost for the LHC ring and also used in a wide range of particle experiments. Their respective location on the LHC line is also shown the CERN complex figure. The protons delivered to the LHC experiments originate from a hydrogen bottle. The hydrogen atoms are ionized and separated where the protons are injected in the first accelerator, the LINAC 2, to be accelerated to an energy of 50 MeV. Then the protons reach the Booster synchrotron to be accelerated to 1.4 GeV. Then to the Proton Synchrotron (PS) where they become ultra-relativistic proton bunches with energy of 25 GeV and bunch structure of 81 bunch packets in 25 ns spacing [34]. Afterwards, an accumulation of

CERN's Accelerator Complex

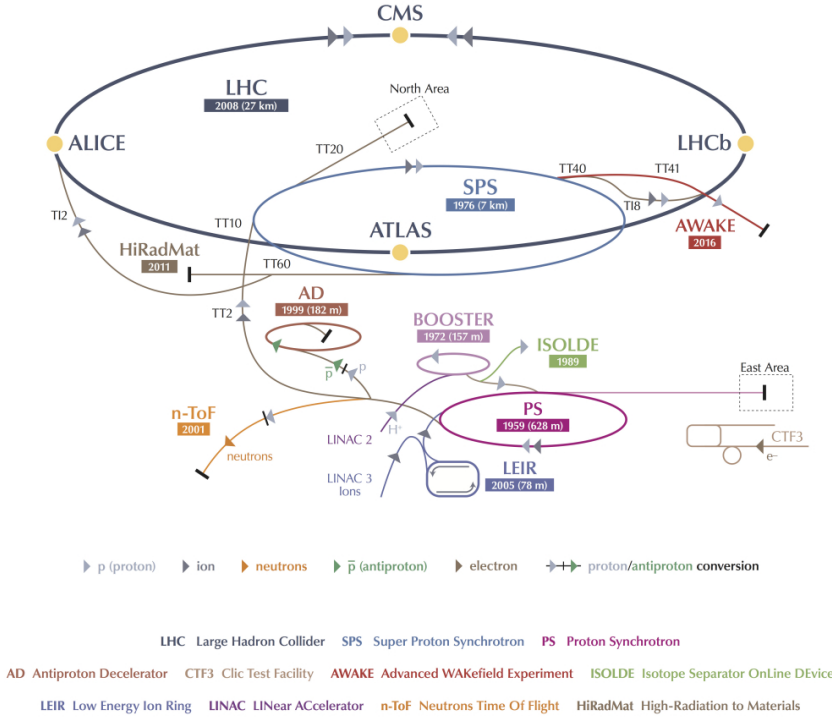


FIGURE 1.6: Scheme of the CERN accelerator complex [39]

three 81 bunches are directed to the Super Proton Synchrotron (SPS) to accelerate the protons to 450 GeV . Eventually, the LHC is filled with the 2808 bunched per beam and are accelerated up to 6.5 TeV . There are four main experiments at the LHC that receive the beam and record the outcomes of the collisions; ATLAS [35], CMS [36], ALICE [37] and LHCb [38].

The proton beam consists of several bunches with about 1×10^{11} protons each bunch. Up to 2808 (per LHC ring) equally spaced bunches are stored in the ring. The ultra-relativistic proton bunches move almost at the speed of light leading to proton collisions in the detector every 25 ns . The corresponding collision frequency of 40 MHz is also called *bunch crossing frequency*. The collisions are independent so the particle interactions within one bunch collision is called an *event*. There is a non-negligible probability that one single bunch crossing may produce multiple proton-proton interactions, *pile-up events*. Bunch crossing frequency imposes constraints on the timing precision of the particle detectors in order to be able to distinguish different events. The rate of events per collision dN/dt is proportional to the instantaneous luminosity \mathcal{L} and the total cross-section σ_i by

$$\mathcal{L} [\text{cm}^{-2}\text{s}^{-1}] = \frac{1}{\sigma_i} \cdot \frac{dN}{dt}. \quad (1.4)$$

The increase of the luminosity increases the probability of occurrence for rare events. Therefore, the luminosity quantifies the performance of a particle accelerator and depends on the revolution frequency f of revolving N particles in each beam where the cross section $\sigma_{x,y}$ is a measure of the transverse beam

profile, this relation is given by

$$\mathcal{L} = \frac{fN^2}{4\pi\sigma_x\sigma_y}. \quad (1.5)$$

The *integrated luminosity* is often used to describe the total data delivered

$$\mathcal{L}_{int} [b^{-1}] = \int \mathcal{L} dt \quad (1.6)$$

The nominal design of integrated luminosity at the LHC is $300 fb^{-1}$ ($1barn = 10^{24} cm^2$) that should be reached by the end of LHC run time in 2024.

The statistical measurement error for the observation of a particle reaction or property depends on the number of observations N by

$$\sigma_{stat} \propto \frac{1}{\sqrt{N}}. \quad (1.7)$$

Thus the statistical error halves when the sample size is quadrupled. A way to increase the integrated luminosity and therefore the measurement precision, is to increase the instantaneous luminosity and the measurement time. For this reason, the LHC will undergo an upgrade schedule to increase its instantaneous luminosity every 3-5 years to extend the physics program reach. The LHC upgrade schedule and the HL-LHC phase are discussed in the following.

1.5 The LHC upgrade Plan

The upgrade plan of the LHC is summarised in figure 1.7. In the first two years of operation in 2011 and 2012, the LHC delivered center of mass energies $\sqrt{s} = 7 TeV$ and $\sqrt{s} = 8 TeV$ respectively. The time-integrated luminosity reached up to $30 fb^{-1}$. With this set of data parameters, it was announced by CERN in July 2012 the discovery of the Higgs boson at a mass of about $125 GeV$.

In 2013-2014, during the LHC first long-shutdown (LS1), the machine underwent an upgrade to reach its original design value of instantaneous luminosity $\mathcal{L} = 1 \times 10^{34} cm^{-2}s^{-1}$. The LHC operated with center of mass of $\sqrt{s} = 13 TeV$ proton collision from 2015 onwards.

After the second long-shutdown (LS2) in 2019-2021, the LHC will operate stably at an instantaneous luminosity around $\mathcal{L} = 2 \times 10^{34} cm^{-2}s^{-1}$. With this value the LHC will reach the full potential of its original design colliding particles at a center of mass energy of $\sqrt{s} = 13 TeV$ and trying to deliver an integrated luminosity of $300 fb^{-1}$. The main purpose of the LS2 is to upgrade the LHC injectors, and further maintenance to be performed. The running time necessary to halve the statistical error for precision measurements of the SM after 2021 will be more than 10 years.

To maintain scientific progress and to exploit the LHC full capacity, it will have a decisive increase of its instantaneous luminosity after 2024. In the third long-shutdown (LS3) in 2025-2027, the upgrade aims to level the peak luminosity to $\mathcal{L} = 5 \times 10^{34} cm^{-2}s^{-1}$ transforming the LHC into High Luminosity-LHC [41], where the physics of this thesis is focused. In the HL-LHC phase, the machine will aim to deliver $3000 - 4000 fb^{-1}$ of integrated luminosity over the duration of Phase-II, which is estimated to be around 10 years.

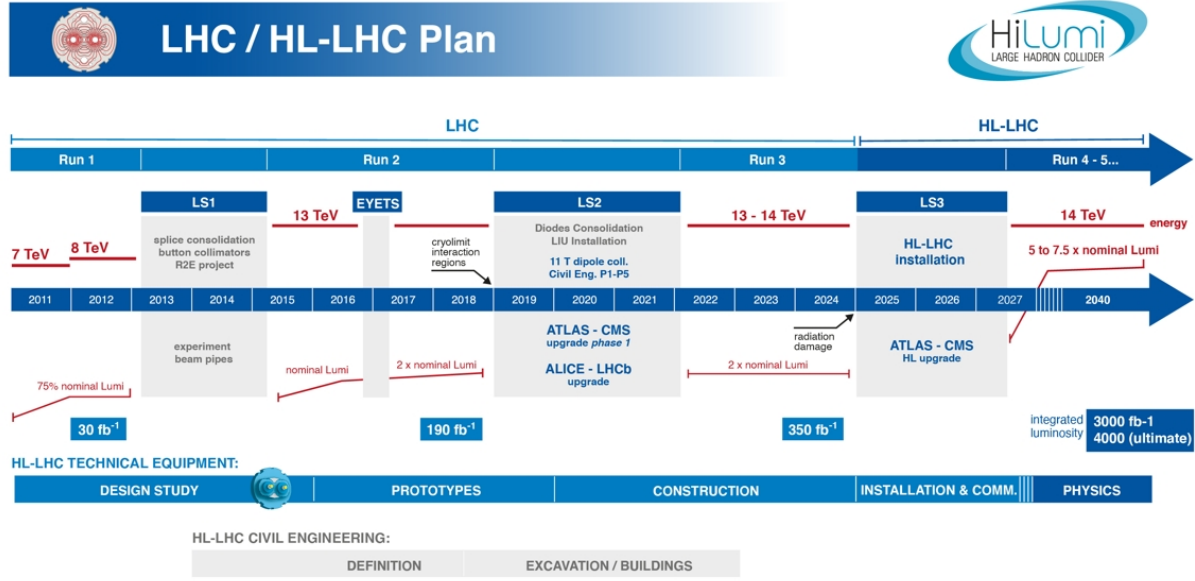


FIGURE 1.7: Upgrade schedule of the LHC for increased beam energy and luminosity. Long shut down periods of about 2 years are used to upgrade the particle detectors [40].

The current LHC system will become vulnerable to breakdown and aging, and it will become a bottleneck for operation in a higher radiation environment. Systems that will need an upgrade in the HL-LHC regime include: inner quadrupoles magnets, cryogenics, collimation, electronics and superconducting links. The LHC experiments will also have to undergo upgrades as an increase in the luminosity will include two main challenges,

- Increase of instantaneous luminosity leads to more interactions per bunch crossing to access rare events. Thus leading to high occupancy that requires finer granularity and larger bandwidth. The high granular pixel sensors for ITk is a main focus of this thesis which will be discussed section 3.2.
- Increase of integrated luminosity leads to more radiation damage in the detectors requiring more radiation-tolerant schemes. Thus leading to investigate thinner sensors for radiation tolerance as will be discussed in section 6.2.

These challenges are particularly true for the innermost detectors, the trackers. The main parameters foreseen for high luminosity operation are shown in table 1.4 where the 25 ns bunch spacing is the baseline operation mode.

1.6 The physics potential of HL-LHC

The analysis of LHC data has confirmed the great physics potential of the LHC to perform precise and sensitive measurements. Collecting large amount of data will give access to new physics and will also be critical to reduce the uncertainties of unknown observables. The determination of the Higgs boson properties, and their connection to EW symmetry breaking is the primary target of the HL-LHC physics program [20]. The HL-LHC program motivates searches for additional Higgs bosons in EW symmetry breaking driven by theories beyond the SM (BSM). The main Higgs boson couplings are expected to be measured at HL-LHC with a precision at the percent level.

TABLE 1.4: Beam parameters for LHC and High Luminosity LHC for proton collisions for the 25 ns bunch spacing [41].

Parameter	[Unit]	Nominal LHC	HL-LHC
Beam energy in collision	[TeV]	7	7
Particle per bunch n_b	[10^{11}]	1.15	2.2
Number of bunches N_b		2808	2748
Beam current	[A]	0.58	1.09
Levelled luminosity \mathcal{L}_{lev}	[$10^{34} cm^{-2} s^{-1}$]	1	5
Peak luminosity \mathcal{L}_{peak}	[$10^{34} cm^{-2} s^{-1}$]	1.0	7
Collisions per bunch crossing $\langle \mu \rangle$	[events]	19	200

A high granular detector will be able to reconstruct with high accuracy the large statistics expected at HL-LHC that will particularly help the study of complex final states, such as those arising from ttH production. The constraining power of the current ttH analyses has been limited to plausible improvements in the theory predictions, in particular in the $H \rightarrow b\bar{b}$ channel. Invisible Higgs boson decays will be searched for at HL-LHC in all production channels, Vector Boson Fusion (VBF) being the most sensitive. The combination of ATLAS and CMS Higgs boson coupling measurements will set an upper limit on the Higgs invisible branching ratio of 2.5%, at the 95% confidence level [20]. Higgs studies at HL-LHC will enhance the sensitivity to BSM physics exploiting indirect probes via precision measurements. Precision measurements is an important tool to search for beyond the SM physics associated to mass scales beyond the LHC direct reach. This done under the scope of the SM as an effective field theory framework.

The measurement of production of pairs or triplets of EW gauge boson will be of great importance to test the mechanism of EW symmetry breaking, since it can signal the presence of anomalous EW couplings, and of new physics at energy scales beyond the reach of direct resonance production. First observations of EW multiboson interactions have recently been achieved in vector boson scattering (VBS) of WW and ZZ and a fuller picture is expected to be accessible at HL-LHC, by statistics, but also through improved detector instrumentation and acceptance in the forward direction [20].

The current world average value of the weak mixing angle is $\sin^2\theta_{eff} = 0.23153 \pm 0.00016$, which is determined based on data from LEP [42] and from SLD [43]. A precision extraction using HL-LHC data will help reduce the uncertainty or discover new physics. where in HL-LHC the statistical precision of $\sin^2\theta_{eff}$ measurements with ATLAS, CMS and LHCb will be better than 5×10^{-5} . Another key measurement to improve is the W boson mass M_W . The HL-LHC will greatly reduce systematics by limiting the Parton Distribution Function (PDF) sensitivity via the extended coverage of $|\eta| < 4$ and via its own PDF constraints. Furthermore, the LHCb experiment combined with enhanced B-physics capabilities of ATLAS and CMS will enable a wide range of flavour observables to be determined at HL-LHC with unprecedented precision [44]. The possibility to test beyond the SM scenarios is motivated by long-standing problems such as EW naturalness, Dark Matter (DM), the flavour problem, neutrino masses, the strong CP problem, and baryogenesis, to name a few. All these new physics manifestations require the existence of new particles that can be search for in HL-LHC profiting from the larger statistics, slightly larger energy at 14 TeV center of mass, and upgraded instrumentations and detectors. Highlights of the HL-LHC expectations for beyond the SM scenarios are summarised in the HL-LHC physics report in reference [20].

1.7 The ATLAS detector

The goal of A Toroidal LHC ApparatuS (ATLAS) experiment is to record and track the decay product of the particles produced by the proton-proton collision of the LHC at the interaction point (IP). The debris of the elementary particles that are created during the interaction decay almost immediately after their production but can be reconstructed from their decay products. The energy, momentum and charge of a particle can be measured, which also yield information about the mass of the particles to identify them. A magnetic field is typically used to bend charged particle trajectories. The charge is derived from the bending direction while the momentum is reconstructed from the curvature. The energy of the particles can be measured by stopping them promptly by the detector. In context, these benchmark physics goals can be turned into a set of general requirements for the ATLAS detector that include:

- fast, radiation-hard electronics and sensor elements. In addition to high detector granularity to reduce the influence of overlapping events.
- large acceptance in pseudorapidity η (refer to equation 1.8).
- good charged particle momentum resolution and reconstruction efficiency.
- very good electromagnetic (EM) calorimetry for electron and photon identification and measurements, complemented by full-coverage hadronic calorimetry for accurate jet and missing transverse energy measurements.
- good muon identification and momentum resolution over a wide range of momenta and the ability to determine unambiguously the charge of high p_T muons.
- highly efficient triggering on low transverse-momentum objects with sufficient background rejection.

The ATLAS detector [35] is a general-purpose detector built on one of the LHC interaction points 100 meter under ground. The ATLAS detector consist of many sub-detectors arranged in cylindrical symmetry and covers almost all the 4π solid angle surrounding the collision point.

ATLAS Coordinate system

The detector description follows a common right-handed coordinate system. The origin is located at the interaction point in the center of the detector. The z axis points along the beam line while the x axis points towards the center of the LHC ring and the y axis points upwards. As shown in figure 1.8 the azimuthal angle ϕ is measured around the beam axis, and the polar angle θ is the angle from the beam axis. The pseudorapidity η is defined in terms of the polar angle as

$$|\eta| = -\ln[\tan(\theta/2)]. \quad (1.8)$$

As the value $|\eta| = 0$ it describes the direction perpendicular to the beam line while $|\eta| = \infty$ is reached along the beam line. A schematic overview of the detector is shown in figure 1.8, the sub-detectors of the ATLAS experiment are nested starting from the IP as follow:

ATLAS detector components

The Inner Detector

The Inner Detector (ID) [46] is the innermost sub-detector of ATLAS. It combines high-resolution detectors at the inner radii with continuous tracking elements at the outer radii, all contained in a solenoidal

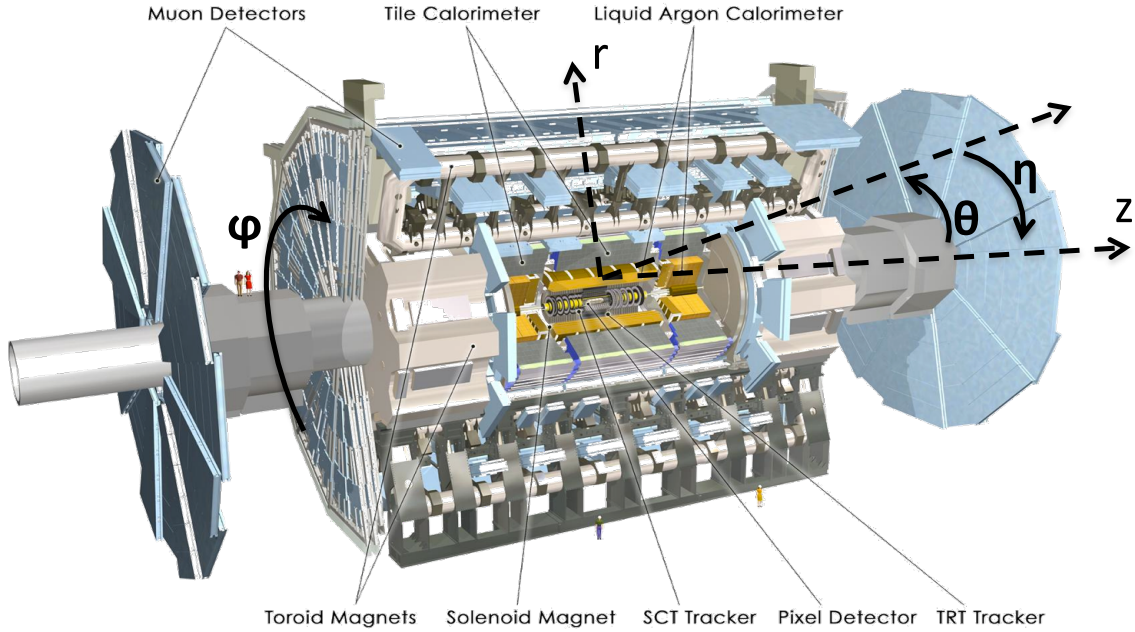


FIGURE 1.8: Schematics of the ATLAS detector viewing major sub-detector components with coordinate system. Image adapted from [45].

magnet with a central field of 2T. It is dedicated to measure the trajectories of charged particles originating from the IP. The tracking information is used to measure the vertex from which each particle is originating. It is the first part of ATLAS to see the decay products of the collisions, so it is very compact and highly sensitive. It consists of three different systems of sensors all immersed in a magnetic field parallel to the beam axis. The main components of the ID as schematically shown in figure 1.9 are: the insertable-B layer, the pixel detector, Semiconductor Tracker (SCT), and Transition Radiation Tracker (TRT).

The innermost part of the ID is the Insertable B-Layer (IBL) [47] that was integrated as a Phase-0 upgrade in 2014 inside the pixel detector. The IBL offers the highest granularity to efficiently disentangle tracks in the high track multiplicity region close to the IP. The IBL modules are in the innermost layer in the ID and are supported by means of fourteen local supports, the Staves, arranged cylindrically starting $\sim 3.3\text{ cm}$ around the beam pipe [48]. The IBL improves the impact parameter resolution by nearly a factor of two for low transverse momentum tracks [47]. The IBL pixel sensors exploits 448 FE-I4 [49] readout chips (see section 3.1.2). The central part of the detector is composed of modules built from $200\text{ }\mu\text{m}$ thick n-in-n planar sensors interconnected to two readout chips. The IBL matrix of pixels per readout chip is increased to 80×336 while the pixel pitch is decreased to $50 \times 250\text{ }\mu\text{m}^2$. With respect to the Pixel detector, the IBL has three main differences affecting the reconstruction of cluster position:

1. wider range of particle incident angles in the $R\phi$ plane.
2. wider clusters in the z direction.
3. lower charge resolution due to ADC dynamical range in the FE-I4 readout chip (see section 3.1.2).

In total, the ID host about 92 million pixels extending 1.7 m^2 from the beam line. The tracking volume of the 4-Layer system extends to a pseudorapidity of $|\eta| = 2.5$.

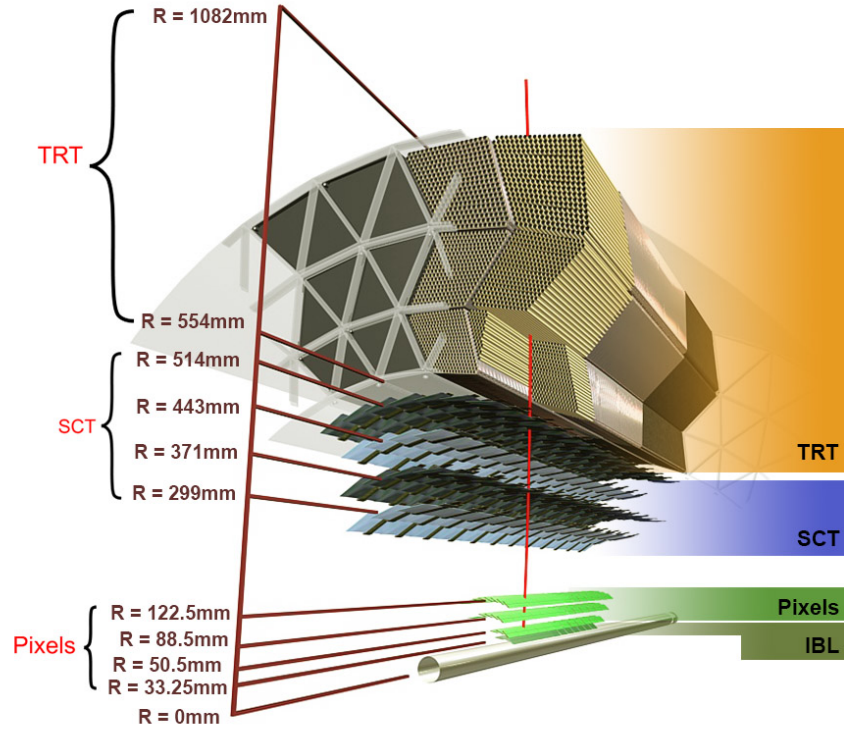


FIGURE 1.9: 3D visualization of the structure of the barrel of the inner detector: the beam pipe, the IBL, the Pixel layers, the four cylindrical layers of the SCT and the three layers of TRT barrel modules [45].

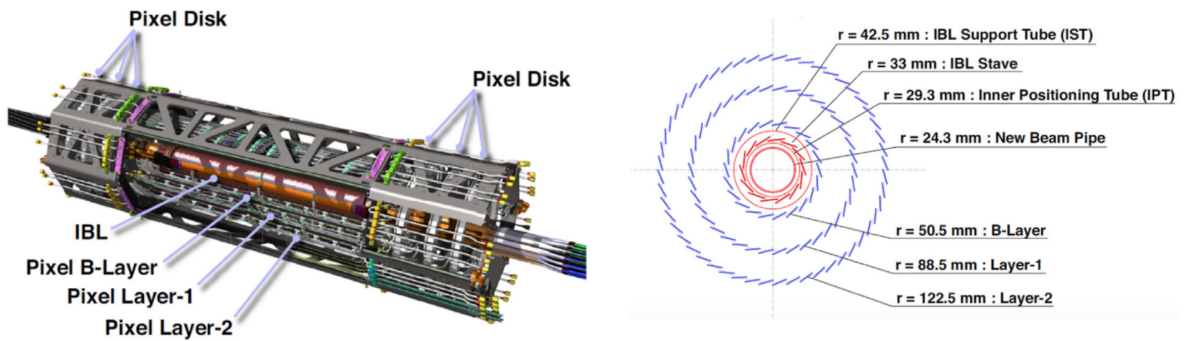


FIGURE 1.10: Schematics of the pixel detector and cross-section view [47].

On the outer side, the pixel detector consists of three barrel layers and three end-cap disks each side. The four layers of the Pixel Detector provide 3-dimensional space points that are crucial for the reconstruction of primary and secondary vertices in ATLAS. A cross-sectional view is sketched in figure 1.10 showing the radii extensions of the pixel detector from the beam line. The three-layer pixel system consist of 1744 pixel detector modules built with FE-I3 [50] readout chips. The pixel layers employ 250 μm thick planar n-in-n sensors (see section 2.3). Each sensor features 328 144 pixel cells with pitch $50 \times 400 \mu\text{m}^2$. 16 readout chips are interconnected to each sensor in a module.

The semiconductor tracker (SCT) [51] is a silicon micro-strip detector placed around the pixel detector. Each SCT module comprises of two (or four) single sided 285 μm thick p-in-n sensors. Two sensors on each side of the modules are wire bonded together to give 768 strips of approximately 12 cm in length. A second pair of identical sensors is glued back-to-back with the first pair at a stereo angle of 40 mrad. Such rotation allow more precise measurements in z axis. The modules are mounted on cylindrical supports such that the module planes are at an angle of 11° tangent to the cylinder for the inner two barrels and 11.25° for the outer two barrels, and overlap by a few milli-metres to provide a hermetic tiling in ϕ direction.

The outermost part of the ID is the transition radiation tracker (TRT) [52], it consists of three parts: one barrel, and two end-caps. Its basic elements are thin-walled proportional drift tubes, called straws. Straw tubes offer a high degree of modularity of the detector and can easily be integrated into a medium producing transition radiation without compromising the continuous tracking concept. The barrel part is comprised of 52 544 straws 144 cm in length oriented parallel to the beam. The two end-caps each contain 122 880 straws 37 cm in length radially aligned to the beam axis. The detector geometry guarantees that particles cross 35–40 straws in a pseudorapidity interval ranging from $\eta = -2$ to $\eta = +2$, providing continuous tracking at larger radii of the ID while enhancing its pattern recognition ability. The straw tubes are filled with a gas mixture of Xenon (70 %), CO_2 (27 %) and O_2 (3%) to increase the electron drift velocity and for photon-quenching. When particles cross the straw tubes, they ionize the gas mixture and create electron drift towards the anode where they are collected. The induced signal allows a particle to be detected with a spatial resolution of 130 μm . Radiation foils and fibers between the tubes cause impinging particles to create transition radiation energy that is used in particle identification. Photons typically deposit transition radiation energy between 8 – 10 keV, while minimal ionizing particles, such as pions, deposit about 2 keV [53]. The effect depends on the ratio of the particle energy and mass and the resulting photons can be used to distinguish pions from electrons.

Magnets

The ATLAS detector is immersed in a non homogeneous magnetic field to measure the momenta of the produced charged particles. The ATLAS magnet system [54] is optimized around the IP and consists of four superconducting magnets:

- the central solenoid (CS) which provides a magnetic field of 2 T for the inner detector.
- the air-core barrel toroid (BT) magnet which provides a magnetic field of maximum 4 T.
- the two air-core end-cap toroids (ECT) which provide a toroidal field configuration of maximum 4 T for the muon spectrometer.

The Electromagnetic Calorimeter

A calorimeter is designed to stop particles entirely, forcing them to deposit all of their energy within the detector. The electromagnetic calorimeter (ECAL) [55] is used to measure the energy of electrons, positrons and photons. The radiation length χ_0 describes the mean distance over which the energy of high energetic electrons or photons is reduced by bremsstrahlung to $1/e$. As the radiation length is related to the atomic number Z of the material that is penetrated, high- Z materials are used to stop particles in a reasonable distance. The Liquid Argon sampling calorimeter technique with “accordion-shaped” electrodes is used for all electromagnetic calorimetry covering the pseudorapidity interval $|\eta| < 3.2$. The gap between the passive lead absorbers an electrode is filled with liquid Argon (LAr) as active material. When a particle crosses the LAr, an output signal proportional to its energy is created by the drift of ionization electrons under high voltage. The ECAL is subdivided into a barrel and two end-caps. The barrel calorimeter is embedded in a barrel cryostats, which surrounds the ID and hosts the solenoid magnet. Two end-caps cryostats house the end-cap electromagnetic calorimeter as well as the end-caps hadronic calorimeter.

The Hadronic Calorimeter

Surrounding the ECAL, the hadronic calorimeter (HCAL) [56] is its hadronic counterpart. It provides good measurements of the energy and direction of hadronic showers. The hadronic analogy to the electromagnetic radiation length is the hadronic interaction length λ_I [57]. It is defined as the average distance between hadronic interactions and is usually significantly larger than the radiation length. The HCAL is divided into a barrel part and two end-caps calorimeter covering $1.5 < \eta < 3.2$. The end-caps are located in the high radiation forward region and is therefore equipped with the intrinsically radiation hard LAr active material. Copper and tungsten absorbers are used as passive material in those regions. The barrel part consists of the tile calorimeter that is divided in central barrel and two extended barrels. It is a sampling calorimeter, thicker than the electromagnetic calorimeter, as the hadronic showers are longer and wider than the electromagnetic showers. The barrels are built of iron absorbers and polystyren scintillators as active material.

The Muon Spectrometer

The Muon Spectrometer (MS) [58] is a stand-alone tracking detector for muons within the toroidal magnetic field. The design and performance of the MS is to satisfy three main categories:

- the largest possible reach for expected and unexpected new physics.
- good discrimination against charged and neutral particle background from minimum-bias events and radiation.
- reliable operation during the lifetime of the LHC.

The MS is a high-resolution spectrometer with stand-alone triggering and momentum measurement capability over a wide range of transverse momentum, pseudorapidity, and azimuthal angle. The concept of the spectrometer is based on the magnetic deflection of muon tracks in a system of three large superconducting air-core toroid magnets instrumented with separate-function trigger and high-precision tracking chambers. The magnets configuration is designed to cover full range of pseudorapidity such as:

- range $|\eta| \leq 1.0$, magnetic bending is provided by a large barrel magnet constructed from eight coils surrounding the hadron calorimeter.

- $1.0 \leq |\eta| \leq 1.4$ referred to as transition region, magnetic deflection is provided by a combination of barrel and end-cap fields.
- $1.4 \leq |\eta| \leq 2.7$, muon tracks are bent in two smaller end-cap magnets inserted into both ends of the barrel toroid.

This configuration provides a field that is mostly orthogonal to the muon trajectories, to enable the determination of the momentum of the muons based on their curvature while minimizing the degradation of resolution due to multiple scattering.

In the barrel chambers tracks are measured by four different detector technologies: Monitored Drift Tubes (MDT), Cathode Strip Chambers (CSC), Resistive Plate Chambers (RPC) and Thin Gap Chambers (TGC). Over most of the pseudorapidity range, a precision measurement of the track coordinates in the principal bending direction of the magnetic field is provided by the MDT. At large pseudorapidities and close to the interaction-point CSCs are used with high granularity to sustain the demanding rate and background conditions. The RPCs are used in the barrel and the TGCs are used in the end-cap region. Both types of trigger chambers provide a ‘second-coordinate’ measurement of track coordinates orthogonal to the precision measurement, in a direction approximately parallel to the magnetic field lines.

1.8 ATLAS Inner Tracker

The dataset that will be collected by the ATLAS detector at the HL-LHC phase will be 10 times larger with respect to the current LHC phase during (2010-2024). In terms of physics, this massive amount of data will allow more precise measurements of SM processes, and precise measurements of the Higgs and couplings to particles. Recalling the parameters that will upgrade the LHC machine into HL-LHC in table 1.4, will require the ATLAS detector to take data in extreme conditions which include:

- instantaneous peak luminosity $\mathcal{L} \simeq 7.5 \times 10^{34} \text{ cm}^{-2} \text{ s}^{-1}$, which is 5-7 times greater than today.
- accumulated luminosity of 4000 fb^{-1} by end of 2039, which means the innermost pixel layer will be exposed to a fluence of $2 \times 10^{16} \text{ n}_{eq}/\text{cm}^2$ (4-6 times the IBL fluence at LHC Run3).
- average of 200 proton-proton interactions collisions per bunch crossing.

The challenges posed by the LHC machine upgrade are all driven by the increased instantaneous luminosity, which results in more proton-proton collisions per bunch-crossing yielding more events in the tracking detector that need to be reliably disentangled. To cope with these conditions, the current ATLAS inner detector needs an upgrade to a high granular Inner Tracker (ITk) to maintain the an equal or better tracking performance despite the harsher conditions. Other sub-detectors in the ATLAS experiment will also undergo some upgrades. A new detector, the High Granularity Timing Detector (HGTD) [59] will be added as a new sub-detector in ATLAS. It will be placed at high η ranging between $2.4 < \eta < 4$ and its goal will be to add timing information on forward tracks. The high timing resolution (30 ps) will help to disentangle pile-up tracks from which origin collision points (primary vertices) are spatially close but separated in time.

The ITk design concept consists of inner pixel detector with high granularity and outer strip detectors. The ITk detector is designed to withstand 10 years of operation at the HL-LHC phase. A schematics of a quarter of the ITk layout is shown in top of figure 1.11. The inner region (Red) consists of five pixel barrel layers arranged in cylinders around the beam axis and four end-cap ring layers. The beam pipe

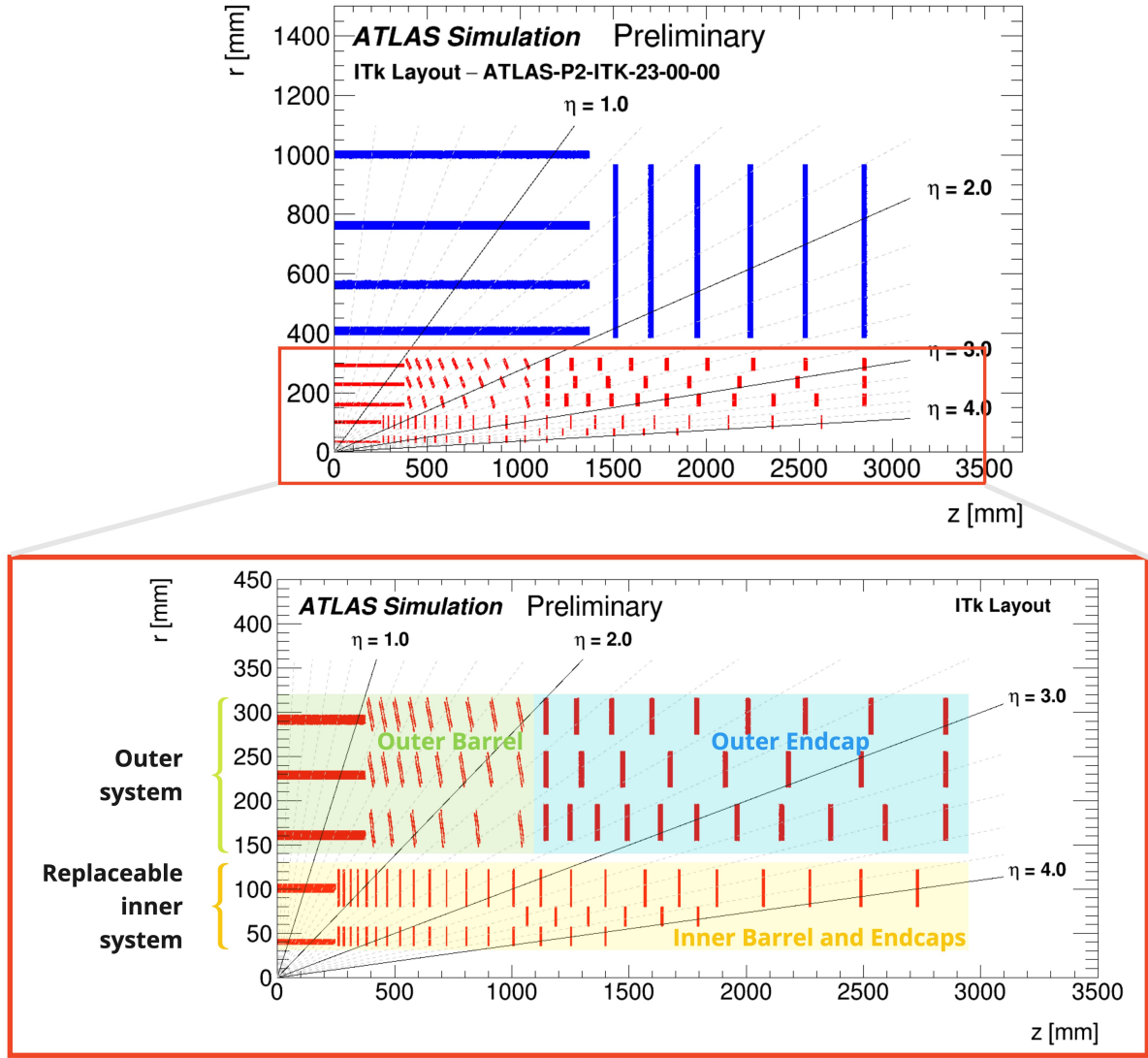


FIGURE 1.11: Quadrant of the ITk pixel layout scheme. The horizontal axis is along the beam line with zero being the interaction point, and the vertical axis is the radius measured from the interaction region. The layout is color coded with yellow for inner barrel and end-cap, green for the 2-4 outer barrels and blue for outer end-caps in the forward region. Image adapted from [60].

with radius 28.3 mm will be reused from Run2 of the LHC. The complete ITk pixel detector covers up to $|\eta| = 4$. Followed by outer strip region (Blue) with two short-strip layers and then two long-strip layers of paired stereo modules and one end-cap on each side with six disks each to provide good coverage with 10° of the beam axis. The strip system covers up to $|\eta| = 2.7$. Including the strip detector, the total length of the ITk in the z direction is $z = 661.0\text{ cm}$ [60].

A quadrant of the ITk pixel sub-detector layout is depicted at the bottom of figure 1.11. It is foreseen for the ITk pixel detector to be divided into an inner replaceable system and an outer fixed system. The inner barrels and end-cap (Yellow) consists of pixel layers 0 and 1 and their coupled ring system in the forward region. The outer barrels (Green) consist of pixel layers 2-4. The outer end-caps (Blue) consist of the rings for the outer system in the forward region. The inner layers 0 and 1, in the replaceable inner system (Yellow) with their innermost ring closest to the beam pipe will be mounted on an inner support tube. The design of the inner support tube is made to be replaceable independently from the outer pixel barrels, as it is expected to be exchanged after integrating half of the luminosity to reduce the impact of radiation damage. Table 1.5 summarises the parameters and positions for the inner coupled rings

TABLE 1.5: Parameters for the ITk coupled rings for layers 0 and 1 [60].

Coupled ring layer	Radius [cm]	$ z $ [cm]	Rings	Sensor per ring	Module type
0	3.32	26.1 - 140.0	15	18	triplets
1	8.00	26.1 - 140.0	23	20	quads

system. All outer barrels will be instrumented with quad modules. Both inner and outer end-caps are designed with flat pixel barrels. Parameters for the ITk pixel flat barrels are summarised in table 1.6 for the five successive barrel layers. Barrel and ring 0 will be instrumented with 3D triplet modules, while ring 1 will be instrumented with planar quad modules. The outer barrel (Green) will host flat and inclined pixel layers as summarised in table 1.7. In all barrel layers, sensors in the central region will be

TABLE 1.6: Parameters for the ITk pixel flat barrel [60].

Barrel layer	Radius [cm]	$ z $ [cm]	Rows of sensors	Sensors per row	Module type
0	3.4	0 - 24.5	16	12	triplets
1	9.9	0 - 24.5	20	6	quads
2	16.0	0 - 37.2	32	9	quads
3	22.8	0 - 37.2	44	9	quads
4	29.1	0 - 37.2	56	9	quads

TABLE 1.7: Parameters for the ITk outer inclined pixel barrel [60].

Barrel layer	Radius [cm]	$ z $ [cm]	Sensor per row	Module type	Angle [deg]
2	15.0	27.3 - 104.7	6	quads	67
3	21.8	27.3 - 104.7	8	quads	58
4	28.1	27.3 - 104.7	9	quads	55

placed tangential to a circle centered around the beam pipe. The "flat" or "non-inclined" sensors are tilted by 14° in the transverse plane, while the inclined barrel is composed of tilted sensors at an angle of 56° with respect to beamline [61]. The inclined pixel layout design aim to increase the efficiency at high η . The advantage of such design is that the particle crosses reduced quantities of sensor material to increase the tracking resolution. The inner end-cap system will be located between $1100\text{ mm} < |z| < 3000\text{ mm}$.

To maintain the current performance in the HL-LHC regime a thinner and high granular detector is required. The planned nominal pixel sizes are $50 \times 50 \mu\text{m}^2$ and $25 \times 100 \mu\text{m}^2$ with a sensor thickness of $100 \mu\text{m}$ for layer 1, and is $150 \mu\text{m}$ thick sensors elsewhere (see section 3.2.1). ITk pixels sensor design include both planar and 3D technologies. The pixel size is chosen to be $50 \times 50 \mu\text{m}^2$ for the planar pixel modules in the Technical Design Report [61] and to be $25 \times 100 \mu\text{m}^2$ for 3D modules in the flat barrel of the innermost layer [62]. The higher cost (due to the custom process) makes the 3D sensors restricted to the innermost layer only. The core of the ITk pixel detector is a hybrid module, containing a silicon pixel sensor coupled to its readout chip. The production and assembly process of hybrid modules will be discussed later in section 3.3.

Due to the increased rate of proton-proton collisions in the HL-LHC phase, the radiation levels are expected to increase by roughly an order of magnitude compared to the current ID. Radiation background simulations have been performed to set an expectation for the radiation levels of the ITk detector [63, 64]. The predictions of particle fluences and ionizing doses for the ITk layout shown in figure 1.12 assumes a baseline scenario of the integrated luminosity in the outer pixel barrel and end-cap detector to collect up to 4000 fb^{-1} , while the inner barrel and end-caps will be replaced after reaching 2000 fb^{-1} . With these expectations, we later study the performance of the ITk pixel modules under accumulated fluence at the same values to test them in an environment close to realistic conditions. It is important to emphasize that

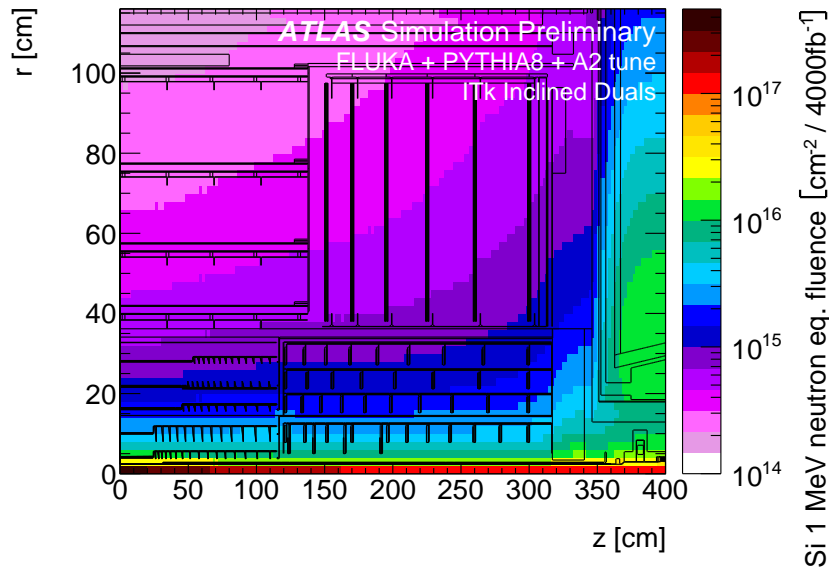


FIGURE 1.12: Simulated prediction of particle fluence over the ITk layout layers of pixels and strips. [65].

accurate fluence and dose predictions require precise modeling of the entire ATLAS geometry in FLUKA [64]. While fluences in the innermost layers of the ITk pixel barrel region are dominated by particles coming directly from the interaction point, the fluences in the outer barrel layers and the pixel end-cap region are increasingly dominated by particles coming from secondary interactions in the calorimeter, beam-line and pixel service material. A summary of the maximum 1 MeV neutron equivalent fluences for ITk layers corresponding to figure 1.12 are shown in table 1.8.

1.9 Status and deficiencies of the current Inner Detector

The current ID was designed for 10 years of operation for a constant instantaneous luminosity of $\mathcal{L} = 1.0 \times 10^{34} \text{ cm}^{-2} \text{ s}^{-1}$, centre-of-mass energy $\sqrt{s} = 14 \text{ TeV}$, and an average pile-up of 23 proton-proton

TABLE 1.8: 1 MeV neutron equivalent fluences for each layer in ITk layout. These results the values have been multiplied by a safety factor of 1.5.

layer	fluence [$cm^{-2}s^{-1}$]
Pixel	1.5×10^{16}
short strip	5.4×10^{14}
long strip	2.8×10^{14}
strip end-cap	8.2×10^{14}

interactions per crossing. In 2016 the LHC has exceeded the peak instantaneous luminosity to $\mathcal{L} = 1.37 \times 10^{34} cm^{-1}s^{-1}$, and the average pile-up was 33.7 proton-proton interactions per crossing [66]. Despite the higher than anticipated pile-up, after the upgrades of the pixel readout, the ID was adequate for the physics program where it's playing a pivotal role in ATLAS physics analyses that rely on charged-particle reconstruction, heavy-flavour tagging, and on the identification of electrons, photons, muons and tau-leptons produced in both proton-proton interactions and heavy-ion collisions.

The current pixel detector was designed to withstand radiation damage equivalent to an integrated luminosity of $300 fb^{-1}$. Similar to the SCT to withstand integrated luminosity of $700 fb^{-1}$. After the insertion of the IBL, which was designed to withstand integrated luminosities equivalent to roughly $850 fb^{-1}$, the radiation tolerance of the ID is sufficient to guarantee high efficiency for the integrated luminosity expected to be collected until the end of 2024, but it is not suitable for operation beyond this level.

Both pixel and SCT detectors can accommodate events with about 50 proton-proton interactions per crossing, pile-up events, which come with sustained instantaneous luminosity of about $\mathcal{L} = 2.0 \times 10^{34} cm^{-1}s^{-1}$. While with $\mathcal{L} = 3.0 \times 10^{34} cm^{-1}s^{-1}$ at 25 ns bunch crossing rate limitation of the buffering between the front-end chip and the Read Out Driver (ROD) will lead to inefficiencies when the limit is more than 0.2 to 0.4 hits per double column per 25 ns bunch crossing. For an average number of superimposed minimum bias events in each beam crossing pile-up events of $\langle \mu \rangle = 70$ at a Level-1 rate of 100 kHz, much of the innermost strip barrel cannot be read out. In the HL-LHC regime with an average proton-proton interactions with pile-up of $\langle \mu \rangle \sim 200$ in the pixel detector, without compensational increase in granularity the efficiency of the pattern recognition and track-finding are impaired, which in turn will significantly compromise the physics reach. Also, the TRT would read 100% occupancy at HL-LHC regime so it will be removed. Furthermore, the trigger system will be one of the main challenges in ATLAS at HL-LHC. The current ID does not provide any tracking information to the first level (L1) hardware trigger system. By adding the tracking information to the trigger objects provided by the calorimeters and muon system, trigger thresholds could be lowered which will directly benefits the physics performance.

These substantial limitations make it necessary to completely replace the current ID for Phase-II upgrade in the HL-LHC phase. The upgraded replacement will be an all silicon Inner Tracker (ITk) instrumenting thin sensors with unique n-in-p technology to tolerate the harsh conditions of the HL-LHC until the end of its life time. The instrumentation of the ITk detector as shown in figure 1.11 is pushing the limits of tracking technology, and hence poses many challenges. One of the main challenges is the development of a suitable readout electronics for the silicon sensors to tolerate the radiation and the high pile-up of the HL-LHC phase. The silicon technology and semiconductor physics of the inner tracker will be discussed in the next chapter and the associated electronics of the inner tracker will be discussed in chapter 3.

668 *"We are what we repeatedly do. Excellence, then, is not an act but a habit. "*

669 Aristotle

Chapter 2

Silicon sensors for High Energy Physics

Semiconductor material is extensively studied and plays a major role in High Energy Physics experiments. Silicon is the most common semiconductor in modern technology widely used in the industrial sector. Silicon based detectors are used in tracking systems since they offer a fast and accurate position information and energy resolution of a passing charged particle. The ATLAS ITk detector upgrade will be an all-silicon tracker. This chapter focuses on the basic principles of silicon sensors and the interesting physical properties that make the instrumentation used in silicon detectors progress in High Energy Physics (HEP). In this chapter I remind the reader of the working principles of silicon sensors in section 2.1. In section 2.2 I continue to explain the detection principles and charge generation in the pn junction. Then, I introduce the n-in-p technology of a segmented pixel detector that will be used in the ATLAS ITk pixel detector in section 2.3, along with the fabrication process, sensor design and properties. Finally, as the ITk detector will be exposed to high particle flux in the high luminosity regime, the impacts of radiation damage are discussed in section 2.4.

2.1 Working principle of silicon sensors

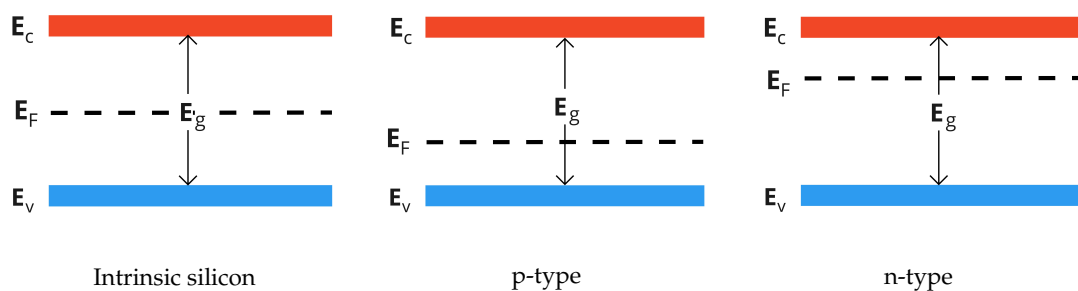


FIGURE 2.1: Energy bands in Silicon for intrinsic, p- and n-type material. Valence band E_v and conduction band E_c and Fermi level E_F are indicated.

Crystalline materials are classified into three types depending on their electrical conductivity, which depends on energy gap between the bands. From smaller to larger conductivity they are named: Insulators, Semiconductors and Conductors. Electrons in individual atoms influence each other and due to Pauli exclusion principle they organize themselves in energy bands as shown in figure 2.1. The highest fully filled energy level in a crystal is called valence band, E_v . The permitted energy band directly above the valence band is called the conduction band, E_c . Charge carriers in a completely filled valence band have little or no sufficient possibility to move, hence conduction is limited or null. These carriers "jump" from the valence band into the conduction band, where they are free to move and thus, conduct. The vacancy left in valence band by an electron when it jumps to the conduction band is called 'hole' and it

behaves exactly as a positively charged particle. The conductivity of a semiconductor depends on the number of charge carriers in the conduction and in the band. As anticipated, the electrical conductivity depends on the energy gap E_g that separates the conduction band from the valence band. At room temperature, the energy gap of the most common semiconductors are: 1.12 eV for silicon, 0.67 eV for germanium, and 1.42 eV for Gallium arsenide. At room temperature, the thermal energy in the energy gap is about 25 meV.

The Fermi level E_F is the top of the collection of occupied electron energy level at 0K. At that temperature, all the allowed energy levels below the Fermi level are occupied, and all the energy levels above it are empty. At $T > 0K$, it is defined as the energy level that has a 50% probability of being filled with electrons in the band gap as

$$E_F \simeq \frac{E_c + E_v}{2}, \quad (2.1)$$

where E_c is the lower energy limit for the conduction band, and E_v the lower energy limit for the valence band. In insulators and semiconductors the Fermi level lies somewhere in between the valence and the conductive band.

From this point forward I will talk only about silicon properties. The Fermi level changes in an extrinsic silicon with different concentration of charge carriers in the conduction or valance band accordingly. The charge carrier concentration, the intrinsic and extrinsic silicon are discussed in the following.

2.1.1 Charge carriers concentration

Intrinsic semiconductor

Intrinsic silicon contain no impurities, i.e. defect free and pure material without doping [67]. The concentration of free charge carriers in the conduction band and the valence band are the same and thus the Fermi level is exactly in the middle as depicted in figure 2.1. The density of the states filled with charge carriers in the energy band is the probability that these states are occupied. At thermal equilibrium, the probability to find the state of the charge carrier $F(E)$ with a given energy E is described by Fermi-Dirac statistics [68]

$$F(E) = \frac{1}{\underbrace{1 + \exp\left(\frac{E-E_F}{kT}\right)}_{\text{Fermi-Dirac}}} \cong \underbrace{\exp\left[-\frac{E-E_F}{kT}\right]}_{\text{Maxwell-Boltzmann}}, \quad (2.2)$$

where E_F is the Fermi level from equation 2.1, E is the energy of the state in the band, k is the Boltzmann constant, and T is the temperature in Kelvin. This expression can be approximated separately for electrons (n) and holes (p). The concentration of intrinsic charge carriers n_i is expressed by

$$n_i = N_c \exp\left[-\frac{E_c - E_F}{kT}\right] = N_v \exp\left[-\frac{E_F - E_v}{kT}\right], \quad (2.3)$$

where N_c and N_v are the effective density of states in the conduction and valence bands respectively. The electrical conductivity σ depends on the density of the free charge carriers and their mobility, which can be determined by

$$\sigma = e \cdot n_i \cdot (\mu_e + \mu_h) \quad (2.4)$$

where $\mu_{e,h}$ is the mobility for electrons and holes and $n_i = n = p$ is the concentration of charge carriers in intrinsic semiconductor. This concentration value depends on the width of the energy gap and is

dependent on the temperature by [69]

$$n_i \propto T^{\frac{3}{2}} \cdot \exp \left[\frac{-E_g}{2kT} \right]. \quad (2.5)$$

This indicate that the concentration of charge carriers, and hence the generation of carriers, is exponentially affected by the temperature.

Extrinsic semiconductor

To enhance the electrical properties of the silicon, it can be modified from an intrinsic semiconductor to an extrinsic semiconductor by doping [67]. The doping process introduces additional energy levels close to either of the conduction or valance band, and hence resulting in a larger electrical conduction. There are two kinds of dopants to create an extrinsic silicon:

- Donors: Donor dopants have one electron more in the valence band than silicon (e.g Phosphorus). A donor impurity has a donor level, which is defined as being neutral if filled by an electron and positive if empty. As electrons are the majority charge carriers, donor doped silicon is called *n-type* silicon. N_D indicates the donor concentration.
- Acceptors: Acceptor dopants have one electron less in the valence band than silicon, which lead to an electron vacancy or hole inside the structure (e.g. Boron). An acceptor level is neutral if empty and negative if filled by an electron. As holes are the majority charge carriers, acceptor doped silicon is called *p-type* silicon. N_A indicates the acceptor concentration.

The new energy levels in the band gap pull the Fermi level towards the respective side by the addition of dopants in the bulk as depicted in figure 2.1 for p-type and n-type. The Fermi level in an extrinsic silicon can be anywhere between the conduction and the valence band. Its position is determined by the charge carrier density. The product of electrons and holes under thermal equilibrium is constant and is equal to $pn = n_i^2$. For donors E_F is shifted towards the conduction band $E_F = E_i + kT \ln \frac{N_D}{n_i}$, and gives rise to a permitted energy level E_D few meV below the bottom of the conduction band, which contains the electrons given by the impurity. Similarly for acceptors, the E_F is shifted towards the valence band $E_F = E_i - kT \ln \frac{N_A}{n_i}$ and give rise to permitted energy level E_A few meV above the top of the valence band. Hence, the electrical conduction depends on the charge carriers concentration, i.e. on the doping. Typical doping concentrations at room temperature range from some 10^{10} cm^{-3} in the bulk of high resistive detector material to 10^{21} cm^{-3} in highly doped implants. Silicon sensors for particle detection employ a high resistive silicon bulk thus, low doping concentrations are usually preferred $10^{12} - 10^{14} \text{ cm}^{-3}$.

2.1.2 The pn junction

The application of semiconductor detectors rely on the combination of both p-type and n-type silicon. The pn junction interface is created by placing p- and n-type silicon into thermal contact as shown in figure 2.2. The formed p-n junction is the building block of the silicon particle detector. At the contact region of the pn junction the free majority charge carriers recombine and create a zone depleted of free charge carriers called depletion region. The immovable dopants in the depletion region are ionized and create what is called a space charge region that is free of charge carriers. The electron-hole pair recombination annihilates the charge carriers while the electron leaves behind a positively charged ion near the conduction band (positive electrode) and the hole leaves behind a negatively charged ion near the valance band (negative electrode). The carriers start to recombine at the interface growing into the depth of the silicon bulk. Whenever there exists a gradient of carrier concentration, a process of diffusion

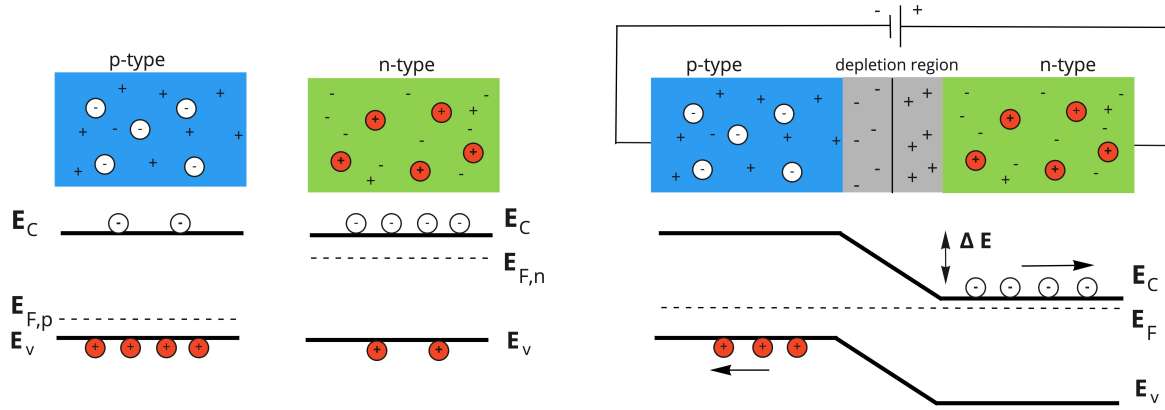


FIGURE 2.2: Schematics of pn junction without biasing voltage (left) and with applied reverse bias voltage (right), electrons drift to the conduction band and holes diffuse to the valence band. Schematics adapted from [70].

occurs by which the carriers migrate from the region of high concentration toward the region of low concentration. Thereby ionized dopants create the space charge region at the junction. This charge causes an electrical field, which acts against the diffusion process due to the carrier concentration. As a result of the charge displacement an internal built-in potential V_{bi} is formed at the junction [71]. Within a multiplication factor of charge $-q$ the junction potential is equal to the curvature of the energy band illustrated in figure 2.2 by:

$$V_{bi} = \frac{kT}{q} \ln \frac{N_a N_d}{n_i^2}. \quad (2.6)$$

The created electric field is proportional to the number of recombined pairs inside the junction. In case no bias is applied to a pn junction the voltage corresponding to the electrical field is the built-in voltage V_{bi} and is typically about 0.7 V [71].

When an external bias voltage is applied across the pn junction, the depleted region can either shrink if the bias is applied opposite to the built-in voltage (forward bias) or expand if it's applied in the same direction as the built-in voltage (reverse bias) as shown in figure 2.2. For a reverse bias, the width of the depletion region d_{dep} , which contains both ionized acceptor and donor impurities is calculated by

$$d_{dep} = \sqrt{\frac{2\epsilon_0\epsilon_r(V_b + V_{bi})}{q} \left(\frac{1}{N_D} + \frac{1}{N_A} \right)} \approx \sqrt{\frac{2\epsilon_0\epsilon_r V_b}{q N_{eff}}} \quad (2.7)$$

where V_b is the external bias voltage and N_D , N_A are the donor and acceptor concentrations respectively, ϵ and ϵ_0 are the permittivity in silicon and in vacuum respectively, N_{eff} is the effective (dominant) concentration in the bulk, and q is the charge of electron. The expression can be simplified since the external bias voltage V_b is usually much larger than the built-in voltage V_{bi} and one doping N is dominant in most applications.

A particle is detected in a sensor by the drift of the charge carriers produced by ionization in the depletion region. Therefore, a depleted sensor is a baseline for the sensor's operation. The depletion voltage is the minimal reversed bias voltage V_b necessary to deplete the entire pn junction with thickness

790 d to maximize the charge collection volume. The depletion voltage V_{dep} is given by

$$V_{dep} = \frac{q|N_{eff}|d^2}{2\epsilon\epsilon_0} \quad (2.8)$$

791 where q is the charge of electron, $|N_{eff}| = |N_D - N_A|$ is the effective doping concentration. Once the
 792 sensor is reversely biased, the net generation of carriers in the depleted area create a current flow com-
 793 monly named as the leakage current I_{leak} . The current in a pn junction is obtained by multiplying the
 794 current density by the cross-sectional area of the junction which gives:

$$I_{leak} = \frac{qn_i A d}{2\tau_g} \quad (2.9)$$

795 τ_g is the generation life time, which is the average time between one generation and the other. It is im-
 796 portant to note that the magnitude of the current flowing in a reverse biased pn junction is independent
 797 of the applied bias and of the electric field, however it is quite dependent on temperature [71]. It was
 798 shown in reference [69] that the leakage current scales with temperature T according to

$$I(T) \propto T^2 \exp\left(\frac{-E_{eff}}{2kT}\right), \quad (2.10)$$

799 where E_{eff} is the effective energy and has a value close to $1.214 \pm 0.014 \text{ eV}$. This leakage current equation
 800 is derived and scaled from the dependence of the charge carrier concentration on temperature (equation
 801 2.5). This value is the current reference for HEP community for temperature correction scaling the leak-
 802 age current for both unirradiated and irradiated sensors.

803
 804 If the sensor is supplied with a higher voltage compared to the depletion voltage, it is then over-
 805 depleted: the electric field inside the sensor is increased and the free charge carriers are faster than if
 806 they were just in a depleted sensor. In the presence of the high electric field, the charge carriers gain
 807 enough energy to excite other electron-hole pairs. This excitations creates a multiplication effect is called
 808 impact ionization [67]. The leakage current can be increased exponentially and leads to an avalanche
 809 breakdown impeding the normal operation of the sensor. The voltage at which the leakage current
 810 exponentially increase is called the breakdown voltage V_{bd} . The V_{bd} defines the maximum operational
 811 bias voltage V_b of the sensor. The performance of the current-voltage relation of planar pixel sensors will
 812 be discussed in chapter 6.

813 2.2 Charge generation and signal formation

814 As a charged particle crosses the depleted region of the sensor's bulk it will loose energy by scattering
 815 with the electrons of the silicon. The electrons gain sufficient energy to cross the band gap and enter the
 816 conduction band. Simultaneously, a hole is created in the valence band. The mean rate of energy loss
 817 induced by the moderately-relativistic charged heavy particle crossing is well described by the Bethe-
 818 Bloch equation [72] ;

$$\left\langle -\frac{dE}{dx} \right\rangle = Kz^2 \frac{Z}{A} \frac{1}{\beta^2} \left[\frac{1}{2} \ln \frac{2m_e c^2 \beta^2 \gamma^2 W_{max}}{I^2} - \beta^2 - \frac{\delta(\beta\gamma)}{2} \right]. \quad (2.11)$$

819 The parameters are explained in table 2.1 below, which hold correct in the region $0.1 < \beta\gamma < 1000$ as
 820 shown in the energy loss function for muons in figure 2.3.

TABLE 2.1: parameter definition for Bethe-Bloch equation

K	coefficient for dE/dx equal to $4\pi N_A r_e^2 m_e c^2$
N_A	Avogadro number
r_e	radius of the electron
z	charge number of incident particle
Z	atomic number of absorber
A	atomic mass of absorber [$g mol^{-1}$]
β	velocity in terms of the speed of light c
$\beta\gamma$	relativistic momentum [GeV/c]
$m_e c^2$	mass of the electron $\times c^2$
W_{max}	maximum possible energy transfer to an electron in a single collision [MeV]
I	mean excitation energy [eV]
$\delta(\beta\gamma)$	density effect correction to ionization energy loss

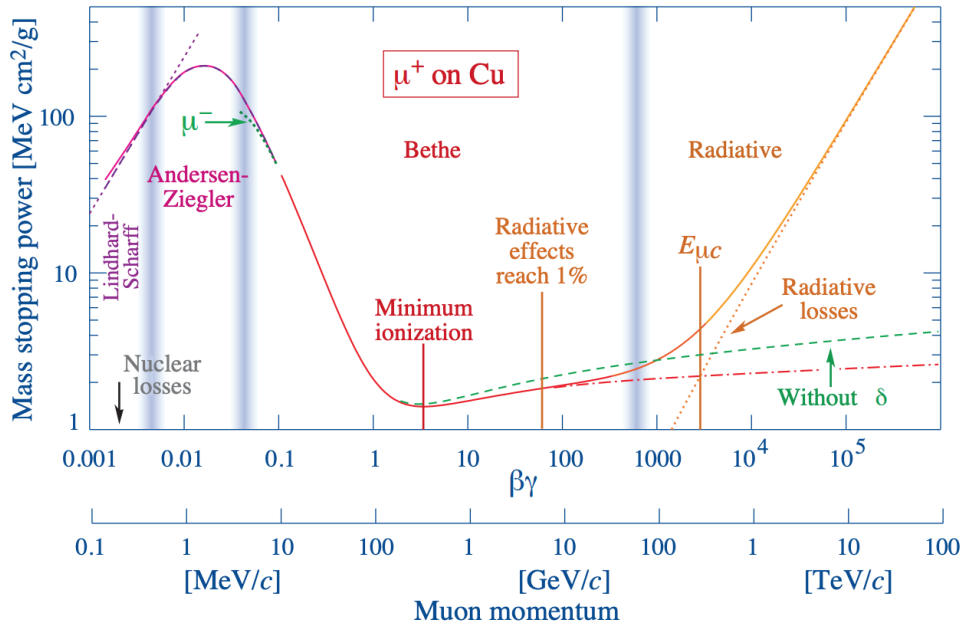


FIGURE 2.3: Mass stopping power ($= \langle dE/dx \rangle$) for positive muons in copper as a function of $\beta\gamma = p/Mc$ over nine orders of magnitude in momentum (12 orders of magnitude in kinetic energy). Solid curves indicate the total stopping power. Further details on Bethe Bloch function in [72].

Most particles relevant in HEP can be categorised by a single energy loss as the Bethe-Bloch equation exhibits a prominent minimum at $\beta\gamma = 3 - 4$ with a very slow increase towards higher values. The so called Minimal Ionizing Particles (MIPs) exhibit an ionization compatible with the minimum of the Bethe-Bloch equation. The first part of the graph in figure 2.3 describe massive charged particles with $\beta\gamma$ between $10^{-4} - 1$ that have large mass stopping power and very small relativistic effects in agreement with the "non-relativistic" description. The second part of the graph shows their behavior at $\beta\gamma$ between $10 - 1000$, which describes the regime with lowest stopping power values for an incident particle determining a MIP. For high momentum particles in the third part of the graph, the energy deposition and charge generation is increased through energy losses by bremsstrahlung and hard scattering processes. Electrons are not accurately described by the Bethe-Bloch equation since they are very light and dominantly emit bremsstrahlung.

The energy loss spectrum of MIPs signal in the silicon can be described by a Landau-Vavilov distribution [73]. The total energy deposited in a sensor approximates a Gaussian distribution due to the central

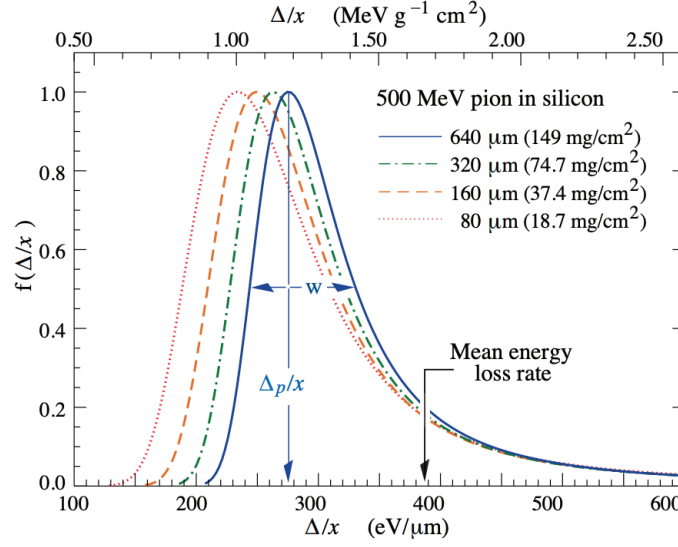


FIGURE 2.4: Example of 500 MeV pions incident on thin silicon detectors.

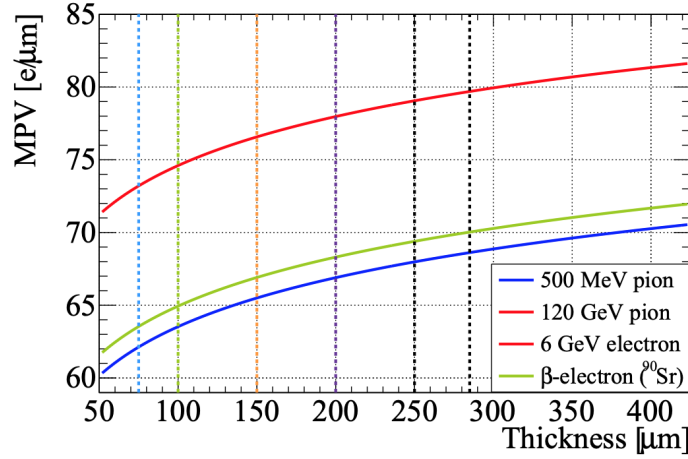


FIGURE 2.5: The MPV of the number of electron-hole pairs created per micron for various particles and energies as a function of the sensor thickness. The vertical lines indicates the most relevant detector thicknesses [74].

limit theorem. But for thin detectors, due to rare inelastic scattering from δ rays or a knock on electrons, this energy-loss distribution is asymmetric with a long high energy tail described by a Landau-Vavilov distribution as shown in figure 2.4. The probability distribution for the Most Probable Value Δ_p is much more stable quantity and is given by [72]

$$\Delta_p = \zeta \left[\ln \frac{2m_e \beta^2 \gamma^2}{I} + \ln \frac{\zeta}{I} + 0.200 - \beta^2 + \delta(\beta\gamma) \right] \quad (2.12)$$

where $\zeta \propto d_a / \beta^2$, d_a is the active thickness of the detector and the rest of the parameters are as explained in table 2.1. Therefore the MPV of the Landau-Vavilov distribution depends on the particle energy and active thickness of the module as shown in figure 2.5. The MPV of energy loss rate increases with increasing thickness.

Carriers mobility

The free charge carriers drifts toward the electrodes in the depletion region with a velocity depending on the electric field \vec{E} as

$$v_{e,h}(\vec{E}) = \mu_{e,h}\vec{E}. \quad (2.13)$$

This mobility μ is constant for low and moderate electrical fields but deviates at higher electrical fields with increasing carrier energy: the mobility itself becomes a function of the electrical field [75].

From a passing charged particle a current is induced on the collecting electrodes as soon as charge carriers drift towards them. The induced current on a given electrode is described by the Shockly-Ramo theorem [76, 77] and is evaluated by

$$I = q\vec{E}_w \cdot \vec{v} \quad (2.14)$$

where q is the electron charge, \vec{v} is the carrier velocity and \vec{E}_w is the weighting field. The weighting field \vec{E}_w is a simple linear function between n- and p-doped electrodes in a 1-dimensional pn junction, but becomes more complex and relevant in segmented detectors such as pixel detector [78]. In pixelated detectors the weighting field accounts for the geometry of the device and can be derived from the weighting potential Φ_w as

$$\vec{E}_w = -\nabla\Phi_w. \quad (2.15)$$

The weighting potential can be found by solving the Laplace equation

$$\nabla^2\Phi_w = 0, \quad (2.16)$$

with the boundary condition that the electrode of interest is at unit potential and all other electrodes are at zero. The weighting potential depends solely on the geometry of all electrodes at fixed potential and is also valid in the presence of space charge and constant magnetic fields in the sensor [76]. The charge collected by the electrode can be calculated by integrating the current received on the electrodes from the starting time of the carrier movement until the carriers are trapped or have arrived at the electrode.

2.3 Pixel detector technology

Silicon sensors in HEP experiments are based on pn junction diodes. Sensors with electrodes that have a two-dimensional segmentation and supply a two-dimensional spatial information are defined as pixels. With the two doping types of material, there are four possible combinations for a sensor to be built: a) $n^+ - in - n$, b) $n^+ - in - p$, c) $p^+ - in - n$, d) $p^+ - in - p$ ¹. Due to the trapping effects after irradiation the $p - in - n$ and $p - in - p$ sensors given that they collect holes, which have lower mobility with respect to electrons, they are more affected by charge trapping. While sensors based on $n - in - n$ and $n - in - p$ collect electrons and are less prone to trapping effects after irradiation. Further, $p - in - p$ and $n - in - n$ join the detrimental properties and high cost due to their processing technique and difficult operation throughout the lifetime. For this reason they cannot be employed in the high radiation environment at HL-LHC. Main advantages (+) and disadvantages (-) of the four combinations of possible dopings are illustrated in figure 2.6.

The preferred silicon sensor technologies for the HEP can be narrowed down to the two concepts with n^+ implants, i.e. collecting electrons:

¹The '+' sign indicate a heavily doped region

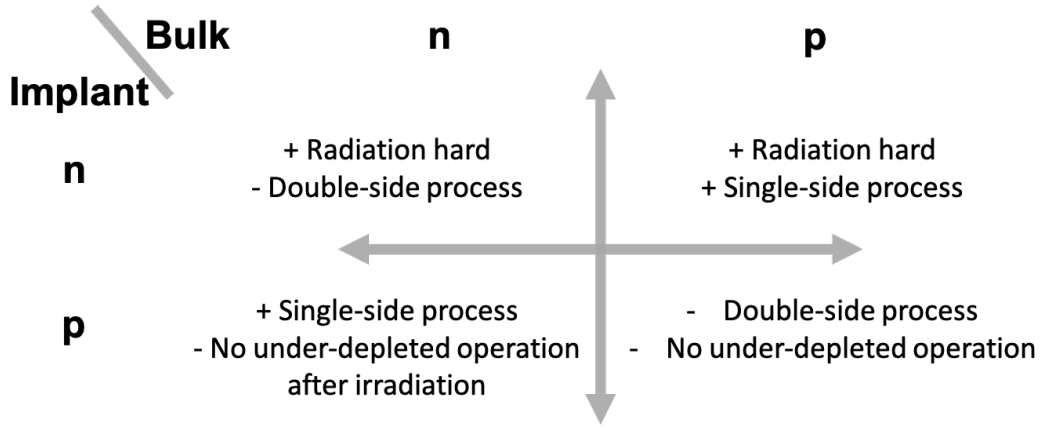


FIGURE 2.6: Possible doping combinations for pixel sensors highlighting their advantages and disadvantages in production and performance.

- n^+ -in-n technology** This technology implements n-type bulk with segmented n^+ implants on the frontside, which are the collecting terminals for electrons, and additional p^+ implants and aluminum structure on the backside, which requires the double-sided processes to plant. Before irradiation, the main junction is on the backside and the depletion starts from the p^+ implant and extends to the full bulk by increasing the bias voltage. Therefore, the sensor must be fully depleted for the e-h pairs to reach the electrodes. After type inversion of the bulk, which is a consequence of irradiation, the depletion region starts from the n^+ electrodes. The detector is then able to operate at partial depletion. These structures require a double-side processing given the fact that the guard ring structure must be implemented on the backside around the main junction. Thus, the n^+ -in-n technology requires a more expensive process making it less suited for large area detectors.
- n^+ -in-p technology** This technology implements p-type bulk with n^+ doped implants defining the pixel cells on the frontside and a homogeneous p^+ implant on the backside. The depletion region begins from the n^+ implants and extends downward toward the backside. The junction is located at the collecting electrode making an under depleted operation after heavy irradiation possible. This technology enables the detector to operate at partial depletion. These detectors are produced with a single-side processing given the fact that the guard ring structure can be implemented on the frontside. This allows for cost effective production particularly interesting to cover large areas in excess of 1 m^2 .

The main argument in favor of the pixel detector over all previously used technologies is the high spatial resolution. The resolution for a pixel detector with pitch p and a binary readout from one single pixel is

$$\sigma = \frac{p}{\sqrt{12}}. \quad (2.17)$$

This is called the binary resolution. In the case of segmented detector, a track near the edge of one pixel will produce two-pixel clusters instead of one-pixel cluster. The width of the pitch region p in two-pixel cluster becomes the region between the two collecting pixels instead of the width of one pixel. Depending on the segmentation size in this case, the region in between two pixel implants is more likely to give rise to two-pixel clusters, which result in better spatial resolution. A more detailed study on the position resolution of pixel cluster can be found in this elaborate reference [79] and in section 5.4.3. Therefore, it is in the interest of HEP experiments to have small pitch pixels to maintain a high resolution tracking.

the deposition of a temporary metal layer to bias the pixel implants for testing purposes [83]. This layer is patterned to connect all the pixels via the aluminum implant. This temporary metal layer is removed by another post-processing step as will be discussed further in the next section.

2.3.2 Pixel sensor geometry

2.3.2.1 Planar pixel sensors

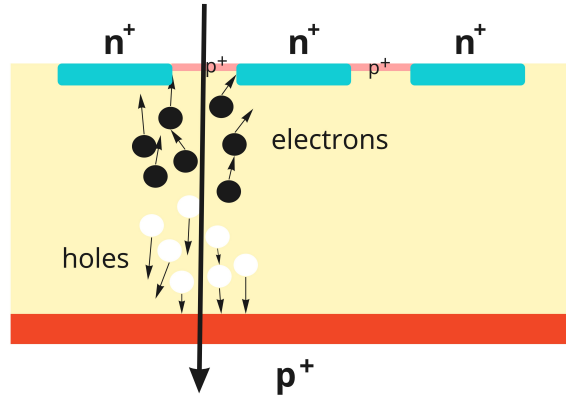


FIGURE 2.8: Reduced schematic layout of segmented planar $n^+ - in - p$ pixel sensor with p^+ spray for inter-pixel insulation .

The cross-sectional layout shown in figure 2.8 is a bare segmented sensor. However, various additional components have to be considered in the design which are not required for the bare pixel cell but are essential for the pixel sensor operation. The array of the n^+ implants define the active area of the sensor and the pixel cell geometry is designed to match the developed ATLAS readout electronics. Features that are necessary for the sensor's operation are discussed in the following:

Inter-pixel insulation

The inter-pixel insulation is used with n-type pixel implants to prevent the formation of an electron layer underneath the top oxide layer and thus assuring proper insulation of the individual pixel. The accumulation of electrons under the surface attracted by positive charges trapped at the interface, would short the pixels together degrading greatly the pixel module performances. This inter-pixel insulation technology is called p-spray, as depicted in between the pixel implant in figure 2.8. It is achieved by the implantation of p^+ dose, which is about $1 - 2 \times 10^{12}$ per cm^2 (low dose p-implantation on all the sensor). This step is part of the fabrication process.

Guard rings

The sensors studies in this thesis were produced in 6 inch wafers as shown in figure 2.9. On a silicon wafer there are several sensor structures that are later diced into single sensors to adapt to the size of the readout chip. The traditional dicing procedure performed by a diamond saw on the silicon wafer creates cracks at the edges of the sensor. This implies that the sensor can not be depleted up to its edge and the electrical field of the backside extends to the front side through the cut-edges. Hence, the use of guard rings (GRs) to gradually control the electrical potential at the edges is necessary. The GRs are a series of ring implants around the matrix of a pixel sensor. An example of guard ring implementation shown in figure 2.10 for IBL pixel sensors. The number, the shape, and the aluminum overhang of the

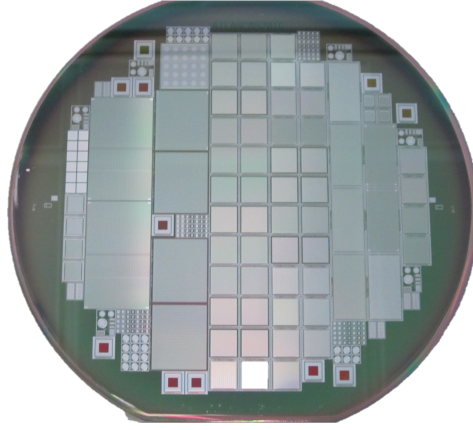
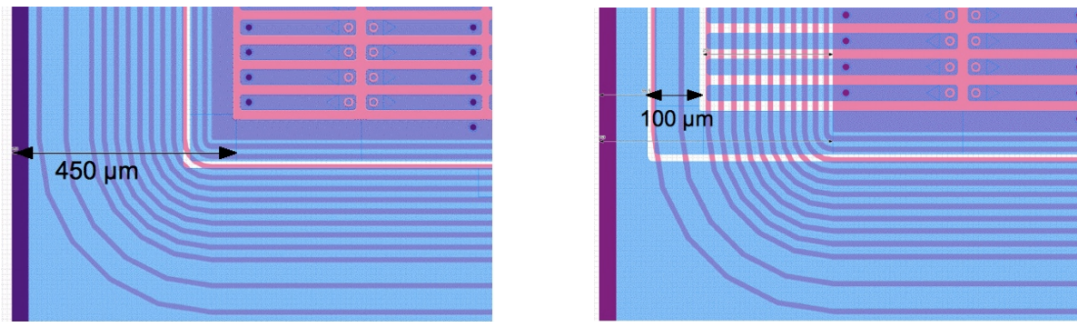


FIGURE 2.9: Image of 6" wafer produced by FBK.

FIGURE 2.10: IBL sensors schematics showing 13 guard rings of 450 μm edge (left) and slim edge sensor where the last pixel implant is extending across the guard rings (right) [84].

GRs as well as the distance between the individual GRs is crucial for the breakdown behavior of the sensor, the performance of the electrical properties based on the GRs will be discussed later in section 6.1. The high number of GRs create an inactive area around the pixel matrix that would ensure a level of safety and high break down voltage. Consequentially, this is considered a limitation as the active area of the pixel detector would be reduced. A low number of GRs have been thoroughly investigated, for example in reference [85], which create what is called an active-edge sensor. Sensors with active edges employ 100 μm wide GR only that enables the last pixels to collect charge outside the sensor's periphery due to the extended potential. Even with numerous GRs, the high voltage still extends to the front-side through the cut-edges, such that the maximum bias voltage is limited by the risk of sparks from the edge to the grounded readout chip, which are only around 30 μm apart. The possibility to mitigate this spark is discussed in the following.

Spark protection

The high voltage potential of the sensor create high risk of spark with the readout chip. To protect the sensor structure the BenzoCycloButene (BCB) passivation layer is deposited on top of the sensor. The advantage of this approach is that the BCB can be applied already during the sensor manufacturing process in relatively thick layers of typically around 3 μm . The BCB has high dielectric strength, which result in a more reliable protection against sparks. However, the vertical side of the sensor cut-edges are not covered by BCB. For complete protection a conformal coating technique with parylene is used for insulation [86]. The parylene is deposited as a chemical vapor that solidifies on the module and acts as a dielectric barrier. A Layer of parylene is deposited on the whole structure after module assembly.

985 Biasing structure

986 Before inter-connecting the sensor to its readout chip it is necessary to test the quality of the sensor. HEP
 987 detectors deals with a large number of sensors, it would be a waste if a bad sensor is processed through.
 988 In order to test the sensor, all pixels have to be biased at the same time. There are two techniques for bias-
 989 ing of the sensor, both require a biasing ring on top of the innermost GR to provide the potential around
 the pixel matrix, where pixel implant remains grounded. First approach consists of a bias grid of alu-

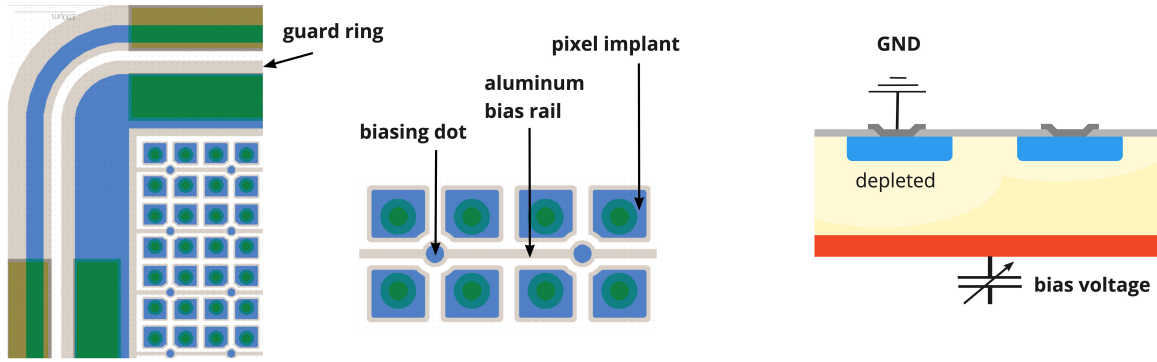


FIGURE 2.11: Schematics of sensor structure (left) showing guard rings around the periphery, biasing dot, biasing rail and the pixel implant for a $50 \times 50 \mu\text{m}^2$ pixel geometry, and cross sectional schematics (right) showing the depleted region around the pixels as the sensor is biased from the back side.

990
 991 minum rails starting from the guard ring and distributed through the sensor structure with additional
 992 connection to a small implants called "biasing dot" that operates with the punch-through mechanism,
 993 (PT) dots, [68] as depicted in figure 2.11. The punch through mechanism is exploited by the biasing dot
 994 implanted inside an opening close to the pixel implant. The pixel implant will stay at a voltage close to
 995 the one of the biasing dot, hence the bulk below the pixel implant will be depleted. The biasing voltage
 996 is distributed to the biasing dot via the aluminum rails. The biasing rails have either straight rail design
 997 in between pixel columns or wavy rail design to connect islands of four floating pixels together. The bias
 998 voltage begin from the grounded pixel and extends to the floating ones. It has been observed that the
 999 biasing structure with a biasing dot² attracts charge carriers generated by the impinging particles and
 1000 induces efficiency losses in the area it occupies after irradiation.

1001
 1002 The second approach of biasing structure is the use of temporary metal technique that is explained in
 1003 the following.

1004 Temporary metal

1005 The temporary metal is a new technique to test the sensors without employing a permanent biasing
 1006 structure [83]. The idea is to remove the biasing structure from the sensor design to prevent any effi-
 1007 ciency losses caused by the biasing rail and the biasing dot. The electrical characterisation is achieved
 1008 by depositing a metal layer over the passivation as part of the wafer post-processing as shown in figure
 1009 2.12. This metal layer is patterned to cover the pixel implants of individual structures to be biased and
 1010 tested individually. The deposited metal strip contacts the underlying pixels via the small opening areas
 1011 foreseen for the bump bonding allowing to operate them without a built-in biasing structure. This tech-
 1012 nique makes it possible to probe the sensor from any position of the metallic layer. As the name indicates,
 1013 the metallic layer must be removed after testing and before bump bonding. The removal of the tempo-
 1014 rary metal requires an etching process for the sensor. This etching step introduces the disadvantage of a

²The biasing dot is commonly referred to as PT dot.

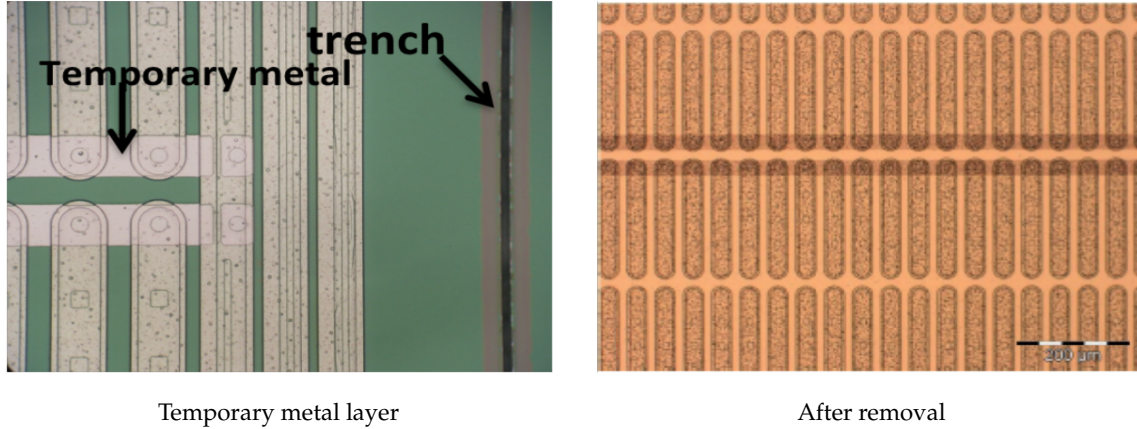


FIGURE 2.12: Image of a sensor employing a temporary metal layer shorting columns of pixels and an image of the same sensor after the temporary metal removal [87].

subsequent processing step before bump bonding to the readout chip. This step is a modification of the production process of pixel sensors. On the other hand, the technique introduces the advantage of no efficiency loss in the sensor. This technique was explored extensively during the time of this thesis and showed promising results in comparison to sensors employing biasing structure. The good performance of sensors measured after the post-processing of removal indicate successful production yield for the sensors.

2.3.2.2 3D pixel sensors

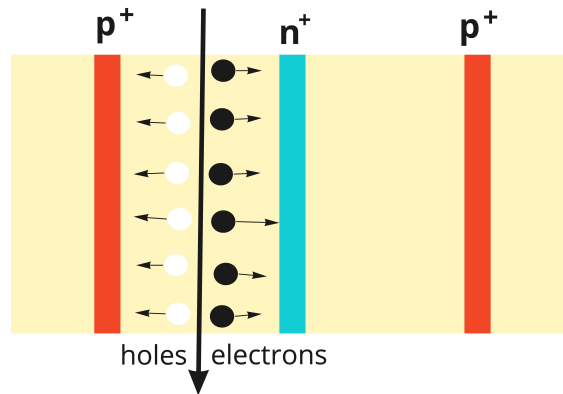


FIGURE 2.13: Schematic layout of a 3D sensor. 3D implants consist of pillars along the sensor thickness.

3D pixel sensors [74, 88] as shown in figure 2.13 are composed of heavily doped pillars passing through a low-doped silicon bulk. The main difference to the planar design is the geometry of the biasing- and readout electrodes. Readout electrodes are etched into the sensor bulk as columns of $6\ \mu\text{m}$ radius by double sided Deep Reactive Ion Etching (DRIE) [89, 90]. The 3D technology is known to be radiation hard with the main advantage of short collection distance allowing operation with relatively low supply voltage of less than 200 V after heavy irradiation. In the ATLAS barrel geometry, another advantage of 3D sensors is that the \vec{E} field and the \vec{B} field are collinear, hence the Lorentz angle shift is negligible. The reduced drift distance of charge carriers decreases the charge collection time and therefore the charge trapping probability making the 3D concept very radiation hard [90].

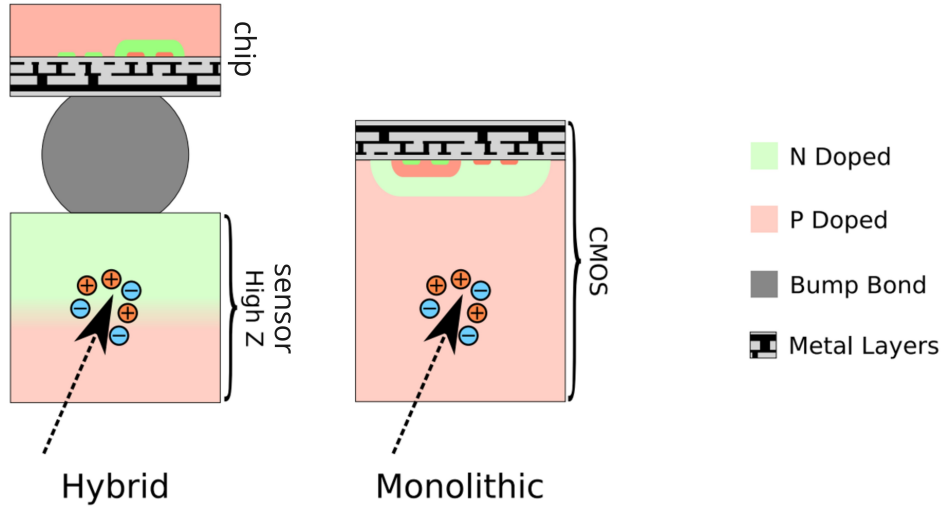


FIGURE 2.14: Schematic layout showing the difference between a Hybrid and CMOS processes [92].

2.3.2.3 Hybrid pixel sensors

Hybrid pixel sensors (3D or planar) [91] are the standard choice of pixel sensors in HEP at the moment. Hybrid refers to the sensors that are interconnected via bump bonds to their readout chip as shown in figure 2.14 in contrast to monolithic sensors (such as CMOS sensors) whose electronics and sensors are processed on the same wafer. Hybridization of planar pixel sensors will be discussed in detail in the following chapter for both IBL and ITk pixel sensors.

2.3.2.4 Monolithic pixel sensors

Complementary metal oxide semiconductor (CMOS) pixel sensors are monolithic sensors, which are intended to incorporate the electronics (analog and digital logic circuitry) on the same wafer as shown in figure 2.14. The electronics use the silicon they are built on as sensor volume and therefore no hybridization is required. They have promising potential cost-reductions and manufacturing simplifications. It is considered an advantage to hybrid sensors having to deal with bump bonding process. CMOS sensors are widely used in the industry and high resistivity CMOS are especially interesting candidates for trackers at future colliders but they do not yet demonstrate the level of radiation hardness as a hybrid pixel sensor. For this reason they haven't been selected for the ATLAS pixel detector.

2.4 Radiation damage

Detectors in HEP experiments are often operating in high particle-flux environments as discussed in the LHC luminosity upgrade plan in section 1.5. The current installed inner detector of ATLAS accumulated about $1 \times 10^{15} n_{eq}/cm^2$ of non ionizing dose, and about 300 kGy of total ionizing dose. At the HL-LHC upgrade it is anticipated that pixels will integrate radiation levels 10 times higher the current level. To develop detectors for HEP experiments, it is essential to have a good understanding of the radiation damage mechanisms. The effects of radiation damage in the silicon bulk are primarily caused by the inelastic scattering of hadrons, which causes atoms to be displaced in the lattice. The R&D of radiation damage concerned in this thesis focuses on displacement damage effects from non ionizing dose.

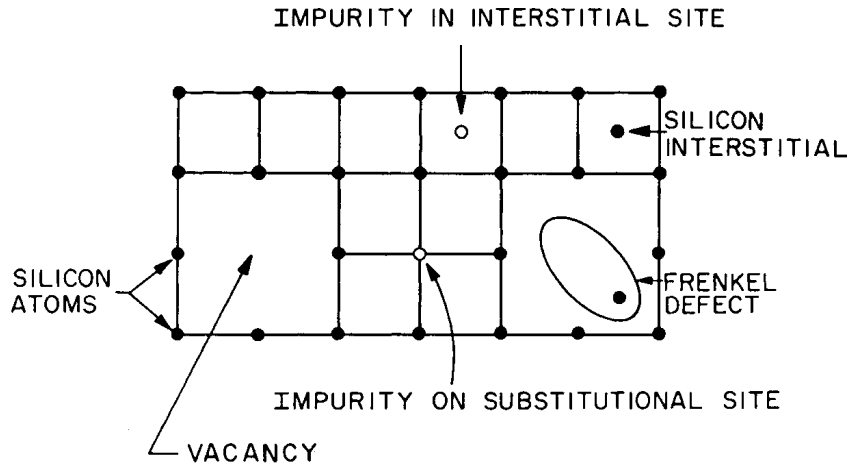


FIGURE 2.15: Interstitial impurities in silicon lattice showing types of defects [67].

An important aspect in estimating the radiation damage on the detector layers is knowing the type of particle and its energy, which has an impact on the radiation-induced degradation of the sensor performance. In the inner pixel layers of the ATLAS detector (see section 1.7) the damage from the charged hadron component (mainly charged pions) is dominating, while for the outer layers the neutron component is dominating [93]. When a highly energetic incoming particle collides with silicon atoms in the lattice the displaced atom is called an interstitial defect (excess semiconductor atoms in the crystal lattice) as shown in figure 2.15. The "hole" left in the lattice is called a vacancy (missing semiconductor atoms in the crystal lattice). A vacancy and an adjacent interstitial site in interaction, form what is called a Frenkel defect pair [67]. Depending on the type and energy of the impinging particle, the defects can be point defect or a cluster of defects *i.e.* a combination of multiple point defects.

Defects could be formed in the silicon bulk, and at the surface. At a macroscopic level, there are three main consequences of radiation on the silicon sensor; the increase of the leakage current, the change of the effective doping concentration, and reduced charge collection. In the following sections I discuss these consequences on the properties of the silicon bulk, and on the operation of the detector.

2.4.1 Bulk damage

2.4.1.1 Non Ionizing Energy Loss

The Non Ionizing Energy Loss (NIEL) gives the portion of energy that is lost by a traversing particle which does not go into ionization and eventually leads to displacement damage *i.e.* defects. The NIEL hypothesis [93, 94] assumes that radiation damage effects scale linearly with NIEL, irrespective of the distribution of the primary defects over energy and space. Thus, the number of interstitials and vacancies should give a measure of the damage irrespective of their distribution or clustering over the volume. The energy loss dissipated in the lattice contribute to the displacement damage by NIEL and it depends on the impinging particle. NIEL is defined in units of MeVcm^2/g or as NIEL cross section (displacement damage function D) in units of MeVmb . A reference value of 1 MeV neutron equivalent n_{eq} has been fixed to 95 MeVmb . The NIEL cross section for various particles is measured as shown in figure 2.16. The damage produced by different particles (or particles with different energy) should be scalable via their damage function as shown in the figure. The hypothesis is a powerful method to be able to relatively normalize the damage of different particles and different energies. It can also predict

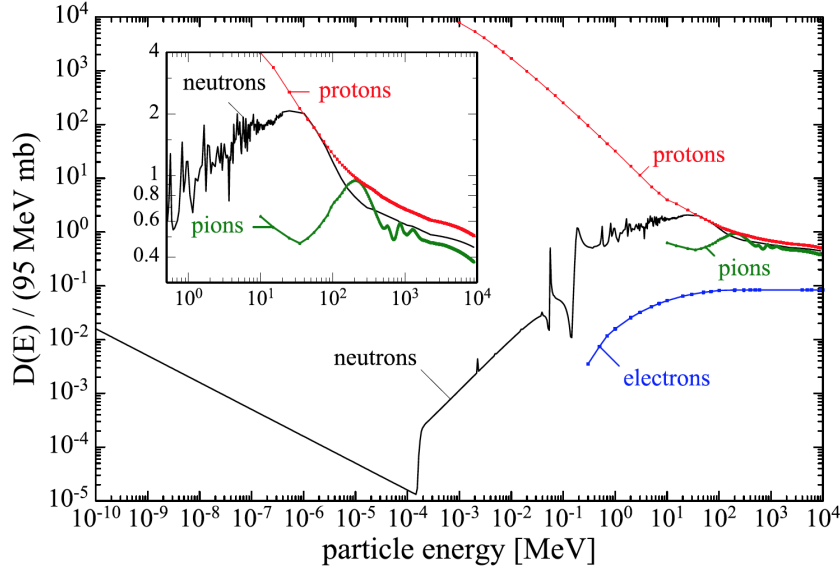


FIGURE 2.16: NIEL cross section normalized to 95 MeVmb. The displacement damage functions are presently used to calculate the 1 MeV n_{eq} radiation fields [93].

displacement damages in complex radiation fields. The NIEL hypothesis can predict the damage from different parameters that have an impact on the leakage current and the effective space charge region. However, for protons and electrons, an *effective NIEL* [95, 96] or the *equivalent displacement damage dose concept* [97] can deliver better linearity between some damage parameters and the calculated NIEL. Silicon sensors under test could be irradiated with different particles depending on the irradiation facility. With the NIEL cross section we could estimate the level of leakage current in the sensor given the amount of displacement damage.

2.4.1.2 Impacts of defects on silicon sensors

The impact of radiation damage on the detector performance can be described in the framework of the Shockley–Read–Hall (SRH) statistics [67, 71]. The impact of each defect can be calculated if the position in the band gap, the capture cross sections for holes and electrons, the type and concentration of defect are known. On the device performance level, three main effects can be identified that would impact the detectors performance:

- increase of the leakage current.
- change in the operational bias voltage, including type inversion for n-type material.
- decrease of the charge collection efficiency, i.e. trapping.

The intensity of these three effects depend on the amount of fluence the sensor has been exposed to, on the temperature, and on time after irradiation. These effects will be discussed in the following with their formulation in the SRH framework.

Leakage current

The leakage current is most effectively produced by defect levels close to the middle of the band gap [93]. The number of defects in the leakage current follows the NIEL hypothesis scaling for hadron damage. As the leakage current depends exponentially on the temperature, HEP detectors are usually operated in

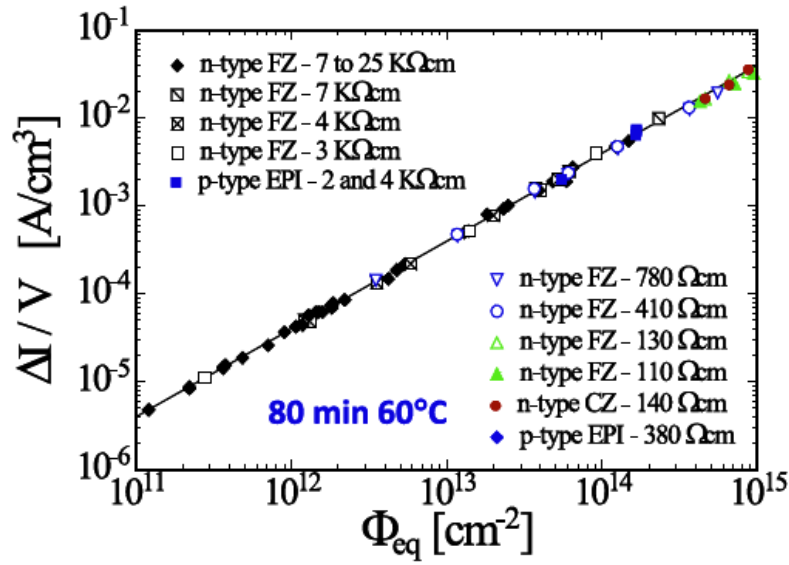


FIGURE 2.17: Radiation induced leakage current increase as a function of particle fluence for various silicon detectors produced with several bulk resistivity values and conduction type. The current was measured after a heat treatment of 80 min at 60°C and is normalized to the current measured at 20°C [98].

low temperature to effectively mitigate the detrimental effects. After irradiation, radiation-induced defect levels produce leakage current by the subsequent emission of electrons and holes from the valence to the conduction band, this current is also called generation current. The generation current is produced at the space charge region.

After exposure to high energetic particles there is sufficient energy to produce defect clusters, which lead to the increase of the leakage current as shown in figure 2.17. Modules that are irradiated to higher fluence are expected to have higher leakage current. The increase of the leakage current is proportional to the particle fluence and independent of any defects type, resistivity, or impurity content of the used silicon material [93]. The radiation-induced leakage current can be scaled with the proportionality factor called *current-related damage factor* α , which is defined by

$$\alpha = \frac{\Delta I}{V \phi_{eq}} \quad (2.18)$$

where ΔI is the increase on the leakage current caused by irradiation, V is the volume contributing to the current, and ϕ_{eq} is the particle fluence. A measurement of the proportionality factor at 20°C $\alpha(80min, 60^\circ C) = (3.99 \pm 0.03) \times 10^{-17} A/cm$ [98]. The increase of the leakage current also lead to the heating of the sensor and a consequential thermal runaway that could destroy the detector. To avoid this effect, the detectors need to be operated at low temperature below room temperature. ITk irradiated modules are operated in -40-50°C in testbeams.

Effective space charge

The radiation-induced defects lead to a change in the effective space charge N_{eff} that is reflected in the change of the depletion voltage V_{dep} of the device expressed in equation 2.8 [93]. In highly irradiated detectors, contrary to undamaged detectors, the space charge is no longer identical to the concentration

in thermal equilibrium. The effective space charge N_{eff} , i.e. depletion voltage, evolves with fluence. For n-type bulk sensors, the irradiation of the sensor results in the formation of negative space charge, which compensates the initial positive space charge. With increasing particle fluence to about $10^{12} \text{ n}_{eq}\text{cm}^{-2}$, the net space charge decreases and reaches very low values corresponding to almost intrinsic silicon. At this point where the net space charge is lowest, is called *type inversion* as the effective doping concentration N_{eff} in the space charge changes from positive to negative as shown in figure 2.18. The increase

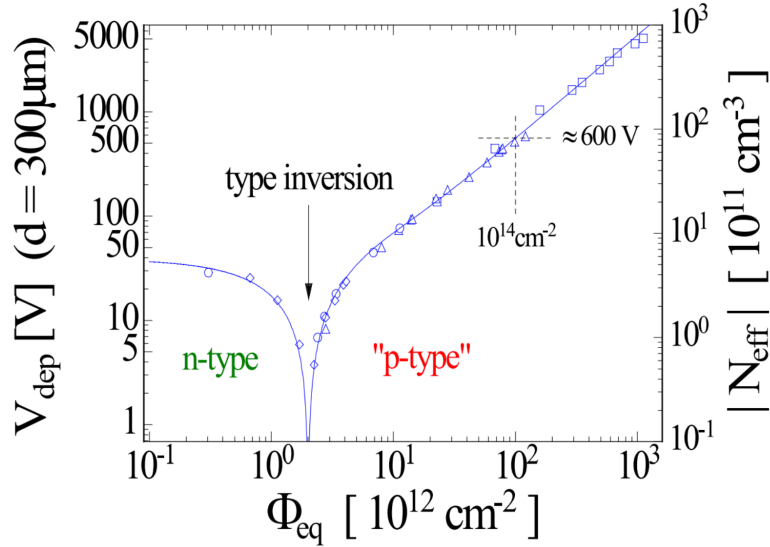


FIGURE 2.18: Evolution of the effective doping concentration as a function of fluence. The data shown here were taken at room temperature while the annealing took place at 60°C [93].

of the particle fluence beyond the inversion point leads to more negative space charge values. Hence, the depletion voltage rises accordingly and reaches higher operational voltage values. The sensor would benefit from increasing the operational voltage values after irradiation to recover trapping defects with high electric field as will be discussed in the next section. For p-type bulk sensors, no type inversion is usually observed as the initial space charge is already negative before irradiation. Even after irradiation p-type bulk still suffers from the increase of depletion voltage with NIEL fluence.

Defects and material engineering have been extensively studied for the dependence of material and irradiating particle on the effective space charge by the R&D collaborations [99, 100]. A wide range of sensors produced on different bulk types, having different impurity contents, exposed to different types of particles, tested under different operational conditions have been studied. These studies demonstrated that the impurity content of the used silicon, which is based on the production of the sensor, and the type of particle used for the irradiation experiment have a strong impact on the space charge and the electric field distribution within the sensor [93].

Trapping

The radiation-induced energy levels in the energy gap are able to capture the charge carriers drifting to their counter electrode. This effect is called *charge trapping* [93]. Charge trapping impacts the charge collection performance of the sensor: if a charge carrier is trapped into a defect level and not released within the signal collection time of the sensor, the charge is lost and the corresponding sensor signal is reduced. With higher particle fluence the defect concentration increases, more charge carriers get trapped,

which leads to the degradation of the spatial resolution, and to the decrease of the charge collection efficiency (CCE) in the silicon detector. Trapping defects in the sensor can be mitigated with high electric field inducing the charge carriers to gain enough speed to arrive to the collecting electrode before being trapped. For this reason, to reach high hit efficiency in irradiated silicon detectors, higher bias voltage must be applied for the charge carriers to overcome trapping levels in time. The effective trapping time τ_{eff} is the average time needed before a carrier gets trapped. τ_{eff} is used to describe the trapping effect assuming that the loss of charge Q depends uniquely on the transport time t of the charge carriers inside the sensor. τ_{eff} can be separately measured for electrons and holes [93, 101] by

$$Q(t) = Q_0 \exp \left[\frac{-t}{\tau_{eff}} \right]. \quad (2.19)$$

A linear dependence of the inverse effective trapping time on the particle fluence is observed and can be described as

$$\frac{1}{\tau_{eff}} = \frac{1}{\tau_{eff,0}} + \beta \phi_{eq} \quad (2.20)$$

where β is the effective trapping damage proportionality factor and $\tau_{eff,0}$ is the effective carrier life time before irradiation. In a recent study [102] focusing on high-fluence irradiation above $3 \times 10^{14} \text{ n}_{eq}/\text{cm}^2$, it is found that the inverse electron trapping time (electron trapping rate) are a factor of 2-3 below the linear extrapolation from low-fluence data. Also, the inverse hole trapping time (hole trapping rate) are about a factor of 3 below the linear extrapolations. These results show that higher signals can be expected at higher fluences. Such studies are important to describe the tracker performance under high fluence in the HL-LHC phase.

Annealing

An important concept in radiation damage is annealing. Radiation damage defects in the bulk act like acceptors attracting charge, which influence the device performance. With temperature and time, these defects can re-configure, break-up, recombine, and diffuse through the bulk. The evolution of defect concentration with temperature and time is called *annealing*. For detector operation, controlled annealing plays an important role in order to minimize the negative effects from radiation damage, this damage type is also called *beneficial annealing*. The beneficial annealing is produced by the decrease of the effective doping concentration after stopping the exposure to particle fluence. Such phenomenon can be controlled and reproduced by heating the sensor at 60°C during 80 minutes to diminish the effective concentration of defects and thereby the depletion voltage [98]. This phenomenon is considerably slowed down at low temperature. It is the reason why irradiated detectors are operated at low temperature about -40°C . The impacts of annealing will be highlighted in each type t of bulk damage described in the following. The discussed types of bulk damages are: the leakage current, the effective doping concentration, and the effective trapping damage constant. For all three types the device performance highly depends on the annealing after irradiation.

After the exposure to highly energetic particles, the radiation-induced leakage current increases proportional to the current-related damage factor described in equation 2.18. The annealing behavior of the current-related damage factor α continuously decrease after irradiation with increasing annealing time [93]. The defect reactions in the silicon bulk can be accelerated by increasing the annealing temperature. The annealing temperature is the temperature at which the samples are stored or heated. The acceleration of the annealing behaviour by increasing the temperature will lead to beneficial annealing.

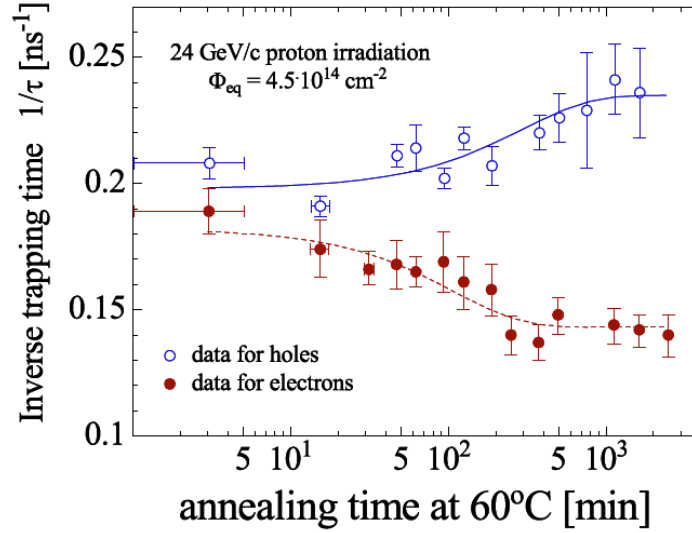


FIGURE 2.19: Evolution of the inverse trapping time as function of annealing time at 60°C [93].

The effective doping concentration after irradiation is changing with time. Annealing can be accelerated at high temperatures and decelerated at low temperatures. The change of the effective doping concentration with irradiation ΔN_{eff} is given by

$$\Delta N_{eff} = N_{eff}(0) - N_{eff}(t) \quad (2.21)$$

where $N_{eff}(0)$ is the value before irradiation and $N_{eff}(t)$ is the value after irradiation. The time dependence of N_{eff} is parameterized as

$$\Delta N_{eff}(t) = N_A(t) + N_C + N_\gamma(t) \quad (2.22)$$

where N_A is the short term beneficial annealing component, N_C is the stable damage component, which does not change with time after irradiation, and N_γ is the reverse annealing component. Further details of parameterization for reverse annealing can be found in [98, 103].

As for trapping defects, results studying the annealing behaviour comparing the inverse trapping time for electrons and holes are shown in figure 2.19. For electrons a decrease in the effective trapping time $1/\tau_{eff}$, less trapping, with annealing time is observed. This emphasize the benefit of instrumenting the ITk detector with p-type bulk *n-in-p* technology.

2.4.2 Surface damage

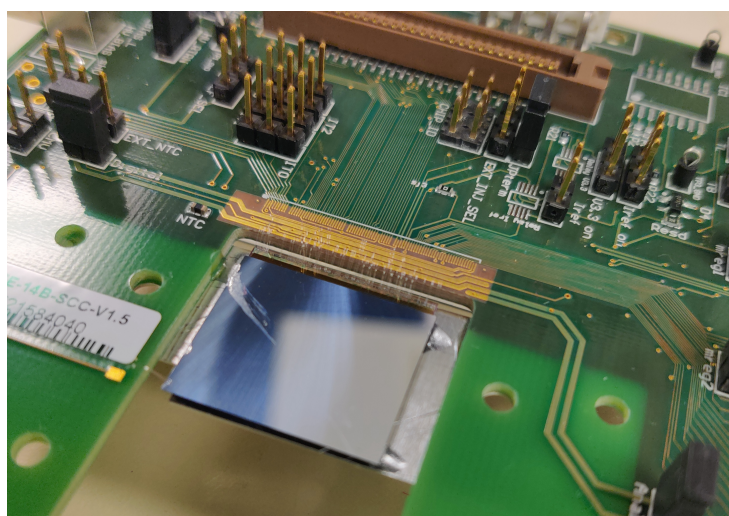
In addition to the effects that rise in the bulk of the sensor, radiation induced electron-hole pairs are released in the insulating silicon dioxide (SiO_2) layer grown on the surface of the bulk. Due to low mobility on the Oxide layer most of the pair recombine immediately, however electrons are fast and could escape the insulating layer before recombination. Holes, on the contrary, are slow and could be captured by deep traps forming a fixed positive space charge in the interface between silicon and silicon dioxide layer. This positive charge attracts electrons, which accumulate on the silicon surface. This layer of accumulated electrons would short all pixel implants in sensors based on n-type pixels. To prevent this effect, a p-spray layer with a low dose p-doped is used around the implant to compensate the accumulating

electrons and ensure the inter-pixel insulation at sufficient levels. This technique is performed at the fabrication process of the sensor and successfully mitigate radiation surface damage.

The deterioration of the pixel detector due to radiation damage is considered in this thesis for the ITk pixel detector operating through the life time of the HL-LHC. The simulated radiation levels of the ITk detector as shown in figure 1.12 anticipate an accumulated fluence up to $1 \times 10^{16} n_{eq}/cm^2$. Such high irradiation levels will deteriorate the detector. Therefore, the performance for the detectors must be studied at the same conditions to ensure its efficient operation in the HL-LHC phase [104]. ITk pixel sensors are required to operate with at least 97% hit efficiency after the expected radiation at a voltage lower than 600 V. Both sensors and readout chips must comply with the radiation tolerance requirements of the ITk. For this reason the ITk layout design is planning to have a layer that could be exchanged after integrating half of the expected luminosity. This replaceable layer would reduce the radiation damage effects on the tracking performance. In the next chapter I will introduce the sensor designs and electronics of the current IBL and future ITk pixel detector.

1234 *"I am among those who think that science has great beauty. A scientist in the laboratory is not only a technician*
1235 *but also a child placed before natural phenomena which impress her like fairy tale. "*

Planar pixel modules for the ATLAS detector



1239
1240
1241
1242
1243
1244
1245
1246
1247
1248
1249
1250
1251

3.1 IBL pixel module

¹<https://lpnhe.in2p3.fr/>

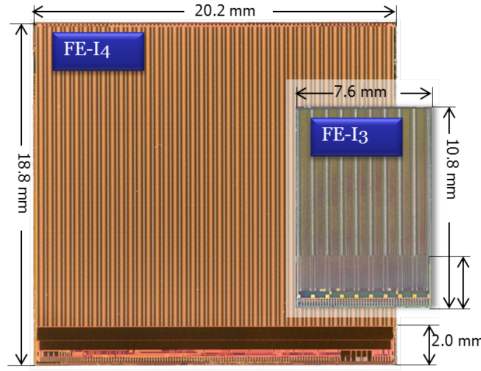


FIGURE 3.2: Picture of FE-I4B readout chip developed for the IBL detector [48] in comparison to its old predecessor FE-I3 developed for the pixel detector.

3.1.1 IBL sensors

One of the main topics of this thesis is the calibration and tuning of the IBL readout chip. For this reason, I introduce both the IBL sensor and its readout chip the FE-I4B in this section before diving into operational details in the next chapter.

IBL sensor designs were based on established prototypes of the original ATLAS Pixel Sensors (APS) using the FE-I3 readout chip [50], but modified to match the specifically developed FE-I4B readout chip geometry [105]. Figure 3.2 shows a geometrical comparison between both readout chips. The main challenge for IBL sensors was to maintain adequate tracking efficiency at fluences up to $6 \times 10^{15} n_{eq}/cm^2$, where the original pixel sensors were developed for a fluence of only $1 \times 10^{15} n_{eq}/cm^2$. The detector is scheduled to operate three more years for Run3. The development of IBL sensors was driven by the ATLAS upgrade planar pixel sensor and 3D Sensor R&D collaborations [106]. The development was based on requirements following from the operational conditions [84] from Run1. To maintain tracking performance with LHC upgrade schedule, IBL modules required:

- sensors with an inactive edge width $< 450 \mu m$ for dual module and $< 225 \mu m$ for a single module.
- sensor thickness between 150-250 μm , as thinner sensors would reduce material budget.
- power dissipation $< 200 mW/cm^2$ at $V_b = -100 V$. This specification is used as input for thermal runaway calculations and cooling design.
- maximum leakage current $< 100 nA/pixel$.
- sensor operating temperature should be $< -15^\circ C$ at $< 200 mW/cm^2$.
- hit efficiency $> 97\%$ after a benchmark fluence of $5 \times 10^{15} n_{eq}/cm^2$ at maximum $|V_b| < 1000 V$. This limit is chosen to limit the degradation of performance after irradiation.
- to withstand integrated luminosity of $550 fb^{-1}$ during IBL operation.
- for electronics to sustain a 250 MRad ionizing dose.

The physical size of the IBL sensor depends on the designated FE-I4B readout chip that addresses the operational requirements to cope with higher hit rates in Run2. Planar sensors for the IBL detector are produced in 200 μm thick n-type bulk with segmented n^+ implants on the front side and a highly doped p^+ implantation on the back side. The schematics of the IBL sensors shown in figure 3.3 have pixel geometry of $50 \times 250 \mu m^2$ that was reduced to improve the granularity of the detector from the original pixel

layers that has pixel geometry of $50 \times 400 \mu m^2$. This finer granularity ensures a good spatial resolution

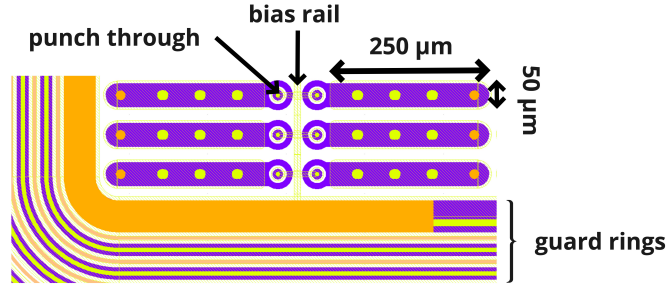
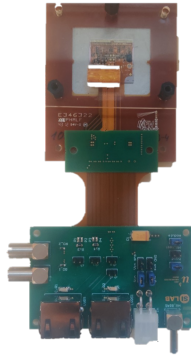


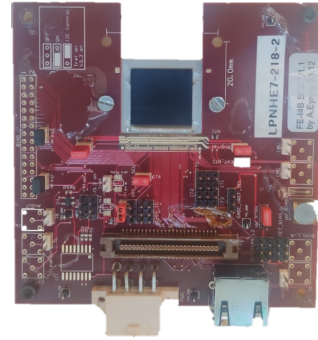
FIGURE 3.3: Schematics of an IBL sensor with pitch size $50 \times 250 \mu m^2$ with a straight bias rail design to connect the pixel matrix via the punch through mechanism, guard rings around the pixel matrix with the bias ring (in orange) to polarize the sensor.

of the order of tens of micrometers for better tracking performance for the inner most layer in the ATLAS detector.

The IBL prototype production included Single Chip Sensor (SCS) modules. The SCS module consists of a single sensor and a single readout chip, which together is called the hybrid module. A module that is used for testing and calibration is assembled on a Printed Circuit Board card (PCB), and a module to be installed in the detector is assembled on a flexible PCB (flex) to reduce material budget and gain flexibility. An example of modules assembled with a PCB are shown in figure 3.4. During prototyping,



Single module on flexible PCB with an adapter card.



Single module on PCB.

FIGURE 3.4: IBL hybrid prototype modules.

PCB cards route pins and connectors to different chip signals for tests and debugging. The PCB provide the passive electronic components to operate the chip for signal termination and power filtration.

In the IBL installation, due to the small radial space between the beam pipe and the B-layer, a flat arrangement of the modules on a local support structures (staves) were made to minimize material and optimize performance. Schematics of IBL layout is illustrated in figure 3.5. It consists of 14 axial local support structures (staves) that are arranged cylindrically around the beam pipe and tilted by 14° in $r - \phi$ with 20% stave-to-stave overlap, while no overlap in the z direction due to space constrains. The total length of the stave in z direction is 724 mm [47]. Each stave as shown in figure 3.6 contains 20 modules, 8 single chip modules on either ends with 3D sensors and 12 double-chip modules with planar sensors covering the central region. 3D sensors populated the ends of the detector with highest $|\eta|$ range where the tracking can benefit from the vertical electrode orientation of the sensor to have better z -resolution

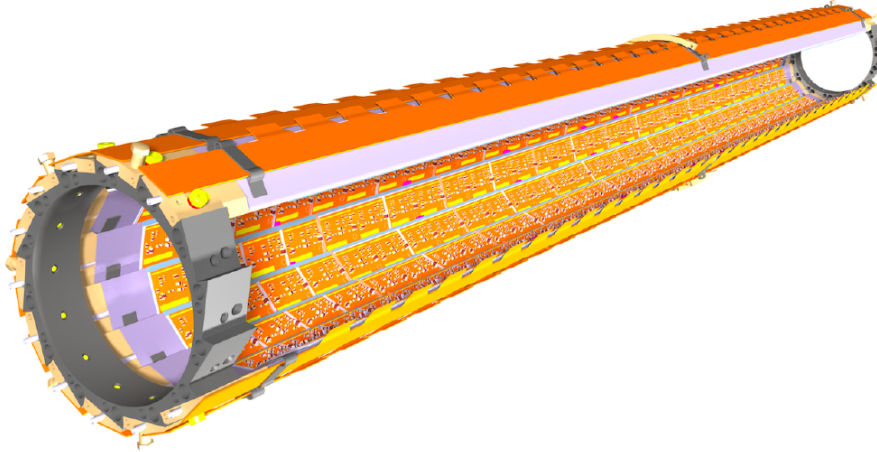


FIGURE 3.5: Layout of the ATLAS IBL. The detector modules are mounted on light-weight carbon fiber support-structures housing CO₂ evaporative cooling tubes. A fraction of the 14 staves are depicted [107].

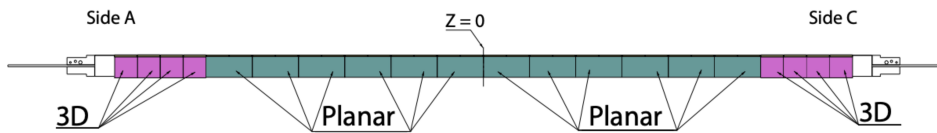


FIGURE 3.6: Schematics of the IBL stave [108].

after irradiation. Due to the spacial constrain in the z direction both planar and 3D sensors were developed with the slim edge guard ring technology [109] to reduce geometrical inefficiencies.

The IBL sensor design in figure 3.7 shows the outermost pixel columns of the modules which contain long pixels that are extended to $500\ \mu\text{m}$ length to overlap the guard ring structure by $250\ \mu\text{m}$. The overlapped region has been shown to remain active for $200\ \mu\text{m}$ thick detectors, this design is referred to as the slim edge design. A sensor with a slim edge design employ $200\ \mu\text{m}$ wide guard rings that has an electric potential smoothly varying to enable the charge collection in the "inactive" edge regions of the sensor and therefore, increasing its geometric efficiency. While an active edge sensor design employ $100\ \mu\text{m}$ wide guard rings overlapping the last pixel implant to extend the charge collection in the inactive edge of the sensor. IBL slim and active edge sensor technologies have been extensively studied in [84, 85, 110, 111].

The inter-pixel insulation technique of IBL is adapted from the APS and follows the moderated p-spray concept as introduced in section 2.3.2. IBL planar sensors were fabricated by CiS². To ease the characterisation of the modules and to avoid a floating potential on pixels having an open bump connection, a punch-through mechanism was implemented (see section 2.3.2). It was later found that this mechanism induces efficiency loss in the biasing structure region after irradiation [84]. For current productions of ATLAS pixel sensors this issue is being addressed by implementing the temporary metal technique.

²CiS Forschungsinstitut für Mikrosensorik und Photovoltaik GmbH, Erfurt, Germany

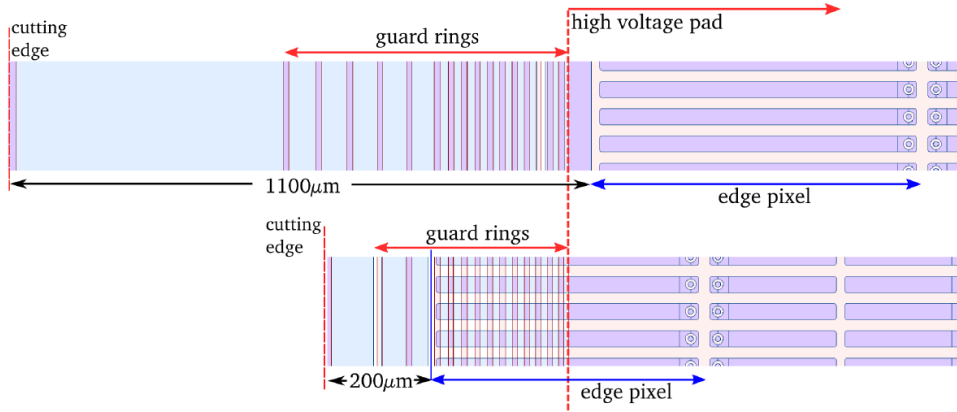


FIGURE 3.7: Comparison of the edge region of the original pixel detector design (upper) and the IBL planar pixel sensor design (lower) [84]. The last column pixel is extended to double its size and overlaps the guard rings structure for the edge potential degradation.

3.1.2 FE-I4B readout chip

The FE-I4B integrated circuit [105] was developed for the IBL upgrade. The FE-I4B was designed to overcome the limitations of the previous readout chip, the FE-I3 [112]. The second version is the FE-I4B chip was further developed to tolerate harsher radiation levels and maintain good performance at closer proximity from the interaction point. The FE-I4B was produced on a 130 nm sized bulk Complementary Metal Oxide Semiconductor (CMOS) process for radiation hardness. It is designed to remain efficient up to integrated luminosities of $6 \times 10^{15} n_{eq}/cm^2$ and 250 Mrad in terms of ionizing dose [84]. The integrated circuit contains readout circuitry for 26,880 hybrid pixels arranged in 80 columns on 250 μm pitch in the z direction \times 336 rows on 50 μm pitch in the azimuthal ϕ direction. The FE-I4B chip has the physical dimensions of $20.2 \times 18.8 mm^2$ including the End-Of-Column pad (EOC) as shown in figure 3.2 in comparison to the previous generation readout chip.

A top level diagram shows the periphery schematic of the FE-I4B in figure 3.8. The FE-I4B pixel array is organized in 40 Double-Column (DC) and divided into 2×2 core pixel regions. Each region contains 4 identical analog sections, ending in a discriminator, one shared memory, and a logic block called Pixel Digital Region (PDR) [105, 113]. The PDR zoomed out in figure 3.8 holds the logic for data processing. It can store up to five events, which are selected with an external counter matching the trigger latency with the nominal clock period of 25 ns. For each event the clock cycles at nominal frequency of 40 MHz that keeps track of the time elapsed since the event took place. The PDR also includes an Analog-to-Digital Converter (ADC), which digitizes the signal and converts it to an amplitude information of the Time-over-Threshold (ToT) (also see section 4.2.2.4). The dimensions of the FE-I4B extends beyond the dimensions of the sensor for the EOC pad to be wire bonded.

The FE-I4B analog front-end circuit [47] shown schematically in figure 3.9 is discussed in some detail here to understand the tuning issues of the circuit that will be investigated in the next chapter. The circuit runs a two-staged AC-coupled Charge Sensitive Amplifier (CSA) per pixel. In the first stage after charge injection, from a real event or during calibration, a preamplifier with an adjustable signal time shaping changes the fall time of the signal. In the second stage, the discriminator retain signals above the adjustable threshold and outputs the analog signal into a digital square wave. The output of the discriminator is a step function that equals to 1 when the signal is above threshold and 0 when the signal is below threshold. Feedback current and threshold DACs (FDAC/TDAC) present in each pixel

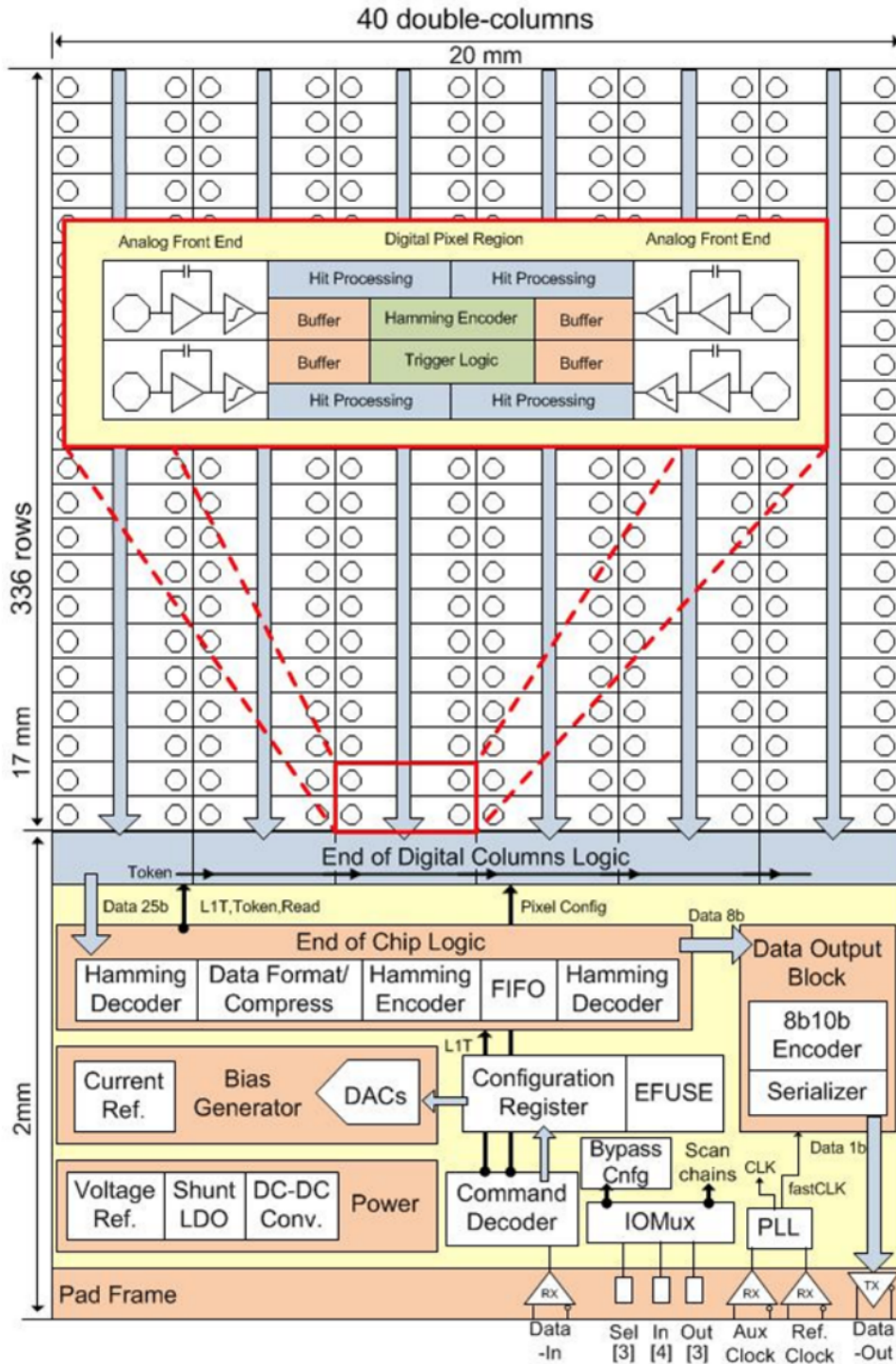


FIGURE 3.8: Schematic overview of the FEI4 readout electronics. The 2×2 pixel core region as enlarged in red includes the pixel digital region and the analog front-end region [105].

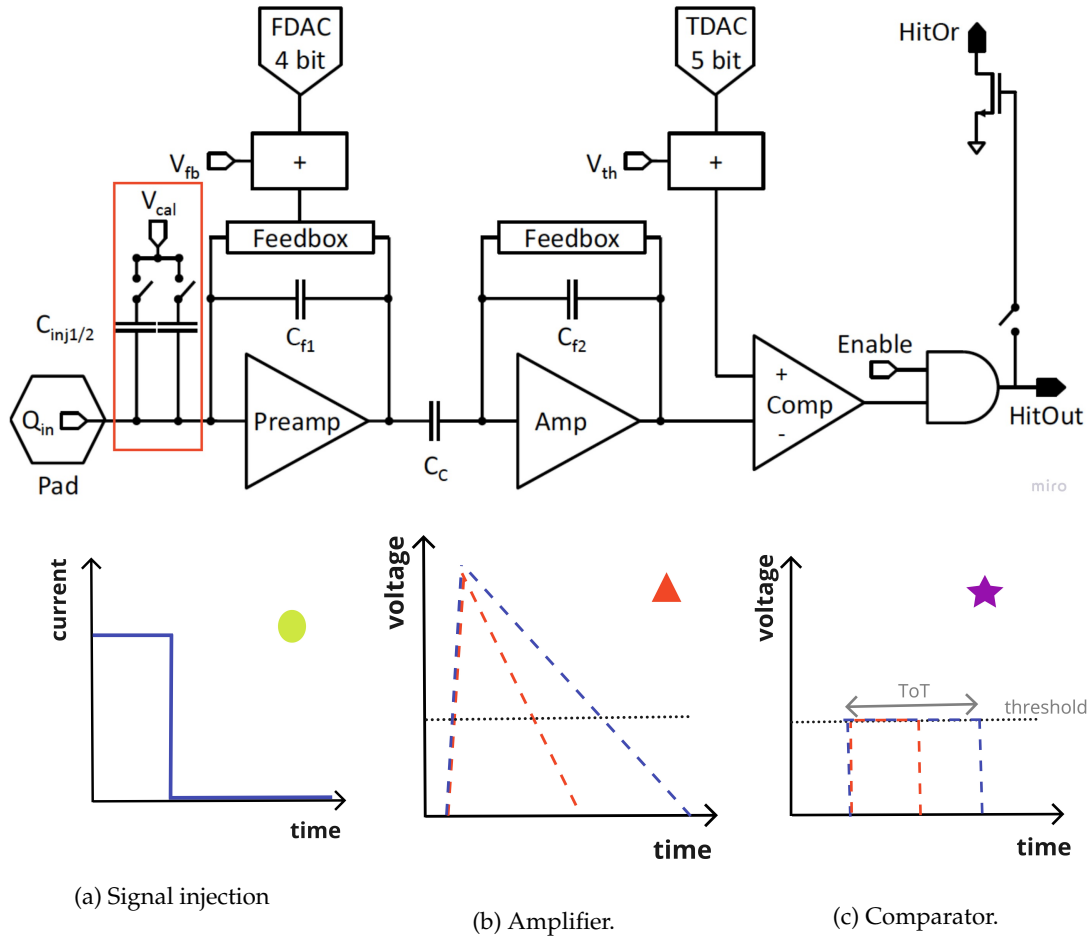


FIGURE 3.9: Analog pixel cell of the ATLAS FE-I4B front-end chip consisting of a charge injection circuit (V_{cal}) framed in red, two AC coupled charge sensitive amplifiers (Preamp, Amp), a comparator (Comp), shaping time and threshold tuning circuits (V_{fb} , FDAC; V_{th} , TDAC), an enable switch (Enable), and the HitBus signal (HitOr). The signal formation from the injected test charge is illustrated in (a). (b) shows the signal amplification and drop. (c) The comparator digitized the signal to ToT information. Image adapted from [84].

allows for adjusting the shape of the time signal and threshold. Charge determination and time stamping is implemented using the ToT technique, which is counted in a 4-bit resolution using the external clock of 40 MHz. This clock is provided by the readout system and synchronized to the bunch crossing frequency during operation at the LHC. The readout chip is also implemented with a charge-injection circuit, framed in Red in figure 3.9, for tuning and testing. It distributes a voltage step (V_{cal}) to selectable injection capacitors (C_{inj1} , C_{inj2}) present in each pixel. The charge injection specifications and limitations is further discussed in chapter 4.2.1. The operation of the analog region requires a voltage of 1.5 V, while the digital region requires a voltage of 1.2 V. The overall specifications for the FE-I4B chip is summarised in table 3.1.

TABLE 3.1: Basic specifications for FE-I4B readout electronics [84].

Item	Value	Unit
Pixel size	250×50	μm^2
Number of pixels	$80 \times 336 = 26880$	col \times row
Bump pad opening diameter	12	μm
Input	DC-coupled negative polarity	
Maximum charge	100 000	e^-
Tuned threshold dispersion	< 100	e^-
Charge \rightarrow Digital coding method	ToT	4 bits resolution
hit-trigger association resolution	25	ns
Nominal analog supply voltage	1.5	V
Nominal digital supply voltage	1.2	V
Nominal analog current	12	μA
Nominal digital current	6	μA
DC leakage current tolerance per pixel	100	nA
Radiation tolerance	250	Mrad
Operating temperature range	-40 to +60	$^{\circ}C$
Maximum number of consecutive triggers	16	
Trigger latency (max)	6.4	μs
Nominal clock input frequency	40	MHz

The introduced parameters of the FE-I4B front-end circuit are essential for the tuning and the operation of the module. A good tuning of the threshold will assure efficiency and high quality data taking. To tune the module, it requires the use of some of the basic parameters presented in table 3.1. The tuning procedures will be the focus of the next chapter to introduce a conclusive study on the threshold tuning for the FE-I4B chip currently installed in the IBL detector.

3.2 ITk pixel module

Following the Phase-II upgrade of the LHC transforming into HL-LHC as discussed in the LHC upgrade plan in section 1.5, the instantaneous nominal luminosity will be 5-7 times its original value and the integrated luminosity will be 10 times the one foreseen by the end of Run4-5. The combination of high instantaneous and integrated luminosity means a much harsher environment for the tracker with respect to LHC runs. The pile-up events will increase to an average of 200 interactions per bunch crossing. These leveling in the performance of the LHC machine are directed by the physics goals, in particular to improve precision in measurements and expand the search for new physics (see section 1.6). These conditions set the requirements for the new ATLAS ITk detector. To meet the challenges introduced by the LHC upgrade, the ITk will be an all silicon tracker and requires:

- efficiency in the innermost layer with particle fluence up to $1.3 \times 10^{16} n_{eq}/cm^2$ and 900 Mrad for the pixel detector and up to $1.2 \times 10^{15} n_{eq}/cm^2$ and 500 Mrad for the strip detector.

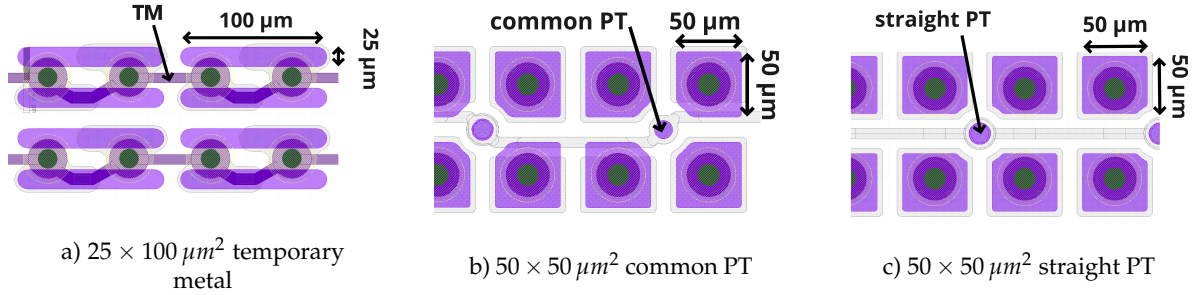


FIGURE 3.10: ITk pixel sensor geometries showing both types of biasing structures: straight and common biasing rail with punch-through mechanism.

- thin sensors of $100 - 150 \mu\text{m}$ as low material budget would improve the tracking benefiting from low radiation length.
- fast and reliable readout electronics to cope with high pile-up of 200 collisions per bunch crossing.
- high hit efficiency of 97% after irradiation.
- high vertex and track position resolution with a high granular detector with $50 \times 50 \mu\text{m}^2$ or $25 \times 100 \mu\text{m}^2$ pitch size.

ITk pixel sensors and its readout chips are developed following these requirements as a guideline. In the following, I discuss in detail the ITk pixel sensor design within the planned layout for the ITk pixel detector. Afterwards, I discuss the basic components and versions of the RD53 readout chip for the ITk pixel detector. The tuning and calibration to operate the RD53A chip will be discussed in the next chapter.

3.2.1 ITk pixel sensors

As introduced in section 1.8 the granularity of the ITk pixels has increased by a factor of five with respect to the IBL pixels. The considered nominal pixel size for ITk sensors is $50 \times 50 \mu\text{m}^2$ and $25 \times 100 \mu\text{m}^2$. Both sensor geometries as shown schematically in figure 3.10 are investigated in prototype productions as part of ATLAS ITk upgrade R&D [60, 61]. The study of ITk pixel module in this thesis explores different biasing structure design of straight, common (or wavy) biasing rail, and no biasing structure with temporary metal technique.

Within the 5 pixel layers of the ITk pixel detector, the pixel pitch is chosen to be $50 \times 50 \mu\text{m}^2$ for all planar layers 1-4, and $25 \times 100 \mu\text{m}^2$ for the innermost pixel layer with their coupled ring for 3D sensors [61]. Sensors thickness will be $100 \mu\text{m}$ for layers 0 and 1, and $150 \mu\text{m}$ for layers 2-4. The main difference in ITk sensors with respect to the current pixel detector is the technology $n^+ - in - p$ versus the traditional $n - in - n$ and the reduced thickness in the range of $100 - 150 \mu\text{m}$ with respect to the $200 - 250 \mu\text{m}$ in the current ATLAS pixel detector. The basic parameters of ITk sensors for size, thickness, and dimensions are summarised in table 3.2 per layer. With $50 \times 50 \mu\text{m}^2$ pitch size the ITk sensor has 400×384 (column \times row) with active physical dimensions of $20.0 \times 9.6 \text{ mm}$. The basic unit of the ITk pixel detector is still a hybrid module that consists of the sensor attached to the ITkPix³ readout chip, which will be explained in detail in the following. The guard ring structure is implemented on the front side of the sensor leaving the edges of the sensor at a potential close to the potential of the backside. This arrangement would potentially generate electrical sparks between the sensor periphery and the chip and therefore,

³All the measured modules were assembled to the first version of the readout chip, the RD53A. The actual ITk pixel sensors will be assembled with the ITkPix readout chip.

TABLE 3.2: Basic parameters of the pixel modules for the ITk pixel system. Parameters updated from [61, 74].

Parameter	Layer 0	Layer 1	Layer 2-4	Rings
Chips (ϕ -z)	RD53-3D	RD53-FE 2×2	RD53-FE 2×2	RD53-FE 2×2
Pixel size [μm^2]	50×50 & 25×100	50×50	50×50	50×50
Last pix to module edge [μm]	150	150	500	500
Last pix active to cut edge [μm]	100	100	100	100
Active size [mm^2]	16.8×20.0	33.9×40.3	33.9×40.3	33.9×40.3
Physical size [mm^2]	18.8×20.2	38.0×40.5	38.0×40.5	38.0×40.5
Sensor thickness [μm]	150	100	150	150
readout chip thickness [μm]	100	100	200	200

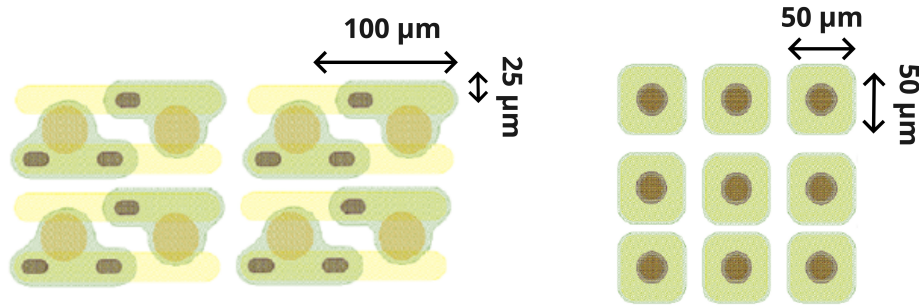


FIGURE 3.11: ITk pixel sensors without biasing structure.

insulation techniques like the deposition of a layer of Benzocyclobutene (BCB) on the sensor surface at wafer level or of the deposition of parylene after module assembly (see section 2.3.2.1) are successfully employed to prevent sparking [74]. The cell optimization is particularly focused on biasing structures to minimize efficiency loss after irradiation. For this reason, the temporary metal solution (see section 2.3.2) that eliminates the need for any biasing structure for characterisation is investigated. A sensor with no permanent biasing structure as shown schematically in figure 3.11 reduce the efficiency loss of the signal because there is no metal to parasitically collect charge. Thanks to the temporary metal technique the sensor can be biased and characterised without any implementation of a punch-through dot. Other biasing structure designs in the sensor is with PT dot common to four floating cells, or wavy, as shown in figure 3.10(b), or the PT dot connected with straight rails around fully grounded pixels in figure 3.10(a). All of these designs were investigated in this thesis. The main effect of the biasing structure is visible in the hit efficiency of the sensor. Several prototype modules from various foundries (ADVACAM⁴, CNM⁵, FBK⁶, CiS⁷, Sintef⁸, VTT⁹) are tested in laboratories in view of the choice for ITk modules. ITk sensors require hit efficiency of at least 97% at the expected maximum fluence of the sensor in order to maintain good tracking performance in the innermost pixel layer for the lifetime of the detector. The performance of ITk pixel sensors studying their biasing structure will be presented later in chapter 6.

⁴<https://advacam.com>⁵<https://www.imb-cnm.csic.es/en/research/projects>⁶<https://www.fbk.eu/>⁷<https://www.cismst.de/forschung/>⁸<https://www.sintef.no/en/silicon-radiation-sensors/>⁹<https://www.vttmemsfab.fi/technology-applications/silicon-detectors/>

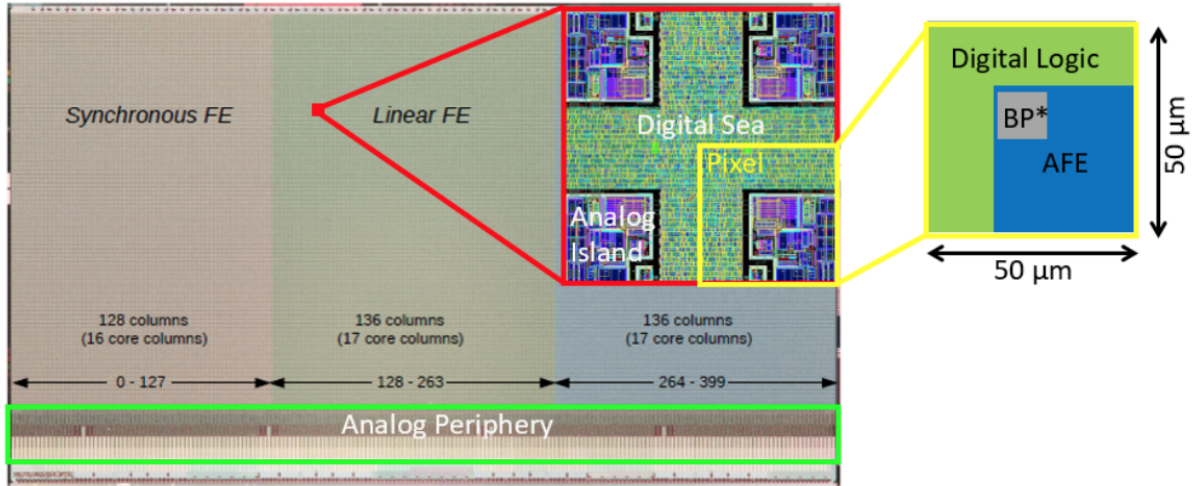


FIGURE 3.12: Schematics of the RD53A chip showing analog and digital parts in the "digital sea" design. The RD53A prototype features the three individual analog front-end flavors: Synchrony, linear and differential [116].

3.2.2 RD53A readout chip

The RD53 Collaboration [114] is developing the readout chip for the high hit rate and high radiation tolerance for both ATLAS and CMS usage at the HL-LHC. In this section I introduce the development of the RD53A chips designated for the ATLAS ITk upgrade. The RD53A integrated circuit [115] is the first prototype chip developed on 65 nm CMOS process at Taiwan Semiconductor Manufacturing Company¹⁰ (TSMC). The basic design for the RD53A addresses the common required specifications for the ATLAS ITk pixel chip including:

1. radiation tolerance of 500 Mrad ionizing dose.
2. stable low threshold operation at $600 e^-$, which is essential to cope with the small signals.
3. high hit-rate and high trigger capabilities.

The ITk prototype pixel modules investigated in this thesis were all assembled with the RD53A chip. The development of the next version, and the final version, of the readout chip are based on it.

The RD53A is designed for single supply serial powered operation connecting core columns from the bottom of chip only. There are two internal voltage rails to power the chip core, analog (VDDA) and digital (VDDD). These two different voltage rails were designed to test the sensitivity of the circuits. The RD53A [115] features analog and digital circuitry on the same chip as shown in figure 3.12. The chip pixels are arranged in matrix of 400×192 (column \times row) that spans the dimensions of $20.0 \times 9.6 mm^2$ of active area or $20.0 \times 11.8 mm^2$ including the EOC logic. This is half the size of the final version of the chip. The pixel cell size of the chip is reduced to $50 \times 50 \mu m^2$ to maintain the occupancy at the desired level in the HL-LHC regime. The pixel matrix is built up of identical 8×8 pixel cores. The 64 front-ends within one core are placed as 16 "analog islands" with 4 fronts-ends each, so called "digital sea" as framed in Red in figure 3.12. The picture marked in Yellow frames the repeating analog islands, which represents roughly a single pixel with the analog front-end and the digital logic. The grey square (BP*) on the top right of the analog front-end is a bump pad to which interconnects the chip front-end to a sensor by

¹⁰<https://www.taiwansemi.com/>

bump bonding.

Three different versions of the analog front-end were implemented in the RD53A chip to study and compare them in one single production. The three analog front-end designs are identified as Synchronous, Linear and Differential as shown in the figure 3.12 and summarised in table 3.3. All three

TABLE 3.3: RD53A analog front-end flavors.

-	Synchronous FE	Linear FE	Differential FE
mark	Red	Green	Blue
columns	[0-127]	[128-263]	[264-399]
cores	16	17	17
			ATLAS ITk choice

front-end flavors feature the common "analog island in digital sea" design. The analog periphery is at the bottom of the chip as framed in Green in figure 3.12. It contains a monitoring block, which is designed with the analog to digital converter (ADC) for digitization of internal parameters such as internal voltages and current, as well as environmental parameters such as temperature and total irradiation dose [116].

The synchronous analog front-end circuitry shown schematically in figure 3.13 is derived with an AC coupling capacitor C_{ac} that is synchronous to the comparator, hence the name. It features a single stage amplifier CSA with a Krummenacher feedback AC coupled to a synchronous discriminator composed of a Differential Amplifier (DA) and a positive feedback latch, which performs the comparison and generates the discriminator output. The synchronous front-end is able to tune the global threshold but lacks a per-pixel tuning. As illustrated in figure 3.13(a) an incoming signal from the sensors's diode goes to the (b) the charge preamplification stage, (c) the two output signals of the differential amplifier is produced to set the average threshold, afterwards, (d) the latch digitizes the signal. From the user experience point of view, the very little parameters required to tune the threshold made it confusing to tune the synchronous front-end.

The Differential analog front-end circuitry shown in figure 3.14 is a pure analog circuit: it contains no memory latches, flip-flops or counters. It is called differential due to its differential pre-comparator design. The ADC function is implemented entirely in the digital core, by digitizing the ToT of the comparator pulse [115]. The pre-amplifier (first stage) has a continuous reset and adjustable gain by choosing between two possible values of feedback capacitance. The signal processed by the pre-amplifier is illustrated in 3.14(b). The DC-coupled pre-comparator (second stage) amplifies the two signals and shifts the signals up or down based on the global and local threshold parameters as shown in 3.14(c). The crossing points of the two differential signals correspond to the threshold. The global threshold is adjustable through two distributed voltages (VTH1 and VTH2), which introduce an offset between the two branches of the pre-comparator. The pre-comparator stage is followed by a classic continuous time comparator stage with output connected to the digital pixel region through logic gates as shown in 3.14(d). After performance studies for all three flavors, the ITk pixel community have chosen the differential front-end for the ATLAS ITk pixel detector [117].

The linear analog front-end circuitry shown in figure 3.15 includes a charge sensitive amplifier featuring a Krummenacher feedback complying with the expected large radiation induced increase in the detector leakage current. It features a linear pulse amplification in front of the discriminator stage. The

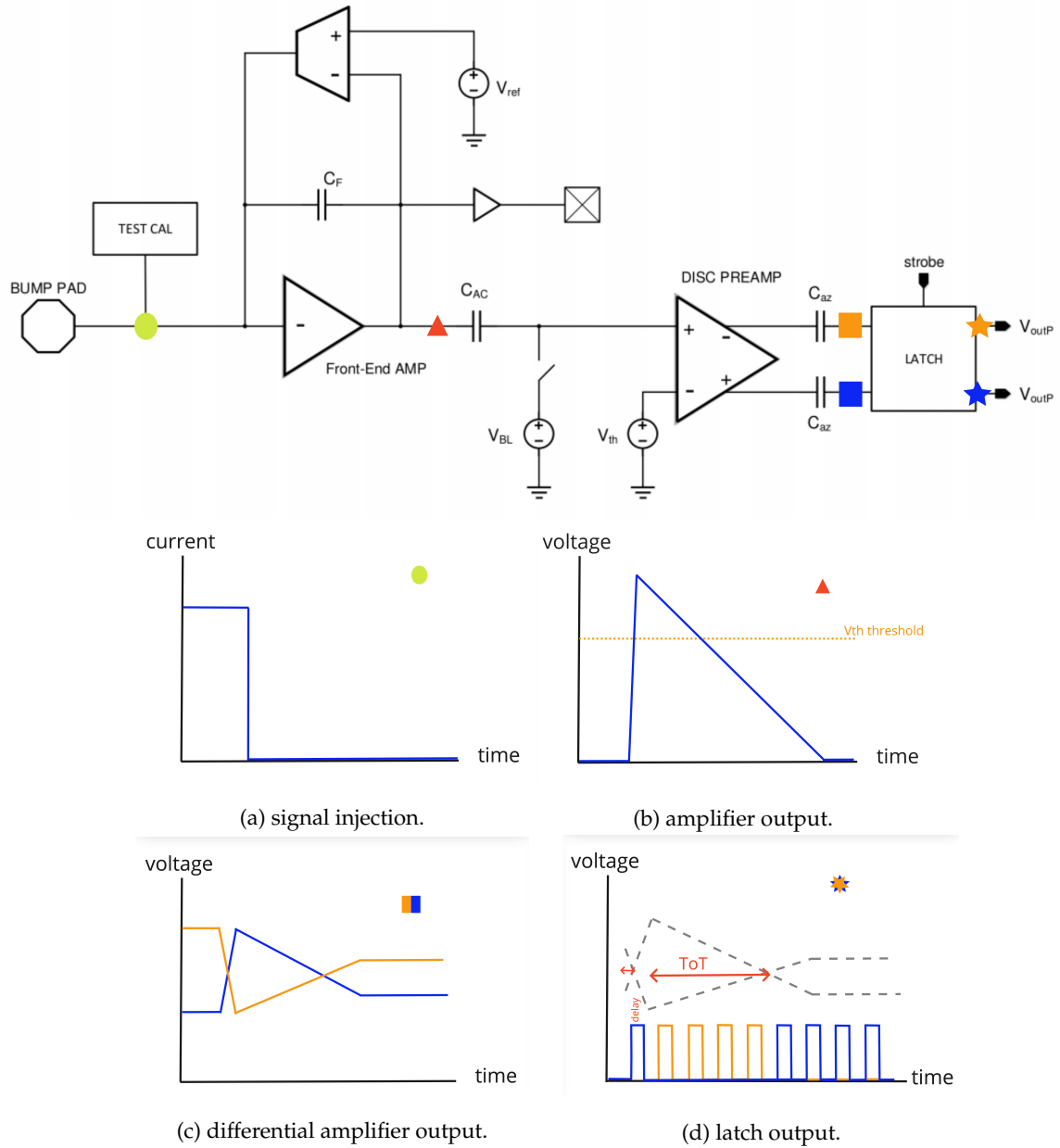


FIGURE 3.13: RD53A synchronous analog front-end scheme [115]. From left to right the current input via detector diode or injection input, a charge sensitive amplifier, a differential amplifier and the latch, which digitizes the analog signal. (a) Signal coming from the sensor diode. (b) Signal after the preamplifier. (c) Two output signals of the differential amplifier. (d) Digitized signal after the Latch.

signal from the CSA is fed to the high-speed, low-power current comparator that is combined with the ToT counter as shown in 3.15(b). The linear front-end implements a linear pulse amplification in front of the discriminator, which compares the pulse to a threshold voltage. The output processed signal is shown in 3.15(c). The grey dotted lines hereby show the effect of the local threshold (TDAC) parameter, which shifts the signal according to a current offset up or down. After the comparator, the signal is digitized as shown in 3.15(d). Common to all front-ends is the calibration injection circuit, as this is important for direct performance comparisons. The bias distribution follows the same organization for all three flavors.

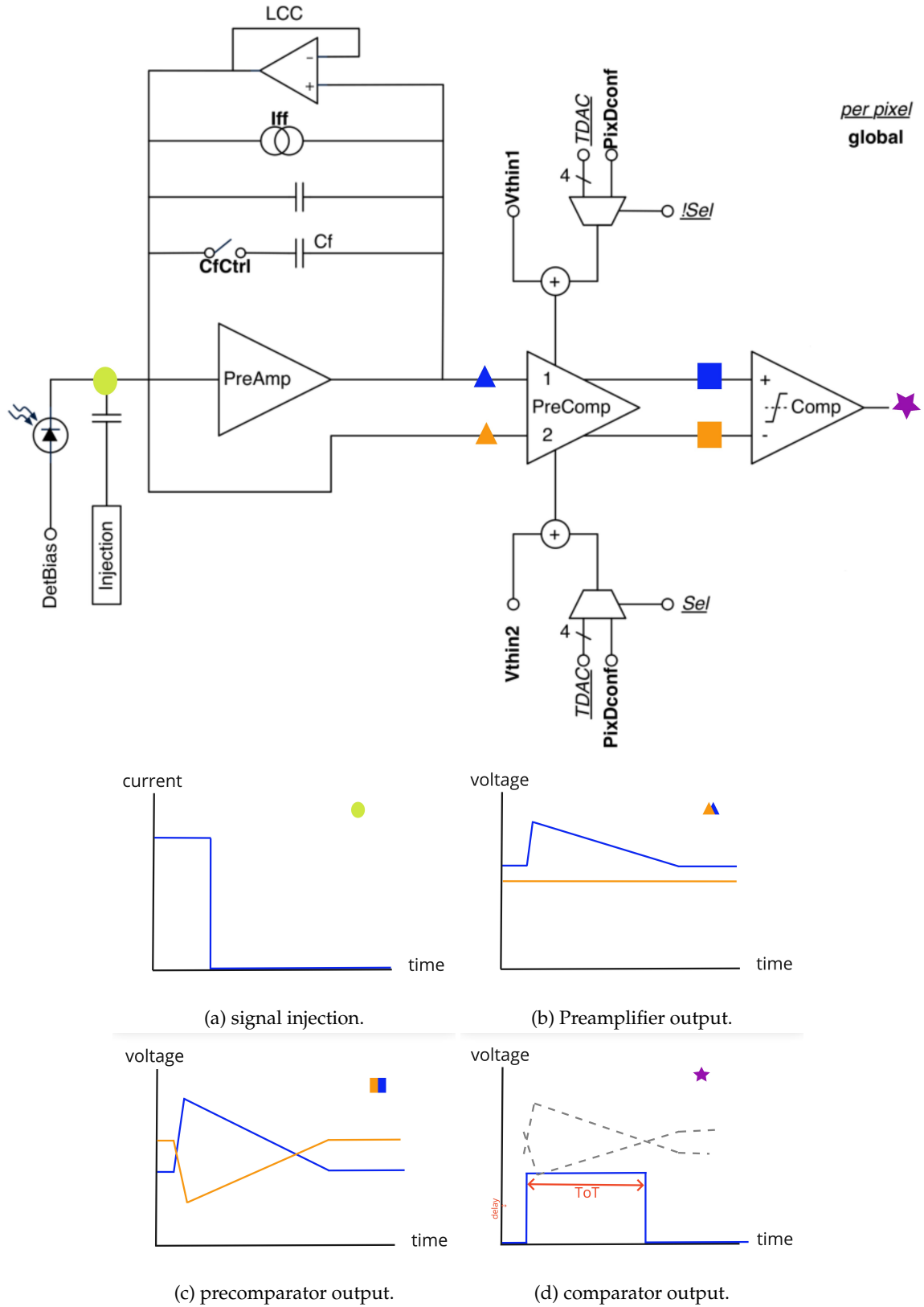


FIGURE 3.14: RD53A differential analog front-end scheme [115]. From left to right the current input via detector diode or injection input, a charge sensitive amplifier, a differential pre-comparator and the comparator. (a) Signal coming from the sensor diode. (b) Signal after the preamplifier. (c) Output signals of the pre-comparator. (d) Digital signal after the comparator.

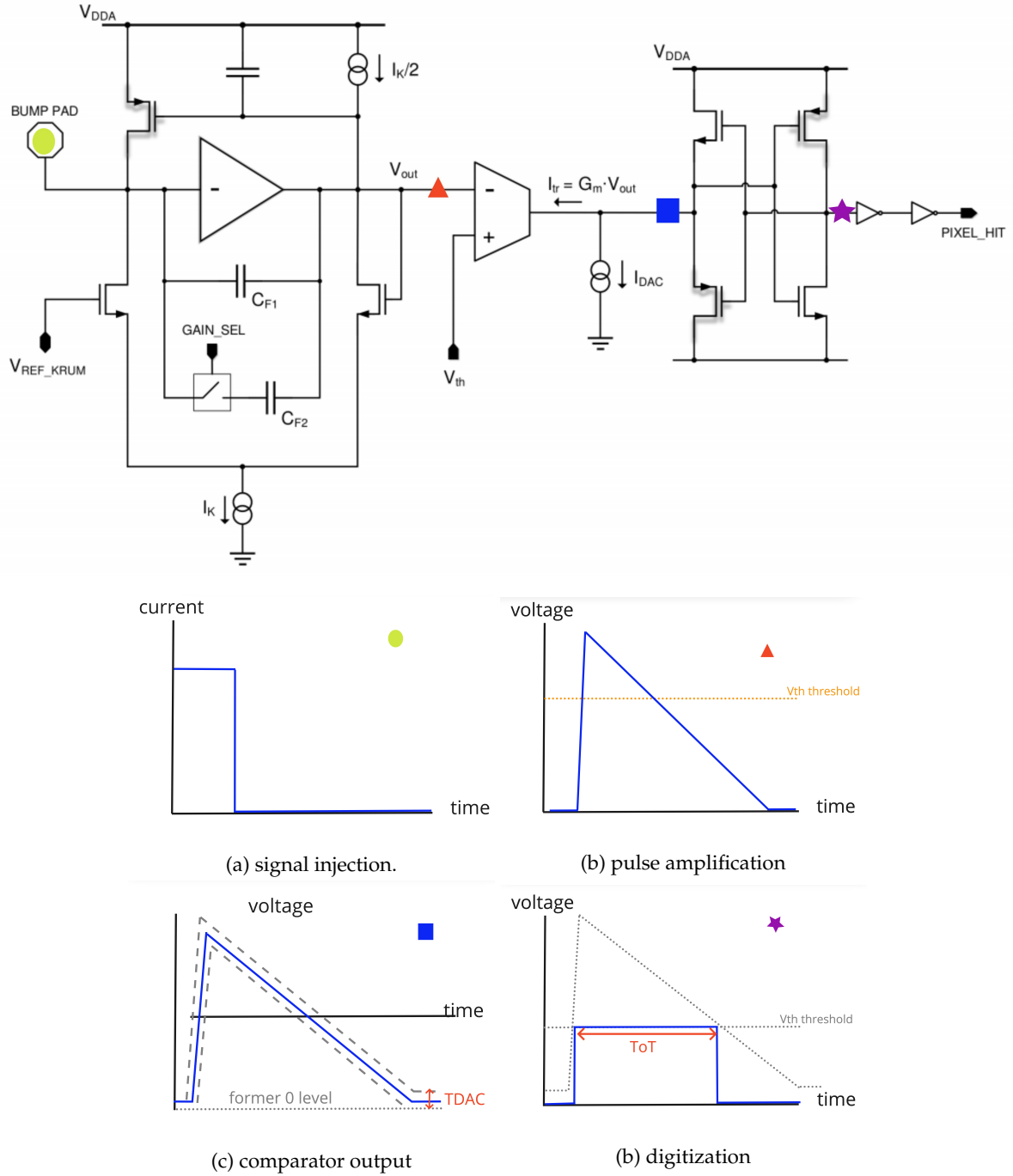


FIGURE 3.15: RD53A linear analog front-end scheme [115]. From left to right the charge input via detector diode or injection input, a charge sensitive amplifier, a trans-conductance stage and the discriminator, which outputs the analog signal for digitization. (a) Signal produced from the sensor diode. (b) Signal after the CSA. (c) Output signals of the trans-conductance stage. (d) Signal after the comparator.

3.2.3 ITkPixV1

The second version of the chip, the RD53B integrated circuit [118] is an evolution of the RD53A to incorporate all production requirements defined by the experiment [119]. The second generation chip is made specifically for each experiment, it is known as ITkPixV1 in ATLAS and is shown schematically in figure 3.16. The ITkPixV1 chip features a new pixel matrix of 382×400 (column \times row) in dimensions of 20.7×20 mm with pixel size of $50 \times 50 \mu m^2$ with a differential analog front-end [118]. The second version

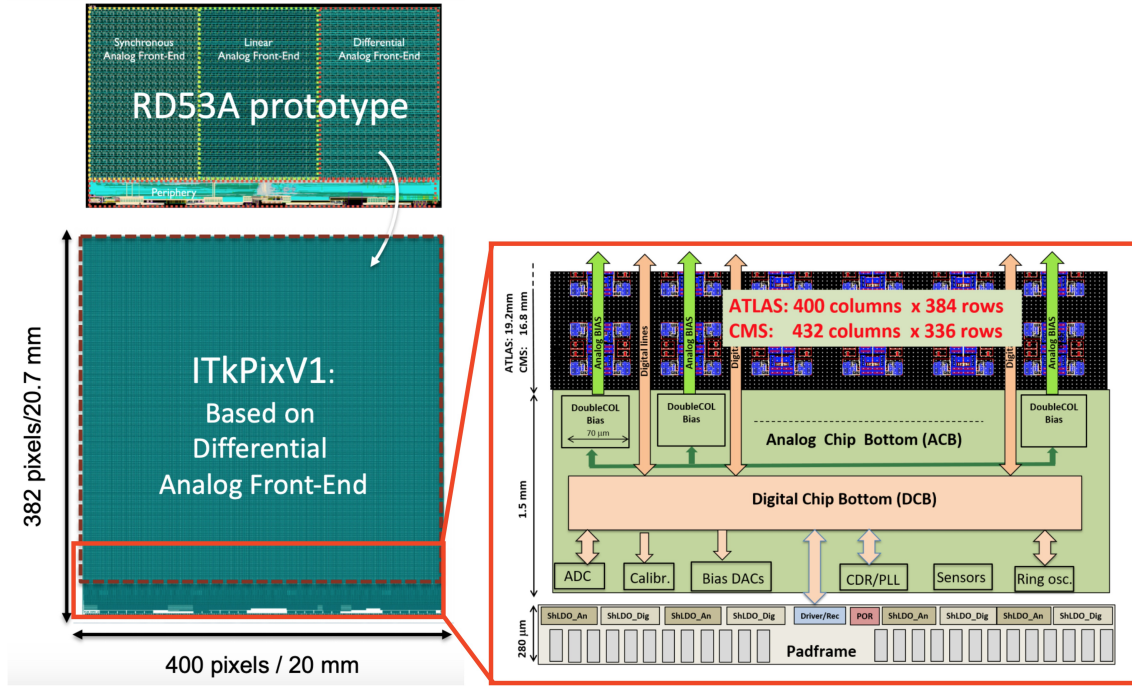


FIGURE 3.16: Schematics of the ITkPixV1 chip in comparison to the RD53A chip. Zoomed out in red shows the physical floor plan with digital chip bottom functional view showing analog pixel islands surrounded by digital pixel region, and the padframe at the bottom [62, 117].

is developed for the first batch of the ITk pixel modules production. The design is very similar to the RD53A with the same control and readout interface. It consists of the pixel matrix and a Digital Chip Bottom (DCB) that holds the digital logic outside the pixel array handling all global control/monitoring and readout of event data. The ITkPixV1 pixel core is organized in 8×8 pixel cores (4 pixel regions) that transfer hit data to the DCB. Basic parameters of the chip are summarised in table 3.4. The pad frame of the chip houses the wire bonding pad, which is discussed in the following section. The wire bond pad is increased from the previous size to allow for wire bond rework [117]. The finalization of the ITkPixV1 is still progressing during this thesis, an updated ITkPixV1 chip design and manual can be found in [118]. After testing and characterising the production batch of the ITk pixel module, which are assembled with the ITkPixV1, it is planned to develop the next version, the ITkPixV2. The ITkPixV2 will be assembled with the actual ITk pixel detector to be installed and operated for the HL-LHC phase.

The pixel geometries and sensor designs introduced in this section are used to develop and optimize the final ITk pixel modules design. The investigated pixel modules in this thesis are all assembled with the RD53A chip hosting the three FE flavours. The tuning of the RD53A chip is performed independently for each front-end flavour based on its analog circuit parameters. The three flavours were characterised in the ITk prototype ITk module. The ITk choice of the front-end flavour is differential for the final chip, ITkPixV1, which is also used in the first production batch of the ITk pixel detector. The first production batch process for ITk planar pixel sensors assembled with the ITkPixV1 chip has already begun end of 2021. The assembly process of the production batch is discussed in the next section.

TABLE 3.4: Basic specifications for the ITkPixV1 readout electronics [120].

Item	Value	Unit
Pixel size	50×50	μm^2
Number of pixels	$400 \times 382 = 152\,800$	col \times row
chip size	20×21	mm^2
Front-end	differential	
Input	DC-coupled negative polarity	
Lowest threshold	600	e^-
Charge \rightarrow Digital coding method	ToT	4 bits resolution
Hit rate	3	GHz/cm^2
Trigger rate	1	MHz
Nominal analog and digital voltage	1.2	V
low power consumption	4	$\mu A/pixel$
Radiation tolerance	500	Mrad
Operating temperature range	-40 to +60	$^{\circ}C$
Maximum number of consecutive triggers	31	
Latency	12.8	μs
Nominal clock input frequency	40	MHz
Data rate	5.12	Gbit/s

3.3 Hybrid module assembly

A hybrid module consists of mainly three components: sensor, chip and PCB as simplified in the schematics of figure 3.17. The prototype pixel sensors studied in this thesis were assembled in this process with

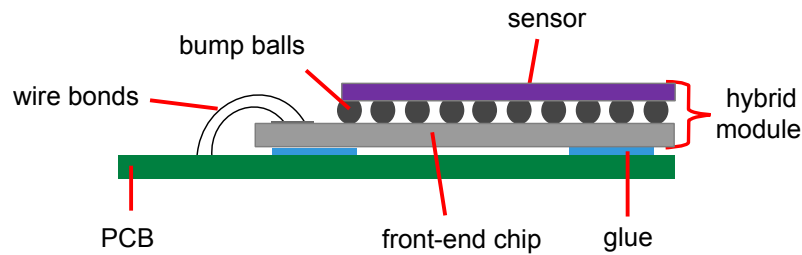


FIGURE 3.17: Cross sectional schematic view of a module consisting of a single sensor and a readout chip bump bonded together, glued and wire bonded into a PCB.

slight variations depending on the production institute. The ITk planar pixel sensors studied in this thesis are designed to fit the RD53A chip. For R&D purposes, sensors with various designs are produced in wafers to maximize its yield. Sensor structures in the wafer are further diced into single bare sensors to adapt to the size of the front-end chip for chip-to-chip interconnection. The interconnection bump bonding process is a key step in the hybridization of the sensor. The specifications for the bump deposition and interconnection are under development based on those successfully used for the IBL production [61].

The hybrid module is glued to a PCB. The utilised glue has to be as robust against environmental influences and thermal stress. The accurate positioning and attachment of the hybrid module with respect to the PCB is crucial for a successful assembly since in the hybrid module concept, the PCB is tailored to the sensor. To reduce material budget and gain flexibility in the detector, the PCB is a thin double sided flexible printed circuit called "flex", or "flex PCB". The flexes are shown in figure 3.18 to connect the module to external electrical services with minimum material budget [122]. The flexes are designed to match the module scheme: for single, triplet or quad modules. Signals and power traces of the hybrid

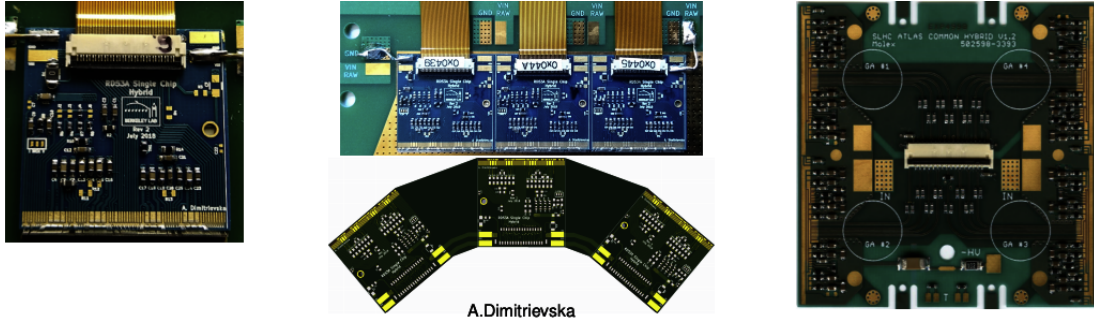


FIGURE 3.18: Pictures of flexes for RD53A modules (left) single chip flex, (center) triplet PCB for L0 barrel and ring, and (right) quad flex [121].

module on the flex are routed via a temporary wire bond to a connector outside the module area, which is used for the qualification assurance (QA). The details of the ITk manufacturing and module assembly process are being developed in collaboration with the vendors that the ATLAS pixel groups are working with during the R&D phase. Module assembly generally follows the following steps:

1. interconnecting the bare sensor to a bare readout chip via bump bonds creating the hybrid module.
2. gluing the hybrid module to a PCB.
3. wire bonding the hybrid module to the PCB.

Each step will be briefly discussed in the following.

3.3.1 Interconnection technology

The key step in the hybridization of a pixel sensor is the fine pitch flip-chip bump bonding process [123], which connects each pixel in the sensor face-to-face with the corresponding front-end readout pixel cell. Bump bonding requirements for the ITk will be similar to those of the IBL modules. There are two major challenges facing the flip-chip bonding of the ITk pixel system [61]. First, is the technical challenge posed by the very thin pixel assemblies for the inner layers of 100-150 μm thick sensors. Second challenge is the production rate and volume required for the substantially enlarged pixel system. The posed challenges technically require:

- the increase of readout chip wafers to 300 mm in diameter (increased from 200 mm).
- the increase of sensor wafers up to 200 mm in diameter (increased from 100 mm).
- reducing sensor thickness to 100 – 150 μm for radiation hardness.
- bump contact pad pitch of the read-out chip with $50 \times 50 \mu\text{m}^2$ pixel geometry.

These requirements does impact the realization of the flip-chip process. However, the bump failure rate is expected to remain the same as for the IBL for which on average approximately 0.56% of pixels on accepted planar modules failed during Quality Assurance tests [61].

The details of the interconnection process are being developed in collaboration with the vendors that are working with pixel upgrade during the R&D phase. The interconnection of chip-to wafer in all measured modules in this thesis were done at IZM¹¹. For more details on the interconnection process refer to Appendix A.

¹¹<https://www.izm.fraunhofer.de/>

3.3.2 Gluing

The hybrid module is glued on a carrier PCB to connect power and data transmission. The modules produced for ITk will be glued on flex PCB (quad, triplet, or single), while the prototypes are glued to a rigid single chip card (SCC). For the prototype module investigated in this thesis, in fact they are placed over a hole in the PCB in order to avoid to have copper metal layers in the path of the beam during test beams. So in order to give enough solidity for wire bonding and handling the sensor, it is glued on a pure Aluminum plate that is screwed on the PCB to hold the hybrid sensor in a fixed position. The Aluminum plate is visible from the image in figure 3.1. The used glue and the gluing procedure has to fulfill several criteria. Studies on modules with different gluing methods have been performed using small-scale sensors to investigating the impact of different glues on the electrical characteristics of sensors before and after gluing, with irradiation and temperature cycles. The chosen glue for the assembly of ITk sensors is the Araldite 2011 epoxy adhesive [124] that is mixed by a powerful mixer¹² with centrifugal force over 400G and de-bubbling high viscosity adhesives.

The gluing procedure [125, 126] is depicted in the images of figure 3.19 and is composed of the following steps. The Araldite adhesive and a mixing substance are added together and mixed in the mixing machine for about 20 min. The flex and the hybrid module are weighted before gluing to deduce the weight of the deposited glue after the procedure. There are three jigs¹³ to support the gluing procedure; one that holds the flex, and second one that holds the hybrid module, these two jigs are made to mate tightly in order to meet the alignment requirement as shown in 3.19(d&e). The third one is a stencil jig to apply the glue as shown in 3.19(g). The flex, shown in figure 3.18, has alignment holes in its corners to be fixed with adjustable screws on the jig. The hybrid module is placed on the jig against the alignment pins to match the position of the flex and is fixed by vacuum suction to secure its position. The positions of the flex and the hybrid module is inspected by a microscope to position them up to $0.5 \mu\text{m}$ uncertainty on the identical jigs. The flex is fixed with the back side upwards and the hybrid module is fixed with the back side of the chip upwards. The third jig is a stencil jig fixed on the top of the flex jig to apply the glue on the backside of the flex. As seen in figure 3.19(g) the glue is deposited on the stencil and then swiped coherently to go through the stencil into the back of the flex. The stencil jig is then removed and the jig with hybrid module is flipped and tightly screwed on top of the flex. The adjustable screws help obtain a specific glue height. The glue is left to dry for 8 hours.

3.3.3 Wire bonding

The wire bonds form the electrical connections between the front-end chip and the PCB as shown in the image of figure 3.1. The wire bonds connection is used for command, data communication, powering, and grounding. For single chip cards (SCC), additional wire bonds are added from the hybrid module to the hybrid panel to allow for electrical testing. The hybrid module is glued on the Aluminum plate that hold it a fixed position to a PCB with the EOC pad extruding from the sensor area to be wire bonded. The wire bond padframe in the RD53A at the chip bottom has a rectangular shape with $58 \mu\text{m}$ wide by $86 \mu\text{m}$ tall passivation opening on a $100 \mu\text{m}$ pitch [115] as shown in figure 3.20. This size is considered large enough to allow for wafer probing followed by reliable wire bonding with the possibility of bond repair. The wire bonding pads are organized as a single row at the bottom chip edge and are separated from the first row of bumps by 1.7 mm in order to allow for wire bonding after sensor flip-chip. Each Aluminum

¹²<https://polydispensing.com/product-details/melangeur-planetaire-thinky-are250/>

¹³A jig is an open frame for holding work and for guiding a machine tool to the work, used especially for locating and spacing drilled holes; fixture.

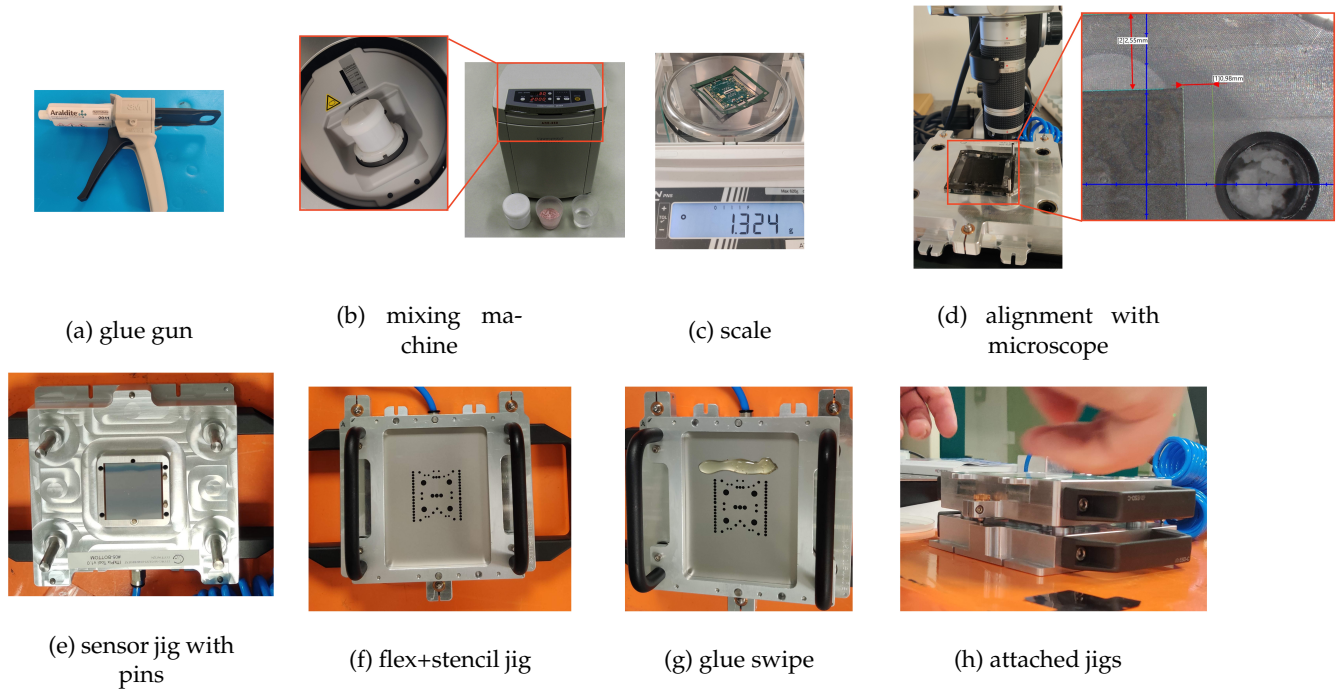


FIGURE 3.19: Procedure of gluing the hybrid module to a PCB at LPNHE.

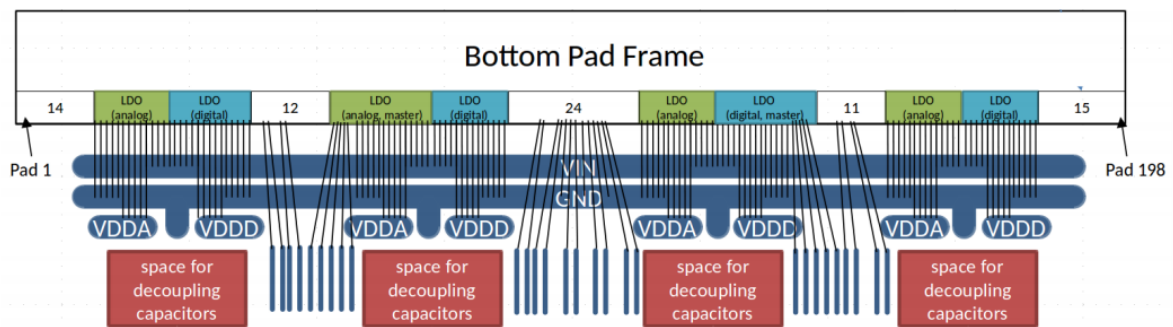


FIGURE 3.20: Organization map of bottom of an RD53A chip pad frame. Typical wire bond connections needed for module operation is also shown [115].

wire-bond is about $25\ \mu\text{m}$ in diameter. They are connected by applying pressure and ultrasonic pulses, "Wedge bonding", to power and readout the complete matrix of the chip.

Quality control of wire bonds is extremely crucial. Wire bonds are operated in strong magnetic field environment of the ATLAS detector, and if time varying currents pass through them with frequencies close to their mechanical resonance frequency, strong resonant oscillations may occur [127]. Wire bonds must be protected (encapsulated) from mechanical stress, Lorentz force, and corrosion [121].

3.3.4 ITk pixel module preparation

Institutes that are participating in the production of the ITk such as LPNHE¹⁴, IJCLAB¹⁵ and CEA¹⁶ in the "Paris cluster" are organizing a site for module assembly. A production site must be qualified to produce full-sized single chip silicon modules to be able to participate in the production of the real modules. The qualification process is validated by the "RD53A mini-production" [128]. For this qualification, each site must build prototypes modules that meet mechanical specifications:

- relative position alignment between hybrid and PCB $\pm 25\ \mu\text{m}$, this detail is still under discussion.
- gluing of module to flex without seeping over wire bond pads.
- automatic wire bonding, in correct locations.

The work flow plan for the module assembly organized by the Paris cluster is shown in figure 3.21. After the reception of sensors and PCBs, electrical tests for quality assurance are performed. Each institute has to send the sensors and the readout chips to the chosen flip-chip vendor. Then, the hybrid module is glued to the PCB and tests for quality assurance are performed after gluing. After the modules are glued to the PCB, they are wire bonded by an automatic wire bonding machine. Operational tests and characterisation of the module is then performed to ensure the functionality of the module. Assembly work information is uploaded into the ITK pixel module database for each sensor, PCB, shipment, logistics and performed tests. The working modules are assembled in construction sites from the qualified institutes. The final assembly of the ITk pixel detector will be in CERN.

Conclusion

In this chapter I introduced the pixel detector technology used in the IBL detector, and the one developed for the ITk pixel detector. The IBL detector utilize a $n^+ - in - n$ pixel sensor assembled with the FE-I4B readout chip. The main elements of the analog front-end circuit was introduced here. The tuning of the FE-I4B front-end will become a main topic in the next chapter.

The ITk pixel detector will be instrumented with $n^+ - in - p$ segmented sensor technology. All the investigated ITk prototype modules are assembled with the RD53A chip, while the real ITk modules will be assembled with the next version of the RD53 chips, the ITkPixV2. The tuning of the front-end is performed by using the parameters introduced for each front-end flavour.

The hybrid modules are the basic unit of the pixel detector, the module assembly process begins with interconnection of the sensor to the readout chip via bump bonding, the gluing the hybrid module to a PCB and wire bonding the End-Of-Column of the hybrid module to the PCB to be able to electrically characterise it. Then the pixel module must be tuned to be able to operate it and measure it with particle

¹⁴<http://lpnhe.in2p3.fr/>

¹⁵<https://www.ijclab.in2p3.fr/en/home/>

¹⁶<https://www cea.fr/>

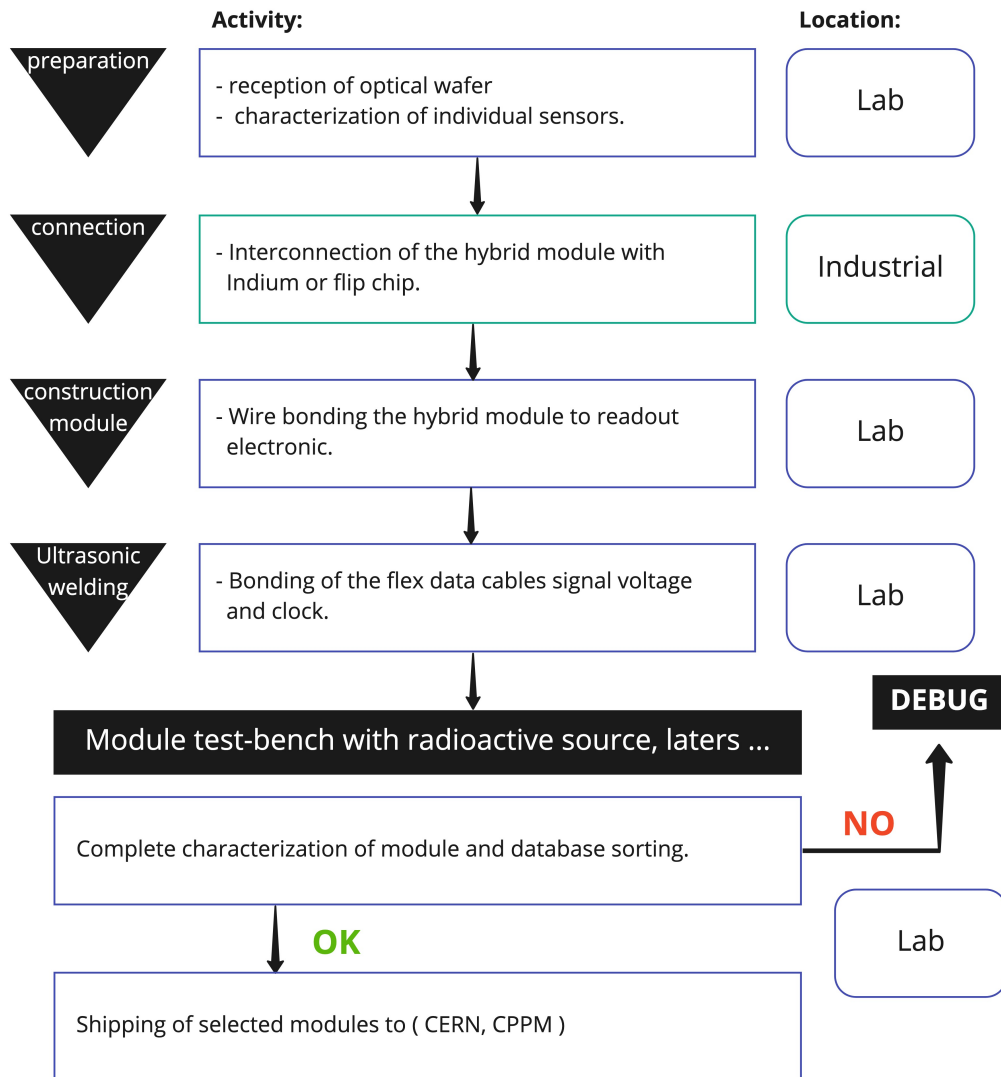


FIGURE 3.21: Work flow plan and structure for module assembly from Paris joint cluster group: LPNHE & IJCLAB laboratories.

1649 beam experiments. The tuning procedure of the pixel module will be explained in the next chapter and
1650 the performance of the investigated ITk pixel modules will be presented later in chapter 6.

1651 *“Those who say it can’t be done are usually interrupted by others doing it. ”*

1652 James Baldwin

Chapter 4

Pixel module calibration

The front-end chip of a tracking detector must be calibrated and tuned to have a response proportional to the input charge homogeneous over the whole pixel matrix. For this reason the tuning is essential for the detector's operation. In this chapter I discuss the used electronics and operating procedures to tune the pixel modules for both the current IBL detector and future ITk pixel detector. The same tuning procedures are extended to tune the complete detector. In section 4.1 I present the tuning setup and data acquisition systems used in LPNHE to tune the FE-I4B chip for the IBL detector, and the RD53A prototype chip for the ITk pixel detector. In section 4.2 I discuss the general tuning concepts and scans to tune the analog front-end chip. Here, I also focus on the charge calibration of the chip as it shows to be the main source of the local threshold asymmetry issue for the FE-I4B modules in the current IBL detector. In section 4.3 I present a conclusive study on the threshold tuning method for FE-I4B modules introducing a novel tuning technique based on noise occupancy scan. The new tuning technique proves to resolve a threshold discrepancy issue reported from Run2 data. Results from laboratory investigations are presented to compare and validate the novel tuning technique. The tuning algorithm is implemented in the ATLAS Data Acquisition system in the aim to be operated for Run3 of the LHC. The technical challenges of tuning the complete IBL detector with the new tuning technique are briefly discussed at the end in section 4.3.4.

4.1 Tuning setup

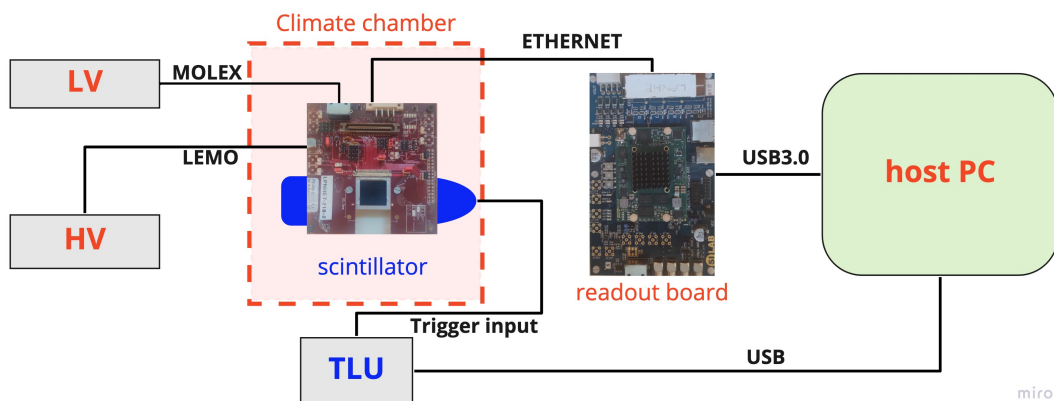


FIGURE 4.1: Schematics of the tuning and charge collection measurement setup.

The setup at the LPNHE institute used for tuning FE-I4B and RD53A modules is shown schematically in figure 4.1. The prototype module is measured inside a hermetically sealed climate chamber for constant temperature and humidity. The climate chamber supplies dry air to maintain the low humidity

level. Unirradiated modules are tuned at 20°C and irradiated modules are kept at low temperature and tuned at −50°C. The module is powered by a low voltage supplier, supplying a FE-I4B module 1.5 V for analog front-end and 1.2 V for the digital front-end in direct powering mode (VDDD) (see section 3.1.2 for FE-I4B), while for a RD53A module 1.2 V is supplied for both analog and digital front-ends together via direct powering mode (see section 3.2.2). To bias the sensor, the module is connected to a high voltage power supply, Kiethley 2410, via a LEMO connector, which provides the sensor bias voltage and measures the sensor’s leakage current. The high voltage power supply can be controlled by the PC for automated high voltage setup. An ethernet cable per front-end is connected to the readout board to receive triggers, detect signals, and send commands. The readout board is connected to the host PC to stream data. Triggers are provided externally by the scintillator that is interfaced to a photomultiplier or by the self-trigger implemented in the front-end chip. At the LPNHE laboratory all measurements were performed with self-trigger internal to the readout chip.

Modules assembled with a FE-I4B chip are readout by using the PyBAR system and the MMC3 board. While modules assembled with a RD53A chip are readout using the BDAQ53 or YARR systems. All three systems and readout boards are introduced in the following.

4.1.1 PyBAR

PyBAR [129] is a versatile readout and test system (in Python) developed by University of Bonn¹ for the ATLAS FE-I4B pixel readout chip installed in the current IBL detector. It uses the basil framework [130] to allow simple and fast Data Acquisition systems (DAQ) design. PyBAR features a field programmable gate array (FPGA) firmware that supports several readout boards; e.g., MIO2, MIO3, MMC3. It supports adapter cards, and can readout multiple multi-chip modules. PyBAR host software is written in Python and has a script based interface. Each tuning/scan/calibration algorithm is implemented in a stand-alone script, which allows fast developing and implementation of new scan algorithms. Configuration files are human readable, easy to setup, and have full control over command generation to the front-end. Data files are compressed and stored in HDF5 (.h5) files. PyBAR software features fast raw data analysis, validity checking, interpretation of results, event and cluster building in a real-time online monitor with GUI. In our PyBar Hardware setup the MMC3 board is used, which is the latest generational board developed by SiLab².

MMC3

Figure 4.2 shows a top view of the MMC3 readout board, which is used for the FE-I4B chip. The MMC3 board [131] features a FPGA that can communicate with multiple front-ends and steer the software on the connected PC. It has RJ-45 connectors with optional AC-coupling that allow direct connection to the FE-I4B module. Each RJ-45 connector is an individual channel. Up to 8 FE-I4B front-end chips can be readout with the MMC3 depends on the clock and command lines sharing. Only up to 4 FE-I4B modules were readout simultaneously at 40 MHz.

4.1.2 BDAQ53

The BDAQ53³ [116] is a versatile readout system and verification framework for the family of readout chips designed by the RD53 collaboration [114] for the ITk detector. The BDAQ53 is based on Python

¹<https://www.uni-bonn.de/en>

²<https://silab-bonn.github.io>

³<https://gitlab.cern.ch/silab/bdaq53>

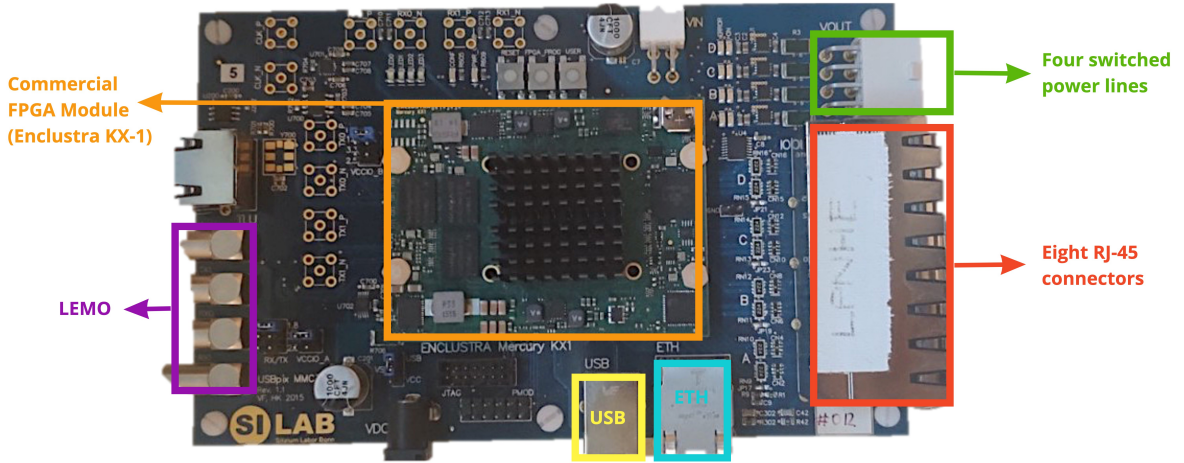


FIGURE 4.2: Image of the MMC3 readout board.

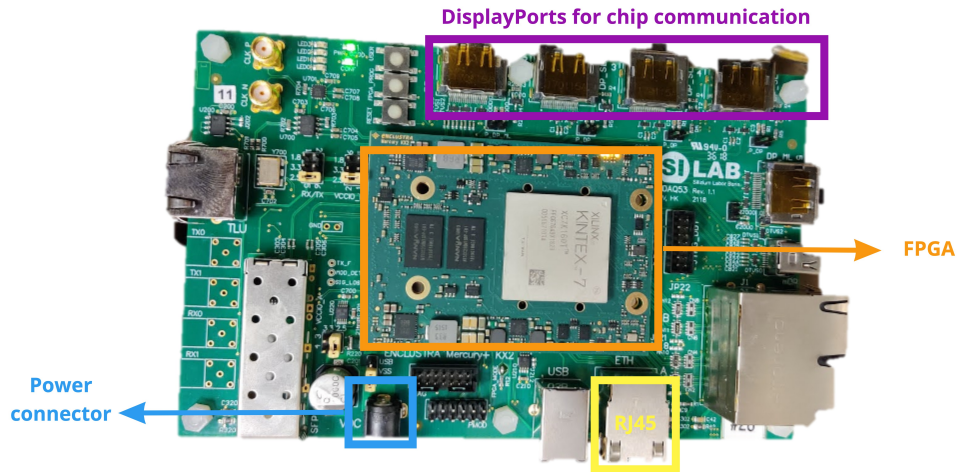


FIGURE 4.3: Image of the bdaq53 readout board

DAQ [132], which is specifically designed for testing and debugging. Its architecture enables full control over raw data words, interpretation and event building in software, which is necessary to evaluate the data format and detect transmission errors. Once the readout thread in the software is started, the raw data are received from the FPGA in HDF5 (.h5) format.

An essential part of the BDAQ53 software are the scan scripts. The scripts are independent of the chip and hardware setup. They perform the essential steps of a scan to initialize, configure, and execute the scan algorithm and also an analysis step can be performed to process and visualize the data. The BDAQ53 hardware uses a specific readout board called bdaq53 that is introduced next.

Bdaq53 board

The readout board called bdaq53 is shown in top view in figure 4.3. The bdaq53 is made by a custom base board hosting a commercial FPGA module daughter board. The base board includes programmable clock generator chips, signal level translators and a multiplexed analog front-end for temperature measurements. It is powered by USB power connector and has the capacity to connects 4 single chip modules via Display Port connectors. A more detailed description of the firmware and software can be found in [133].



FIGURE 4.4: Image of a Trenz TEF1001 board, one of the PCIe FPGA FMC boards supported by the YARR firmware.

4.1.3 Yarr

The Yet Another Rapid Readout (YARR) [134] is a simple and powerful DAQ system for both the current generation of pixel readout chips, FE-I4B, and the next generation pixel readout chips, RD53A. The data is read from, and commands are sent to the pixel readout chip via a Peripheral Component Interconnect Express (PCI-e) FPGA board that is installed in the host PC. An image of a Trenz TEF1001 board⁴ supported by YARR firmware is shown in figure 4.4 (other boards are possible). The FPGA has a simple firmware implementing only a basic buffer for commands and data, while all of the scans and analysis are implemented in the software on the host PC. This basic feature of no data processing enables high PCI-e bandwidth. The increase of bandwidth for the DAQ system was critical for the new RD53A readout chip to achieve a bandwidth of 5 Gbit/s [135]. The YARR software operates on multi-core CPU to perform all the data processing. It is optimized for multi-threaded processing, allowing scan loops and analyses of scan results to occur in parallel, which greatly improves the performance of the system. The software needs three core pieces to perform the readout: a kernel driver to communicate with the firmware via PCIe, which is used by the user to control and configure the chip, an engine driving the scans, and processors which analyze the received data.

Both BDAQ53 and Yarr systems are able to efficiently characterise all versions of the RD53 modules but differ slightly on threshold behaviour. Tuning configuration between both systems have identical TDAC-bit and mask mapping. Fitting a threshold tuned via BDAQ53 into Yarr shows the same result within $\pm 10e$ in the threshold distribution. Measurements with both systems were investigated in test beam experiments. Both BDAQ53 and Yarr data acquisition systems show compatible behaviour. The ITk pixel community is using the Yarr system for maintenance convenience. A comparison between both systems can be found in (ATLAS internal) [136].

4.2 Charge calibration and chip tuning

A description of the FE-I4B chip was introduced in section 3.1.2, and for the RD53A chip it was introduced in section 3.2.2. Both chips have an integrated charge injection circuitry as shown in the schematics of the FE-I4B analog front-end in figure 4.5, but each chip has its own individual features. The tuning

⁴Simple PCIe Carrier: <http://www.ohwr.org/projects/spec/wiki>

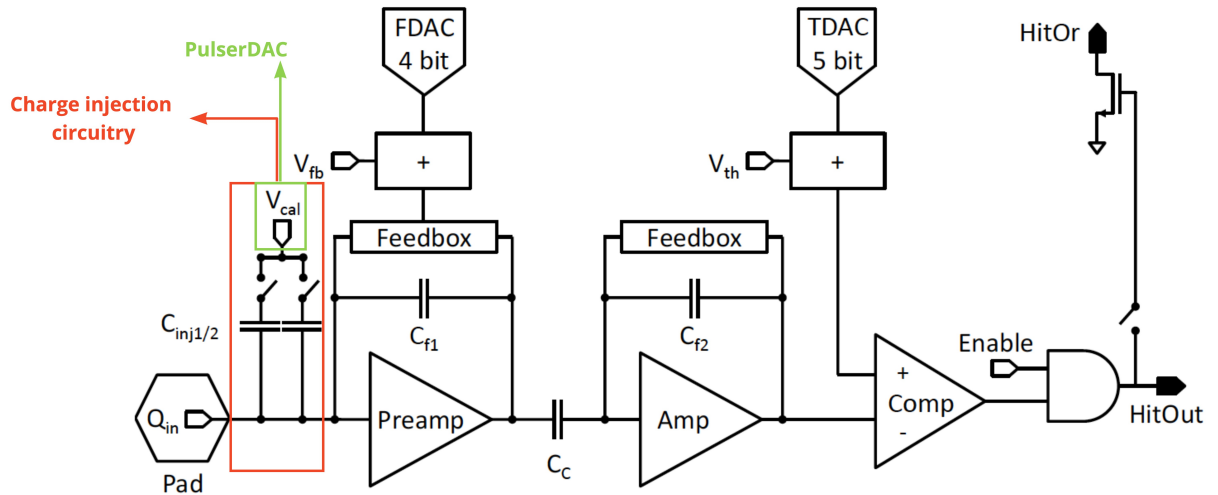


FIGURE 4.5: Schematics of the FE-I4B Analog front-end. The Pulser circuit is labeled in green and the charge injection circuit is labeled in red. Image adapted from [105].

of the threshold and the Time-over-Threshold (ToT) is performed based on the injected test charge. So to determine the absolute threshold, and the effective charge conversion gain via the ToT, a charge calibration relation is necessary. A thorough discussion on the charge injection circuitry for both FE-I4B and RD53A is presented in the following. Building on the charge injection tool several threshold tuning issues that rise from it in the FE-I4B front-end chip, will be the focus of discussion of the next section.

4.2.1 Charge injection calibration

4.2.1.1 FE-I4B readout chip

The charge calibration is an important preparation step before measurement, which is performed on each individual readout chip to relate its settings and measured values to common units, and also to their theoretical expectations. This calibration, which takes place within the charge injection circuitry, relates to two characterisations in the FE-I4B chip: a) the pulser circuitry characterisation, and b) the injection capacitance measurement. The schematics of the charge injection circuitry in the FE-I4B front-end is framed in Red in figure 4.5, and the PulserDAC pad, which is able to arbitrarily inject a charge Q_{in} into the pixel is framed in Green. The injection circuit is present in each pixel of the chip and is used for testing and calibration purposes. Both chip aspects were characterised at the University of Bonn, and are discussed below. For further details on the performance of the FE-I4B readout chip refer to reference [137].

Pulser circuitry characterisation

The calibration voltage V_{cal} defines the voltage step over the two injection capacitance C_{inj} connected in parallel. I will focus on the injected voltage V_{cal} here and the injection capacitances are discussed in the following. V_{cal} is measured using an external voltmeter and the resulting voltage is a function of the corresponding DAC setting $PlsrDAC$ as shown in figure 4.6. Injection modes correspond to the number of pixels injected simultaneously; all DCs means all Double-Column pixels, $1/n$ DCs means every n^{th} pixel is injected simultaneously, and single DC means one pixel at a time. The charge injection mode $1/4$ DCs (injection every 4 pixels per DC) allow a voltage step across the injection capacitors above 1.1 V with good linearity. There is a significant saturation observed in all DC mode (injection into all 26880

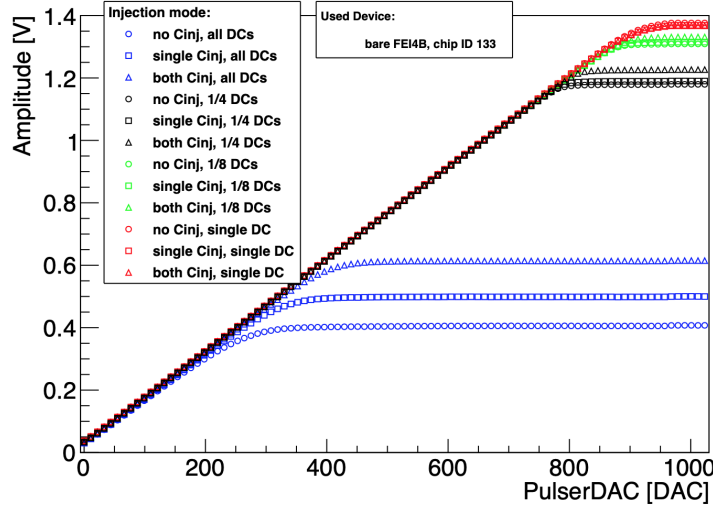


FIGURE 4.6: Test charge injection circuitry output pulse amplitude as a function of the corresponding 4-bit DAC (V_{cal}) for FE-I4B in all injection modes [137].

pixels at the same time). The saturation in single DCs mode is due to the limitation of the supply voltage of the PulserDAC circuit. The ideal voltage amplitude is obtained from a fit to the result in single DC injection mode with both injection capacitors enabled, because this is the mode which is expected to have the best performance as shown in figure 4.6. With this setting, a linear behavior is obtained between the measured amplitude and the ideal amplitude of the calibration voltage PulserDAC in the pulser circuitry.

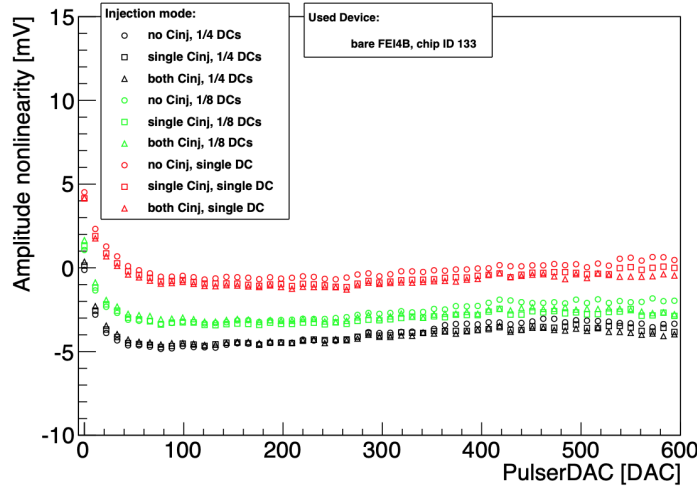


FIGURE 4.7: Difference between the measured amplitude and the ideal amplitude obtained from a linear regression to the single DC injection mode for FE-I4B. The maximum distance from zero in this representation corresponds to the integral nonlinearity (INL) [137].

Deviations from linearity between V_{cal} and PulserDAC can be shown by the integrated nonlinearity (INL), which is defined as the maximum distance of the measured value from the ideal one for an expected linear dependence [137] and is defined for a DAC with N_c output by

$$INL_c = |V_{ideal}(c) - V_{real}(c)| = |(V_{max} - V_{min}) \frac{c}{N_c - 1} - V_{real}(c)|, \quad (4.1)$$

where V_{max} and V_{min} are the maximum and minimum ideal output voltages of the DAC. INL characterisation tests for FE-I4B shown in figure 4.7 show linear performance with some deviations at very low or very high PulserDAC. This nonlinear deviation from the Pulser circuitry can rise from three sources. First, the higher leakage current from injection more DC at the same time limits the maximum output voltage of the pulser. Second, the same leakage current passing through resistors causes a small offset for the whole PulserDAC range. Third source rises at very low PulserDAC values that could be referred to the output voltage of the DAC itself. These sources are thoroughly studied in reference [137]. Despite the nonlinearity of the DAC at very high or very low values, it does show linearity for the large range in the middle.

Injection capacitance measurement

The charge injection circuit of the FE-I4B is also capable of measuring the average value of the representative two injection capacitors in parallel

$$C_{inj} = C_{hi} + C_{low}. \quad (4.2)$$

The two capacitors, or one of them, can be selected for the charge injection circuitry and the average

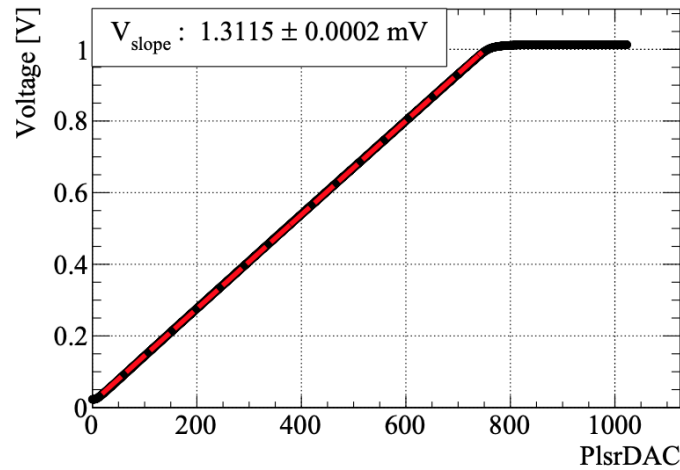


FIGURE 4.8: Measurement of the injection capacitance slope, the voltage across the injection capacitance V_{cal} is measured as a function of the PulserDAC register setting. The fit in red measures the steepness of this relation V_{slope} , and the voltage interception [74].

value of the injection capacitance will affect the calibration voltage step. The extracted values of the capacitors including layout parasitics are 1.9 fF and 3.90 fF [105]. Both can be selected in parallel giving 5.85 fF , while if neither is selected there will still be a parasitic capacitance in the order of 0.1 fF . Measurements of the injection capacitors must be performed at wafer level as they are no longer accessible once the modules have been assembled. The value of the capacitors depend on the production and so it can differ from chip to chip within the same wafer. The value of the capacitors is measured by applying a voltage across an array of 1000 replicas in parallel, the voltage pulse is switched with variable frequency between input and ground using non-overlapping clocks. The average current is measured resulting in the linear behavior shown in figure 4.8. The total charge injection capacitance is computed from the slope m of the linear regression using

$$C_{inj} = \left(\frac{m}{N} + a \right) \cdot \frac{1}{b}, \quad (4.3)$$

where N is the number of capacitors in parallel, a is the slope offset and b is the correction factor, which follow from the exact implementation of the injection capacitance measurement circuitry. The slope value measures the gradient of a line to describe its steepness and interception with the voltage scale. The intercepted point, the slope offset value, of the PlsrDAC output is dominated by the voltage drop across the resistance of the wire bonds. From the slope fit in this relation $V_{slope} = 1.3115 \pm 0.0002 \text{ mV}$ is taken into account in the total injected charge Q_{in} value to compensate for any parasitic voltage drop. Then the injected charge Q_{in} can be accurately calculated from the amplitude of the voltage step per DAC (plserDAC) in terms of electrons by

$$\frac{Q_{in}}{DAC} = m \cdot \frac{C_{inj}}{e} \quad (4.4)$$

with the slope of the pulser output calibration m . And in term of ToT the injected charge is represented by

$$Q_{in} = \frac{ToT \cdot c - a \cdot b}{a - ToT} \quad (4.5)$$

where the three parameters a , b and c are the same fit parameters per pixel used to convert the ToT to charge in measurements with external particles.

4.2.1.2 RD53A readout chip

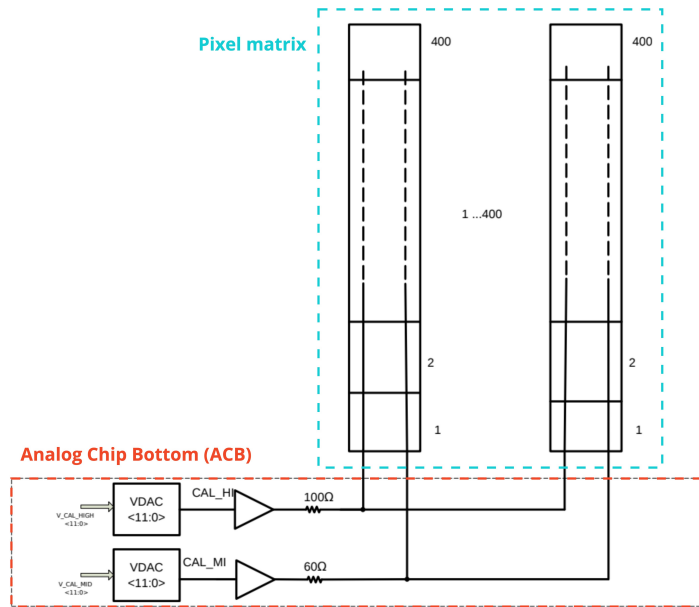


FIGURE 4.9: Charge injection voltage generation in the RD53 readout chip [115]. V_{cal} -high and V_{cal} -med are generated in the ACB.

The charge injection method developed in the RD53A chip is achieved by applying a well defined voltage steps V_{cal} via an injection capacitor directly to the input of the analog front-end in the analog chip bottom (ACB) as shown in the schematics of figure 4.9. There are three different voltages that are routed from the pulse generator to each pixel; V_{cal} -high, V_{cal} -med, and GND [115]. Both V_{cal} -high and V_{cal} -med voltages are defined by two 12-bit voltage DACs. The injected charge is given by the voltage step generated by switching between the three voltage levels using two digital-domain signals controlled by a user command and the value of the injection capacitance. When injecting the charge by switching between V_{cal} -med and V_{cal} -high the effective charge injection is independent of voltage drops in the analog ground distribution to the pixel array [115]. This two-step scheme is important to have simultaneous

calibration input in all enabled pixels. The injected charge is quoted for the RD53A in terms of ΔV_{CAL} , which is the difference between the high and low V_{cal} parameters.

The performance of the readout chips are thoroughly tested in single chip cards in testbeam environment before installation. The injection scheme in RD53 chips overcame many of the limitations of the previous FE-I4B chip, and its behaviour shows as expected in single chip cards. However, some issues might appear only when connecting a complete detector, or with time. For this reason the novel tuning algorithm developed for FE-I4B chip, will be discussed in section 4.3.2, could be relevant also for RD53 chips in the future.

4.2.2 Chip tuning

Prior to data taking, the readout chip must be tuned. The user targets a threshold level and a gain between charge and Time-over-Threshold (ToT). Thus, a passing signal is digitized into the 4-bit ToT. Before starting the ToT counter, the chosen threshold is applied to the discriminator of each pixel. The main goal of tuning the readout chip is to ensure a uniform value of threshold and ToT gain over the entire chip. In the following I introduce the main scanning procedures to test the functionality of the readout chip, e.g. digital test and analog test. Also procedures that tunes the chip configuration, e.g. global threshold tuning, TDAC tuning, ToT tuning, and noise occupancy scan are introduced. All these scans, except the noise occupancy scan, use the charge injection circuit to inject a test charge into the pixels.

4.2.2.1 Digital test

In a *digital_scan* a number of digital hit injections (or events) is injected after the discriminator to simulate the discriminator's output of the same number of events. If all the logic units, input and output mechanisms are functioning correctly, the same number of events is recorded as occupancy in an occupancy map histogram as shown in figure 4.10(a) for a FE-I4B. Any malfunction along the readout chain after the pixel discriminator is thus revealed by the number of occupancy for each pixel differing from the number of injections. As can be seen from the *digital_scan* occupancy histogram, there are 4 white pixels indicated with 0 occupancy and thus identified as dead pixels. A digital scan is performed to check enabled/disabled pixels in the module.

4.2.2.2 Analog test

An *analog_scan* is the most basic scan that uses the charge injection circuit to inject a certain number of charge n times into the pre-amplifier (CSA) leading into the discriminator. The result is an occupancy histogram as shown in figure 4.10(b). In the *analog_scan* the injected charge is injected into each pixel according to the mask pattern or 'injection mode', which represents how many pixels are injected simultaneously. As can be seen from *analog_scan* occupancy histogram each pixel was injected 100 times. Dead pixels are indicated with 0 occupancy and noisy pixels show number of hits more than number of injections indicated by pink on the top edge of the module. Thus, the response of the readout chip can be tested and an overview of the operation of all the pixels is obtained.

4.2.2.3 Threshold tuning

The injected charge into the pre-amplifier is used for threshold tuning across the pixel array to determine the mean threshold and the effective charge conversion gain via the ToT. It is critical to have a

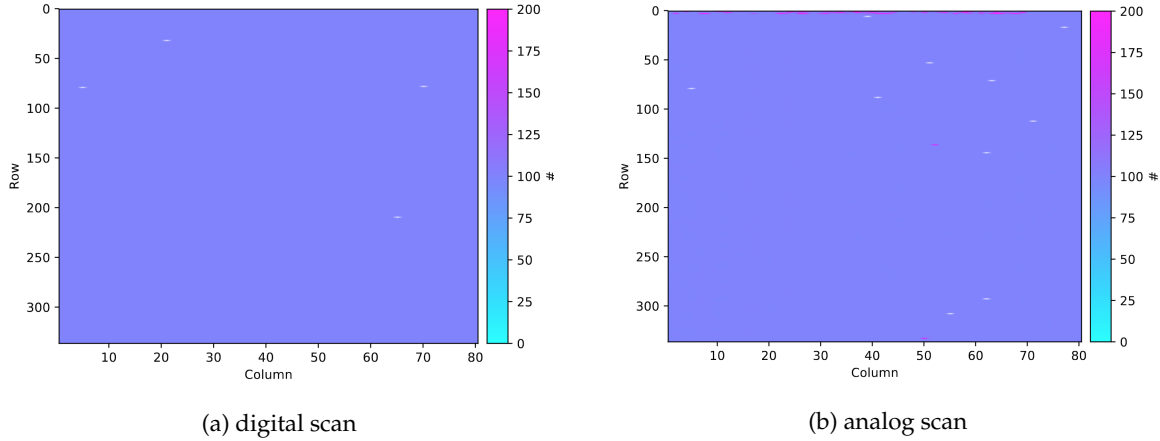


FIGURE 4.10: Occupancy maps for a FE-I4B module from (a) digital scan and (b) analog scan with 100 injection per pixel using PyBAR system.

stable threshold tuning to get a stable hit detection and reliable charge/ToT measurements. The process of tuning is a multiple scanning procedure to set the discriminator at a target level to have a uniform response over the entire pixel matrix. The tuning is executed by the analog front-end circuitry described in section 3.1.2 for the FE-I4B readout chip, and in section 3.2.2 for the RD53A readout chip. The tuning is performed in the measurement setup described in figure 4.1. The scans are performed by injecting a well defined charge Q_{in} via the injection capacitance C_{inj} into the pre-amplifier. The output of the pre-amplifier is fed into a discriminator to distinguish signal from noise. For each pixel, the charge is injected multiple times and the response of the pixel is recorded. The charge value that is above the discriminator threshold results into a hit. The discriminator has a 0 and 1 response that analogously results in a digital square wave function. Due to the electronic noise and other factors, the resultant response of the discriminator can be modeled as a step function convoluted with a Gaussian distribution. The threshold Q_{thr} is defined to be the charge for which 50% of injected charge are recorded. The hit probability P_{hit} , which is a convoluted step function and a Gaussian distribution is given by

$$P_{hit}(Q) = \frac{1}{2} \operatorname{erf} \left(\frac{Q_{in} - Q_{thr}}{\sqrt{2}\sigma_{noise}} \right), \quad (4.6)$$

where Q_{thr} is the charge that corresponds to the discriminator threshold and Q_{in} is the injected charge. The error function $\operatorname{erf}(x)$ describes the probability of a random Gaussian variable x with a mean value 0 and variance 0.5 falling in the range $[-x, x]$. It is defined by

$$\operatorname{erf}(x) = \frac{1}{\sqrt{\pi}} \int_{-x}^x e^{-t^2} dt. \quad (4.7)$$

A successful tuning of the threshold is achieved by injecting the charge for each pixel and producing a response with a narrow and symmetrical Gaussian distribution around the target value. The corresponding threshold response is the mean value of the distribution as shown in the Gaussian histograms of figure 4.11 produced by PyBAR, and figure 4.12 produced by BDAQ53. The figure produced by PyBAR records the response of 100 repetition of charge injections for each pixel at a mean value of 2000 e.

The pixel occupancy above 100 injections for the S-curve indicate that these pixel fire more than 100 times and thus are considered noisy pixel or pixels in cross-talk. Pixel occupancy shown on the left side of the S-curve indicate pixels with lower threshold values, while pixel occupancy on the right side on the S-curve indicate pixels with higher threshold values. A narrow dispersion of threshold distribution indicates the homogeneous threshold over the entire chip.

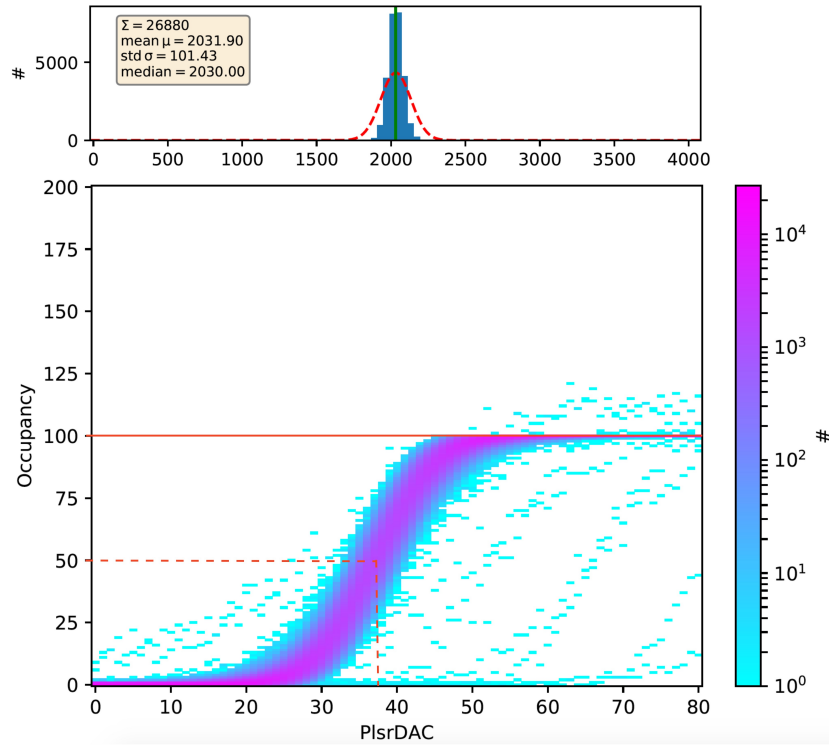


FIGURE 4.11: Tuning results for a FE-I4B module using PyBar. Top graph shows the threshold distribution fitted by a Gaussian showing mean value at the tuned threshold of $2031 \pm 101 e$. Bottom graph shows the S-curve map for the pixel response at the targeted threshold of 37 PlsrDAC.

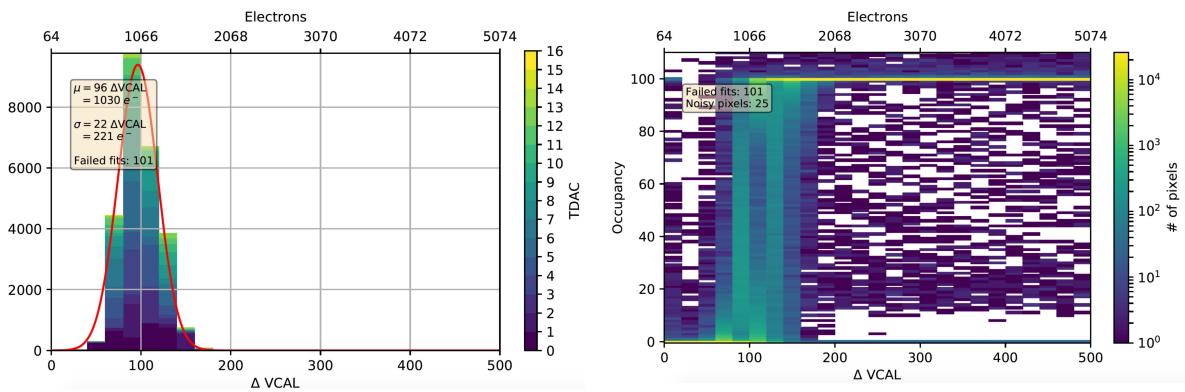


FIGURE 4.12: Tuning results for a RD53A module using bdaq53. Left graph shows the threshold distribution fitted by a Gaussian showing mean value at the tuned threshold of $1030 \pm 221 e$. Right graph shows an S-curve map at the targeted threshold of 96 PlsrDAC.

The threshold for any front-end chip is tweaked by mainly two parameters: the global average threshold of the entire chip, and the local per-pixel threshold. The dynamics of these parameters depend on the analog design of the front-end chip. For FE-I4B chip, the threshold is adjusted globally by the GDAC register *VthinAlt* [16-bit register], which controls the discriminator stage of the chip by setting a common value for all pixels. *VthinAlt* is divided into two: *VthinAltFine* [8-bit register] ranges from (0-255) and adjusts the threshold up about $10\,000\,e$, and *VthinAltCoarse* [8-bit register] and ranges from (0-255) to tune to thresholds above $10\,000\,e$ where each increment is the full range of the *VthinAltFine*. This range defines the maximum charge range of the chip (refer to table 3.1). Throughout this thesis, we try to tune modules to low threshold and thus the *VthinAltCoarse* is always = 0. On the other hand for the RD53A chip, the threshold is adjusted globally using specific registers for each front-end flavour. Although the threshold is controlled by different registers, the tuning mechanism is the same and I will focus more on commands and procedures used for the FE-I4B chip using PyBar framework.

The *GDAC_tune* scan command to tune the global threshold performs a scan over a range of injected charge and calculates the threshold using equation 4.6. The scan adjusts the average threshold over the entire module. The threshold value achieved by the *GDAC_tune* is the average value to the target threshold over all pixels with a threshold dispersion that determines the outlier pixels from the target. The local per pixel tuning of the threshold is adjusted by the register *TDAC* [5-bit register], which controls the discriminator stage by setting the threshold value for each pixel independently. For FE-I4B chip, the *TDAC* range from [0-31]. The *TDAC_tune* scan tunes the per pixel threshold by performing a scan over a range of injected charges and calculate the threshold of each pixel. The threshold is dependent on the *TDAC* steps that adjusts the least significant bit of the 5-bit *TDAC* register. The steps of the *TDAC* are called the step size and are controlled by the register *TDACVbp* [8-bit register]. During the scan procedure if the threshold of the pixel is recorded lower than the target value, the *TDAC* is increased by one defined step. In contrast, if the threshold of the pixel is recorded to be higher than the target value, the *TDAC* is decreased by one defined step. This procedure centers the average threshold value achieved by the *GDAC* and minimizes the threshold dispersion. The threshold dispersion can get narrower with tuning iterations.

In general, the tuning of the *GDAC* allows for a coarse tuning of the threshold globally, whereas the local *TDAC* superimposes the global *GDAC* and allows for fine tuning within a limited range.

4.2.2.4 Time over Threshold tuning

The tuning of the ToT works in a similar way as the tuning of the threshold. The mean ToT is tuned to the average of the expected signal amplitude that traverse the sensor. The expected amplitude can be sampled by a radioactive source with a well known energy. A typical ToT tuning for $150\,\mu m$ thick sensor targets 8 ToT at $12\,ke$ injected charge. Table 4.1 lists the Most Probable Value (MPV) of injected MIPs used for tuning the ToT based on the sensor thickness. The MPV of the released charge by a MIP in Silicon is in the range of about $80\,e$ per micron distance depending on the sensor thickness (see section 2.2 figure 2.5).

In the FE-I4B, the global ToT of the entire chip is tuned by adjusting the register *PrmpVbpf* [8-bit register], which controls the feedback current of the preamplifier for each pixel. The local per pixel setting for the ToT is adjusted by the register *FDACVbn* [8-bit register], which configures the step size (least significant bit) for the feedback current for all pixels for the level of injected charge.

TABLE 4.1: The injected charge to tune the ToT varies with the thickness of the module, the MPV of injected charge from MIPs based on sensor thickness.

Thickness [μm]	Injected charge [e]
50	4000
100	8000
150	12000

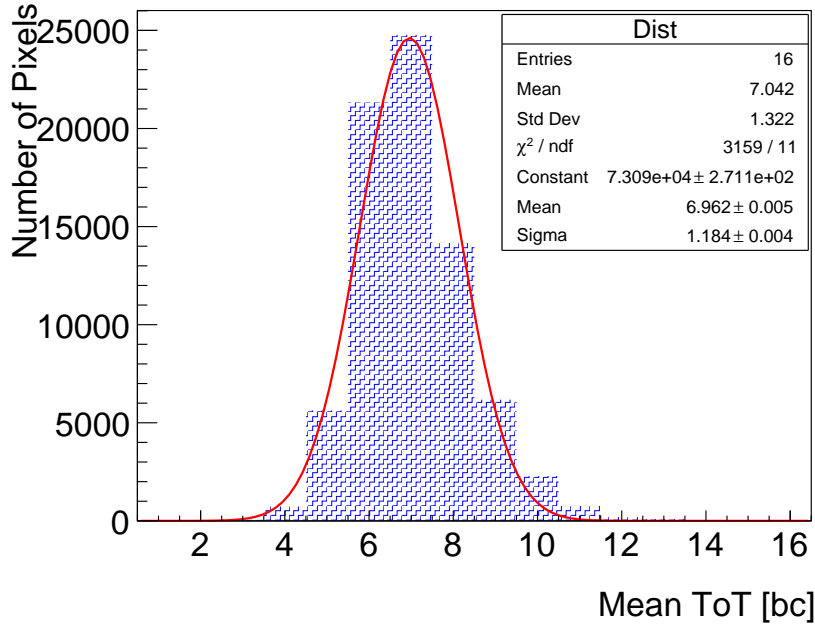


FIGURE 4.13: ToT distribution fitted with a Gaussian convoluted with a Landau showing MPV at about 7 ToT per bunch-crossing.

If a charge signal is shared exactly between two pixel cells, the ToT value theoretically lowers to half correspondingly. Thus, the ToT of a signal is used to reconstruct the deposited charge in the module. For the signal coming from β -electrons of a radioactive source, the resulting ToT distribution after the tuning is a Landau convoluted with a Gaussian distribution as shown in figure 4.13 where the MPV corresponds to the mean ToT. The relation between the range of injected charge into the pre-amplifier and the ToT as explained in the charge calibration measurement of section 4.2.1.1 is measured during the ToT calibration. Although a homogenous nominal ToT tuning is achieved over the entire chip, the ToT calibration measurement shows a difference in the pixel-to-pixel response to a fixed injected charge. The ToT values exhibit a linear relation at small injected charge values, but the relation diverges with increasing injected charge as shown in figure 4.14. With higher injected charge the ToT tends to saturate. The correlation between the ToT-charge values is obtained for every pixel as demonstrated from equation 4.5. This correlation reduces the uncertainty of the direct conversion from ToT values to real charge values.

In contrast to the ToT tuning, where only a fixed amount of charge is injected, the ToT calibration aims to cover a charge range as large as possible. The ToT is calibrated by scanning the ToT values against a wide range of injected charge with the same mechanism performed in the tuning procedure. The ToT-to-charge relation is calibrated by the fit parameters of the ToT. The calibrated charge function is defined by

$$Q = a + b \cdot ToT + c \cdot ToT^2 \quad (4.8)$$

where a, b and c are the fit parameters per pixel and are the same parameters of equation 4.3 and 4.5.

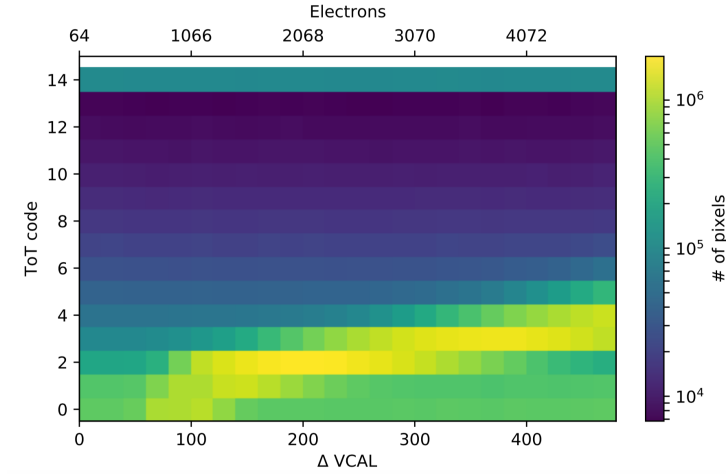


FIGURE 4.14: The ToT as a function of the injected charge measured in VCAL shows non-linear relation. Most pixels have ToT value between 3-5 as VCAL increases. Produced by bdaq53 for a RD53A module

These parameters are fit constants for all pixels in the module and they're used to convert the ToT values into charge values.

4.2.2.5 Noise occupancy scan

To have a good signal-to-noise ratio (SNR) after tuning, the noise performance of the pixel module is measured by a *Noise_occupancy_scan*. The scan sends random triggers to the chip and counts number of hits from each pixel. Pixels that respond more than the expected rate of hits due to the global noise level are interpreted as noisy pixels. These pixels are masked during data taking to maintain a high SNR. Keeping the noise level low is necessary, as high noise occupancy can lead to loss of event data due to the high data rate. A noise occupancy above a certain level will also deteriorate tracking performance. Occupancy due to noise hits or "noise occupancy" is required to be 10^{-5} or below for the ATLAS pixel detector in order not to influence the tracking efficiency [138]. This scan is performed on all the prototype modules after tuning and before data taking.

4.3 Threshold investigation in FE-I4B modules

Analysis of data and MC simulation from LHC runs in 2015-2016 indicated a significant discrepancy between the expected charge collection from original MC and the measured data from IBL detector and was first documented in reference [139]. Charge measurements in the pixel detector and IBL are based on the ToT information that has to be properly associated to the corresponding value of deposited charge by a dedicated calibration as mentioned in section 4.2.2.4. The measured energy spectrum of the source is reconstructed from the deposited charge and compared with the expected values to check the quoted discrepancy in the charge collection of IBL modules. Another study by University of Bonn [110] quantifies the observed results into a global discrepancy of charge collection to the loss of about $1000e$. This global discrepancy is referred as the *global threshold shift*. In addition, a second discrepancy of charge collection was also observed within the FE-I4B chip. Only after tuning the chip using the charge injection circuitry, the left region (within columns [0-39]) of the FE-I4B chip sets a higher threshold setting than the right region (within columns [40-79]). This leads to lower hit counts and asymmetric collection of charge within the same module as visible in the occupancy histogram of figure 4.15. This asymmetry

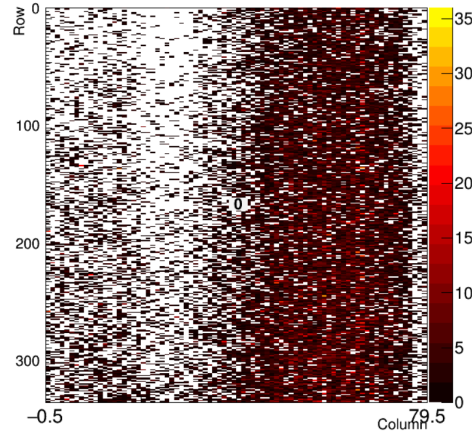


FIGURE 4.15: Hit occupancy map for a FE-I4B module showing local threshold asymmetry between left and right region.

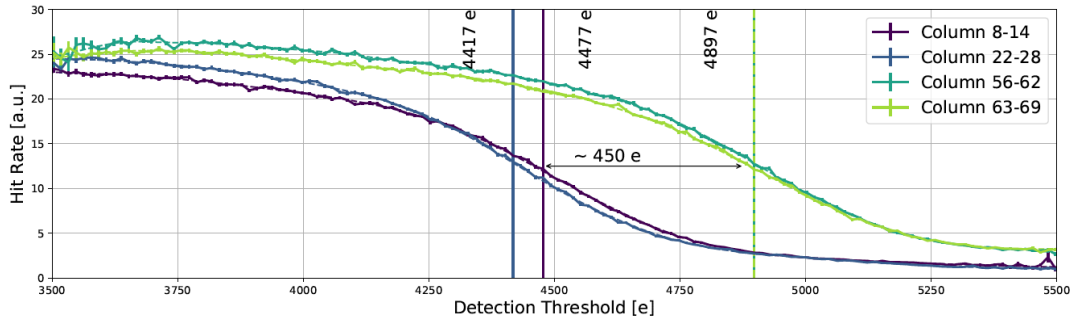


FIGURE 4.16: Measurement of integrated single-pixel charge spectrum of ^{109}Cd γ -source after tuning showing the change of injected charge across the columns using the internal charge injection circuitry [110]. The measurement quantifies 450 e difference of tuned threshold between left and right region.

appears after tuning, and it results into different threshold values between left and the right side of the module. This local discrepancy is quantified to have up to 450 e difference between left and right regions of the chip [110] as shown in figure 4.16. This regional asymmetry will be referred to as the *local threshold asymmetry*.

This section introduces the tuned threshold issues found in the FE-I4B chip of IBL modules. Section 4.3.1 shows the global and local threshold shifts that illustrates the charge collection issues, section 4.3.2 introduced the new tuning mechanism to solve the local threshold asymmetry issue. To realize the new tuning method for the IBL detector, in section 4.3.4 I discuss the challenges in implementing the tuning algorithm in the ATLAS pixel DAQ to tune and test the IBL detector.

4.3.1 Threshold discrepancy

Reports of the discrepancy of charge collection in the IBL detector indicate a systematical error in the calibration of the detector. The methods of calibration affect also the digitization step of the detector simulation, where the simulated charge collected by the pixels is converted into ToT hit. And so the ToT spectrum predicted by the simulation (MC ToT, in the following) from collisions does not match with the calibrated measurements [139]. Miscalibration of the module affects the MC prediction of measured ToT spectra causing the observation of this charge collection defect also in MC to collision data comparison. A corrected calibration for the charge analysis with MC is proposed in reference [139] to recover

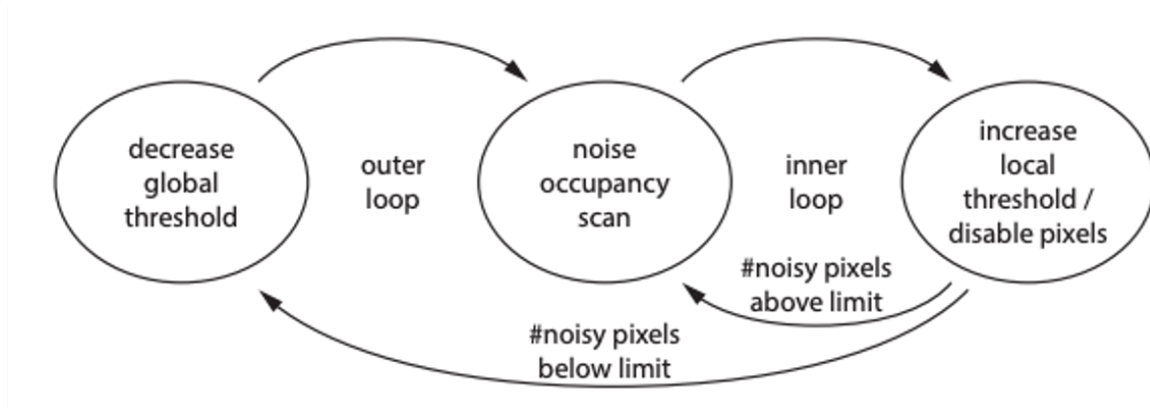


FIGURE 4.17: Sketch for the threshold baseline tuning algorithm [140].

predictability on ToT values that is in agreement with data. This section addresses and discusses the discrepancy that is originating from the front-end chip after tuning and compares the results with a novel method of tuning.

A successful tuning of the threshold requires setting both global and local threshold registers to achieve a mean value close to the target threshold with a narrow centered Gaussian distribution. This tuning mechanism as explained in section 4.2.2.3 will be referred to as the standard tuning method. The standard tuning method uses the injection circuitry, which uses the PlsrDAC, to generate a given voltage on the injection capacitance for each pixel. Due to the physical location of the PlsrDAC in the chip in the proximity of column no. 26, the injected charge is highest close to that column. While for further away columns the injected charge becomes lower due to voltage drop as discussed in the pulser circuit measurements of section 4.2.1.1. Consequently, the per-pixel threshold distribution $TDAC$ is adjusted accordingly with the voltage drop causing a biased threshold distribution. This behavior creates the local threshold asymmetry issue. As the asymmetry is originating from a voltage drop causing injected charge variability that is used in the tuning mechanism, our attempt to solve the asymmetry is by tuning the module without the use of the charge injection circuit. A new tuning method, the threshold baseline tuning, is presented in the following and used in comparison to the standard tuning method to solve the local threshold asymmetry in FE-I4B chips. The following investigation was done for my ATLAS qualification task and continues beyond that.

4.3.2 Threshold baseline tuning algorithm

The threshold baseline tuning was introduced within the RD42 collaboration for hybrid diamond detectors [140]. The tuning algorithm has been developed to individually tune the threshold of each pixel to the lowest possible threshold that does not exceed a given noise hit rate. It is based solely on counting hits of individual pixels by a noise occupancy scan (see section 4.2.2.5). The response of each pixel gives an independent hit rate. So, the tuning algorithm measures the noise hit rate of each pixel and sets the threshold level accordingly.

The threshold baseline tuning makes use of the global threshold register ($GDAC$) and the local per-pixel register ($TDAC$) to adjust the comparator threshold for each pixel. Figure 4.17 shows a sketch to aid the explanation of the threshold baseline tuning algorithm. The algorithm starts from initial conditions, in which the global threshold is set to be high and the local threshold is set to the lowest value, the baseline tuning algorithm performs a noise occupancy scan on all pixels. The baseline tuning is performed

with target occupancy limit, for example, the IBL detector is set to 10^{-5} hits/bunch-crossing as an upper limit. There are two main loops in this threshold baseline tuning algorithm: an inner loop for local threshold, and outer loop for global threshold. As shown in the sketch of figure 4.17, the local threshold is increased for pixels that show an excess of noise hits. The sum of hits is described by Poisson statistics following its Probability Density Function (PDF) [141]

$$f(k, \lambda) = \frac{\lambda^k e^{-\lambda}}{k!} \quad (4.9)$$

where e is Euler's number, k is the number of hits ($k > 0$), and λ is the expected number of hits per-pixel per scan. The number of consecutive triggers in the scan is set to be sensitive to reach the desired limit⁵. The noise occupancy scan and subsequent increase of the local thresholds of noisy pixels are repeated in the inner loop until the total number of pixels showing noise hits is below a certain limit that is calculated by the PDF.

Next, while keeping the local threshold constant, the global threshold is decreased in the outer loop. At lower thresholds, the probability for more hits will increase so the inner loop iterates again to increase the local threshold starting from the TDAC settings of the previous loop. Pixels reaching the upper limit of the local threshold TDAC are disabled. The nested loops iterate until the exit condition is satisfied. The outer loop of the global threshold exits under one of three conditions:

- number of disabled pixels reach maximum limit.
- the mean of the local threshold value reached its center value, meaning all pixels have evenly distributed local thresholds around the central value.
- the algorithm reached lower possible global threshold value and cannot decrease any lower.

When one of these conditions is satisfied the tuning ends. When the condition of the TDAC distribution reaching its average value is met the module is considered stably tuned. The threshold baseline algorithm results into a threshold for each pixel at the lowest possible value above noise level with high signal-to-noise ratio and a centered distribution of the local threshold.

This tuning mechanism is referred to as the *Threshold Baseline tuning* method. It is the proposed solution to solve the per-pixel asymmetrical threshold distribution in FE-I4B chips for IBL modules by avoiding the use of the charge injection circuit in the tuning process. The study of the threshold baseline tuning method on IBL prototype modules is presented in the following.

4.3.3 Threshold baseline tuning investigation

In this section I present the investigation on the tuning procedures in a comparative way between the standard tuning method and the threshold baseline tuning method. Measurements with a radioactive source are carried as a validation step for the threshold level of the module after tuning. Afterwards, source scans are measured on each module for both tuning methods. Hence, each module is tuned and measured with a source scan twice. Presented results are produced from the tuning setup described in figure 4.1 with PyBAR system, and using FE-I4B modules that are listed below in table 4.2 with their details. The investigation procedure is illustrated in the following.

⁵For occupancy limit of 10^{-5} hits/bunch-cross the trigger is set to 10 000.

TABLE 4.2: summary of the investigated IBL modules

Module	Institute	FE	HV	fiducial region
IBL	CERN	double	80 V	[5:75,:]
LPNHE7	LPNHE	single	80 V	none
CERN _{FE0}		quad	80 V	[100:,:7:]
CERN _{FE1}	CERN		80 V	[100:,:70]
CERN _{FE2}			80 V	[70:,:7:]
3D module	Bonn University	single	50 V	[:,5:75]

4.3.3.1 Tunings

The threshold baseline tuning method sets an occupancy limit target to define the noise baseline. The current ATLAS IBL detector has an occupancy limit at 1×10^{-5} hits/bunch-crossing⁶ [47]. The default occupancy limit target for this investigation is set to 1×10^{-6} hits/bunch-crossing. During the tuning process all columns and rows of the pixel matrix are scanned. But in case of module defects a fiducial region is applied in the analysis. The baseline tuning outputs a .h5 file (refer to section 4.1.2) that is analyzed in SWAN⁷ python3 environment to produce the presented results in this section. The threshold baseline algorithm does not tune the ToT. The ToT is tuned beforehand with the only available procedure using the charge injection circuitry. Thus, the tuning procedure starts from a previous configuration file where the ToT is tuned to 7 ToT to 10 ke.

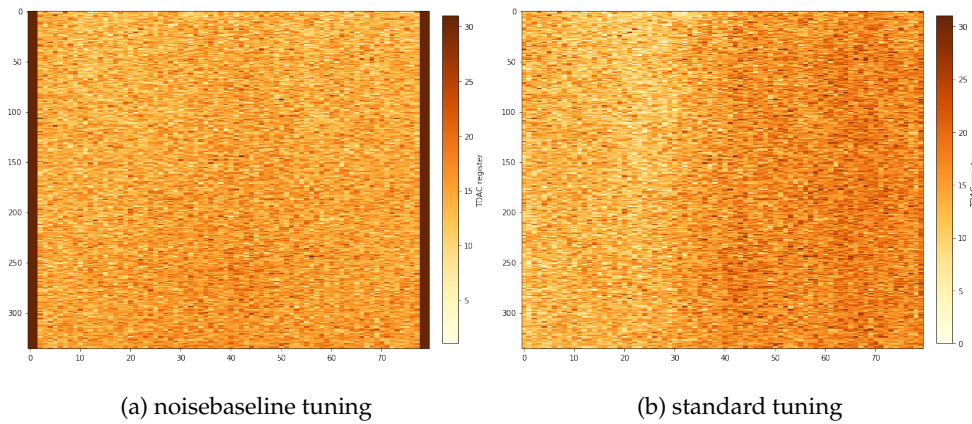


FIGURE 4.18: Visual representation in 2D map for TDAC values across an IBL module after tuning.

Tuning the per-pixel threshold on the chip produces a matrix of *TDAC* values for each pixel. The *TDAC* 2D map as shown in figure 4.18 is a visual representation for the per-pixel *TDAC* values resulted from a tuning scan. Figure 4.18(a) shows the *TDAC* map from the threshold baseline tuning and figure 4.18(b) shows the *TDAC* map from the standard tuning.

To estimate the difference between the results of both tuning methods, the average *TDAC* values per column are extracted and plotted across the columns as shown in figure 4.19 for an IBL planar module. The plots were fitted with a constant, the RMS, and the $\chi^2/Ndof$ are calculated. The figure shows the *TDAC* behaviour comparing between both tuning methods. The *TDAC* values represent the per-pixel threshold to compensate the difference of global tuning from the *VThinAlt* register. Hence, a non-homogenous *TDAC* map represents a bias in the tuning process. The average *TDAC* per column for standard tuning plot in figure 4.19 (Black) has RMS of 2.18, and $\chi^2/Ndof$ of 359.5/74, which indicates a

⁶A channel is considered noisy and is masked if it has occupancy $> 10^{-5}$ hits/bunch-crossing

⁷<https://swan005.cern.ch>

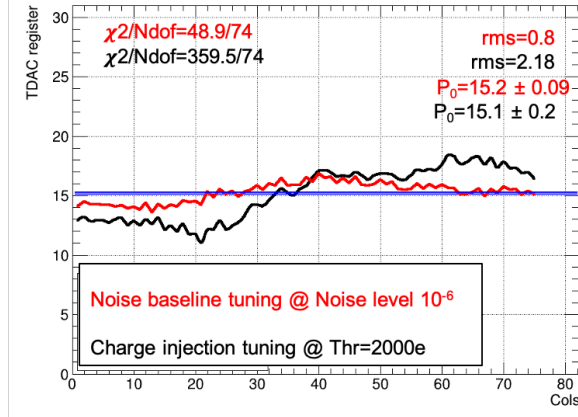


FIGURE 4.19: Average $TDAC$ per column comparison for IBL module after tuning with standard method (Black) and baseline method (Red). Both plots are fitted with constant at their mean value.

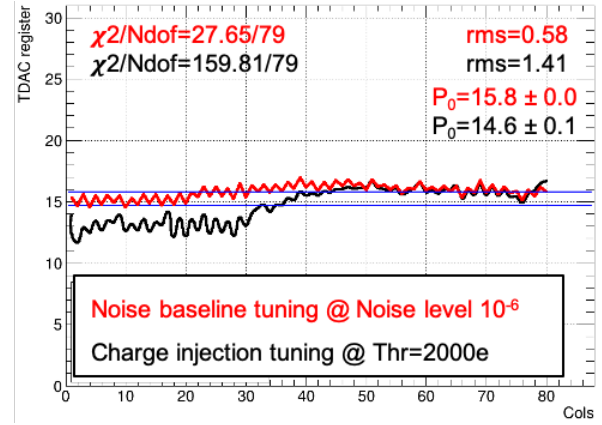


FIGURE 4.20: Average $TDAC$ per column comparison for single FE-I4B module after tuning with standard method (black) and baseline method (red).

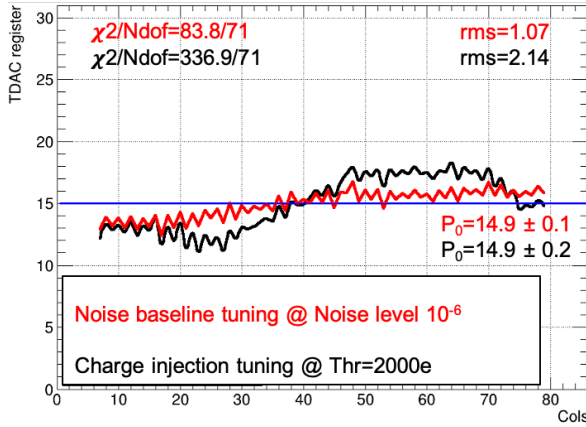


FIGURE 4.21: Average $TDAC$ per column comparison for quad module after tuning with standard method (black) and baseline method (red).

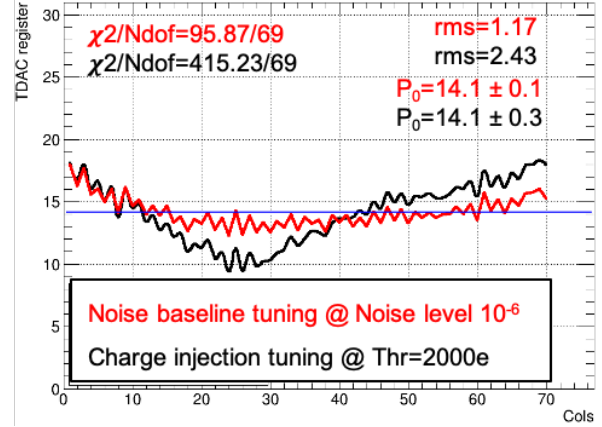


FIGURE 4.22: Average $TDAC$ per column comparison for $CERN_{FE1}$ module after tuning with standard method (black) and baseline method (red).

large deviation from the constant value. Lower $TDAC$ values indicate higher effective threshold within the region. Contrary, the threshold baseline tuning plot in figure 4.19 (Red) has RMS of 0.8, and $\chi^2/Ndof$ of 48.9/74, which indicates a more homogeneous per-pixel threshold distribution. The $TDAC$ map produced by the threshold baseline tuning method shows a smoother and symmetrical per-pixel threshold around the $TDAC$ mean value $P_0 = 15$.

The comparative study on other modules presented in figures 4.21, 4.22, 4.23, and 4.24 show similar behaviour after tuning, separately for each of the two methods. The fluctuations and pattern of the $TDAC$ values in the figures are module dependent. The asymmetry on the average $TDAC$ per column verifies the asymmetrical threshold issue this study is attempting to solve. While, a symmetrical distribution of the average $TDAC$ per column as shown by the Red plot for baseline tuning method indicates a homogeneous threshold on the module. The average $TDAC$ per column distribution after threshold baseline tuning shows more symmetrical distribution across the module than the standard tuning. A symmetrical threshold would satisfy the tuning purpose to have a uniform response over the entire module.

As already said, the $VthinAlt$ register controls the global threshold. The threshold baseline tuning sets the module at the lowest possible $VthinAlt$ value above noise limit. The lowest $VthinAlt$ varies for each

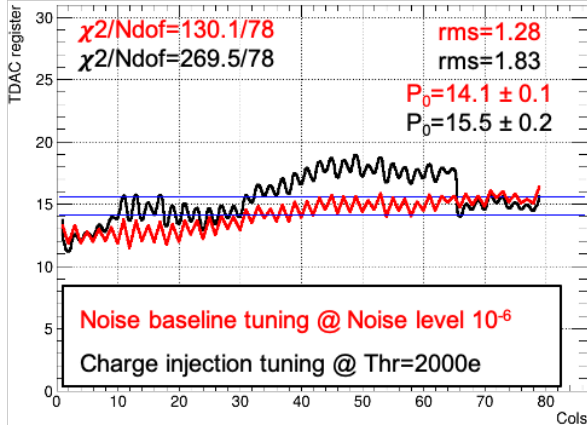


FIGURE 4.23: Average $TDAC$ per column comparison for IBL module after tuning with standard method (black) and baseline method (red).

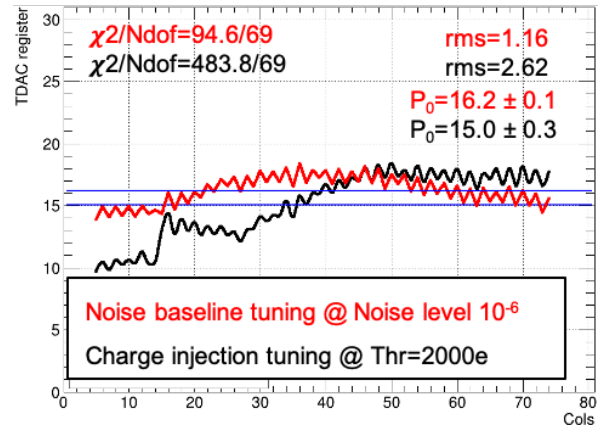


FIGURE 4.24: Average $TDAC$ per column comparison for 3D module after tuning with standard method (black) and baseline method (red).

module and noise target level. The reader can get a feeling for it from table 4.3.

TABLE 4.3: Time performance of the threshold baseline tuning at different noise rate levels for an IBL module.

noise rate [hits/bc]	triggers	duration [minutes]	threshold [$V_{thinAlt}$]	rms per column
10^{-5}	10 000	7	43	0.54
10^{-6}	100 000	15	46	0.53
10^{-7}	1000 000	1h 47	47	0.55

At very low thresholds, the standard method to measure the FE-I4B threshold doesn't work as the S-curve shape is not visible due the presence of noise at immediately lower threshold. In this case the effective threshold is too low to distinguish the S-curve to fit the 50% crossing point. For this reason to study the local thresholds, only the global threshold $V_{thinAlt}$ is manually increased to reach a range where the S-curve fit would work. The lowest value that can be fitted is found to be $V_{thinAlt}=70$ for voltage step $TDACVbp^8=100$, which corresponds to a mean threshold of $700e$. In all shown results for the threshold baseline tuning, $V_{thinAlt}$ was increased manually to a mean threshold value of about $2000e$ to compare it with the standard tuning result. For standard tuning method, the modules were initially tuned to 37 PlsrDAC, which is equivalent to a threshold of $2000e$.

After tuning for the IBL detector, the threshold value in electrons can be extracted with the knowledge of the in-pixel threshold step size. How much does the threshold increase with each increment of the $V_{thinAltFine}$ is defined by the register $TDACVbp$. This register controls the $TDAC$ least significant bit size [105]. In standard tuning mechanism the $TDACVbp$ changes the distribution of the per-pixel threshold as shown in figure 4.25. The figure shows a comparison between different $TDACVbp$ values and its effect on the $TDAC$ distribution. It shows higher asymmetrical behaviour of the threshold between left and right region at lower step size than the IBL default value. The higher the $TDACVbp$ value the larger the threshold step is, and the lower the $TDACVbp$ is the smaller the threshold step is allowing the threshold to be tuned at lower values. The IBL detector default value of $TDACVbp = 180$. While figure 4.26 shows the same study when the threshold baseline tuning is used, the produced average $TDAC$

⁸The $TDACVbp$ controls the voltage step at each increment of the threshold, a higher value of $TDACVbp$ reaches further in threshold.

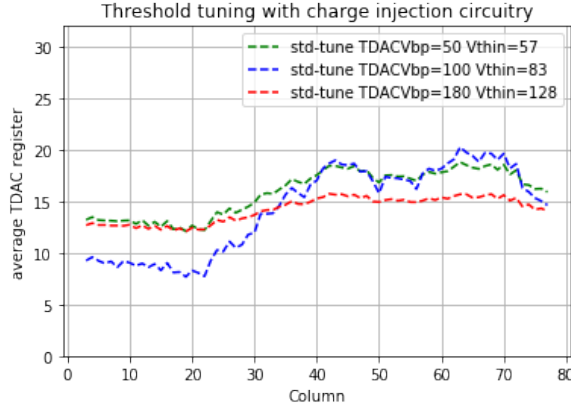


FIGURE 4.25: Average TDAC value per column showing the effect of tuning parameter $TDACVbp$ with standard tuning method, smaller $TDACVbp$ values result into smaller steps in tuning allowing to reach low global threshold such as $vthin=57$.

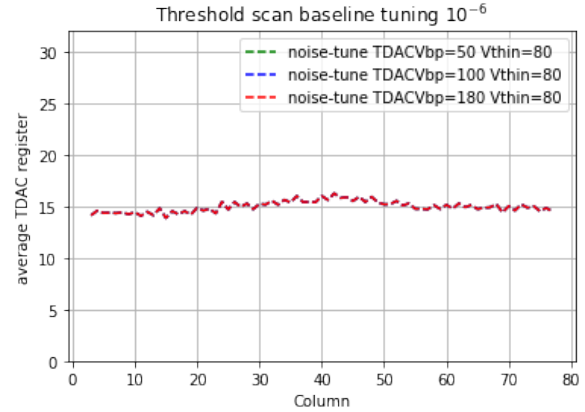


FIGURE 4.26: Average TDAC value per column shows no effect to the $TDACVbp$ parameter when tuning with the threshold baseline method because there is no voltage dependency in this tuning method.

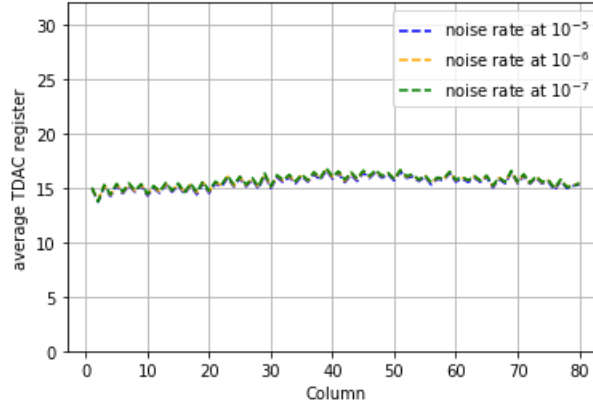


FIGURE 4.27: Average $TDAC$ per column distribution at different noise occupancy targets for the threshold baseline tuning.

map shows a homogeneous per-column threshold independent of the $TDACVbp$ register. In addition, the noise occupancy limit is the target parameter in the threshold baseline tuning. Investigating the behaviour of the tuned threshold of one IBL module at different noise baseline levels shows similar average $TDAC$ per column distribution as shown in figure 4.27. Target noise limits at 10^{-5} and 10^{-6} and 10^{-7} hits/bunch-crossing tune the threshold to the lowest possible level with the same $TDAC$ distribution. As summarised in table 4.3, tuning a single front-end to target noise limit 10^{-5} with 10 000 triggers takes 7 minutes and sets the global threshold at $VthinAlt=43$. Tuning to target noise limit 10^{-6} with 100 000 triggers takes 15 minutes and sets the global threshold at $VthinAlt=46$. Tuning to target noise limit 10^{-7} with 10 000 triggers takes 1hr47 minutes and sets the global threshold at $VthinAlt=47$.

4.3.3.2 Source scans

A source scan measurement probes the module using an external, known, radioactive source. A source scan records the hits on each pixel of the module when triggered. The same experimental setup described in chapter 4.1 is used for measurements with source scans. The radioactive source is placed in a fixed position about 1 cm on top of the module. The position is fixed on the module with a 3D printed source holder, put on top of the module as shown in figure 4.31. ^{109}Cd X-ray source is used in this setup. ^{109}Cd

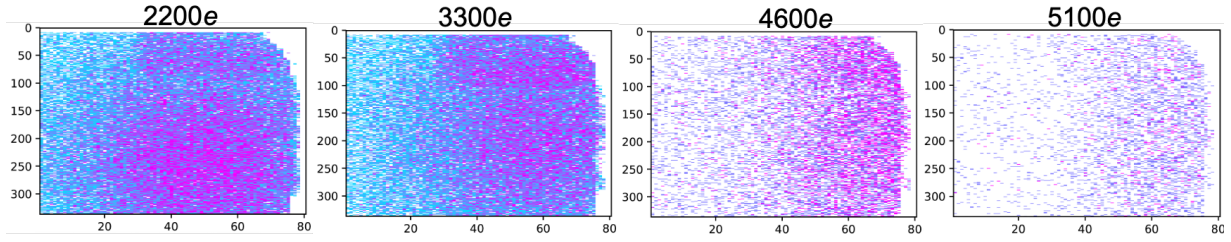


FIGURE 4.28: The evolution of hit maps per tuned threshold from source scans with ^{109}Cd after tuning for standard tuning. Tuned threshold value quoted on top.

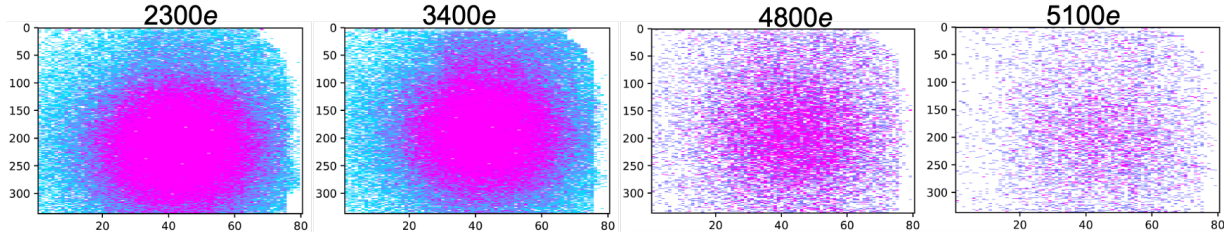


FIGURE 4.29: The evolution of hit maps per tuned threshold from source scans with ^{109}Cd after tuning for baseline tuning. Tuned threshold value quoted on top.

has photon energy of 22.2 KeV and an average signal in Silicon 6.1 ke. A self trigger mode is set on the FE-I4B chip. Scans are run for constant time of 10 mins over depleted modules at reverse biased voltage of 80 V for all modules except the FE-I4B 3D, which was biased at 50 V. Module and source are kept inside the climate chamber for constant temperature and humidity.

A source scan counts the number of hits, or number of particles that have triggered a signal across the module, and produces a hit map over the pixel matrix. To investigate the per-pixel threshold asymmetry, a source scan is performed at each tuned threshold. Figure 4.28 shows the hit maps from a source after a standard tuning. The hit maps produced at each threshold point, expressed in electrons on top of the figure, shows an evolution of the hit occupancy per tuned threshold. It is visible that more hits on the right side of the module is registered where, due to the asymmetry, the threshold is lower. The evolution of the hits per increasing threshold as expected shows less hits while maintaining the threshold asymmetry. Figure 4.29 shows the evolution of the hits per increasing threshold after threshold baseline tuning. The hit maps does not visualize any asymmetry across the column, rather it shows a dependance on the circular source shape from the saturated number of hits at low thresholds at occupancy limit of 10^{-6} hits/bunch-cross. The scan as a function of threshold is performed on the global threshold by increasing the register *VthinAlt* in constant increments. The increments differ based on the module and was chosen to cover periods of approximately 1000 electrons at each tuned threshold value.

To quantify the hit map results, lets take a fiducial region as indicated in figure 4.30: left region within columns [10-35], and a right region within columns [45-70] including all rows in case of no front-end defects. Figure 4.32(a) shows the number of hits vs. *VthinAlt* for standard tuning method. Both regions are normalized and plotted separately to be able to quantify the threshold asymmetry correlating it with the number of hits on the region. The **right** region in standard tuning, which has lower threshold value, shows about 20% more hits than the **left** region. The number of hits are extracted at each point from the same scanning result. In comparison, figure 4.32(b) shows the number of hits vs. *VthinAlt* for the same module after threshold baseline tuning. The figure shows similar number of hits for both regions, which indicates threshold symmetry across the columns of the module. The same comparison is shown

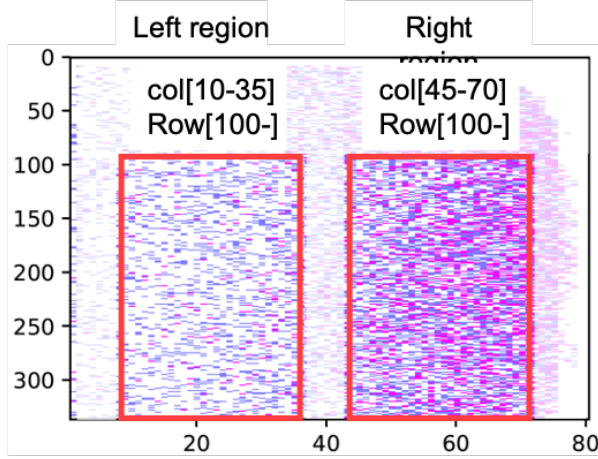


FIGURE 4.30: Left and right fiducial regions for source scan analysis

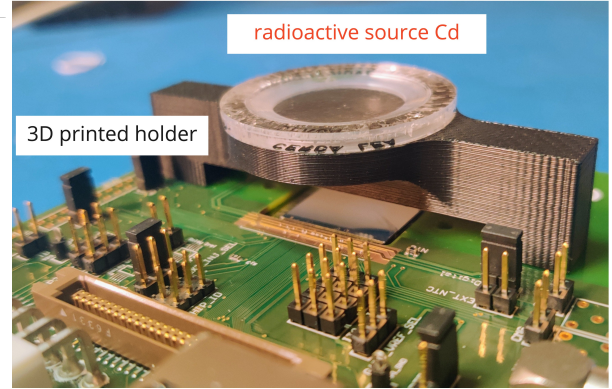
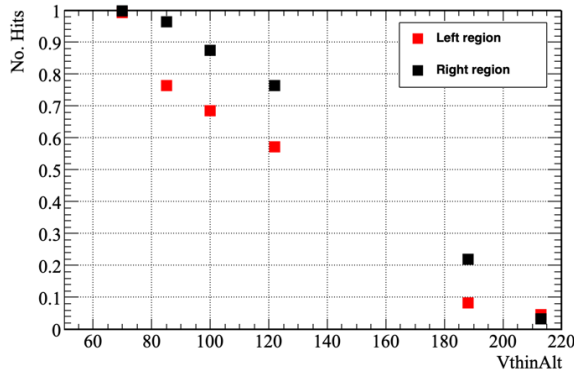
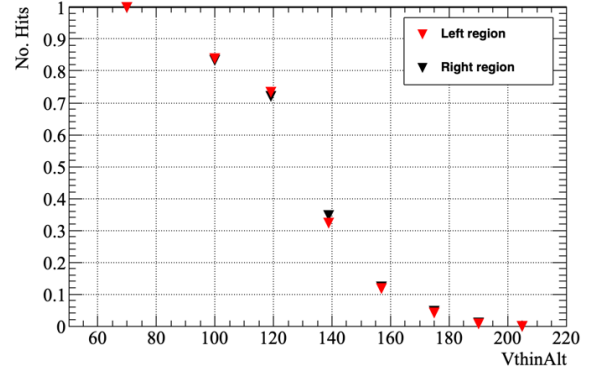


FIGURE 4.31: An image of a FE-I4B module with a 3D printed source holder fixing ^{109}Cd source on top.



(a) standard tuning



(b) baseline tuning

FIGURE 4.32: No. of hits Vs. $V_{thinAlt}$ for the CERN_{FE1} quad module. Source scans with ^{109}Cd for a FE-I4B quad module.

for another front-end for both tuning methods in figure 4.33 for an IBL module.

2180

2181 Measured front-ends show similar behaviour for each tuning method across different FE-I4B mod-
 2182 ules. To produce these plots using an external source, which provides constant and known charge, we
 2183 vary the global threshold values in order to cross the expected critical values to define the threshold at
 2184 50% occupancy. We observe that the threshold baseline tuning method results in a more uniform charge
 2185 collection across the columns. Hence solving the asymmetry of the threshold caused by the standard
 2186 tuning procedure with charge injection circuit. The threshold baseline tuning method can be a valid re-
 2187 placement for the standard method. This study was performed on individual IBL-like modules. In order
 2188 to test the tuning algorithm for the complete IBL detector it must be integrated with the pixel Data Ac-
 2189 quisition infrastructure. The technicality of the pixel DAQ infrastructure and the implementation of the
 2190 algorithm software is discussed in detail in Appendix B. The results of the implementation is discussed
 2191 in the following.

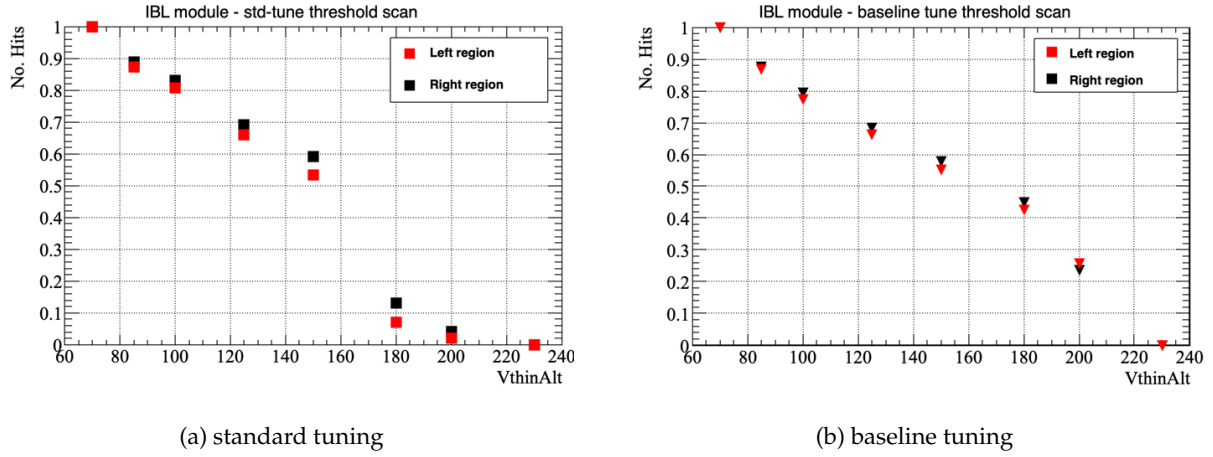


FIGURE 4.33: No. of hits Vs. $V_{thinAlt}$ for the IBL module. Source scans with ^{109}Cd for an IBL module on flex.

4.3.4 Implementation of threshold baseline tuning algorithm

The threshold baseline tuning algorithm is intended to solve the local asymmetry issue for IBL modules, in the aim to have uniform charge collection results in LHC Run3. The algorithm of the threshold baseline tuning was implemented to the pixel detector DAQ system to be tested and operated on the IBL detector in CERN-SR1 test facility. The algorithm is executed on nested loops to tune the global and per-pixel threshold, and to avoid the use of the charge injection circuit by the software. Following the algorithm logic explained by figure 4.17, the parameters of the scan is set to:

- 10 000 events per trigger
- target occupancy limit at 10^{-6} hits/bunch-crossing
- time window of 16 consecutive triggers
- masking step of scanning 1 Double-Coupled (DC) at a time
- disabled injection capacitances

The algorithm logic runs successfully testing one module at a time in the IBL detector in the SR1 test facility. However, the faced challenge is the time it takes to tune the module, or the full detector. For reasons that will be discussed below, the total time of tuning is 8.3 seconds per DC per TDAC per GDAC step. The algorithm requires to scan 40 DCs, 30 TDACs, and at least 100 GDACs. This would accumulate an unreasonable amount of time to tune the IBL detector with this method.

The scanning time is prolonged due to several reasons: The noise occupancy scan is performed for random pixels, the scan per 1 DC allows to scan each pixel independently to perform the noise scan. This issue could be solved by scanning per 8 DC simultaneously and thus will reduce the time to $\frac{1}{8}$. Another reason was a debugging delay time encoded in the software. This feature was removed for the threshold baseline scan and the tuning time is expected to be reduced to half. Another complicated reason is the protection trigger delay time for wire bonds. This delay is set to 3 seconds per DC per trigger, with a sleeping time of $300\mu\text{s}$ between triggers. This feature is to protect the wire bonds from mechanical resonance at the frequency of the triggers. The increase of the simultaneous scanning of DCs would increase the voltage transferred via the wire bonds. The wire bonds operating in a magnetic field of 2 T experience a Lorentz force when a current passes through them. Considering the length and diameter

of the wire, the current, the orientation angle with respect of the B field and the strength of the B field, the wire can experience oscillation. This sensitive problem prevents us from modifying the wire bonds protection delay for the safety of the modules. A compromise between increasing the DC scanning per trigger and wire bonds protection delay time per trigger must be considered.

With the improved scanning procedure increasing the scanning to 8 DC per trigger, and removing the debugging delay time, the scanning time is reduced from 8.3 seconds to 3.8 seconds per DC per TDAC per GDAC step. This modification actually improved the scanning time for all tuning procedures for the ATLAS pixel detector and IBL. The tuning procedure is expected to tune all the IBL modules in parallel, hence requiring the same tuning time as one module. The challenges for tuning the complete detector was out of scope of the investigation to solve the asymmetry threshold issue in the FE-I4B chip.

Conclusion

In this chapter I introduced the readout systems that are used to operate the hybrid modules for both the IBL detector and ITk pixel detector. The charge calibration and the tuning procedures for the hybrid module was discussed to understand the origin of any discrepancy in the charge collection of the module. For all the investigated modules in this thesis the threshold was tuned as described in this chapter. Targeting low threshold would ensure the collection of the full signal from the passing charged particle in the test beam experiment. The tuning and calibration of the chip defines a baseline for our understanding of how to operate the hybrid modules and of the produced results after data taking. In the next chapter I will discuss the test beam experiment where the hybrid modules are tested for their performance in data taking after tuning. The next chapter will introduce all the necessary tools and setup to measure the hit efficiency of the pixel detector.

Building on previous observations of the local threshold asymmetry problem in the FE-I4B front-end chip [110, 142] we find that the origin of the problem is the tuning method of the modules. After testing for the new threshold baseline tuning method, we observe that it is able to set a homogenous TDAC distribution across the columns achieving a symmetrical threshold tuning across the module. The measurement with the external source scans after tuning shows symmetrical occupancy quantifying the same number of hit between the left and right sides of the module. Also, the threshold baseline tuning is able to tune to low threshold values targeting $1500 e^-$ for the IBL detector. Further advantages include that the threshold baseline tuning method is based on a noise limit target only and therefore rely on counting hits, which makes it acquire low computational demand. On the other hand, without using the calibration voltage from the charge injection circuitry the ToT calibration will not be straight forward. The ToT value can be extrapolated from the chip parameters to convert collected charge from an external source to ToT. I think the advantages of the threshold baseline method is promising for the IBL detector and probably for the future ITk pixel detector.

The implementation of the tuning algorithm in SR1 test facility needs some improvement to be able to tune the complete IBL detector in reasonable time without causing resonance in the wire bonds of the hybrid module. The optimisations to reduce the tuning time in the IBL detector helped reduce the scanning time for all other scans for the ATLAS pixel detector. Compensations between number of scans per trigger, computation demand, maximum current passing through the wire bonds must be considered to

2263 improve the tuning time for the complete IBL detector.

2264

2265 *"Logic will take you from A to B. Imagination will take you everywhere. "*

2266 Albert Einstein

Chapter 5

Characterisation tools for ITk pixel modules

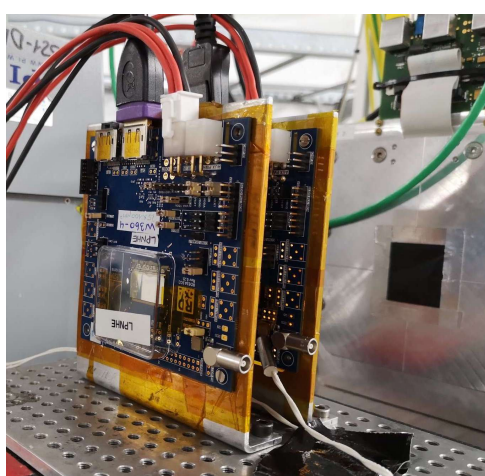


FIGURE 5.1: RD53a modules mounted in testbeam to be characterised with a particle beam source.

A *test-beam* is a characterisation setup with minimum-ionizing particle-beam from a particle accelerator illuminating a device under test (DUT). Testbeam campaigns allow measurements and system tests under realistic conditions anticipated at LHC experiments. These measurements are a powerful tool to study the hit efficiency and the position resolution of a sensor. This chapter presents the instrumentation and techniques used to characterise a module with a particle beam, beginning from the testbeam setup to the track reconstruction and analysis softwares. Before mounting a pixel module in front of a particle beam source as shown in figure 5.1, it is important to measure the leakage current and the operational bias voltage limits for the sensors safety. In section 5.1 I introduce the electrical characterisation technique and instrumentation to obtain the leakage current of the sensor. Then, in section 5.2 I introduce the main component used to characterise the pixel modules in a testbeam setup, the EUDET beam telescope. Testbeam setups with an EUDET beam telescope are present in several locations, they are presented in section 5.3. After data taking with the pixel module mounted in front of the particle beam, tracks are reconstructed from raw data using EU Telescope software. Then they are analysed with an offline track analysis using Tbmon2 software for user-specific analysis, efficiency position resolution studies, and visual representation of the results. The track reconstruction methodology and track analyses software are discussed in section 5.4. The performance results and analysis of the measured ITk modules using the instrumentation and techniques of this chapter will be discussed in the two next chapters.

5.1 Electrical characterisation

A fundamental measurement for a silicon sensor is the leakage current of the bulk as a function of the bias voltage V_b to determine the current-voltage (IV) characteristics of the sensor. The characteristics of the sensor design are indicated by the behaviour of the IV curve from measuring the current as a function of bias voltage. From the IV curve, the range of operational limit of the sensor can be determined as well as the breakdown voltage V_{bd} of the sensor. These properties help identify a good sensor from a bad one in terms of operation.

To obtain the maximum signal from a charge particle passing through the pixel detector, the sensor must be fully depleted. This depletion region is expanded by biasing the pixels to create the "space-charge region", or the depletion region (refer to section 2.1.2). The increase of the bias voltage over the full depletion voltage will strengthen the electric field in the sensor. Thus, the sensor is able to be operated beyond full depletion at stronger electric fields where carriers move faster and result to faster charge collection. The breakdown voltage, at which the value of the leakage current increases exponentially due to the multiplication effect in impact ionization, defines the maximum voltage limit at which the sensor can operate. A measurement of a very early breakdown voltage or higher leakage current than expected indicate a defect in the sensor. The depletion and breakdown voltage values differ from one sensor to the other, but they can be extracted from the IV curve of the sensor.

The leakage current as a function of the bias voltage can be measured at wafer level and at module level. The investigated sensors for this thesis were already assembled into a readout chip and therefore, only results of IV properties at module level are presented. The leakage current I_{leak} level depends on the sensor thickness and temperature (see section 2.1.2). So, unirradiated modules are measured at room temperature, while irradiated modules are measured at -50°C . The leakage current of unirradiated ITk pixel sensor prototypes is expected to be within $5\mu\text{A}$. While irradiated sensors host more bulk defects (see section 2.4.1) that generates a higher leakage current, and so it depends on the fluence.

To perform the IV measurement, the module is connected to a voltage supply e.g., Kiethley 2410 electrometer, as indicated in the characterisation setup (refer to figure 4.1). The electrometer reads the leakage current at each voltage step providing the I-V relation for the sensor. In this procedure two main features must be set; the voltage step and the compliance current. The compliance current provides the safety upper limit measure of the leakage current to reach the breakdown voltage value without breaking the sensor. The increase of the bias voltage improves the charge collection signal in the sensor. But to operate a pixel module safely without breaking it, we must determine its operational limits. Results discussing the IV properties of ITk pixel sensors will be presented in section 6.1.

5.2 EUDET beam telescopes

Beam telescopes are vital tools for R&D projects focussing on position sensitive particle detection sensors. The EUDET project [143, 144] supported by the European Union in the 6th framework program aimed to provide a high-resolution pixel beam telescope for testbeam studies. The EUDET telescope allow an easy integration of custom data acquisition systems achieved by a well defined interfaces on both hardware and software level [144]. Responding to the demands of sensor R&D community, there are several replicas for EUDET-type beam telescopes have been built for the HEP community. Two of

those replicas are introduced in the following: one at CERN testbeam site (section 5.3.1) and one at DESY testbeam site (section 5.3.2).

Coordinate system

Before describing the setup I find it useful to define the global coordinate system used to describe the geometry of the beam telescope. The ITk planar sensor, with its 2D pixel geometry, is defined as shown in figure 5.2(a), the long side pitch is on the x-axis and the short side is on the y-axis, while for the $50 \times 50 \mu\text{m}^2$ it is the same on x- and y-axis. The ITk sensors are produced to match the size of the RD53A

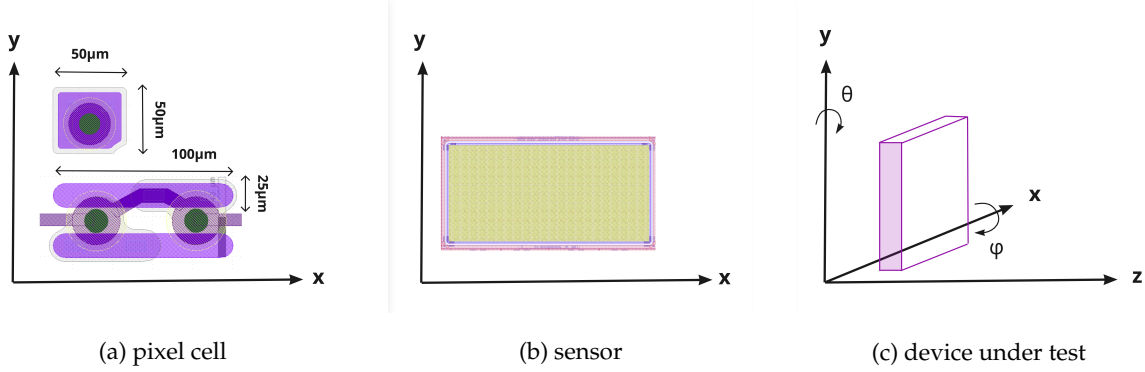


FIGURE 5.2: Coordinate system

readout chip having three different front-end flavors (refer to section 3.2.2). Therefore, the sensors are rectangular, with the long side on the x-axis as shown in figure 5.2(b). The origin point of the testbeam system at zero is the beam axis, which is parallel to the z-axis of the system. The devices under test (DUT) is mounted perpendicular to the beam on the z-axis for particles to have perpendicular incidence on the planes as shown in 5.2(c). The x- and y-axis are perpendicular to the beam horizontally and vertically. In the CERN SPS testbeam hall, x-axis points toward the Jura mountain and y-axis points upwards.

The EUDET beam telescopes [144] are table top tracking detectors as shown in the picture of figure 5.3 featuring six silicon sensor telescope planes. The six telescope planes are organized in two arms; first three planes closer to the beam line are the 'upstream planes', the second three planes down the beam line are the 'downstream planes'. The telescope arms are movable along the z-axis in the direction of the beam in order to allow for variably sized devices to be fitted into the test setup. The DUT is mounted inside a cooling box in between the telescope arms, along with a reference plane in the last position at the end of the down stream arm. The reference module is a known module, it is used to ensure the temporal coincidence between the MIMOSA26 telescope sensors [145]. A MIMOSA event is in the order of $200 \mu\text{s}$ long, while for ITk/IBL detector, the events are shorter in the order of 400 ns ¹. The cooling box details are described in the following sections 5.3.1 & 5.3.2 specifically for each testbeam location.

The sensor planes, upstream and downstream, are enveloped by four scintillators with PhotoMultiplier Tubes (PMT) for triggering, two on each side. A Trigger Logic Unit (TLU) [146] provides time stamp information and trigger logic when a particle passes through, and a data acquisition system EU-DAQ [147] (see section 5.2.1) is connected for the readout. The information from the beam telescope is used to reconstruct the particle trajectory and determine the impact point on the DUT with high resolution. The six telescope planes are equipped with MIMOSA26 sensors that are built with 350 nm CMOS

¹The event cover 25 ns per trigger.

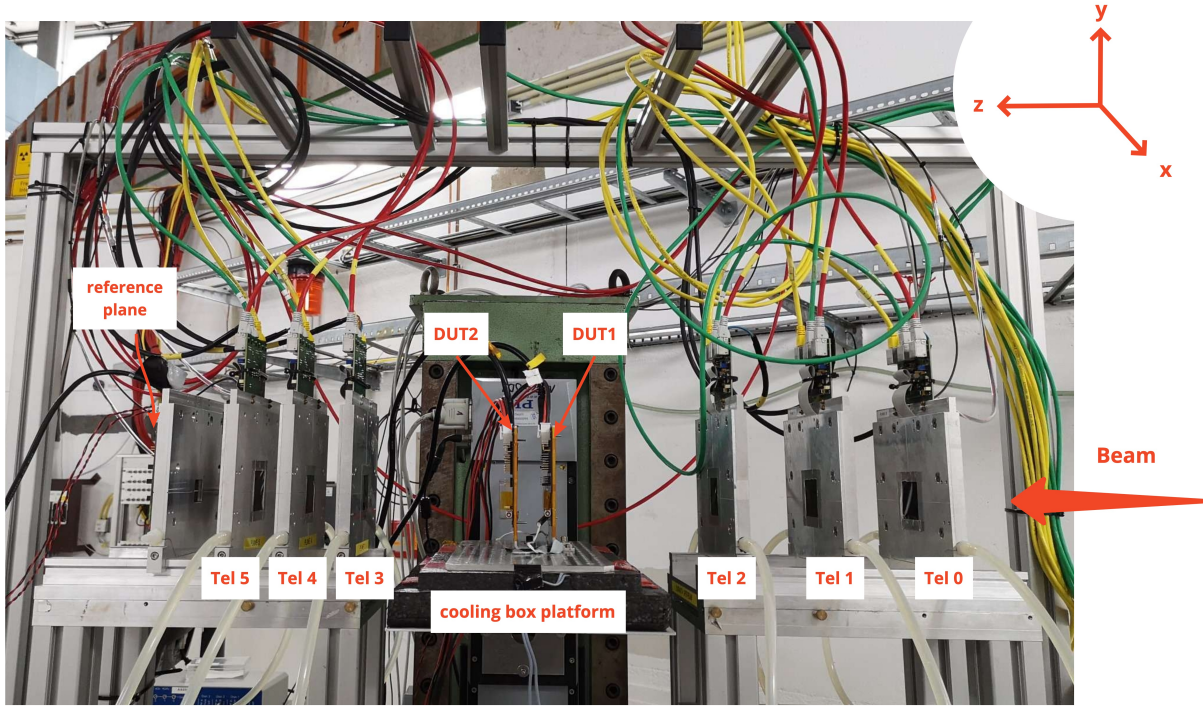


FIGURE 5.3: Picture of testbeam setup with EUDET beam telescope at DESY. The EUDET telescope consists of six sensor planes separated into two arms to fit the DUT in the middle of the telescope

technology to fulfill the EUDET beam telescope requirements of fine granularity, high spatial resolution, and low material budget. A MIMOSA26 sensor have thickness of $50\ \mu\text{m}$. Each sensor has pixel size of $18.4 \times 18.4\ \mu\text{m}^2$, arranged in $1152\ \text{columns} \times 576\ \text{rows}$ making an active area of $21.2 \times 10.6\ \text{mm}^2$. The quoted binary resolution is of $5.4\ \mu\text{m}$ and it is improved by charge sharing [144].

Each sensor is installed in an aluminum jig, three jigs at each arm holding the MIMOSA26 sensor planes are visible in the picture of figure 5.3. The position description of the telescope planes as shown in the figure will be summarised in the geometry file in section 5.4.1. The jigs feature beam window around the sensor minimizing material budget. The sensors are connected to water pipes for cooling. They are protected by a lightproof Kapton foils of $25\ \mu\text{m}$ thick on each side. The total material of the EUDET beam telescope thus amounts to $300\ \mu\text{m}$ of silicon and $300\ \mu\text{m}$ of Kapton[144]. The two scintillators on each side are crossed defining a rectangular acceptance window of $20 \times 10\ \text{mm}^2$ matching the MIMOSA26 sensor active area. The MIMOSA26 sensors are readout with a continuous rolling-shutter mode reading all columns in parallel. This technique allows for correlated double sampling and zero suppression on-chip. At the clock frequency of $80\ \text{MHz}$, the integration time equals $115.2\ \mu\text{s}$. The expected rate of detectable particles through the active area of the beam telescope is estimated to be about $1\ \text{MHz}/\text{cm}^2$ due to the limited on-chip buffer size [144]. The data of all planes are collected in an aggregator board and are then feed into an FPGA in a National Instruments (NI) crate [147].

5.2.1 Data Acquisition software

The data acquisition framework EUDAQ [148] schematically shown in figure 5.4 has been designed and developed to serve as flexible and simple-to-use data taking software for the EUDET-type beam telescopes, allowing for easy integration of devices. It consists of completely independent modules communicating via TCP/IP enabling a distributed data acquisition with modules running on separate machines.

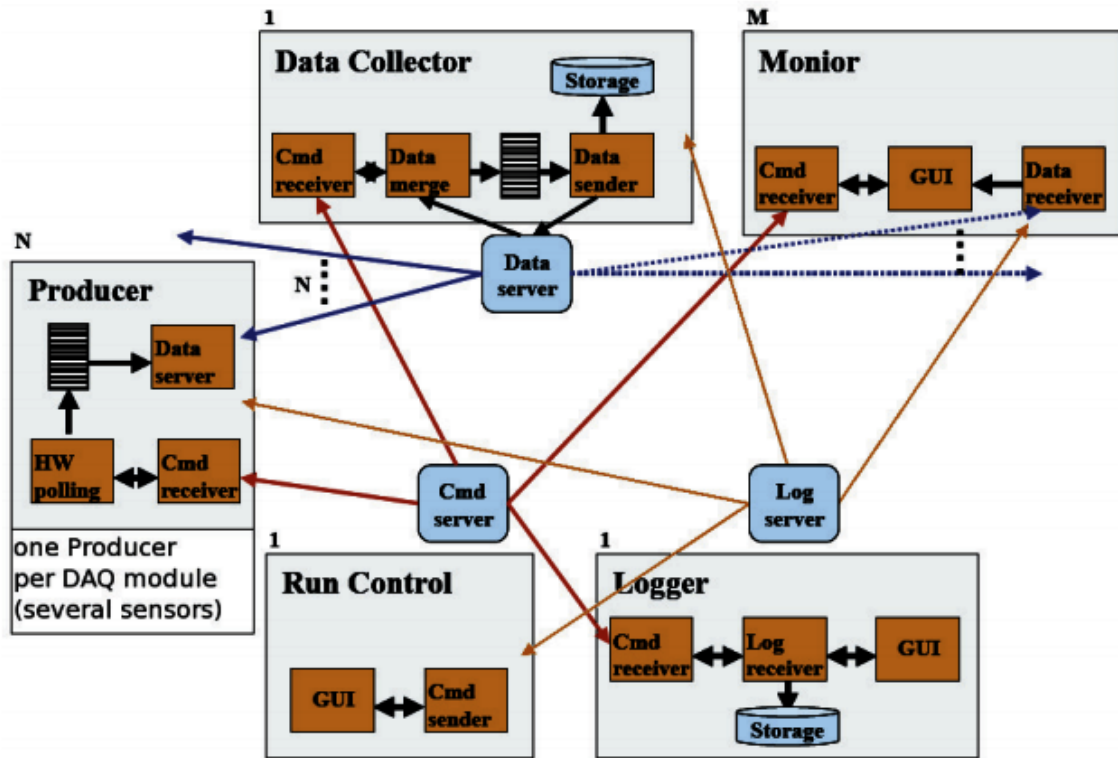


FIGURE 5.4: Data Acquisition software EUDAQ scheme for EUDET beam telescope [147].

A central Run Control displays a graphic interface GUI to the user allowing to control all processes. The Data Collector receives data from the Producers, merging the separate streams into one and writing it to a file. The Producers, e.g. the DUT, communicate with the different pieces of hardware and generate data. For example, the TLU Producer controls the TLU and sends the timestamps to the Data Collector, while the EUDET Data Reduction Board (EUDRB) Producer controls the readout boards and sends the telescope data to the Data Collector [147]. Currently, EUDAQ is designed for synchronous DAQ systems requiring one event per trigger per attached sub-detector system before building the global event. Thus, the trigger rate is always limited by the slowest device. In addition, a Log Collector collects log messages from all other processes into a central location. In parallel, the online monitor reads the data file from disk, generating histograms so that the user may monitor the quality of the data.

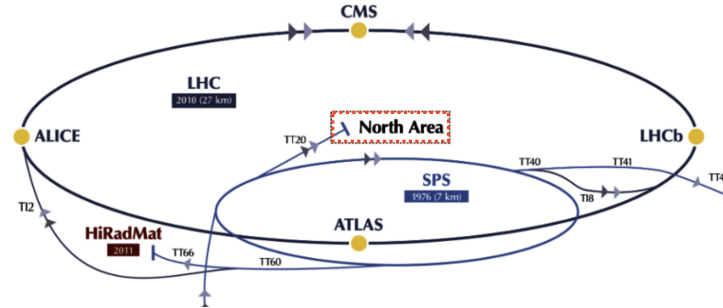
Recent developments of EUDAQ serves the emerging need for running several detectors together with a telescope as one system, this extends the use of EUDAQ beyond its original conception. Therefore, a major upgrade to EQUADAQ2 [149] has been completely rewritten using modern C++ and designed to be even more versatile and usable for an extended range of detectors. EUDAQ2 is freely available [150] and distributed under open-source license. Further details on EUDAQ1/EUDAQ2 hardware and software can be found in [144, 147–149]. A thorough practical documentation is available internal for testbeam users to operate the software.

5.3 Particle beam lines

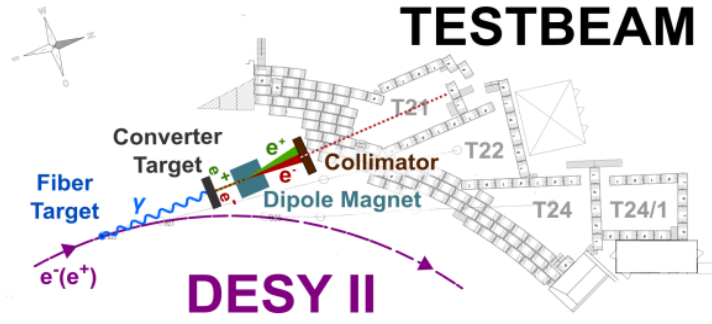
There are few locations that provide high energetic particle beams for the research and development of future detectors and are equipped with the EUDET-like beam telescope. The results that will be discussed

in this thesis were measured in two particle beam facilities:

1. The CERN Super Proton Synchrotron (SPS) [151] section 5.3.1.
2. The Deutsches Electron Synchrotron (DESY) [152] section 5.3.2.



(a) CERN accelerator complex with North area highlighted



(b) DESY testbeam lines

FIGURE 5.5: Schematics of beam test facility area provided at (a) CERN SPS and at (b) DESY.

Figure 5.5 shows schematics of the beam lines at (a) CERN SPS and (b) DESY that provide the testbeam area with high energetic particles. Both beam lines are presented in the following.

5.3.1 CERN SPS

The proton beam at CERN starts from a linear accelerator then it is sent to the LHC pre-accelerator Proton Synchrotron (PS) and then to the Super Proton Synchrotron (SPS). The protons from SPS [153] are accelerated and then ejected out of the circulating beam to induce reactions into a target to feed a pion π^\pm beam to the North hall area. The provided beam has an energy of 120 GeV and intensity of 2×10^8 particles per spill. A typical duration for a spill lasts about 5 seconds with frequency between 14-48 per seconds per spill. The particle type is selected by the magnetic field. Wire chambers and collimator are installed along the beam line to determine the position and width of the beam. Due to the fact that the SPS is the main particle injector of the LHC, the particle beam is not always available for measurements. The LHC was scheduled for its long shutdown at the beginning of 2019 therefore, only two testbeams in October and December 2018 were achieved at the CERN location during this thesis.

There are two EUDET-type beam telescopes installed one after the other on the same beam line available at CERN in the H6 North hall area. This is possible thanks to the negligible multiple scattering effect (see section 5.4.4) at high beam energy of 120 GeV . The high energy rate at CERN also enabled the use of a cooling box made of rather dense material. The cooling box permanently installed at CERN is

developed by the Max Plank Institute of Physics (MPP) in Munich² and is shown schematically in figure 5.6(a). The MPP box is a hermetically sealed box consisting of 1.5 mm aluminum plates from the outside and coated with a 46 mm Polyurethane rigid foam insulation layer from the inside. It is connected to a chiller pumping silicon oil through a custom made heat exchanger equipped with a fan for efficient heat transfer [154]. Temperatures can go as low as -50°C and constantly kept by the chiller and the fan assuring efficient thermal convection. Also, nitrogen is supplied inside of the box in order to avoid condensation at low temperature.

The MPP cooling box can fit maximum of 5 DUTs at the same time, with limited multiple scattering effects thanks to the high energy beam at CERN. Each DUT is mounted on an aluminum jig along the beam line separated by minimum of 20 mm.

5.3.2 DESY

The DESY II synchrotron [152] accelerates electrons and positrons to energies up to 6 GeV. The test beams are generated by a double conversion instead of using a direct extraction of the primary beam in DESY II. Photons are generated by electrons from the injection energy of 0.45 GeV up to full energy of 6 GeV. Initially, bremsstrahlung photons are generated by a fixed 7 μm thin fiber targets, which are installed in a primary target station in the main DESY II beam orbit in order to produce the highest rate of bremsstrahlung photons. These bremsstrahlung photons travel along an extraction beam pipe tangentially to the DESY II orbit and then leave the DESY II vacuum through a 500 μm thick aluminum exit window. They travel through the air for up to 22 m and then hit a secondary target with dimensions of 45 mm \times 60 mm where electrons and positrons are generated through the pair production process. The secondary target station can be remotely controlled by the user to choose from eight different targets allowing the user to adjust the particle rates and yields to their needs. The electrons and positrons then pass through a dipole magnet, depending on the polarity and strength of the magnetic field of the magnet it allows the selection of the particle flavor and momentum. Afterwards the beam of selected particles travel in an evacuated beam pipe that can be collimated to pass the beam shutter to enter the test beam experimental areas. This beam is guided to the experimental areas as shown in figure 5.5(b). Three beam lines are available for three independent experimental halls at DESY. Two of the three experimental halls in DESY are equipped with EUDET-type telescope, details of the area will be explained in detail in the following. The final beam has particle energy between 1-6 GeV, and an intensity up to 1000 particles per cm^2 with a 5% energy spread and an angular divergence of 5 mrad. The intensity is limited by the $1/E$ dependence of the bremsstrahlung spectrum. The energy of the particles is limited to the maximum beam energy of 6 GeV. Thus, due to the low energy, multiple scattering of electrons can not be neglected in DESY. The typical energy selection at DESY testbeam is 5 GeV being a good compromise between rate and energy. The energy plays an important role as the telescope space-resolution deteriorates for low energies due to multiple scattering. Due to the low energy, only two detector planes are measured simultaneously to reduce multiple scattering effects.

The cooling box installed at the DESY facility is a light-weighted cooling box made of PPO³ foam, DoBox, shown in figure 5.6(b). The design and the material of the DoBox were chosen to reduce the material budget as much as possible and maintain high mechanical stability. At the bottom of the box, there is an aluminum board with a grid of M5 threaded holes is provided with 1 cm holes distance to mount the DUTs on it. The DoBox is divided into two compartments separated by thin plastic plate, one chamber houses the DUTs and the other chamber contains dry ice blocks to cool the modules. The

²<https://www.mpp.mpg.de/>

³Poly Phenylene Oxide

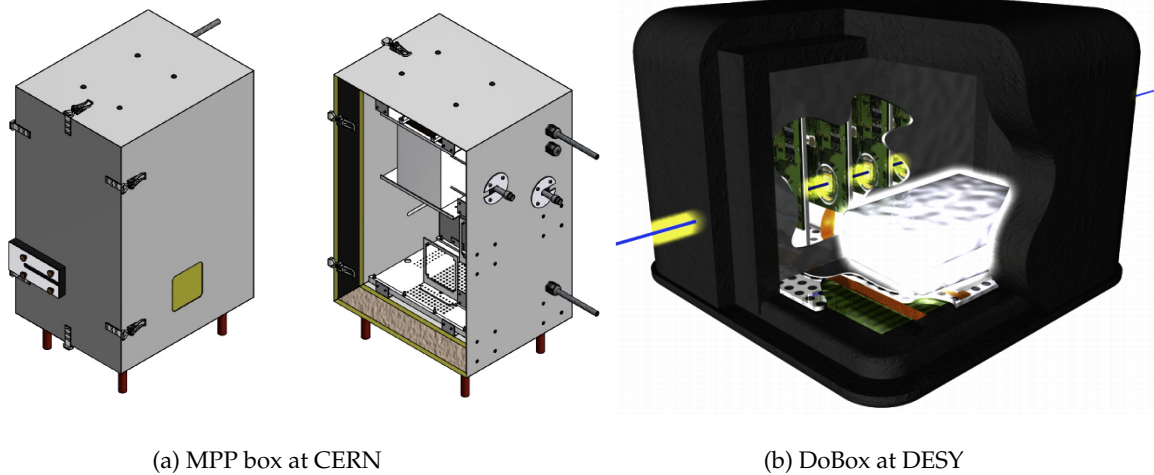


FIGURE 5.6: Cooling boxes installed for testbeams (a) at DESY [155] (b) at CERN.

bottom aluminum plate helps with heat transfer to cool the DUTs. The dry ice is used to realize the cooling without a chiller system. A block of dry ice has a surface temperature of -78°C and lasts for about 10 hours. A constant nitrogen flow is supplied inside the box to maintain humidity at low level to avoid any condensation. Inside the cooling box, the DUTs are mounted on an aluminum jig and fixed accordingly on the bottom aluminum plate in-between the telescope arms. For multiple DUTs, each jig is placed at a minimum distance of 20 mm for the best position resolution.

5.4 Reconstruction and analysis

Beam telescopes as described above provide spatially well-resolved particle trajectories, which are used to investigate sensor technology and test the detector's modules. The study of decay vertices requires accurate reconstruction of events therefore, it is very important to align and calibrate the detector as precisely as possible. The particle trajectories are reconstructed using the testbeam reconstruction modular and comprehensive software framework EUTelescope [156, 157], which is discussed in details in the following. Reconstructed data are further analysed to specific interesting quantities such as hit efficiency and charge-collection efficiency using the post-reconstruction analysis framework Tbmon2 [158] that will be discussed in the following section 5.4.2.

5.4.1 Eutelescope

EUTelescope uses the Modular Analysis and Reconstruction for the Linear Collider (MARLIN) framework, which is part of the International Collider Software package (ILCSOFT) [159]. EUTelescope consists of a set of algorithms called *processors*, which are implemented in the framework to process raw data into tracks. Marlin job consists of the execution of these processors. Each processor will read data from a file, processes it, and outputs a new or modified data. Each step of the reconstruction thus calls a certain set of processors defined and steered by steering files, which are written in XML. The steering file specifies the order of execution of the processors. Individual parameters are written in the processors or passed via the steering file. MARLIN processes data on an event basis, each processor will perform tasks during initialization for each event and after all events have been processed [160]. The reconstruction flow can be divided into five main steps as shown in figure 5.7, that will be individually expanded in the following, each step correspond to a steering file that contains multiple processors. The first step after data

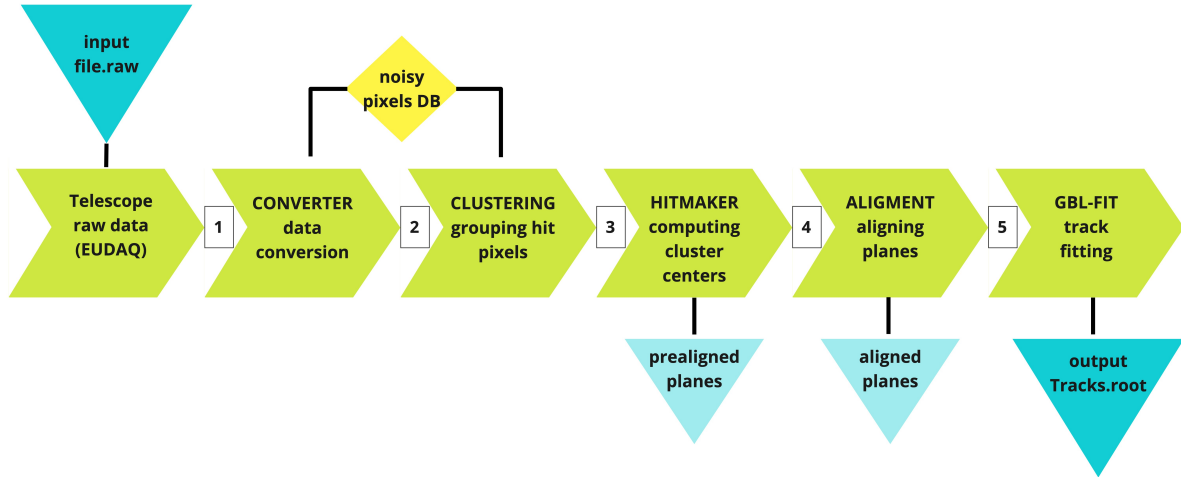


FIGURE 5.7: Scheme of testbeam data reconstruction in EUTelescope framework.

taking, *the converter step* converts the raw data into hits and creates a data bank for all planes to tag noisy pixels, which are pixels that fire at a frequency higher than a certain threshold. The standard setting for the threshold probability is 0.001. This means that if a pixel was hit more than once in 1000 events it is dismissed. Next comes the clustering, in each plane *the clustering step* counts the neighboring pixels which fired at the same bunch crossing, and groups the hits together to form a cluster. The hit coordinates for each cluster is computed in a global frame coordinates. Then *the hitmaker step* transforms the hit positions from its global frame to a local coordinate frame and a first step of pre-alignment is performed. The *alignment step* uses the pre-aligned hits for each plane independently to find tracks in the global coordinates. The alignment procedure modifies the positions of each plane to find a continuous track that can pass through them. The alignment is based on the General Broken Lines (GBL) model [161]. The GBL track model takes into account multiple scattering and measures the transformation matrices from each plane to accurately describe the particle trajectory traversing all the material. In the final fitting step *GBL fit*, the alignment of each plane is applied to the hits, tracks are fitted by minimisation passing through all planes. Each step is further explained in the following and a more thorough documentation for EUTelescope can be found in [149, 162] and for GBL fitting method can be found in [161, 163].

In addition to the steering files, a GEAR file that describes the physical geometry of the setup must be included to define positions, resolution, details of each plane. Also, a general configuration file that links the processors is typically prepared for easier integration of all steps, where config parameters could be passed on to the steering files of each processor. This config file allows to run multiple actions with adjustable configuration in one command instead of running separate commands for each processor in the reconstruction process.

GEAR

The Geometry application program interface for Reconstruction (GEAR) package in ILCSOFT software is used by MARLIN and so it is also part of the EUTelescope framework. The GEAR file is an XML file that specifies the physical geometry for all planes including position, pixel layouts, dimensions, rotation, and thickness. The GEAR file contains a node, or a section with ID number, for each sensor plane, which contains all the information for that specific plane. The positions on the z direction of the telescope planes starts at 0 cm for plane 0. The three planes in one arm are spaced with 10 cm in between them. In

TABLE 5.1: An example of the positions of the beam telescope and DUTs on the z direction for measurement at DESY testbeam facility in June 2020.

reference	Tel 5	Tel 4	Tel 3	DUT 2	DUT 1	Tel 2	Tel 1	Tel 0	plane
835	793	681	571	525	355	222	111	0	z-position [mm]

TABLE 5.2: Details of radiation length for silicon.

layer	material	total thickness [μm]	density [g/cm^3]	radiation length [cm]
Mimosa26 sensors	Silicon	270	2.328	9.37

DESY, between the arms there about 30 cm space to fit in the DoBox, while at CERN its 45 cm to fit in the larger MPP cooling box. For example the geometry of the telescope planes setup including two DUTs in the middle as shown in figure 5.3 is summarised in table 5.1. Also, the radiation length for each sensor is defined in the gear file. The radiation length for each silicon plane is set as $X_0 = 93.66 \text{ mm}$ to count for the scattering angle of each plane. The radiation length details of the silicon hybrid pixel module is summarised in table 5.2. In fact, there are more passive materials that are present in the testbeam setup but not in the geometry file. The study of multiple scattering from passive materials will be thoroughly discussed in simulation results in chapter 7.

5.4.1.1 Converter

The converter performs the initial step of the reconstruction flow. It decodes the raw data files that contains the events triggered by the TLU and converts them into the LCIO format utilized within the EUTelescope framework. Data acquired with EUDAQ framework are converted to event-based collection using EUTelNativeReader processor. The occupancy of all pixels is monitored while converting the hit information from each plane independently. All pixels that signal for more than 0.1% of the triggered events are flagged as noisy pixels and are registered in the noisy-pixel database.

5.4.1.2 Clustering

Within each event, the clustering processor EUTelSparseClustering finds clusters from adjacent hit-pixels. A cluster is defined by hit-pixels next to each other registered in the same event with a high signal to Noise Ratio (SNR) cut, i.e. no noisy pixels in the cluster. The sparse clustering processor groups pixels together based on their x and y indices, which are defined by the user. The distance between

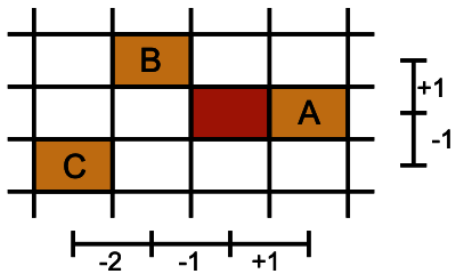


FIGURE 5.8: Example scheme of sparse clustering logic [160]. Assuming the red pixel is the center of the cluster, pixel A is one distance unit away, pixel B is 2 distance units away, and pixel C is 5 distance units away. A cut is applied to define which pixels to include in the same cluster.

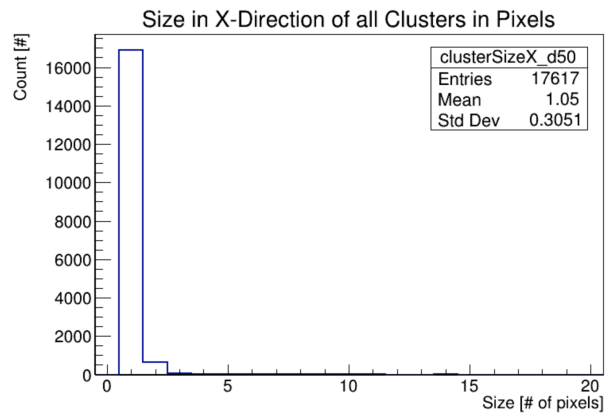


FIGURE 5.9: Mean cluster size in x-axis for a 50 μm thick sensor with pixel pitch of 50 \times 50 μm^2 .

hit-pixels is computed in index space, which is the distance in pixel index squared in arbitrary units. Illustrating by example from figure 5.8 starting from the red pixel as the center of the cluster, the distance to pixel A is 1 distance-unit-squared away from the center. Pixel B is 2 distance-units-squared away from the center, and pixel C is 5 distance-units away. The distance units defines the actual cuts on the hit-pixel. Therefore, a cut value of 1 will include only pixel A into the cluster, while cut value of 2 will include pixels A and B into the same cluster, and similarly cut value of 5 will include pixels A, B and C into the same cluster. In typical clustering process a cut of 2 is applied on the hit-pixels. Thus, pixels with a distance smaller than 2 will be grouped together into one cluster. The Clustering processor generates histograms showing the mean cluster size on x- and y-axis for each plane. Figure 5.9 shown an example cluster size on x-axis for a $50 \mu\text{m}$ thick sensor with pixel pitch of $50 \times 50 \mu\text{m}^2$. The figure shows mean cluster size of 1.05, which means that most clusters include pixels only to the first neighbor (pixel A).

5.4.1.3 Hitmaker

The hitmaker step converts the clusters to hit information, it finds the corresponding cluster centers from the clustering step and creates a collection of hits. The hitmaker reads the geometrical parameters of the planes from the GEAR file. Accordingly, the hit coordinates are transformed from the local coordinate frame of each pixel to the global coordinate frame of the telescope. With this local to global frame transformation, the position of each plane is identified by the EUTelPreAligner on the x- and y-axis as shown in figure 5.10(a&b) respectively. The peak in the histogram shows that all hits are centered around zero on the particular axis, which means that the position of the plane was accurately found as described in the gear file. In case the geometry of the pixel or the orientation of the sensor did not match the description in the gear file, the hitmaker will not be able to transform the correct position of the sensor in global coordinates and the hits will be distributed equally on the axis contrary to what is visible in the the pre-aligner histograms of figure 5.10. The hitmaker pre-aligns the planes with few hundred μm

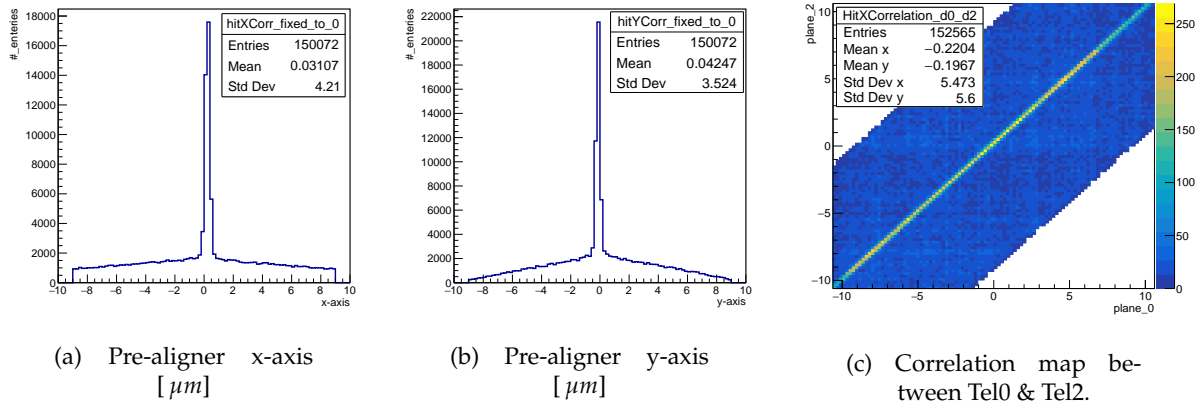


FIGURE 5.10: The pre-aligner and correlator histograms of the Hitmaker step. (a) the pre-aligner on the x-axis shows all hit centered at zero, which indicate that the correct position of the plane in μm has been successfully transformed into global telescope coordinates, (b) the pre-aligner on the y-axis, and (c) the correlator map is an overlap of the pre-aligner histogram on one axis and shows the aligned hits between two planes, a diagonal line with maximum number of hits from top right to bottom left indicate good alignment of the planes.

precision and the mean value of the position where the most of the hits correspond is centered at zero for both x- and y-axis. Shifted pre-align distributions on the axis indicate that the plane is shifted relative to the telescope global coordinates. With this transformation the correlation information between successive planes is also obtained by the EUTelCorrelator as shown in figure 5.10(c) The correlator maps the axis from two successive planes, e.g. plane Tel0 & Tel2, the correlation in the figure demonstrated by

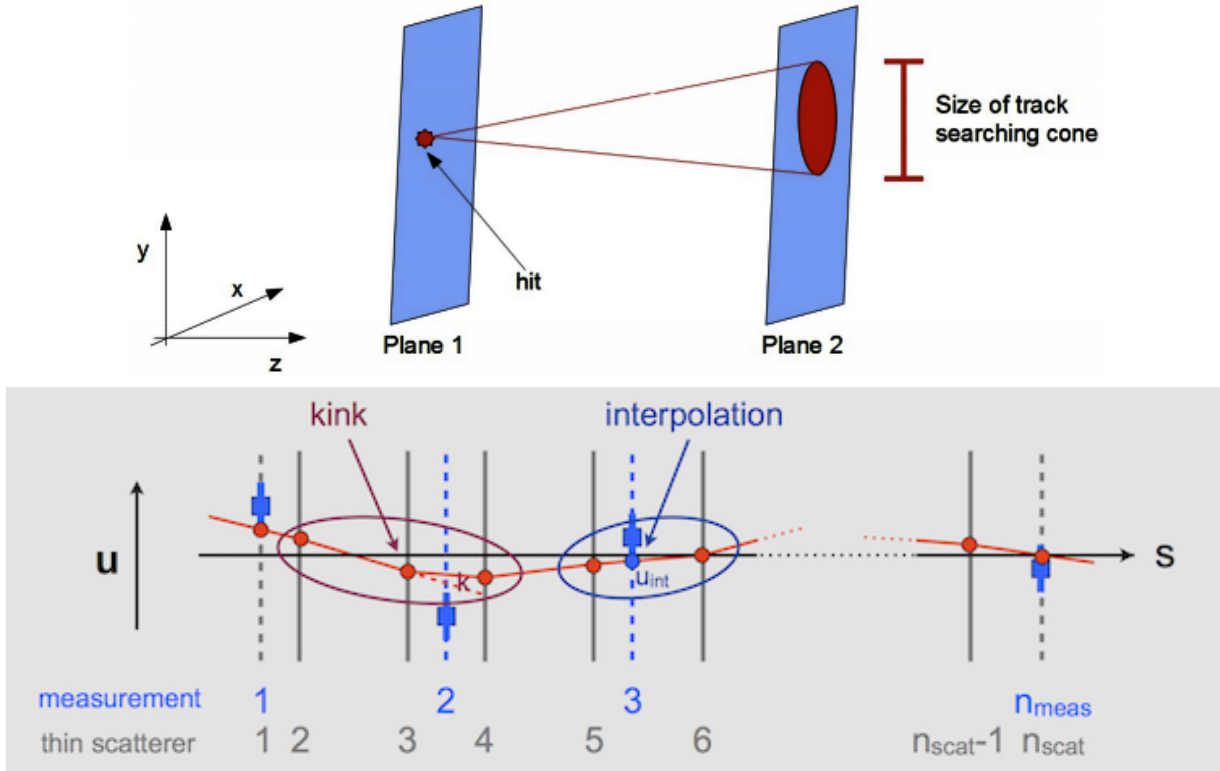


FIGURE 5.11: Schematics of trajectory reconstruction with general broken lines model [165].

the maximum number of hits in the yellow diagonal line from top right down to left bottom shown that the two planes have transformed global coordinates correctly. In the case that rotation information of the plane was not defined correctly, or the local to global coordinate transformation was not successful, there will be no uniform hit distribution or no hits at all showing in the correlation.

5.4.1.4 GBL-Align

The GBL method allows for a proper description of multiple scattering through layers of scatterers, or planes. It is mathematically equivalent to the Kalman filter [164] but computationally different. The alignment step in EUTelescope uses the EUTe1GBL processor for a pattern recognition algorithm that selects hits belonging to the same physical track. The processor expects the geometry of the beam telescope consisting of six sensors grouped into an upstream and downstream triplets with x-, y-, and z-direction as defined in the coordinate system. Two telescope planes are set fixed in global position frame, while the other telescope planes are aligned according to the track center. From the origin hit point, an initial zero value, a cone is propagated onto the next consecutive plane as shown in the top illustration of figure 5.11. The diameter of the searching cone is the residual cut defined at $200\ \mu\text{m}$, which is the maximum allowed distance between a hit and a candidate track between the two consecutive planes. Each plane is a thin scatterer that deviates the track from the origin hit with a scattering angle k^4 . For each triplet, three points are measured, one on each plane, creating three broken lines as shown in the bottom illustration of figure 5.11 with a kink in the middle. A straight line is calculated from the three points creating a slope between the first and the last plane of the triplet, which are called the doublet. Doublets with a slope within a $3.0\ \text{mrad}$ cut are selected, and the distance between the doublets and the hit on the central plane is calculated. As shown in the figure, if the hit position is within the cut of the slope (circulated in

⁴In EUTelescope outputs its called the kink angle, it is based on the material budget of the plane

blue) the triplet position is validated. If the hit position is outside the defined cuts (circulated in red) the positions of the planes are further iterated. Then, the track trajectory from the upstream and downstream triplets are extrapolated to the center of the beam telescope to be matched with hits on the DUTs. If the distance of the extrapolation to the hit position on the DUT is within a residual cut of $500\text{ }\mu\text{m}$, the hits are grouped to form a track. As the DUT planes are unbiased, the position of the plane is corrected by interpolation from the broken line fit on the triplets. The corrections on the plane position are measured to have the residual distribution centered around the hit origin, then it is output in a modified GEAR file for the next alignment iteration. With these modifications, the residuals are minimized fitting the track closer to the hit origin. The residual distributions show the FWHM of the difference between the position of the candidate track and the hits on the same plane. An example of a residual distribution for a $50 \times 50\text{ }\mu\text{m}^2$ pixel geometry plotted in figure 5.12 showing an average of $21.5\text{ }\mu\text{m}$ as the difference of the interpolated track on the x-axis of the plane minus the position of the associated cluster ($x_{hit} - x_{trk}$). The

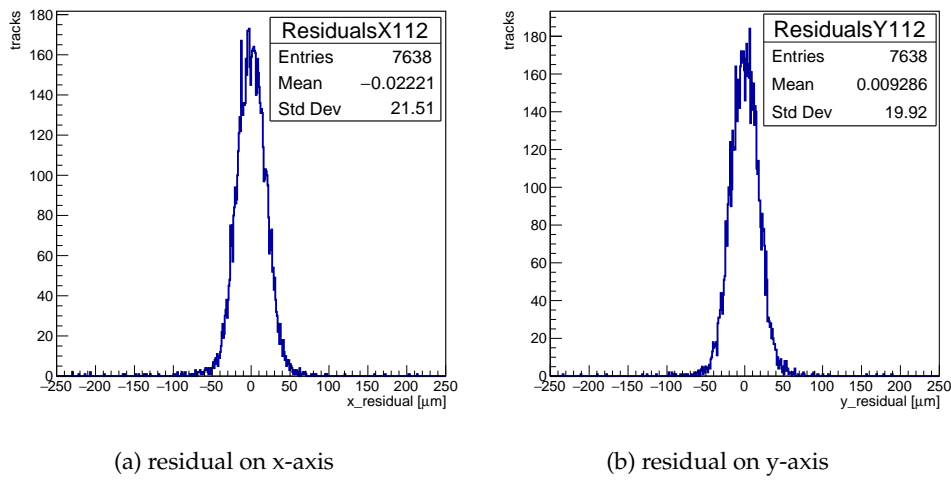


FIGURE 5.12: Residuals of GBL-align step for a module with $50 \times 50\text{ }\mu\text{m}^2$ pixel geometry.

alignment procedure only corrects the positions of the planes to constrain the residual distribution to be centered around zero, i.e., the position of the hit, and outputs the new corrected measurement in a new GEAR file. In case the alignment parameters do not converge closer to the hit position, the alignment is iterated few times (typically 3). The iterations start from the previous aligned position of the planes to minimise the distance of the extrapolated track to the position of the hit.

5.4.1.5 GBL-fit

The final step of the reconstruction, the GBL-fit, uses the same alignment procedure to fit tracks on the DUT planes from the pool of extrapolated tracks through the telescope planes. Assuming that the telescope planes are already aligned from the previous step, the GBL-fit applies the last modification of positions to fit the tracks on the DUTs. A maximum χ^2 value, which measures the quality of candidate tracks, is defined for all fitted tracks.

In the GBL-fit steering file, the user is able to include/exclude DUT planes. Only when the DUT planes are specified the material budget of the plane is included in the fitting of the tracks and hence, the multiple scattering is estimated accordingly.

Contrary to the GBL-align, the GBL-fit does not correct the positions of the scatterers any more but rather outputs the hit collections and fitted data collection in a ROOT file. The output ROOT file includes

all the track information, hit position, kinks and angles, and residuals on each plane. Residuals from this

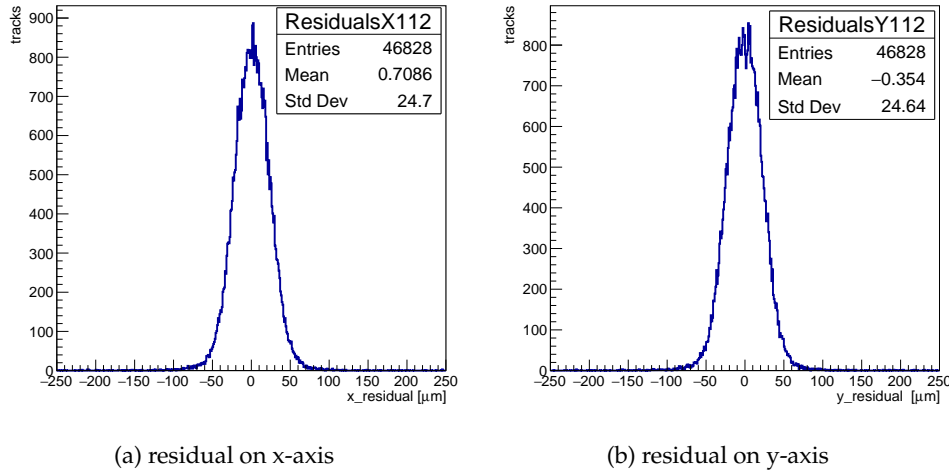


FIGURE 5.13: Fitted residuals of GBL-fit step for a module with $50 \times 50 \mu\text{m}^2$ pixel geometry.

fitting step are shown in figure 5.13 for x- and y-axis. They have a little wider standard deviation than the alignment step because it convolutes the pointing resolution of the telescope, effects of multiple scattering, and its binary resolution. A more detailed discussion on the residuals and spatial resolution is presented in the following.

A remark for EUTelescope, the software is no longer maintained by the developers. Therefore, the baseline choice of track reconstruction for testbeam data for ATLAS is switching to the Corryvreckan software [166], which is developed and maintained by DESY. Corryvreckan is highly versatile software developed to cater the needs of the testbeam community for a new generation of silicon detectors and for the diversification of the R&D programs. The software works the same described chain logic for track reconstruction fitting with General Broken line method with more flexible configurations. And is able to further analyze the efficiency results of the device. In a study comparing results between EUTelescope/Tbmon2 and Corryvreckan [167] shows very similar performance from both softwares making them compatible. Corryvreckan still does not substitute Tbmon2 with graphical and user-defined offline analyses.

5.4.2 Tbmon2

Tbmon2 [158] is an offline analysis framework for post-reconstruction. It was chosen to be the official analysis tool for all IBL, 3D, planar and diamond testbeams and is still in use for ongoing analyses [162] for ITk pixel studies. Tbmon2 uses as input file the same ROOT output from EUTelescope reconstruction, which contains the hits and track positions and all relevant information to perform the DUT analysis. The versatile interface of tbmon2 allows for the integration of user-defined analyses. The central set of information is built up consisting of matched hits and cluster properties. In this step, hits are matched with tracks, which are identified as "good tracks", and tracks with no corresponding hit are tagged as "bad tracks" and recorded as inefficiency. Tbmon2 studies quantities such as hit efficiency, in-pixel efficiency, residuals, cluster size, efficiency as function of columns and rows, the efficiency of different pre-defined regions of each sensor and other efficiency related quantities. These observables demonstrate the sensor's performance and are discussed in the following.

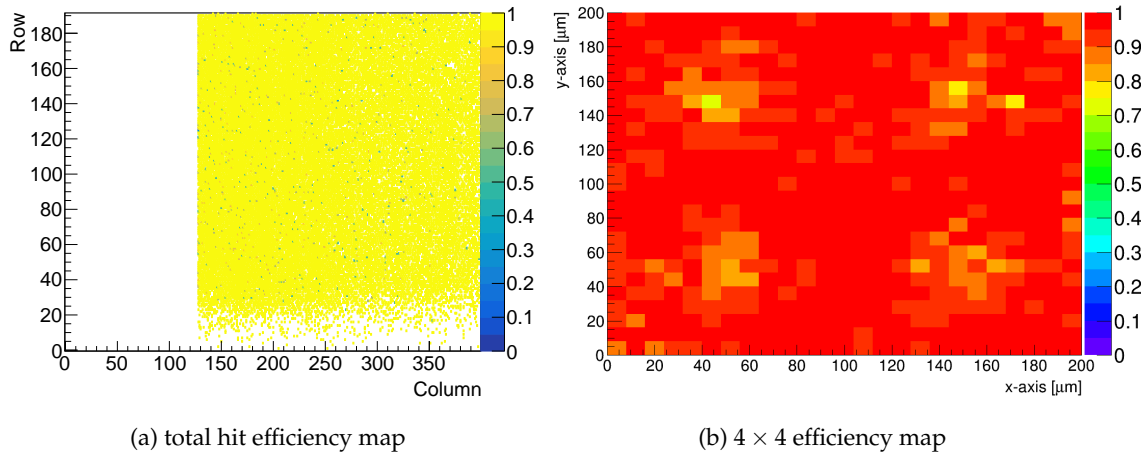


FIGURE 5.14: Example for Tbmon2 efficiency results for a $50 \times 50 \mu\text{m}^2$ module (a) shows the total hit efficiency map showing good tracks across the pixel matrix, (b) in-pixel hit efficiency map where tracks are folded into 4×4 pixels showing inefficiency in position of punch through dots.

Hit Efficiency

One of the most interesting properties of a device in testbeam measurements is the hit efficiency. The hit efficiency of the sensors is defined as the ratio of the number of reconstructed tracks with matching hits as shown in figure 5.14(a) to the total number of reconstructed tracks which are passing through the sensor,

$$Eff = \frac{\text{number of hits matched to a track}}{\text{number of reconstructed tracks}}. \quad (5.1)$$

The statistical uncertainty is the binomial error given by

$$\sigma(Eff) = \sqrt{\frac{Eff \times (1 - Eff)}{\text{total number of tracks}}}. \quad (5.2)$$

For this calculation only in-time tracks that go through the central region of the sensor and pass the applied χ^2 cut are considered. In-time tracks are tracks from hits triggered within 25 ns through the trigger scintillator area and matched with clusters within a given matching radius [162]. Shown in figure 5.14(a) is the total hit efficiency map for a RD53A module showing tracks passing through the sensor matrix $192 \text{ row} \times 400 \text{ col}$. The map is only active for the linear and differential front-end, the synchronous was disabled and hence no measurement is visible in that region. The hit map shows good tracks with efficiency up to 100% in yellow and bad tracks with no matching hits with lower efficiencies.

In-pixel efficiency

The in-pixel hit efficiency is obtained by superimposing the 2D map of efficiency as a function of the local position in each pixel cell of the sensor. The efficiency of each track is folded into an analogous position on the $n \times n \text{ pixel}$ efficiency map. This 2D map in figure 5.14(b) is a visual representation of the efficiency in the sensor, which indicate the homogeneity of the charge collection, stressing the presence of low efficiency areas due to permanent biasing structures or charge sharing between pixels. In the 4×4 efficiency map of figure 5.14(b) we can see low efficiencies specifically in 4 positions mapping the PT in the biasing structure of the sensor. The PT attracts the charge and so efficiency loss is observed in the region. The granularity of this analysis is of the order of the total pointing resolution (sum of the telescope resolution and the multiple scattering).

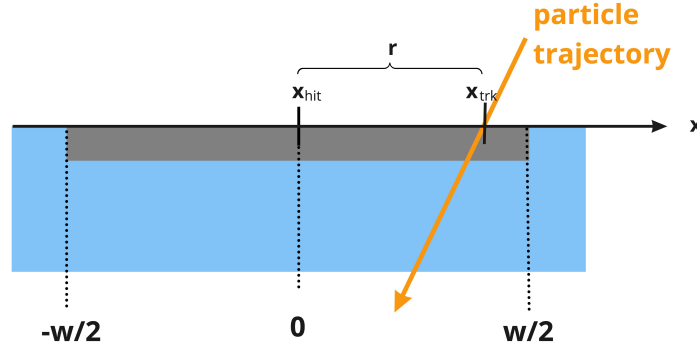


FIGURE 5.15: Definition of hit position x_{hit} , track position x_{trk} , and residual r in a segmented detector with segmentation width w .

5.4.3 Residuals

The study of the residual distribution gives valuable information on the spatial resolution of the sensor. Hit residuals along a generic x direction are defined as the difference r between the position of the measured hit x_{hit} and the fitted track position x_{trk} on the detector plane along the same axis as shown in figure 5.15 and defined by

$$r = x_{hit} - x_{trk}. \quad (5.3)$$

The binary residual width of one pitch can be calculated by

$$residual\ width\ [\mu m] = \frac{pitch\ [\mu m]}{\sqrt{12}}. \quad (5.4)$$

For a segmented detector, the standard deviation of the residual distribution, i.e. residual width⁵, depends on three main contributions:

1. the intrinsic resolution of the sensor⁶
2. the pointing resolution of the telescope planes, depending on the pitch and alignment of the set of planes w.r.t. the sensor.
3. the amount of multiple scattering, depending on the material budget in the setup.

In the following equations the multiple scattering effect is included in the pointing resolution. There are biased and unbiased tracks in the track fitting procedure. Biased tracks are built using hits from the same plane, in our case from the telescope planes and the DUTs as well. While unbiased tracks are built using hits only from the telescope planes. Residuals from biased tracks are called biased residuals, and residuals from unbiased tracks are called unbiased residuals. In the reconstruction for all data in this thesis, telescope residuals are biased, and DUT residuals are unbiased. The residual distribution from biased tracks r_{bias} depends on the intrinsic resolution of the sensor, and the pointing resolution of the set of planes. The squared width of the bias residual is:

$$\sigma_{r_{bias}}^2 = \sigma_{int}^2 - \sigma_{pointing}^2 \quad (5.5)$$

As the hits from the DUTs were not included to build the tracks therefore, the DUTs have unbiased residuals r_{unbias} . The squared width of the unbiased residual depends on the intrinsic resolution and

⁵in literature it is defined as the spatial resolution

⁶The intrinsic resolution of the sensor can be better than the binary resolution of the pitch when the average cluster size contains more than one pixel indicating some charge sharing between pixels.

pointing resolution by:

$$\sigma_{r_{unbias}}^2 = \sigma_{int}^2 + \sigma_{pointing}^2. \quad (5.6)$$

The residuals set the expectations for the quality of data after track reconstruction where the intrinsic resolution is calculated, the effects of multiple scattering can be estimated from material budget, and the pointing resolution of the telescope should remain the same for the same setup.

The residuals follow a distribution according to a certain probability density function $P(r)$ that depends on the segmentation, particle characteristics, and tracking characteristics. The convolution of the resolution effects can be approximated by a gaussian distribution centered at the hit position x_{hit} . The resolution of the detector is the standard deviation σ of the residual distribution that is denoted as the residual width r . In an ideal residual, assuming uniform track distribution dN_{trk}/dx over the detector with negligible effects on the resolution ($\sigma \approx 0$), the residual distribution $P_{ideal}(r')$ is

$$r' \sim P_{ideal}(r') = \frac{1}{w}, \quad r' \in [-w/2, w/2], \quad (5.7)$$

where w corresponds to the width of the region from which carriers generate clusters as shown in figure 5.16(a) for pixel cluster size = 1 and figure 5.16(b) for cluster size = 2. [h] Considering realistic situation

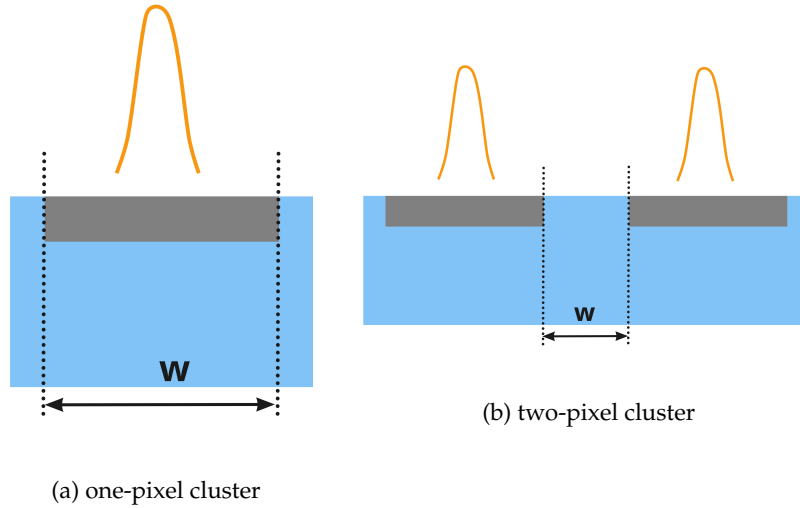


FIGURE 5.16: Example of segmentation width w shows hit formed in case of (a) single readout channel hit, (b) two neighboring readout channels firing.

of sizeable resolution effects, the convolution of the residual function $P_{ideal}(r')$ will give us the observed residual distribution,

$$P(r) = \int_{-w/2}^{w/2} dr' \frac{1}{w} \frac{1}{\sqrt{2\pi}\sigma} e^{-\frac{(r'-r)^2}{2\sigma^2}} = \frac{1}{2w} \left[\text{Erf} \left(\frac{w/2 - r}{\sqrt{2}\sigma} \right) - \text{Erf} \left(\frac{-w/2 - r}{\sqrt{2}\sigma} \right) \right] \quad (5.8)$$

In the case that the resolution is much smaller than the region between two electrodes ($\sigma \ll w$) the convolution of the residual distribution will look like a flattened gaussian as shown in figure 5.17(a), which looks like a constant line in the center for all segmentation while the tails extend to have the shape of the error function. The resolution in this case is closer to the binary resolution described by residual width in equation 5.4. In the case that the resolution is larger than the segmentation width ($\sigma \gg w$) the residual distribution curves more into a gaussian shape as shown in figure 5.17(b). The charge sharing in

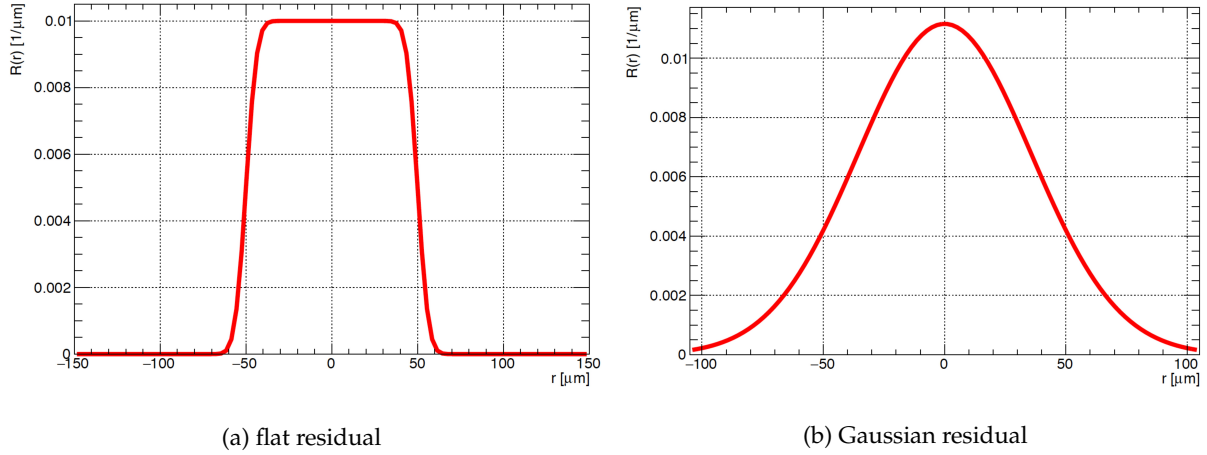


FIGURE 5.17: Example residual distributions calculated from equation 5.8 (a) flat residual distribution when $\sigma \ll w$ for $w=50 \mu m$ and $\sigma=3 \mu m$, and (b) Gaussian residual distribution when $\sigma \gg w$ for $w=100 \mu m$ and $\sigma=5 \mu m$.

a segmented detector occurs in the area between two pixel, which is narrower than the pixel pitch, consequently the spatial resolution for two-pixel cluster is better than for one-pixel cluster. The resolution in this case is closer to the intrinsic resolution of the sensor.

In the case of our investigated detectors, effects of tracking and multiple scattering are not negligible and thus, we observe Gaussian residuals as shown in the reconstruction alignment example of section 5.4.1 in figure 5.4.1.4. Similar discussion about hit residuals can be found in [74]. Residuals are important to study as they ultimately assess the spatial resolution performance of the DUT. The residuals will be further investigated from testbeam data and simulation to quantify the contribution of multiple scattering. With low energy beam, the contribution from multiple scattering is dominant.

5.4.4 Multiple scattering

A charged particle passing through a medium is deflected by many small-angle scatters forcing it to diverge from its trajectory. This divergence is due to Coulomb scattering from the nuclei. The angular scattering distribution is centered around zero and the standard deviation depends on the particle energy, particle type, and the radiation length of the matter traversed. For Silicon the radiation length is $X_0 = 93.66 mm$. The Coulomb scattering distribution is roughly Gaussian for small deflection angles, but at larger angles it behaves like Rutherford scattering, having a larger tail than does a Gaussian distribution. The root mean square (RMS) of the multiple scattering θ_{plane}^{RMS} through small angles at one layer of a particle with atomic number z and momentum p can be parameterised by [72]

$$\theta_{plane}^{RMS} = \frac{13.6 MeV}{\beta c p} z \sqrt{\frac{x}{X_0}} \left[1 + 0.038 \ln\left(\frac{x}{X_0}\right) \right], \quad (5.9)$$

where βc is the velocity, and $\frac{x}{X_0}$ is the thickness of traversed medium x in radiation length X_0 . The effect of multiple scattering increases drastically for low energies and large material budget $\frac{x}{X_0}$. Equation 5.9 describes the scattering from a single material while in reality the particle traverse many different layers. Since the equation follows a fit from a Molière distribution [168], it is incorrect to add the individual θ contributions in quadrature, the result is systematically too small. It is much more accurate to apply the equation once, after finding x and X_0 for the combined scatterers. The effects of multiple scattering from testbeam setup is further expanded on in comparison to simulation in chapter 7.

Conclusion

In this chapter I introduced the tools to characterise the modules of the pixel detector. The electrical characterisation of the pixel module requires a table top setup to measure the current-voltage (IV) relation of the sensor to define the operational limits of the module. The performance of the detector is estimated based on the performance of the hybrid modules. The modules are characterised with a particle beam in a testbeam setup that requires the EUDET beam telescope for high tracking precision, a data acquisition system, and a dedicated track reconstruction and analysis softwares to analyse the results. The hit efficiency of the pixel module is the main qualifier parameter of the performance of the device, while hit residuals indicate the resolution of the performance and hence the quality of the results. ITk pixel modules are characterised under realistic environment which will reach to fluence up to $\Phi = 1 \times 10^{16} n_{eq}/cm^2$ in the inner layer. Therefore, pixel modules are characterised before and after irradiation. Modules can be irradiated in different facilities. The irradiation facilities that are relevant in this thesis are described in Appendix C. Each facility provides a different irradiation beam energy and type, which could affect the performance of the module.

The performance of irradiated modules will be discussed in chapter 6. While in chapter 7 I will discuss in further details the hit residuals and multiple scattering produced from the testbeam. The residual results indicate the quality of measurement, they are compared with the simulated performance of the testbeam setup to lay down some predictions of the pixel module performance.

2763 *“An expert is someone who has made all the mistakes that can be made in a very narrow field.”*

2764 Niels Bohr

Chapter 6

Performance of planar pixel modules



FIGURE 6.1: Mounting modules in DESY testbeam facility to be characterised with 5 GeV electron beam. Results in this chapter are produced from this setup.

In this chapter I present the characterisation results of planar pixel modules and discuss their performance according to the ITk requirements. The performance of the module depends on its hit efficiency measured with the particle beam. The hit efficiency results are discussed in this chapter to understand the physics behind them and to set the threshold for pixel modules to be qualified for the production of the ITk pixel detector.

The ITk R&D prototype sensors were designed and fabricated as discussed in section 2. These sensors are assembled to the RD53A readout chip discussed in chapter 3. Before characterising the modules with a particle beam the threshold is tuned as discussed in chapter 4. Afterwards, the modules are characterised with particle beam in a testbeam setup as described in chapter 5 and shown in the picture of figure 6.1. The modules were measured before and after irradiation, they were irradiated in one of the irradiation facilities presented in Appendix C to study their performance under realistic conditions. In section 6.1 I discuss the electrical properties of pixel modules before and after irradiation. In section 6.2 I present the performance of the planar pixel modules. First I discuss the resolution of the beam telescope and the investigated modules, then present the hit efficiency. To best illustrate the performance and status of the investigated modules, the results are divided in three sections based on the sensor production.

- In section 6.2.1 I present the performance of ITk R&D pixel modules. In this section I discuss all the properties that impact the efficiency of the module before and after irradiation.

- In section 6.2.2 I present the results from the ITk planar pixel module Market Survey (MS) -anonymously- and discuss the status and overall qualification of ITk pixel modules.
- In section 6.2.3 I present the results of 50 μm thin sensors for future colliders. The performance of these modules are discussed before irradiation only.

In the last section of this chapter, section 6.3, I discuss the impact of thickness from all production runs. Finally I conclude the chapter with a summary from all the results for ITk planar pixel modules and the 50 μm thin planar pixel modules.

6.1 Electrical characterisation

Sensors are characterised for their electrical properties by measuring the current-voltage (IV) relation to determine their operational limits and how the sensor design affects the IV characteristics. The measurement of the leakage current as a function of the bias voltage allows to assess the sensor's breakdown voltage V_{bd} . The V_{bd} value defines the maximum voltage value for the sensor bias. A fully depleted region with high electric field contributes to the carriers' speed and the formation of the charge signal (see section 2.1.2). In the following, the presented IV curves are studied for the R&D of ITk pixel modules before and after irradiation in section 6.1.1. Afterwards, the IV curves for future thin pixel modules with 50 μm thick sensors are also investigated before and after irradiation in section 6.1.2. Both productions of modules host sensors that were produced for LPNHE¹ by FBK².

6.1.1 ITk R&D pixel module

The LPNHE R&D pixel sensors were produced from two 6 inch wafers with thickness 100 μm and 130 μm [169]. After dicing, the qualified sensors are attached to the RD53A readout chip (see section 3.2.2) to make a prototype of ITk planar pixel module. The current-voltage (IV) characteristics of an unirradiated module shown in figure 6.2 in Blue. The figure shows the IV curve for W398_1 module that host a 130 μm thick sensor with $50 \times 50 \mu m^2$ pixel geometry with no PT in the biasing structure using the temporary metal technique (see section 2.3.2). The figure shows the IV curve before irradiation in Blue and after irradiation in Red for the same module. The IV measurement before irradiation was performed in room temperature (20°C) with a compliance for the leakage current set at 5 μA as an upper limit. The leakage current is generated by the charge carriers in the depleted region, so sensors with wider depletion volume generate more leakage current than thinner sensors. Unfortunately, only few bias voltage steps were taken before the module got irradiated and there is no record of the break down voltage value. We can observe from the IV curve that the operational limits reaches about 140 V before irradiation where the sensor is in over-depletion.

After irradiation, the leakage current and the breakdown voltage of the sensor increases considerably. Irradiated modules are expected to operate at higher bias voltage and also generate higher leakage current according to the current-related damage proportionality factor α (see section 2.4.1.2). The module was irradiated at Birmingham irradiation facility (see Appendix C.2) to fluence $\Phi = 1.7 \times 10^{15} n_{eq}/cm^2$. This measurement was performed inside the cooling box in the DESY testbeam setup (see section 5.3.2) at $-50^\circ C$ with low nitrogen flow to maintain humidity of the environment. The leakage current after irradiation is constantly increasing reaching a value of about 16 μA at 600 V. We can observe how the level of leakage current after irradiated is about 200% higher than before irradiation. The leakage current

¹<http://lpnhe.in2p3.fr>

²<https://www.fbk.eu/en/>

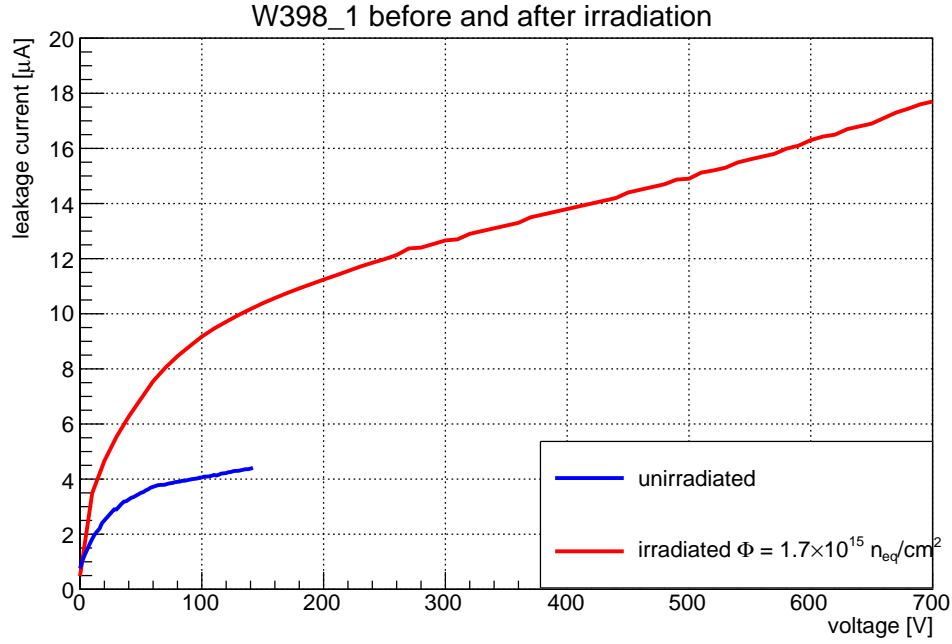


FIGURE 6.2: IV curve for a RD53A module W398_1 with $130\ \mu\text{m}$ thick sensor $50 \times 50\ \mu\text{m}^2$ pixel geometry without PT before and after irradiation to fluence $\Phi = 1.7 \times 10^{15}\ \text{n}_{\text{eq}}/\text{cm}^2$ at Birmingham university. Before irradiation the module was measured at room temperature and after irradiation it is measured at -50°C .

has a linear dependence on the depleted volume, which is expected after irradiation. Irradiated modules must be operated at low temperature to prevent thermal runaway and keep low leakage current. Maintaining a low leakage current during measurement is an indication of low noise level to ensure a smooth operation of the module. The operational range of the module is defined from full depletion, typically when the leakage current is linear and stable, up to the breakdown voltage. The breakdown voltage of the irradiated module extends the operational limit beyond 700 V. The measurement was stopped at 700 V not to risk breaking the module.

6.1.2 Thin pixel modules

In this section I present the electrical properties for RD53A modules hosting $50\ \mu\text{m}$ thin sensors and employ a pixel geometry of $50 \times 50\ \mu\text{m}^2$ [170, 171]. Reduced sensor thickness leads to reduced leakage current and require lower bias voltage for operation. Thinner sensors also lead to an increased radiation tolerance. They suffer less bulk damage after irradiation, and so they are considered as R&D for future colliders such as the Future Circular Collider (FCC) [172]. Since the breakdown voltage value V_{bd} and IV distribution depends on the sensor biasing structure design, in figure 6.3 I present a comparison of the IV characteristics between the biasing structure designs for RD53A modules hosting $50\ \mu\text{m}$ thick sensors. There are two design characteristics to be compared, the guard ring (GR) width around the pixel matrix and the PT design in the biasing structure as depicted on top of the figure. The guard rings functionality is to control the potential at the edges of the sensor, a wider strip of guard rings would be able to control the decrease of higher potential gradient coming out of the last pixel column/row. Thus, a larger GR width of $450\ \mu\text{m}$ would allow the sensor to operate at higher bias voltage values before reaching their breakdown limit, but a large width of guard rings would also minimize the active area around the sensor. The width of the guard rings becomes more important after irradiation when a higher voltage is required to fully deplete the sensor.

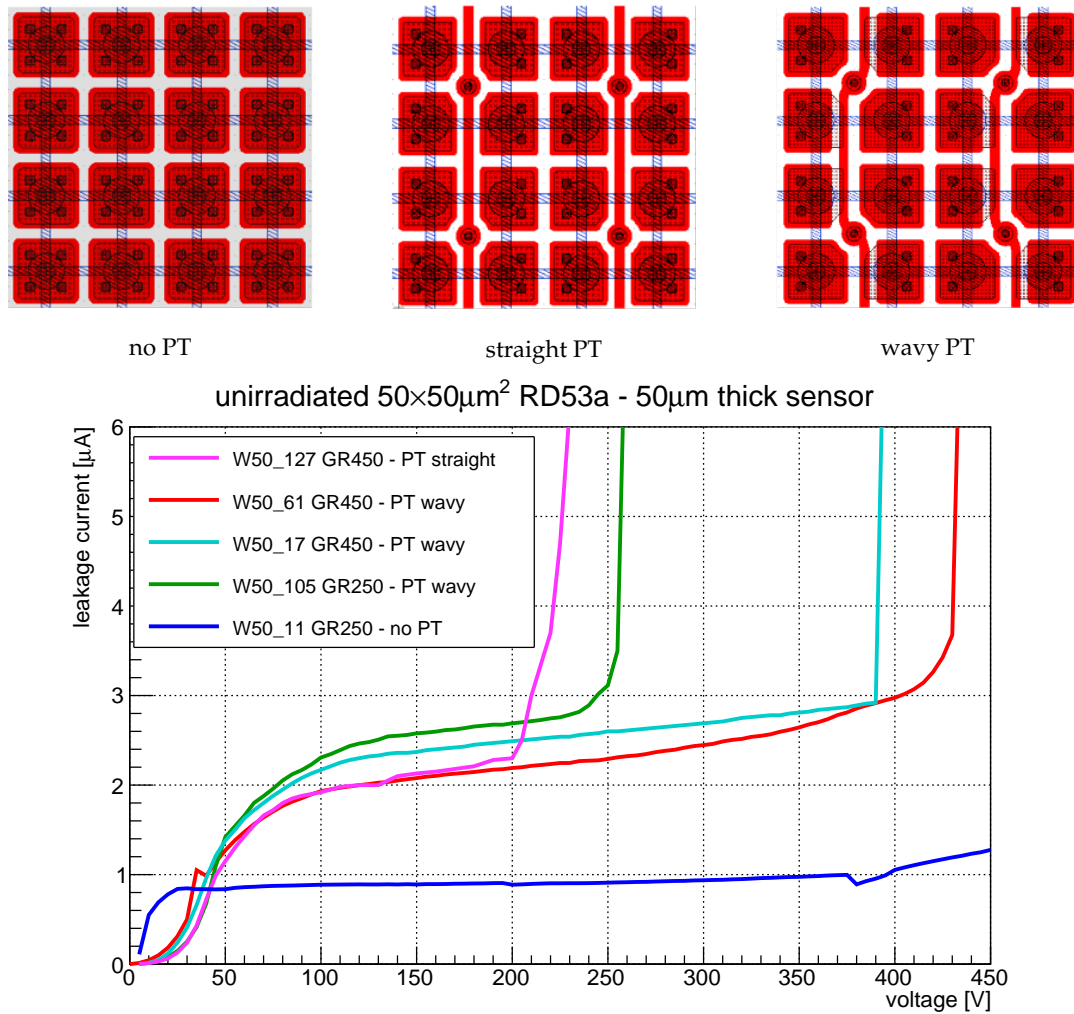


FIGURE 6.3: IV characteristics for unirradiated modules hosting $50 \mu\text{m}$ thick sensors with two different guard ring widths and biasing structure designs. (top) layout of investigated pixel sensors, (bottom) the IV characteristics of thin pixel sensors.

The IV characteristics of *W50_61* plotted in **Red** and module *W50_17* plotted in **Cyan** with $450\ \mu\text{m}$ wide GRs and wavy PT, we observe leakage current between $2 - 3\ \mu\text{A}$ and an operational limit around an average of $410\ \text{V}$. For the IV curve in **Red**, the sensor reaches $V_{bd} = 430\ \text{V}$, and for the IV curve in **Cyan** the sensor reaches $V_{bd} = 390\ \text{V}$, which define the operational limits of the sensors. A higher supply of voltage would create an avalanche of e-h pairs generating high leakage current that will overheat and break the sensor.

The IV characteristics of *W50_127* sensor also with $450\ \mu\text{m}$ wide GRs that employs a straight PT biasing design, plotted in **Pink**, the sensor generates leakage current within the same range of about $2\ \mu\text{A}$, but due to the larger number of PTs in the straight PT biasing design (see section 2.3.2) the charge overflows faster to the edges of the sensor and results in an earlier breakdown. The breakdown voltage for the sensors with $450\ \mu\text{m}$ wide GRs and PT straight reached $V_{bd} = 200\ \text{V}$.

The IV characteristics of *W50_105* sensor with $250\ \mu\text{m}$ thick guard rings around the pixel matrix and a wavy PT design in the biasing structure, plotted in **Green**, we observe that the sensor is able to be operated only up to $250\ \text{V}$. The lower V_{bd} value is due to the thin GRs around the pixel matrix that can not sustain high voltage coming from the last pixel col/row. Typically unirradiated sensors are operated at bias voltages below $200\ \text{V}$, higher breakdown voltage values are achieved from sensor design features of the PT and GRs.

The IV characteristics for the *W50_11* sensor with $250\ \mu\text{m}$ thick guard rings and no PTs in the biasing structure design, plotted in **Blue**, the sensor shows lowest leakage current within $1\ \mu\text{A}$. While the leakage current mainly depends on the thickness of the sensor, *W50_11* shows about half the value for the same thickness in comparison to all other sensors. This is perhaps because the IV measurement was performed at lower temperatures with nitrogen flow in the cooling box before data taking and without powering the chip. While in the log book during data taking an average leakage current of $2.8\ \mu\text{A}$ at $50 - 100\ \text{V}$ is recorded. Leakage current at this level shows that the module agrees with the rest of sensors at the same thickness.

To sum up, sensors with guard ring structure around the pixel matrix control the electric potential at the edges of the matrix, wider guard ring structure plotted in **Red** & **Cyan** allows for a smooth decrease of the potential at high bias voltage and hence increasing the operational range of the sensor. While the sensor with straight PT plotted in **Pink** shows a dominant effect on the GRs of decreasing the break down voltage value to similar range as the sensor with only $GR250\ \mu\text{m}$ plotted in **Green**. the sensor with no PT plotted in **Blue** shows the highest operational limits.

After irradiation it is expected for the leakage current to increase due to the damages in the sensor's bulk. Figure 6.4 show the IV characteristics of two modules hosting $50\ \mu\text{m}$ thick sensors that employ a pixel geometry of $50 \times 50\ \mu\text{m}^2$ that were irradiated at the Birmingham irradiation facility (see Appendix o fluence $\Phi = 5.3 \times 10^{15}\ n_{eq}/\text{cm}^2$ and measured at -50°C without powering the chip. Both sensors differ only in biasing structure design, one employs wavy PT and the other has no PT as depicted in the figure. For comparison, the same sensors are plotted in the same colors before and after irradiation. The leakage current for both sensors as expected is higher after irradiation, they show double the leakage current reaching $10\ \mu\text{A}$ at $400\ \text{V}$. Afterwards, the leakage current is increasing with increasing bias voltage. Thin sensors have smaller depleted volume and are expected to generate less leakage current in comparison to thicker sensors. The operational limits after irradiation considerably increases as observed in the figure for a sensor with wavy PT, plotted in **Green**, the breakdown voltage goes up to $V_{bd} = 600\ \text{V}$ which is $+350\ \text{V}$ increase in comparison to its breakdown voltage before irradiation in figure 6.3. For the irradiated sensor without PT, plotted in **Blue**, we observe a smooth breakdown at about $V_{bd} = 500\ \text{V}$. A sensor employing a biasing structure exhibits a sharper breakdown properties than a sensor without any

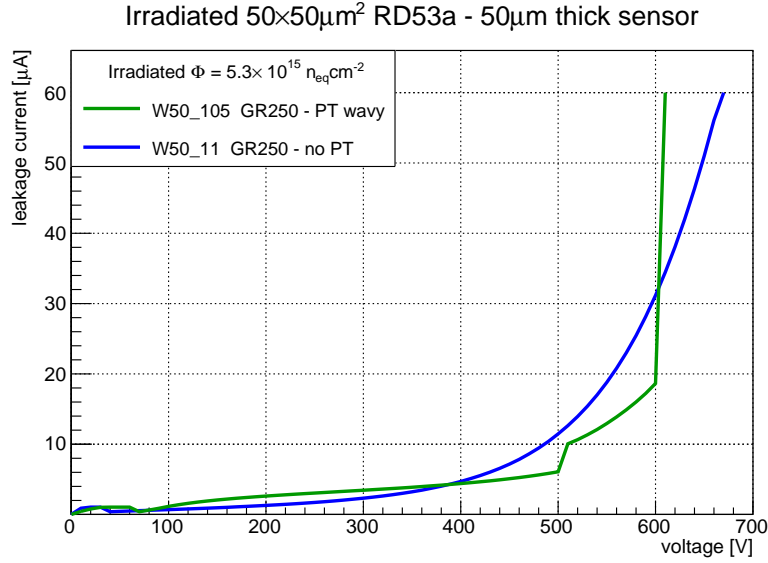


FIGURE 6.4: IV characteristics of RD53A modules hosting $50\ \mu\text{m}$ thick sensors Irradiated to $\Phi = 5.3 \times 10^{15}\ n_{eq}/\text{cm}^2$. Both sensors are measured at -50°C without powering the chip.

aluminum structure on its surface.

In summary, the leakage current properties of thin sensors are expected to be below $5\ \mu\text{A}$ at 20°C (room temperature) before irradiation and up to $10\ \mu\text{A}$ at -50°C after irradiation, keeping in mind that the leakage current increases as a function of fluence (see section 2.4.1.2). The operational limit before irradiation starts after depletion and is typically measured with bias voltage up to $200\ \text{V}$ after full depletion, even if the sensor's limits extends beyond. While after irradiation, modules are typically measured with bias voltage up to $600\ \text{V}$. The biasing structure employed on the sensor limits the operational voltages of the module by inducing an earlier breakdown. In combination with the width of the guard rings structure around the pixel matrix, which increases the breakdown voltage value, a compromise on the design can be chosen based on the requirements for the sensors.

6.2 Performance of planar pixel modules

After the initial IV measurements and readout chip calibration to operate the pixel modules, modules are examined with a particle beam (see chapter 5) to measure their performance under realistic conditions. The modules are measured before and after irradiation in the testbeam setup as shown in figure 6.1. The presented results throughout this thesis are obtained from perpendicular incident tracks mimicking the central region of the detector close to the interaction point. All investigated modules are assembled with the RD53A readout chip. They will be presented here in three categories according to their production runs:

1. R&D ITk planar pixel modules, in section 6.2.1, which are LPNHE modules that employ sensors with thickness $100\ \mu\text{m}$ and $130\ \mu\text{m}$ and were produced by FBK.
2. Planar pixel modules for Market Survey (MS) campaign, in section 6.2.2, which are produced anonymously from six different foundries and are measured to be qualified for ITk preproduction. These modules employ sensors with thickness $100\ \mu\text{m}$ and $150\ \mu\text{m}$.

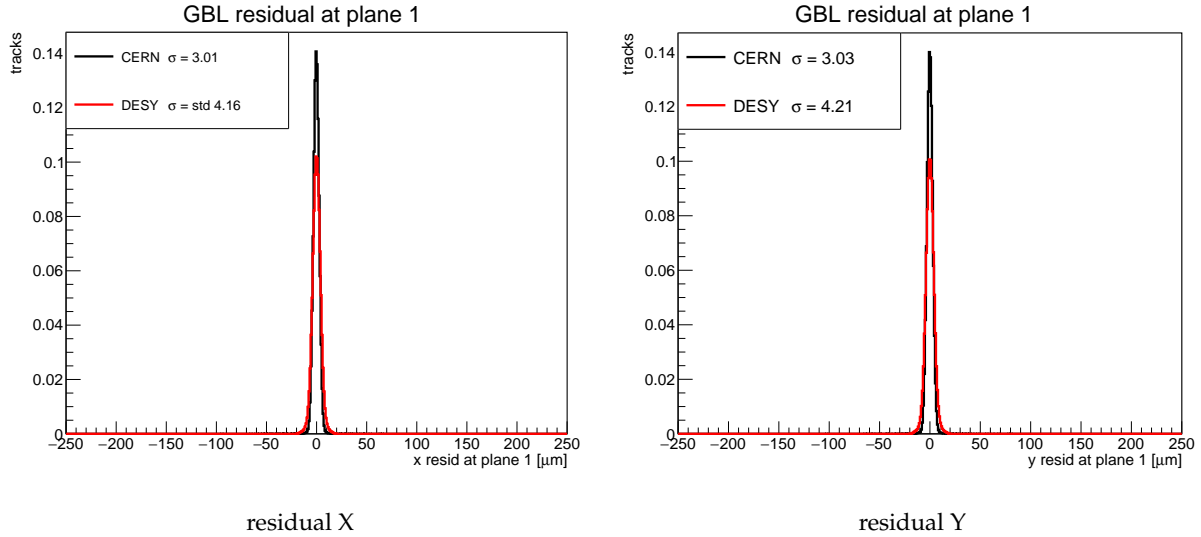


FIGURE 6.5: Superimposed residual of fitted tracks for EUDET beam telescope plane 1 measured at CERN (Black) with particle beam energy of 120 GeV and at DESY (Red) with particle beam energy of 5 GeV. RMS width indicates the pointing resolution of the plane having $\sigma = 3 \mu\text{m}$ at CERN and $\sigma = 4 \mu\text{m}$ at DESY.

3. Thin sensors for future colliders, in section 6.2.3, which are studied as R&D for future colliders.

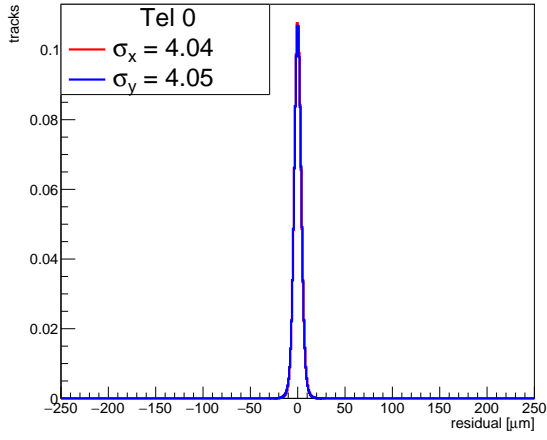
These are LPNHE modules employ sensors with 50 μm thickness and were produced by FBK.

The spatial resolution of the telescope and of the modules are presented prior to the efficiency results. The hit efficiency results from each production are presented in the following sections in the same order. The hit efficiency of the pixel modules is studied as a function of several impacting parameters, such as bias voltage, threshold, fluence, and biasing structure. The effects of these parameters are mainly discussed in the R&D of ITk modules in section 6.2.1.

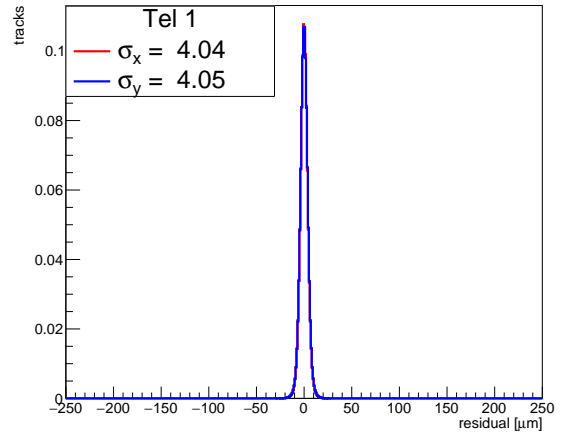
Spatial resolution

The study of the hit efficiency of the modules require good understanding of the track reconstruction that leads to these results. Tracks from all presented results were reconstructed using EU Telescope software (refer to section 5.4.1). The precision of the reconstructed tracks is indicated from the residual width of the extrapolated tracks. The residual width indicate the contribution from the binary resolution of the device itself, folded with the pointing resolution of the setup as described by equation 5.5 for biased residuals. The contribution of multiple scattering in the residuals is expected to be different between results measured at the DESY testbeam facility with 5 GeV particle beam and at the CERN testbeam facility with 120 GeV particle beam. And for different setups the pointing resolution of the telescope is expected to slightly differ. A comparison on the spatial resolution from both facilities on the investigated modules is discussed here.

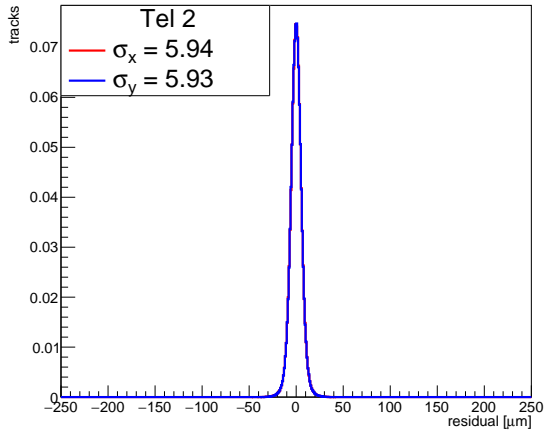
As shown in figure 6.5 the EUDET beam telescope plane 1 achieves residual width of $\sigma = 3 \mu\text{m}$ measured at CERN testbeam, where multiple scattering is negligible. Superimposed in the same figure with the residual from the same plane measured at the DESY including the cooling box and a distance of about 10 cm between the telescope planes, the residual width is higher than $\sigma = 4 \mu\text{m}$. To remind the reader the pixel geometry of the telescope is $18.4 \times 18.4 \mu\text{m}^2$. The telescope planes are measures in a similar telescope geometry between DESY and CERN testbeam setup w.r.t to plane positions (refer to table 5.1). The difference between the particle beam energy increases multiple scattering for lower energies and results into larger residual widths.



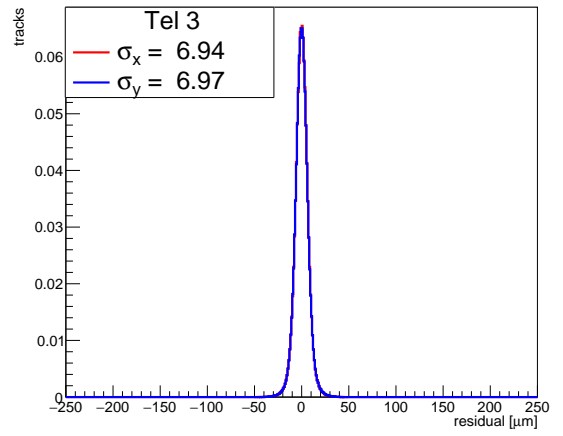
(a) Tel 0



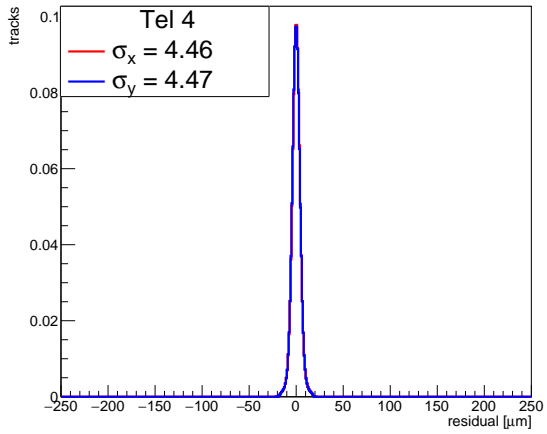
(b) Tel 1



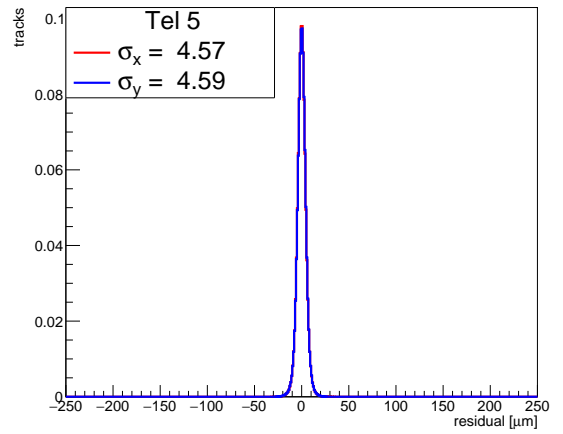
(c) Tel 2



(d) Tel 3



(e) Tel 4



(f) Tel 5

FIGURE 6.6: Residuals for EUDET telescope planes from ITk pixel module MS campaign measured at DESY with particle beam energy of 5 GeV . Residuals on x and y-axis are superimposed for the same telescope plane.

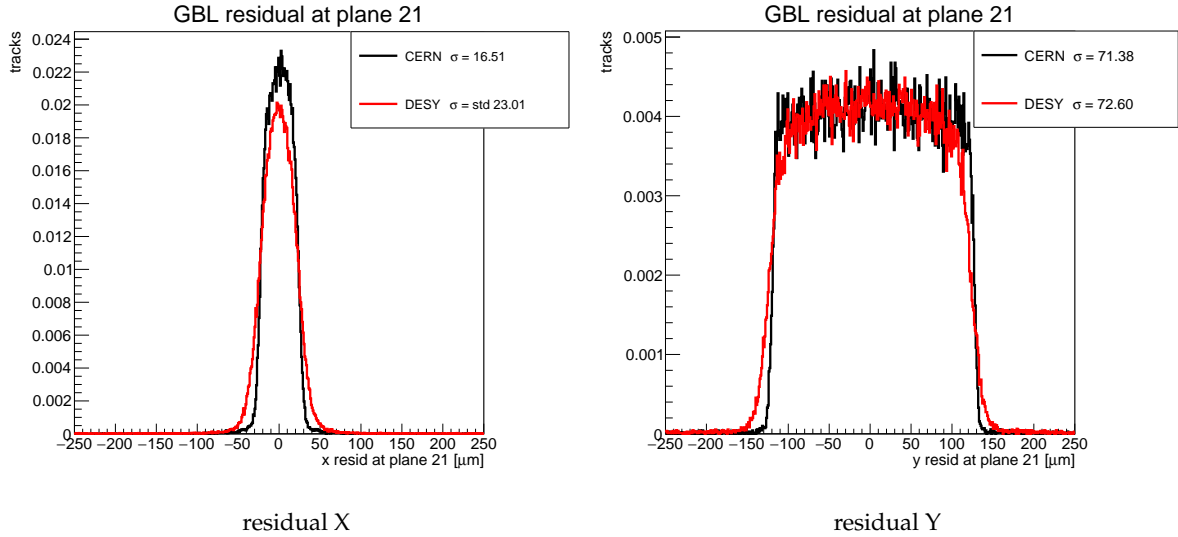


FIGURE 6.7: Superimposed residuals of fitted tracks for FE-I4B reference plane measured at CERN (**Black**) with particle beam energy of 120 GeV and at DESY (**Red**) with particle beam energy of 5 GeV. The residual width indicates the spatial resolution of the plane.

Figure 6.6 shows the residuals from all six telescope planes for both x- and y-axis superimposed. To remind the reader, all telescope planes have biased residuals (refer to section 5.4.3). The residual width decreases due to the increase of the pointing resolution for the telescope planes as discussed in equation 5.5. So, telescope planes 0, 1, 4, 5 show intrinsic resolution better than the binary resolution of the pitch ($\sigma_{binary} = 5.1 \mu m$). The higher residual width of planes 2 and 3 indicate high deflection angles close to the unbiased DUT planes. The minimization of the residual width around the biased planes are due to the GBL method, which corrects for scattering angles from the included material budget. The residuals of the telescope planes will be further discussed in the next chapter in comparison with simulation results.

The included unirradiated FE-I4B reference plane in the testbeam setup serves as an in-time reference for the hits³. A good spatial resolution for the reference plane is important to ensure no efficiency loss due to lost hits. Shown in figure 6.7 the residuals of an FE-I4B module measured at CERN with particle beam energy of 120 GeV and at DESY with particle beam energy of 5 GeV, the two residuals are superimposed for comparison. The short pixel side on the x-axis has residual width of $\sigma = 16.5 \mu m$ at CERN and $\sigma = 23.0 \mu m$ at DESY, which folds the resolution of the DUTs and multiple scattering effects. While the long pixel side on the y-axis has residual width of $\sigma = 71.3 \mu m$ at CERN and $\sigma = 72.6 \mu m$ at DESY. The residual distributions are centered around 0, which indicate that the plane is well aligned on both x- and y-axis. The residual width results are compatible with the binary resolution for $50 \times 250 \mu m^2$ pixel cell. The residuals of the beam telescope and reference plane can both be a reference check to validate the results of the DUT.

In the DESY testbeam setup, only two DUTs are measured at a time keeping the distance between them at minimum to minimise the impacts of multiple scattering from low beam energy. Using equation 5.4 to calculate the binary resolution of a pixel pitch for an ITk sensor, the calculated resolutions are summarised in table 6.1. The binary resolution sets the expectation for one pixel pitch, while the standard deviation of the residuals give the spatial resolution of the segmented detector, i.e. all pixels, that are convoluted with a Gaussian and multiple scattering effects (also see discussion on residuals in section

³It is also possible to use two DUTs to reference each other, in this case the efficiency calculation will depends solely on the DUTs.

TABLE 6.1: Summary of the binary resolution values for each pitch for ITk sensors. Values calculated from equation 5.4.

pitch [μm]	binary resolution [μm]
25	7
50	14
100	28

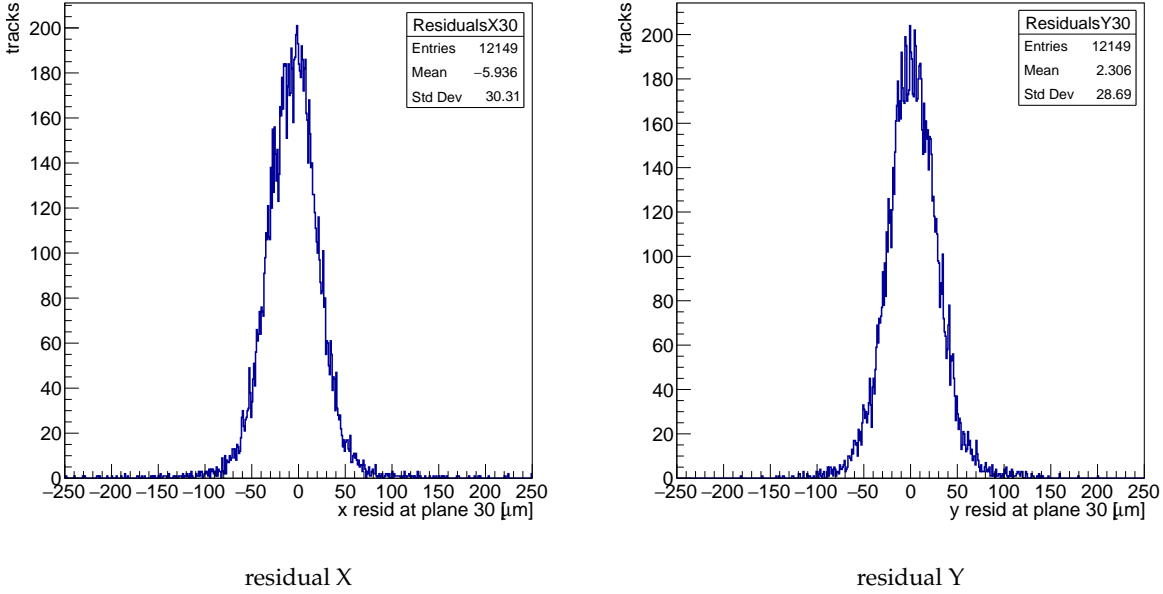


FIGURE 6.8: Residuals of fitted tracks for an ITk module W398_2 with $50 \times 50 \mu\text{m}^2$ pixel geometry measured at the DESY with particle beam energy of 5 GeV. The residual width shows an average of $30 \mu\text{m}$ for both x- and y-axis.

2973 5.4.3).

2974

2975 Shown in figure 6.8 the X and Y residuals for W398_2 module, an unirradiated ITk module hosting
 2976 a $130 \mu\text{m}$ thick sensor employing a pixel geometry of $50 \times 50 \mu\text{m}^2$ measured at DESY. The residuals on
 2977 both x- and y-axis are similar, they both show almost double the expected RMS. This large residual
 2978 width is a contribution from the pointing resolution and multiple scattering at 5 GeV. The shape of the
 2979 residual is convoluted with a Gaussian distribution folding tracks that are passing on all planes and
 2980 including hits from two pixel clusters. The residual distributions show non-zero mean value, which
 2981 means that their alignment is slightly off with $-5.9 \mu\text{m}$ on the x-axis and $2.3 \mu\text{m}$ on the y-axis. This
 2982 misalignment is probably due to slight changes in the position of the whole cooling box during data
 2983 taking. The misalignment decreases the number of good tracks from the data set but should not affect
 2984 the hit efficiency of the module, rather only the visible resolution of the 2D hit efficiency map.

2985 As for an ITk module hosting a $100 \mu\text{m}$ thick sensor with pixel geometry $25 \times 100 \mu\text{m}^2$ measured at
 2986 CERN with particle beam of 120 GeV, the X and Y residuals are shown in figure 6.9. With high energy
 2987 particle beam the resolution of the detector shows residual width much closer to the intrinsic resolution.
 2988 The residual on the x-axis for the $100 \mu\text{m}$ pitch shows residual width $\sigma = 28.7 \mu\text{m}$, while on the y-axis
 2989 for the $25 \mu\text{m}$ pitch shows $\sigma = 11.2 \mu\text{m}$. The values on the figures are in mm. The X residual distribution
 2990 shows a mean value of $2.1 \mu\text{m}$, which means the alignment is slightly off on the x-axis, while the mean
 2991 value of Y residual distribution around 0 shows that the plane is well centered on the y-axis.

2992 We can observe from figures 6.8 and 6.9 that tracks produced from lower energy particle have wider

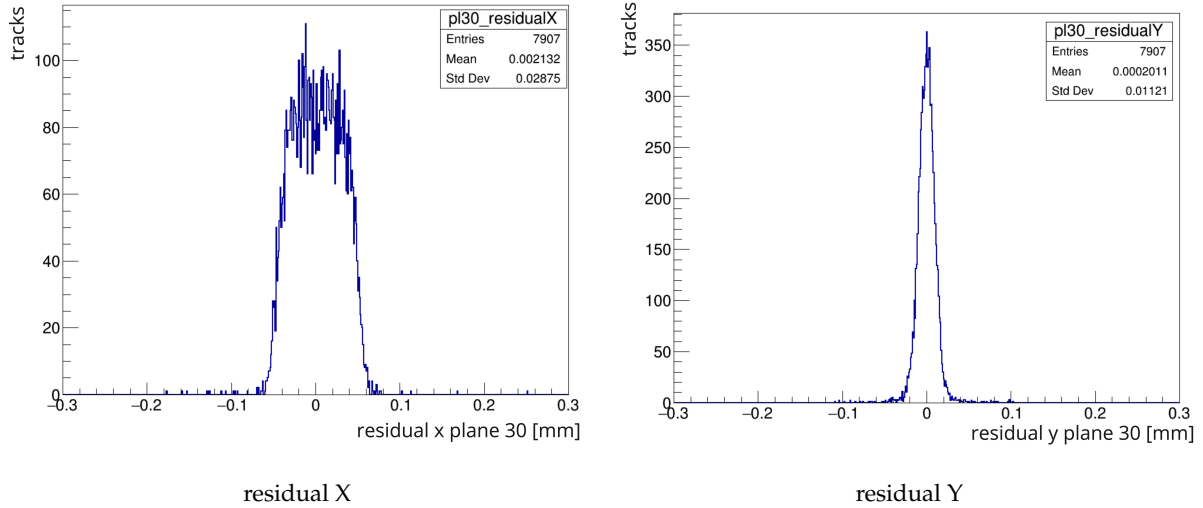


FIGURE 6.9: Residuals of fitted tracks for an ITk module with $25 \times 100 \mu\text{m}^2$ pixel geometry measured at CERN with particle beam energy of 120 GeV. The standard deviation indicate the residual width.

residuals and worse resolution due to two main effects: multiple scattering and pointing resolution, which is the contribution of the alignment. Tracks from higher energy particle beam have smaller residual widths closer to their intrinsic resolution. When multiple scattering effects are negligible, it is possible to resolve the pixel cell itself as observed in the $100 \mu\text{m}$ long pixel side of figure 6.9.

The validation of the residual alignment from the pointing resolution, and the residual width close to its expected width is a good indication of the quality of the produced results. Hence, the quality of performance depends on the alignment. The uncertainty of the alignment is the uncertainty of the pointing resolution of the telescope for unbiased planes given by equation 5.6.

6.2.1 R&D ITk planar pixel production

The R&D ITk planar pixel modules were assembled from sensors that were produced at FBK, sensor fabrication discussed in section 2.3.1. Presented sensors are produced from two wafers of thickness of $100 \mu\text{m}$ or $130 \mu\text{m}$ [169]. The sensors included for two different pixel geometries with higher granularity, as explain in the ITk requirements in section 3.2. In the following sections, I discuss the hit efficiency as a function of the bias voltage of unirradiated modules in section 6.2.1.1 In section 6.2.1.2 I discuss the irradiation beam profile and the impact of fluence on the hit efficiency. Then in section 6.2.1.3 I discuss the impact of tuned threshold on the hit efficiency. The presented results are R&D work to understand the physics behind the results and to optimize the performance of ITk planar pixel modules.

6.2.1.1 Hit efficiency for unirradiated modules

A critical aspect for tracking devices is the hit efficiency of the device. Low hit efficiency for an ITk module would affect the precision of track and vertex reconstruction and hence, the over all particle detection efficiency and fake track rejection. For this reason ITk pixel modules are tested and required to meet the ITk requirements.

The ITk sensors are bump bonded to the RD53A readout chip, which has three different analog FE designs (see section 3.2.2). The hit efficiency as a function of the bias voltage for an unirradiated module W360_4 hosting a $100 \mu\text{m}$ thick sensor employing a pixel geometry of $25 \times 100 \mu\text{m}^2$ without PT, measured

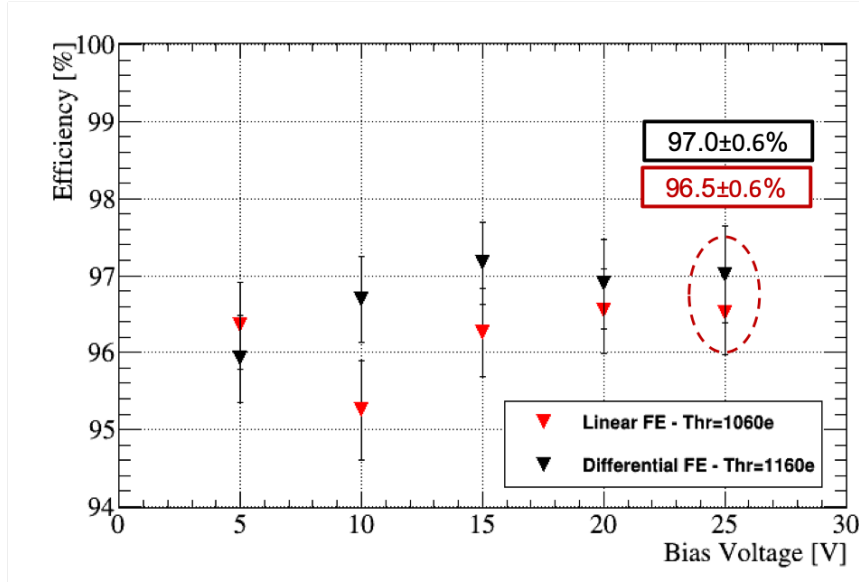


FIGURE 6.10: Hit efficiency for W360_4, an unirradiated ITk module with $100\ \mu\text{m}$ thick sensor pixel geometry of $25 \times 100\ \mu\text{m}^2$ without PT measured at DESY with particle beam energy $5\ \text{GeV}$. Plot comparing the hit efficiency for linear and differential front-ends.

at DESY with particle beam energy of $5\ \text{GeV}$ is shown in figure 6.10. The figure shows a comparison between the hit efficiency of the linear and differential front-end (FE) for the same module. Each analog FE was developed by a different institute and are meant to be compared to decide for most suitable readout electronics for ATLAS ITk. In this analysis each FE was analysed separately to obtain the hit efficiency. Using the bdaq53 board, the linear FE was tuned to threshold of $1060 \pm 100\ e$, and the differential FE was tuned to threshold of $1160 \pm 98\ e$. Within the uncertainty these threshold levels are considered compatible for comparison. For W360_4 in figure 6.10, it is fully depleted at $5\ \text{V}$, the increase of the bias voltage show slight increase in the efficiency until it saturated at $20\ \text{V}$. Within the statistical uncertainties the hit efficiencies are similar. At the highest bias voltage $25\ \text{V}$ the differential FE achieves $97.0 \pm 0.6\%$ hit efficiency, and the linear FE achieves $96.5 \pm 0.6\%$ hit efficiency. This particular module was soon irradiated after this measurement and the achieved hit efficiency after irradiation at sufficient high bias voltage agrees well with ITk requirements. Nevertheless, I show that the hit efficiency at the highest measured bias voltage and low threshold tuning is similar for the linear and differential FEs at about 97% efficient.

Another unirradiated module W398_4 hosting a $130\ \mu\text{m}$ thick sensor with $50 \times 50\ \mu\text{m}^2$ pixel geometry employing straight PT design was measured at DESY with particle beam energy $5\ \text{GeV}$. The hit efficiency as a function of the bias voltage is shown in figure 6.11. The module was tuned to mean threshold of $1060 \pm 88\ e$ on both linear and differential FEs. As we can observe in the figure, the module shows very well performance at all bias voltages achieving $98.8 \pm 0.1\%$ at $60\ \text{V}$ agreeing well with ITk requirements before irradiation. After this measurement, the module was irradiated at Birmingham irradiation facility to be measured after irradiation but unfortunately it broke with high current testing in the testbeam.

6.2.1.2 Hit efficiency of irradiated modules

The radiation fluence and particle type of the irradiation has an effect on the hit efficiency, and hence performance of the module. The main cause of inefficiency after irradiation is the decrease of the collected charge in the sensor due to trapping (see section 2.4.1). In this section I discuss the irradiation beam profile for the presented modules and then the impact of fluence on the hit efficiency.

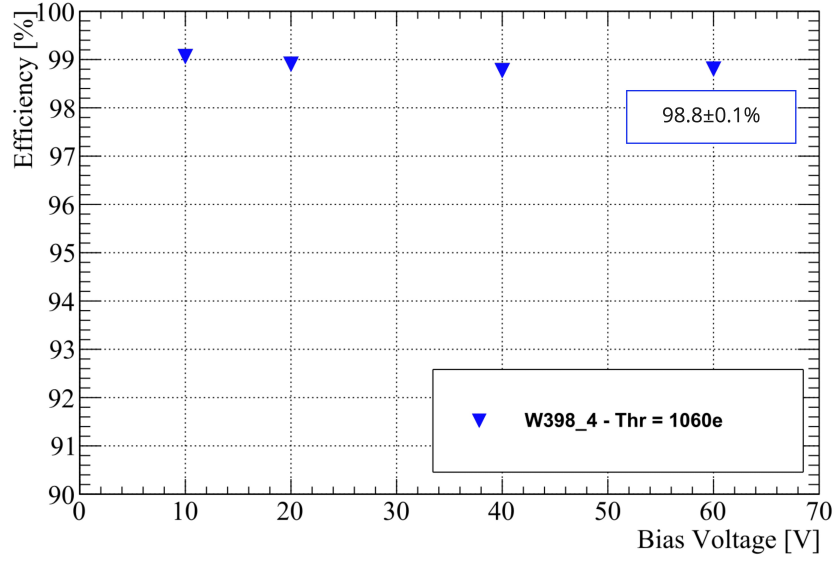


FIGURE 6.11: Hit efficiency as a function of bias voltage for unirradiated module W398_4 hosting $130\ \mu\text{m}$ thick sensor. Module tuned to mean threshold of $1060 \pm 88e$ and achieved hit efficiency $98.8 \pm 0.1\%$ at $60\ \text{V}$.

3045 CERN PS Irrad beam profile

3046 Modules irradiated at the CERN Irrad facility receive an inhomogeneous fluence over the pixel ma-
 3047 trix due to the irradiation beam profile (also see Appendix C.3). A RD53A module W398_5, hosting
 3048 a $130\ \mu\text{m}$ thick sensor with $25 \times 100\ \mu\text{m}^2$ pixel geometry was irradiated there to an average fluence of
 3049 $3.3 \times 10^{15}\ n_{eq}/\text{cm}^2$. After analyzing the irradiation beam profile to extract the average fluence separately
 3050 for each front-end region, figure 6.12 shows the beam profile shape depicted for each regions. The average
 fluence over the FE regions is summarised in table 6.2.

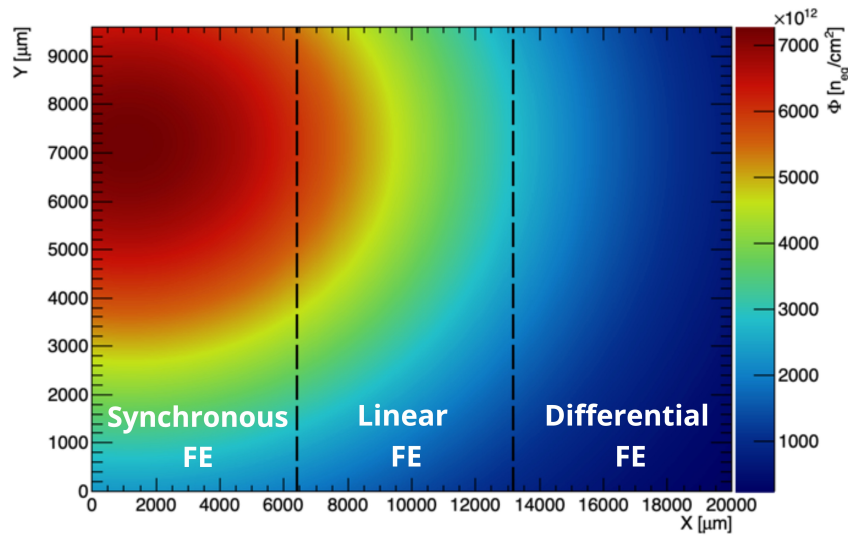


FIGURE 6.12: Irradiation beam profile at CERN PS Irrad facility for the W398_5 RD53A module hosting a $130\ \mu\text{m}$ thick sensor irradiated to an average fluence of $3.3 \times 10^{15}\ n_{eq}/\text{cm}^2$. Average fluence for each region summarised in table 6.2.

3051

3052

TABLE 6.2: Summary of the average fluence achieved for each analog front-end region for a RD53A module irradiated at the CERN Irrad facility to an average fluence of $3.36 \times 10^{15} n_{eq}/cm^2$.

	Synchronous FE	Linear FE	Differential FE
$\Phi \times 10^{15} [n_{eq}cm^{-2}]$	5.4	3.4	1.3

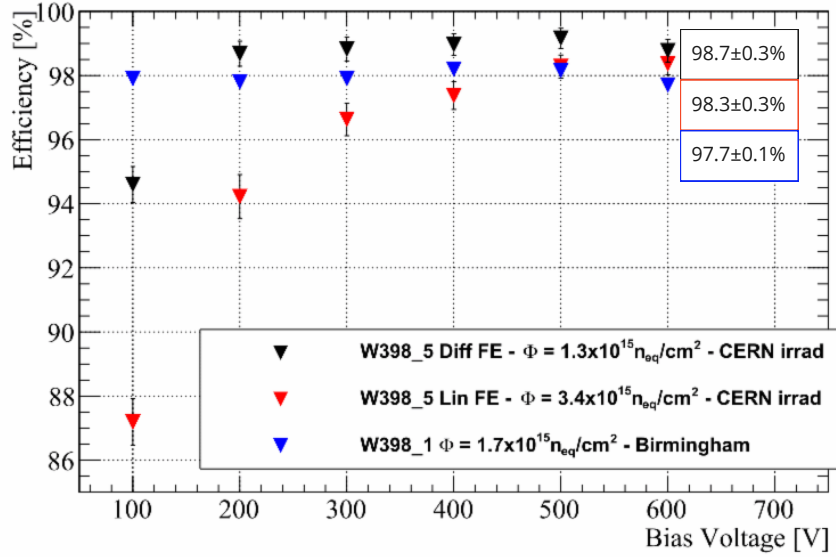


FIGURE 6.13: Efficiency as a function of bias voltage for different irradiation level from CERN SPS and Birmingham facility. At the highest bias voltage, W398_5_Diff tuned to mean threshold 1300 e achieves 98.7 ± 0.3 hit efficiency. W398_5_Lin tuned to mean threshold 1300 e achieves 98.3 ± 0.3 hit efficiency. W398_1_Lin+Diff tuned to mean threshold 1100 e achieves 97.7 ± 0.1 hit efficiency.

As for the rest of the modules irradiated at different facilities they all receive homogeneous fluence over the pixel matrix as discussed in Appendix C.

Impact of fluence on the hit efficiency

To study the impact of fluence on the hit efficiency for the RD53A module we compare the hit efficiency as a function of the bias voltage for different fluence levels. Figure 6.13 compares three different fluence levels from two different modules. The first module W398_5 hosting $130 \mu m$ thick sensor with $25 \times 100 \mu m^2$ pixel geometry irradiated to fluence $\Phi = 1.3 \times 10^{15} n_{eq}/cm^2$ for the differential FE, and $\Phi = 3.4 \times 10^{15} n_{eq}/cm^2$ for the linear FE at the CERN Irrad facility. The module was measured at CERN, and tuned to mean threshold of 1300 e. The second module W398_1 hosting $130 \mu m$ thick sensor with $50 \times 50 \mu m^2$ pixel geometry irradiated to an average fluence of $\Phi = 1.7 \times 10^{15} n_{eq}/cm^2$ at the Birmingham irradiation facility, which provides homogenous irradiation. The module was measured at DESY, and tuned to mean threshold of 1100 e. All modules in this comparison employ a sensor without PT in the biasing structure. As expected, modules irradiated to lower fluence, which have less trapping damages in the sensor bulk, achieve higher hit efficiency.

The comparison between $\Phi = 1.3 \times 10^{15} n_{eq}/cm^2$, plotted in **Black**, and $\Phi = 3.4 \times 10^{15} n_{eq}/cm^2$, plotted in **Red**, for lower fluence the hit efficiency saturates earlier at $V_b = 200$, while at higher fluence charge carriers still can not completely traverse the sensor at the same bias voltage so the hit efficiency reaches saturation at $V_b = 500$. At the highest bias voltage $V_b = 600$ V where the electric field is higher inducing the drift of charge carriers toward the electrodes both measurements achieve similar hit efficiency; at $\Phi = 3.4 \times 10^{15} n_{eq}/cm^2$ the module is $98.3 \pm 0.3\%$ efficient, and at $\Phi = 1.3 \times 10^{15} n_{eq}/cm^2$ the

module is $98.7 \pm 0.3\%$ efficient. Beyond full depletion, modules irradiated at the CERN Irrad facility up to $\Phi = 3.4 \times 10^{15} n_{eq}/cm^2$ are in good agreement with the ITk requirements.

The RD53A module W398_1 irradiated to fluence $\Phi = 1.7 \times 10^{15} n_{eq}/cm^2$ at the Birmingham irradiation facility obtaining a homogenous irradiation over the pixel module, plotted in [Blue](#), shows high hit efficiency at bias voltage $V_b = 100 V$, earlier saturation of hit efficiency than the module irradiated at CERN. The hit efficiency of the module is saturated across all bias voltage steps up to $V_b = 600 V$ where an efficiency of $97.7 \pm 0.1\%$ is achieved.

This measurement confirms that the hit efficiency is slightly better for lower fluences and gets worse with higher fluence, i.e. more radiation damage in the bulk. Both irradiated modules agree with ITk requirements achieving hit efficiency $\geq 97\%$ when operated at the highest bias voltage value of 600 V. These measurements also prove that hit efficiency results are consistent if measured with high particle beam energy at CERN or low particle beam energy at DESY, even if the resolution is worse with low particle beam energy.

Impact of biasing structure on the hit efficiency

The main cause of inefficiency in an irradiated sensor is the decrease of the collected charge due to trapping and partial depletion in the bulk of the sensor. In figure 6.14 I show the in-pixel efficiency map for W398_2, an irradiated module hosting a $130 \mu m$ thick sensor with $50 \times 50 \mu m^2$ pixel geometry employing a straight PT biasing structure design. The module was measured at CERN with particle beam energy of 120 GeV (see section 5.3.1) with the beam centered between the linear and the differential FEs. The high resolution of the measurement allows the study of different structures inside the sensor with few microns precision. The module was irradiated to an average fluence of $\Phi = 3.3 \times 10^{15} n_{eq}/cm^2$ at the CERN PS irradiation facility (see Appendix C.3), which mean it does not have a homogeneous fluence over the entire pixel matrix. The module was tuned to a mean threshold value of about 1180 e. Figure 6.14 shows the evolution of the hit efficiency represented by the in-pixel efficiency map folding 2×2 pixels (also see section 5.4.2). At 100 V the module is not in full depletion as shown in its IV characteristics in figure 6.2. At 100 V the average hit efficiency in the sensor is about 60%, we can observe that the low efficiency is due to the partial depletion. As the bias voltage increases the formation of the signal becomes clearer showing the geometry and design of the sensor. The effect of the PT on the hit efficiency of the module depends on the potential difference between the PT and pixel implant. So, when the electric field is high enough to collect charge from the entire pixel volume the detrimental effect of the PT is evident as observed at 500 V, while at lower potential the effects of the PT inducing charge loss is comparable as observed at 100 V. The hit efficiency increases with increasing bias voltage, up to 500 V where we can observe the biasing structure depicted by the hit efficiency loss at the PT dot and bias rail region. The map folds 4 pixels of $50 \times 50 \mu m^2$ together with the bias structure design overlaid on top of the pixel efficiency map at the highest bias voltage. At 500 V the PT can be observed with good resolution in comparison to lower potential at 400 V.

The hit efficiency as a function of the bias voltage for the same W398_2 is plotted in figure 6.15. The module was irradiated at $\Phi = 3.3 \times 10^{15} n_{eq}/cm^2$, measured at CERN with particle beam of 120 GeV with the beam centered on both linear and differential FEs. The figure shows two curves, one for the full pixel region plotted in **Black** with the straight PT design included, which reaches hit efficiency of $95.2 \pm 0.1\%$ at the highest bias voltage. While if we restrict the analysis to the central area of the pixel by taking a 'fiducial region' to exclude the PTs of the sensor as depicted of the right side in figure 6.15 including only the inner geometry of the pixel without the PT structure, then plotted in **Red** the sensor

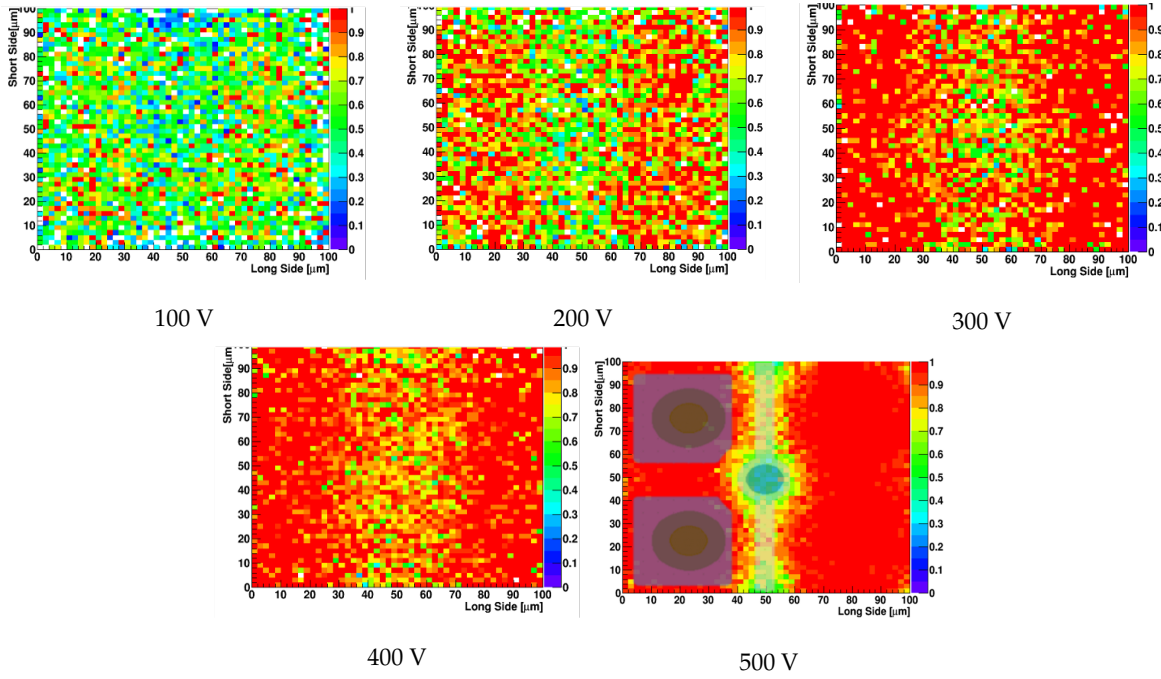


FIGURE 6.14: Evolution of the hit efficiency map with bias voltage for the W398_2 module with $130\ \mu\text{m}$ thick sensor irradiated to an average fluence of $3.3 \times 10^{15}\ n_{eq}/\text{cm}^2$ measured at CERN with particle beam of $120\ \text{GeV}$ for both linear and differential FE at various bias voltage.

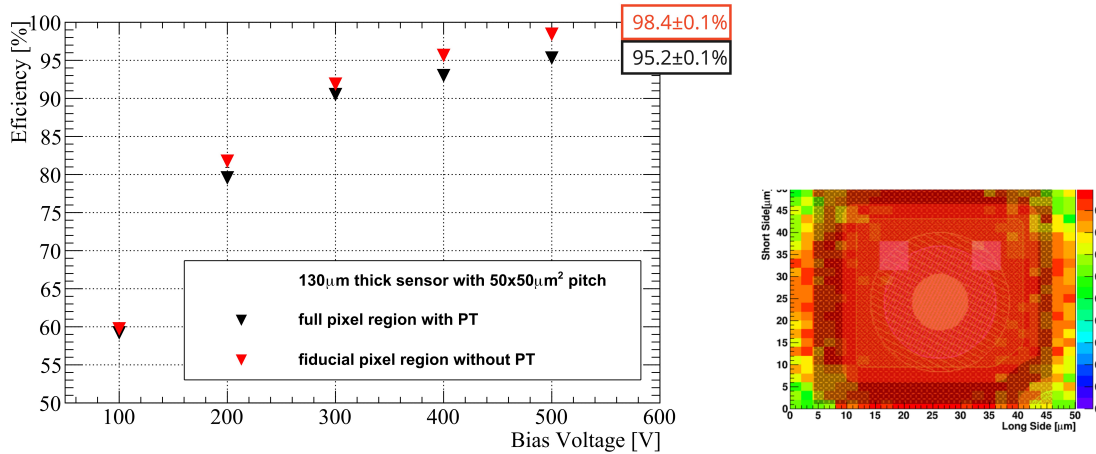


FIGURE 6.15: Hit efficiency as a function of bias voltage for W398_2 module with $130\ \mu\text{m}$ thick sensor irradiated to $\Phi = 3.3 \times 10^{15}\ n_{eq}/\text{cm}^2$ measured at CERN with particle beam energy of $120\ \text{GeV}$. The hit efficiency is plotted for the whole sensor in Black and for a fiducial region excluding the PT in Red, as shown in the right side, comparing the effects of the PT on the hit efficiency.

achieves hit efficiency of $98.4 \pm 0.1\%$ at the highest bias voltage. This analysis is done to check the hit efficiency of the pixel implant and the sensor fabrication irrelative to the biasing structure. But the comparison shows the impact of the biasing structure with PT design on the hit efficiency, where the PT acts like a charge competing electrode and result into overall efficiency loss for the implants. A reduction of performance is observed on the hit efficiency when including the straight PT biasing structure in the analysis by 3.2%. While restricting the analysis without PT, the module shows a better performance with hit efficiency of $98.4 \pm 0.1\%$ that agrees well with the ITk requirement of planar pixel sensors to operate at high luminosity after irradiation.

Biasing structures were subject to many studies, documented in references [87, 162, 169, 173, 174]. The latest improved biasing structure mechanism for ITk sensors opens the possibility to have no PTs in the final sensor design thanks to the temporary metal technique (see section 2.3.2). An ITk sensor without bias rail and without PT will recover charge loss that is induced by the biasing structure as shown in the evolution in the in-pixel efficiency maps of figure 6.16.

Impact of pixel geometry on the hit efficiency

For the irradiated ITk module W398_5 hosting $130 \mu\text{m}$ thick sensor and a pixel geometry of $25 \times 100 \mu\text{m}^2$ measured at CERN with particle beam of 120 V, figure 6.16 shows the 2×2 in-pixel efficiency maps at three bias voltage points to observe the evolution of the hit efficiency for a module without PT in the biasing structure. The module was irradiated to an average fluence of $\Phi = 3.3 \times 10^{15} n_{eq}/\text{cm}^2$ at the CERN PS Irrad facility (see Appendix C.3), which means it does not have a uniform irradiation over the pixel matrix. The module was tuned to a mean threshold value of $1180 \pm 230 e$. At 100 V, where the sensor did not yet reach full depletion, the figure shows about 20% efficiency loss around the pixel implants. The geometry of the pixel cell, as depicted above it, can already be observed to be $25 \times 100 \mu\text{m}^2$. The efficiency loss is higher at the edges between two pixel implants and is maximum towards the center of four pixel implants. This is due to charge sharing, the collected charge is shared amongst the neighboring pixel implants at partial depletion. Consequently, charge sharing is maximum for smaller implants on the y-axis for the $25 \mu\text{m}$ pitch than for the $100 \mu\text{m}$ pitch on the x-axis. Smaller pitch size increases the charge sharing probability due to diffusion of the charge carriers, specially at partial depletion. The collected charge improves significantly for all pixel implants under high electric field. At 300 V the charge sharing between the two pixel implants is reduced, while an inefficiency at the center of four pixel implants can still be observed. As the bias voltage increases we can observe the evolution of the in-pixel efficiency map up to the highest voltage point at 500 V, where the full sensor is fully depleted and the charge signal is fully formed. At high voltages, charge sharing is suppressed to minimum by the electric field. At the highest bias voltage the module achieves hit efficiency of $98.3 \pm 0.3\%$.

In this module with $25 \times 100 \mu\text{m}^2$ pixel geometry, although there are no PTs implemented, there are Aluminum structures overlaying the neighboring pixel implants as shown in pixel geometry on top of figure 6.16. The question now turns regarding to whether this layout due to the small pixel pitch of $25 \mu\text{m}$ causes any cross talk between the pixels. Cross talk is when to the signal of the traversing particle is channeled to the neighboring pixel. This effect creates the undesired effect of connecting the signal to several different pixels. Contrary to charge sharing between pixels when the charge is divided amongst the pixels with the same ToT weight.

Figure 6.17 shows a cluster size map folding 2×4 pixels for (a) cluster size = 1, and (b) cluster size = 2. This measurement is performed at CERN with particle beam energy of 120 GeV. The cluster size map is produced by folding the cluster size number of each pixel onto its relative position in the 2×4 pixels

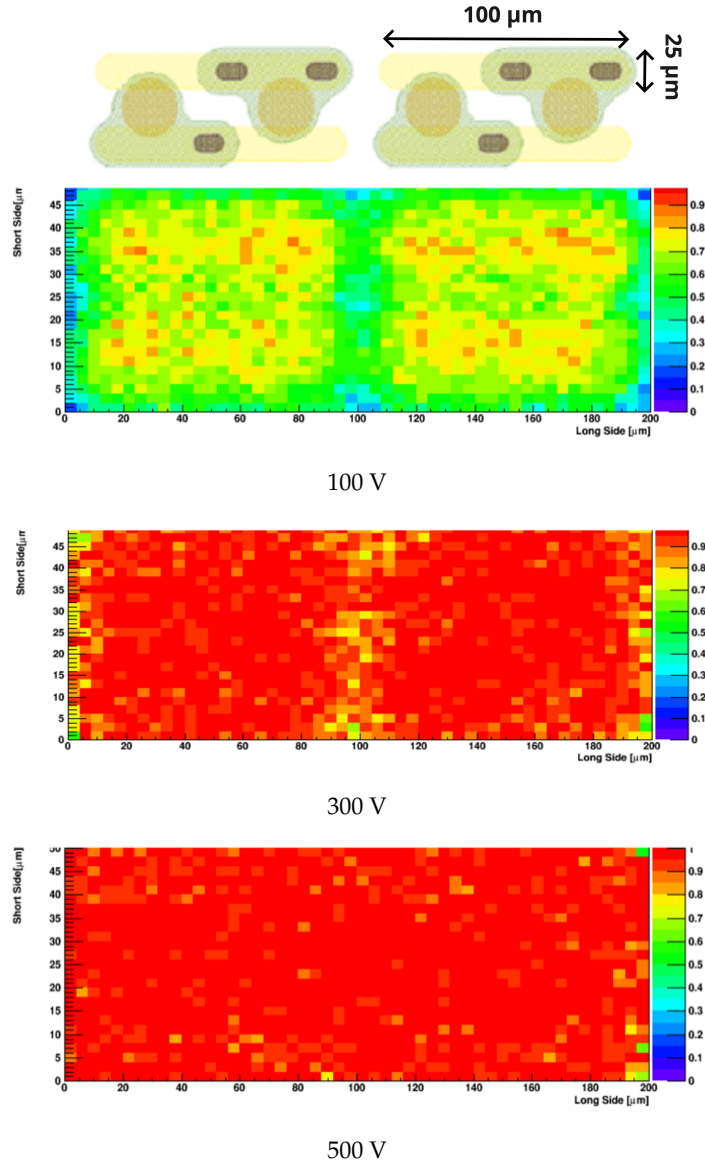
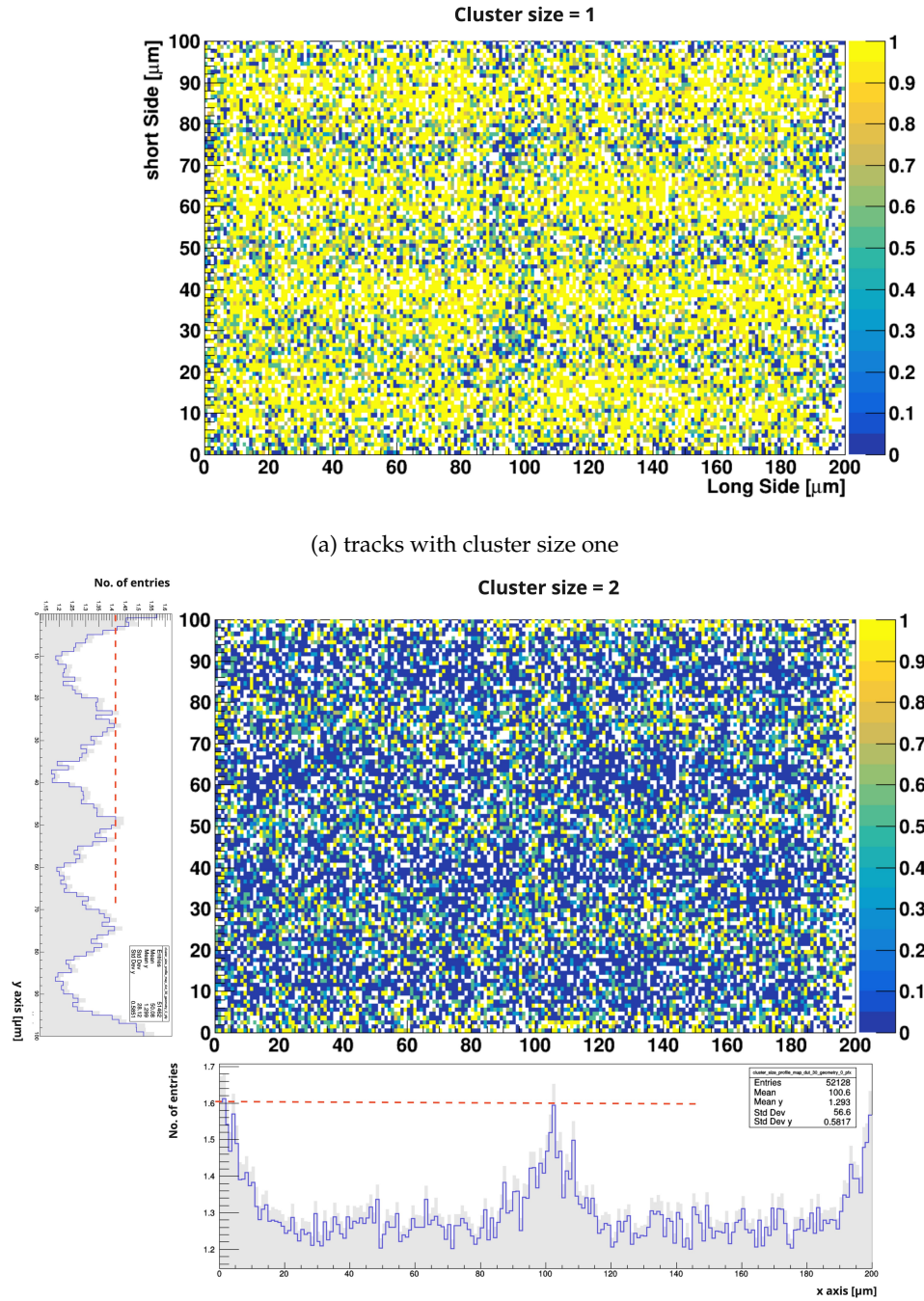


FIGURE 6.16: Evolution of a 2×2 in-pixel efficiency map with bias voltage for an irradiated module W398_5 with $130 \mu\text{m}$ thick sensor without PT irradiated to $\Phi = 3.3 \times 10^{15} n_{eq}/\text{cm}^2$ measured at CERN with particle beam of 120 GeV .



(b) tracks with cluster size two

FIGURE 6.17: Cluster size map for an irradiated module hosting $130\ \mu\text{m}$ thick sensor with $25 \times 100\ \mu\text{m}^2$ pixel geometry irradiated to an average fluence of $\Phi = 3.6 \times 10^{15}\ n_{eq}/\text{cm}^2$ at the KIT irradiation facility. The maps shows 2×4 folding of the pixels for (a) cluster size = 1, and (b) cluster size = 2 with its number of hits projection on x- and y-axis. The Red line indicates the mean cluster size between pixels.

folded map. Figure 6.17(a) shows the hit pixels with cluster size = 1, which means the reconstructed track passes completely through one pixel and not shared amongst more. As can be observed in the map cluster size = 1 with higher number of tracks corresponds to the middle of the pixel implants, while at the edges of the implants the number of tracks is reduced indicating larger cluster size. If we compare with the map plotting only cluster size = 2 in figure 6.17(b), we can observe that tracks with cluster size = 2 corresponds to hits at the edges of the pixel implants as they are shared among two pixels. The folded positions of the cluster size in the sensor geometry allows us to observe if there are any differences in cluster size due to the hit position in the sensor. Around the map of cluster size = 2 the x- and y-projections of the map are plotted as the number of entries on respective axis. The total number of entries is 52128 events plotted in blue, while the propagated uncertainty is plotted in gray. The higher population of cluster size = 2 at the edges of the pixels is reflected on the x- and y-projections where number of hits increase between the pixels and decrease at the center of the pixel. On the x-axis projection for the long pitch the mean cluster size = 1.4, while on the y-axis for the short pitch the mean cluster size = 1.6. This shows an increase of mean cluster size of about 1.1% between the axes, which indicate that there is a small increase in cross talk for the short pixels in the $25 \times 100 \mu\text{m}^2$ pixel geometry. A similar study was also done in reference [154] comparing cross talk between $25 \times 100 \mu\text{m}^2$ and $50 \times 50 \mu\text{m}^2$ pixel geometry with PT in the biasing structure reaching a similar conclusion.

6.2.1.3 Impact of threshold on hit efficiency

The threshold of the pixel module is investigated with a particle beam to study the effect of the tuned threshold on the hit efficiency for an irradiated module. Tuning the module to low threshold is essential to maintain high hit efficiency, especially for irradiated modules. This measurement study was performed at the DESY testbeam with particle beam energy of 5 GeV, using two RD53A modules; W398_4 & W398_2 both hosting a $130 \mu\text{m}$ thick sensor. W398_4 is an unirradiated with $50 \times 50 \mu\text{m}^2$ pixel geometry with straight PT, and W398_2 is irradiated to an average fluence of $\Phi = 3.3 \times 10^{15} n_{eq}/\text{cm}^2$ at the CERN PS Irrad facility hosting a $50 \times 50 \mu\text{m}^2$ pixel geometry with wavy PT. The unirradiated module was tuned at room temperature and measured at constant bias voltage of 75 V, while the irradiated module was tuned at -60°C and measured at 500 V. The hit efficiency as a function of the bias voltage for both modules is shown in figure 6.18. The mean value of the tuned threshold and the noise dispersion of each point is detailed in table 6.3. All tuning was performed on the linear front-end only using the bdaq53 board (see section 4.1.2).

TABLE 6.3: Mean value of tuned threshold and tuning dispersion corresponding to the tuned modules shown in figure 6.18. Modules were tuned using bdaq53 board.

	Tuned threshold [e^-]			
Unirradiated module	790±270	1030±142	1180±240	1370±203
Irradiated module	900±170	1243±184	1460±139	

After tuning the module, a noise occupancy scan is performed to mask very noisy pixels that could affect the data taking. As shown in figure 6.18 the unirradiated module achieves high efficiency about 99% on all threshold points. Up to a mean threshold of 1500 e the effect of the threshold maintains a consistent performance. Contrary, the irradiated module loses some efficiency after radiation damage in the bulk, which is expected. At low threshold of about $900 \pm 270 e$ it achieves hit efficiency of about $93.1 \pm 0.8\%$. With increasing threshold and effects of charge trapping after irradiation the module achieved slightly lower hit efficiency of $90.1 \pm 1.0\%$ at $\text{thr}=1243e$, and $91.7 \pm 0.6\%$ at $\text{thr}=1460e$. This hit efficiency is considered low for the irradiated module at $V_b = 500 \text{ V}$. The fluctuation in the hit efficiency

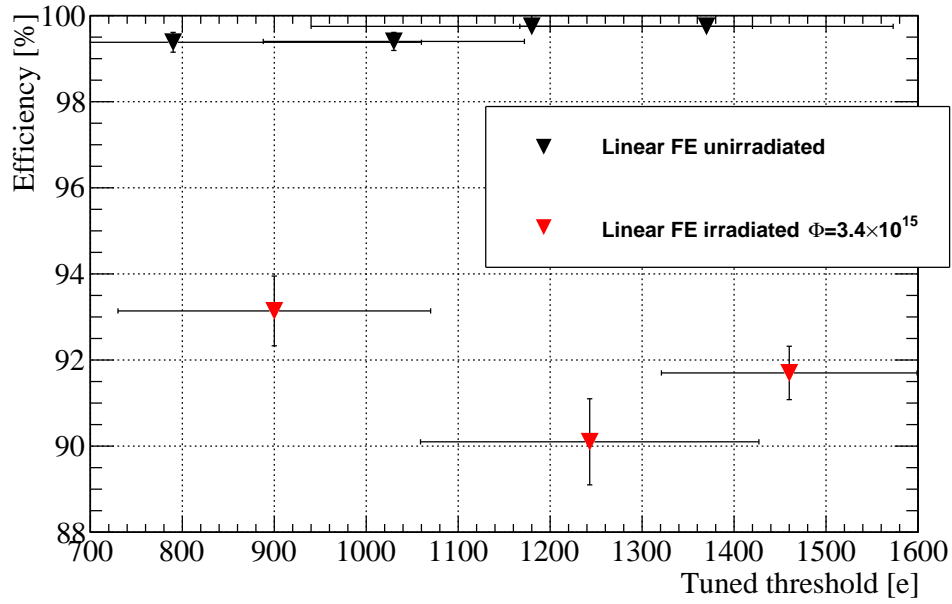


FIGURE 6.18: Hit efficiency as a function of the tuned threshold measuring only the linear front-end of an unirradiated (Black) and a module irradiated to fluence of $\Phi = 3.4 \times 10^{15} n_{eq}/cm^2$ (Red). Threshold was retuned for each point in the range [800-1500] e, the horizontal uncertainty bar is the threshold dispersion. The measurement was performed at DESY with particle beam energy 5 GeV at $V_b = 75$ V for unirradiated and $V_b = 500$ V for the irradiated module.

value can be due to several reasons; retuning the module achieving smaller threshold dispersion gives better efficiency, effect of noisy pixels. The mean tuned threshold of the readout chip has larger effects on the hit efficiency for irradiated modules. It is worthwhile to operate the modules in low threshold and lower noise dispersion to maintain the required performance especially towards the end of the tracker life when collected charge is reduced due to radiation damage.

To summarize the results of the ITk R&D prototype modules, I can say that hit efficiency results obtained from linear and differential front-ends are compatible. Higher fluence on the irradiated modules decreases the hit efficiency, due to radiation damage the signals do not fully reach the electrode in time. Higher electric field applied to the module result in higher resolution inducing the charge carriers to travel to the electrodes in time. The biasing structure of the sensor is the dominant parameters for efficiency loss in the sensor. Thanks to the temporary metal technique, sensors can achieve their full efficiency. Tuning the threshold to lower value while maintaining high signal-to-noise ratio result in higher hit efficiency. Unirradiated prototype module investigated from LPNHE achieves hit efficiency $> 98\%$, and irradiated modules achieve hit efficiency $> 97\%$ agreeing well with the ITk requirements. The hit efficiency of the studied modules and their details are summed in table 6.4. Almost all modules passed the ITk requirements, and in the case of low hit efficiency it is related to the presence on the PT in the structure.

6.2.2 ITk pixel sensors Market Survey production

Several Market Survey (MS) campaigns have been launched to identify potential suppliers for major cost items for ITk construction that will be purchased by CERN [61]. The ITk pixel sensor MS is aimed to qualify the potential suppliers during a preproduction phase before the final tendering process. The qualification of the supplier follows the qualification of their ITk pixel sensors, which are produced

TABLE 6.4: Summary of the results from ITk prototype modules. Efficiencies quoted in **green** are in agreement with ITk requirements for a pixel sensor and efficiencies quoted in **red** are below the requirement limit.

Fluence [$\times 10^{15} n_{eq}/cm^2$]	Name	Pixel geometry [μm^2]	Thickness [μm]	Biasing structure	Voltage [V]	Mean threshold [e]	Efficiency [%]
unirradiated	W360_4	25×100	130	no PT	25		97.0 \pm 0.6
	W398_4	50×50	130	PT	60	1060	98.8 \pm 0.1
1.3	W398_5	25×100	130	no PT	600	1180	98.7 \pm 0.3
1.7	W398_1	50×50	130	no PT	600	1100	97.7 \pm 0.1
3.3	W398_2	50×50	130	with PT fiducial region	500	1180	95.2 \pm 0.1 98.4 \pm 0.1
3.4	W398_5	25×100	130	no PT	600	1300	98.3 \pm 0.3

based on the requirements from the technical specification document for ITk planar pixel sensors [175]⁴. The qualification process is tested on enough prototype devices produced from six different foundries designed to the final ITk specifications. This section is focused on the qualification of the production foundry by the qualification of the sensors by their performance. The qualification procedure of the prototypes, which are described below, is carried anonymously for the foundries for ITk preproduction.

There are 9 contributing institutes that are in charge of testing the ITk sensors prototypes for the MS and preproduction of ITk planar pixel sensors; University of Liverpool⁵, Lancaster University⁶, University of Göttingen⁷, University of Glasgow⁸, University of Oxford⁹, LAL¹⁰, LPNHE¹¹, KEK¹², Technical university of Dortmund¹³. Each institute must have the necessary equipments to operate a hybrid module to pass a 'site qualification' step. The qualification of a ITk-pixel-MS includes the inspection of both the bare sensor before bump bonding, and then the inspection of the hybrid module after bump bonding. Also, sensors and modules are inspected before and after irradiation. The qualification procedure for these four phases is explain here [176].

Bare sensors before irradiation

Qualification of the sensor include:

- visual inspection: no stains or scratches on the sensor, no shorted pixels, front-end chip not larger than $40\mu m$ at edges.
- checking thickness and planarity.
- measurement of depletion voltage: $V_{dep} < 100 V$ for $150 \mu m$ thick sensors .
- measurement of leakage current per area: $I_{leak} < 0.75 \mu A/cm^2$ at $V_{dep} + 50 V$.
- stability test of leakage current: $\Delta I_{leak} < 25\%$ measured over 48 hours.

⁴Internal document to CERN

⁵<https://www.liverpool.ac.uk/particle-physics/experiments/atlas/>

⁶<https://www.lancaster.ac.uk/oed/academic-and-research-staff/atlas/>

⁷<https://www.uni-goettingen.de/en/atlas+experiment/550884.html>

⁸<https://www.gla.ac.uk/schools/physics/research/groups/particlephysicsexperiment/research/atlasatglasgow/>

⁹<https://www2.physics.ox.ac.uk/research/atlas>

¹⁰<https://atlas.lal.in2p3.fr/>

¹¹<http://lpnhe.in2p3.fr/spip.php?rubrique7>

¹²<https://www.kek.jp/en/Facility/IPNS/ATLAS/>

¹³<https://www.tu-dortmund.de/>

- measurement of breakdown voltage: $V_{break} > V_{dep} + 70 \text{ V}$.

Bare sensors after irradiation

ITk bare planar sensors are irradiated at irradiation facilities based on the testing institute's choice to two different fluences; $2 \times 10^{15} n_{eq}/cm^2$ and $5 \times 10^{15} n_{eq}/cm^2$. Sensors are characterised at -25°C . Then annealed for 10 days at room temperature. The breakdown voltage and leakage current is inspected after irradiation to study their electrical behavior.

Hybrid modules before irradiation

After bump bonding (see section 3.3.1) to the RD53A front-end chip, unirradiated modules are characterised to be qualified to ensure their functionality. The specification of electrical properties for a module is the same for a bare sensor listed above in addition to measurement with particle beam at the ITk-pixel-MS testbeam campaign. The inspections include:

- measurement of leakage current per area.
- measurement of breakdown voltage.
- test of bump bonds.
- source scan measurement after thermal cycling.
- Hit efficiency measurement in testbeam: required $> 98\%$ hit efficiency

Hybrid modules after irradiation

ITk planar pixel modules were irradiated at CYRIC irradiation facility (see Appendix C.4) to two different fluences; $2 \times 10^{15} n_{eq}/cm^2$ and $5 \times 10^{15} n_{eq}/cm^2$. After irradiation the modules are measured again in testbeam to be qualified assessing their hit efficiency. Irradiated modules are required to have $> 97\%$ hit efficiency (see section 3.2) for ITk planar pixel sensor requirements.

In preparation for the pixel MS testbeam campaign a team was formed to carry out the reconstruction and analysis of testbeam data. A reconstruction hands-on workshop was given by myself and a colleague Mareike Weers [177] from Technical university of Dortmund during the March and July 2019 testbeam at DESY. At the end of the training, the six participants were able to reconstruct data with RD53A modules with EUTelescope software (see section 5.4.1) and analyse efficiencies with Tbmon2 (see section 5.4.2). ITk-pixel-MS campaign needed four Testbeam periods to measure all modules before and after irradiation. All testbeam periods were at the DESY testbeam facility. The setup was unified to use the YARR readout board (see section 4.1.3). A communication and local database platform was initiated to update the progress and analysis results.

Modules from all foundries were first measured unirradiated at the beginning of the MS testbeam campaign. Unirradiated modules were measured first during 25thSeptember-7thOctober 2019 testbeam and second during 25thNovember-9thDecember 2019. The third testbeam, which was planned in March 2020 was postponed for global pandemic reasons to 26thJune-6thJuly 2020, where a smaller group of colleagues were able to be on site with the remote support of the ITk pixel community. And the final testbeam period 5-19thOctober 2020, all modules were measure after irradiation. The reconstruction of the data was standardised among the reconstruction team to validate the results, in which I participated in since the beginning. The hit efficiency for modules before irradiation reached the ITk requirement at

least 98% hit efficiency. After irradiation the hit efficiency was expected to decrease slightly and most modules were still qualified to have 97% efficiency, while other modules revealed some issues that invited us to improve the track reconstruction configuration. All foundries are qualified according to the qualification of the module after irradiation. A selection of results of the MS modules are presented anonymously in the following starting with a discussion on the resolution of the pixel geometry from track reconstruction in section 6.2.2, and then a selection of the results of hit efficiency from the variety of measured modules in section 6.2.2. The total amount of modules that were measured for ITk planar pixel module Market Survey were about 43 modules from 6 different vendors. The final results of the MS campaign are circulated internal in the ATLAS ITk pixel community.

Spatial resolution

For this MS campaign, the track reconstruction procedure was standardized using EUTelescope with GBL method (see section 5.4.1) and then analysed with Tbmon2 (see section 5.4.2). The alignment and fitting parameters are the same for all modules to produce fair results that were cross checked among the reconstruction team. All modules were characterised at DESY testbeam facility with particle beam energy of 5 GeV in perpendicular incidence.

Figure 6.19(a&b) shows fitted residuals on x- and y-axis for $50 \times 50 \mu m^2$ respectively. Recalling the binary resolution of a $50 \mu m$ pitch is $\sigma \simeq 15 \mu m$. The residual width is a contribution of the binary resolution and the pointing resolution. The residual width is smeared out as shown in the figure to have $\sigma = 24 \mu m$ for both x- and y-axis. Similarly for the modules hosting a $25 \times 100 \mu m^2$ pitch sensor, the residuals are shown in figure 6.19(c)&(d) for x- and y-axis. The binary resolution for $25 \mu m$ and $100 \mu m$ pitch are $\sigma = 8 \mu m$ and $\sigma = 30 \mu m$ respectively. The residuals in the figure show a larger width of $\sigma = 24 \mu m$ for the $25 \mu m$ pitch, and $\sigma = 40 \mu m$ for the $100 \mu m$ pitch. The residual distributions are well centered around zero, which means that the modules were well aligned. Calculating the contribution of the pointing resolution from equation 5.6 for unbiased residuals, for $50 \mu m$ pitch it is $\sigma_{point} = 20 \mu m$, for $25 \mu m$ it is $\sigma_{point} = 22.6 \mu m$, and for $100 \mu m$ it is $\sigma_{point} = 26.6 \mu m$. The $50 \mu m$ pitch from figure 6.19(a&b) and the $25 \mu m$ pitch from figure 6.19(d) show the same residual width of $\sigma \simeq 24$, this indicates to me that the pointing resolution is dominating over the $25 \mu m$ pixels. The contribution of both multiple scattering and pointing resolution convoluted in the residuals indicate the resolution of the results from the Market Survey modules.

Hit efficiency performance

The hit efficiency results of pixel modules from the Market Survey campaign are presented in this section. The modules were measured at DESY with particle beam energy of 5 GeV, tracks were reconstructed with EUTelescope and analysed with Tbmon2. The tuning of the modules was done systematically using the YARR board (see section 4.1.3), and noisy pixels were masked before measurement and all modules were tuned to a mean threshold of 1500 e at 7 ToT to 10 ke. Unirradiated modules were measured at room temperature of about 20°C, and irradiated modules were measured at about -60°C cooled with dry ice. Figure 6.20 shows the in-pixel efficiency map folding the hit efficiency from all pixels into the 4×4 pixel map or 2×8 pixel map as depicted in the sensor geometry to its right. The analysis of these results include the full sensor without any exclusions. For figure 6.20(a), it shows the map for a V6S02 module with $25 \times 100 \mu m^2$ pixel geometry with PT, the module was measured at $V_b = 130 V$ achieving a hit efficiency of 98.01 ± 0.12 . For figure 6.20(b), it shows the map for a V2S14 module with $25 \times 100 \mu m^2$ pixel geometry without PT in biasing structure, the module was measured at $V_b = 75 V$ achieving a hit efficiency of 98.97 ± 0.03 . For figure 6.20(c), it shows the map for a V6S05 module with $50 \times 50 \mu m^2$ pixel

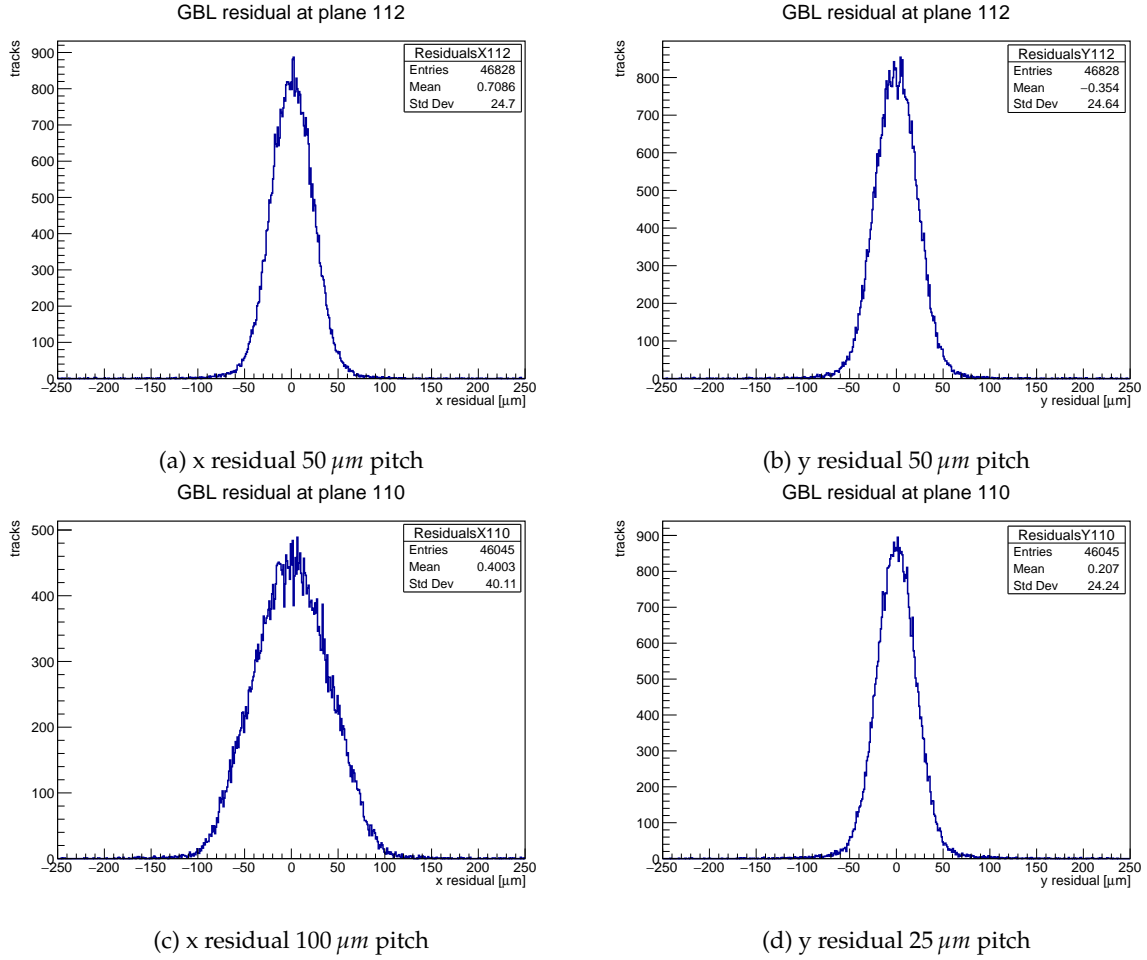


FIGURE 6.19: Residuals for unirradiated ITk pixel MS module hosting 100 μm thick sensor with pixel geometry of $50 \times 50 \mu\text{m}^2$ with no PT (a) x-axis and (b) y-axis, and pixel geometry of $25 \times 100 \mu\text{m}^2$ with no PT (c) x-axis and (d) y-axis. Measurement performed at DESY with particle beam energy of 5 GeV.

geometry with PT, the module was measured at $V_b = 130$ achieving a hit efficiency of $97.12 \pm 0.11\%$. As discussed earlier regarding efficiency loss due to PTs in biasing structure, we can also observe this clearly here in the pixel efficiency maps showing where the PT regions are visible with lower efficiency.

Further, figure 6.21 shows the in-pixel efficiency map for four more unirradiated modules. The modules employ different sensor properties as indicated in each map. Figure 6.21(a&b) show hit efficiency value about 99% at 80 V which agrees well with the ITk requirements. While 6.21(c&d) show hit efficiency at 130 V below the ITk requirement limit for un-irradiated modules. To remind you the unirradiated ITk pixel sensors require to achieve a hit efficiency of $\geq 98\%$, most of the modules agree well with this requirement. Modules that achieve lower hit efficiencies due to their biasing structure, a fiducial region excluding the PT is analysed to check if the fabrication of sensor still comply with requirements. The quoted efficiencies in this section are from the full sensor region.

The MS modules were irradiated to two levels: $2 \times 10^{15} n_{eq}/\text{cm}^2$ and $5 \times 10^{15} n_{eq}/\text{cm}^2$ at the CYRIC irradiation facility in Japan (see Appendix C.4) and were sent back to the DESY testbeam facility to be measured again. It is expected for the hit efficiency to deteriorate after irradiation, but to still comply with the ITk pixel sensors requirements to achieve hit efficiency $\geq 97\%$. Figure 6.22 shows the in-pixel efficiency map for four irradiated modules folding the hit efficiency from all pixels into the 4×4 pixel map. Modules are characterised with 5 GeV particle beam and were tuned to mean threshold of 1500 e

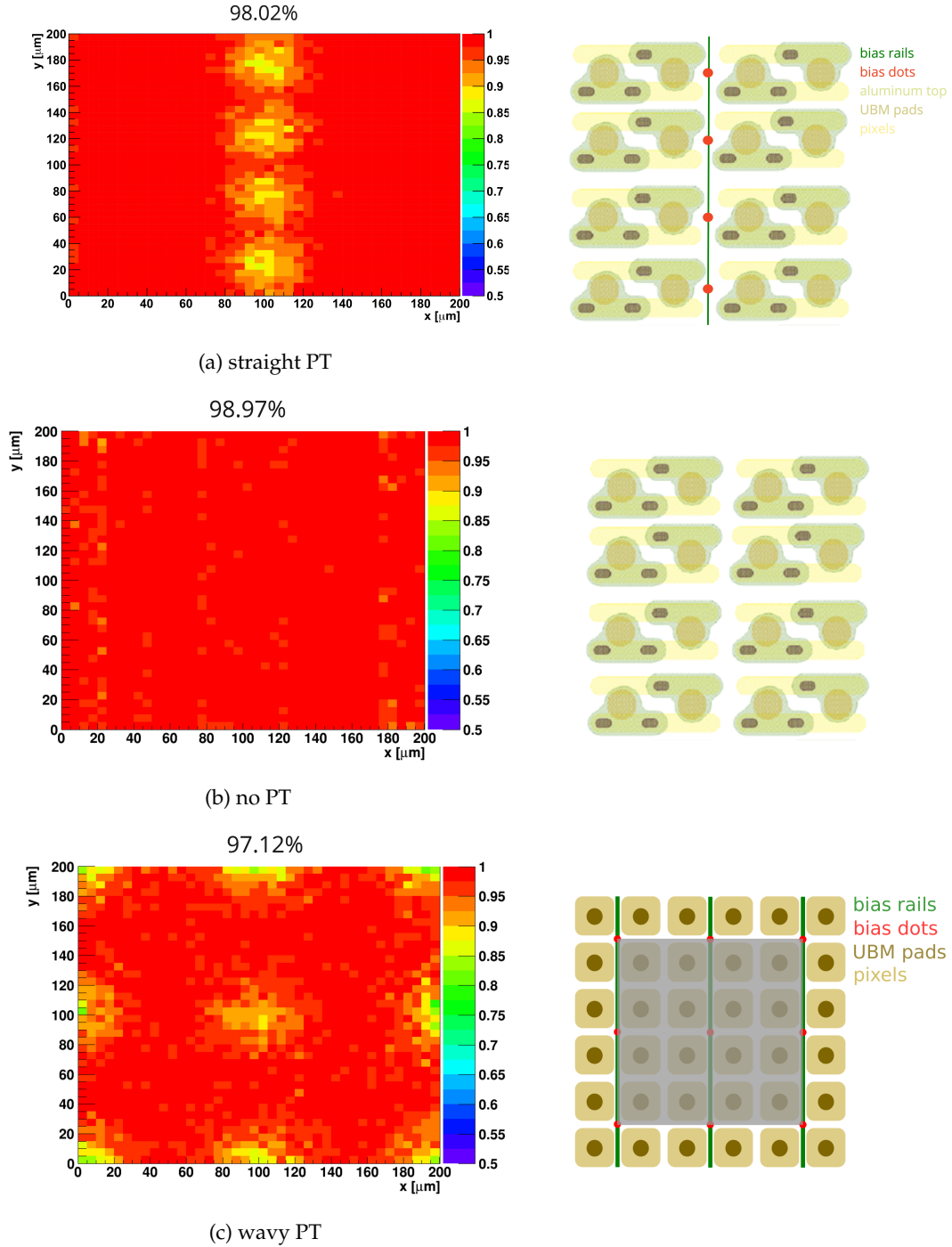


FIGURE 6.20: In-pixel efficiency maps for **unirradiated** MS modules measured at DESY with particle beam energy 5 GeV . Modules are hosting $150 \mu\text{m}$ thick sensor (a) V6S02 with $25 \times 100 \mu\text{m}^2$ with PT measured at $V_b = 130 \text{ V}$, (b) V2S14 with $25 \times 100 \mu\text{m}^2$ without PT measured at $V_b = 75 \text{ V}$, and (c) V6S05 with $50 \times 50 \mu\text{m}^2$ with PT measured at $V_b = 130 \text{ V}$. The hit efficiency of the module is quoted on top, and the sensor bias structure design is depicted on the right side.

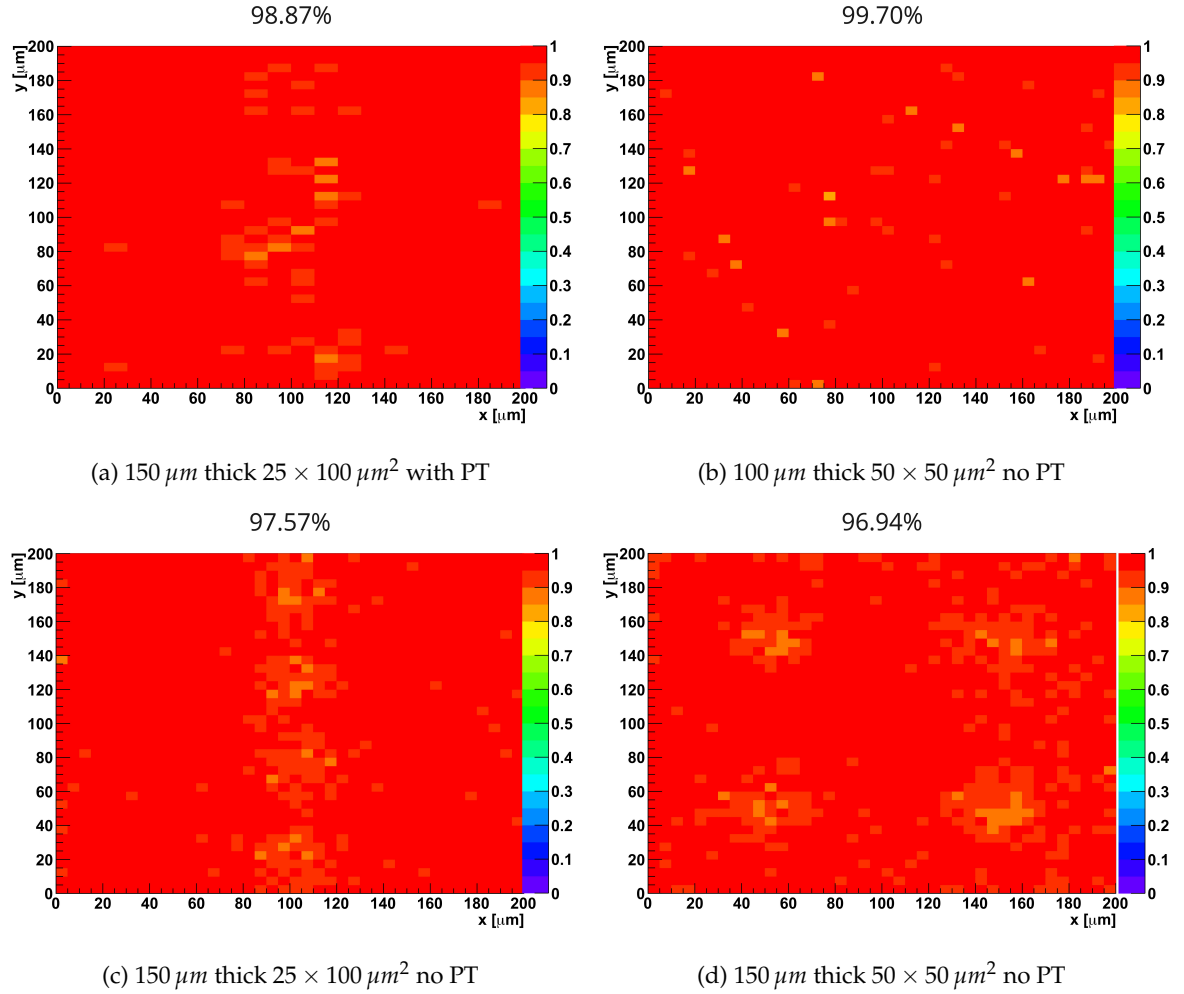


FIGURE 6.21: In-pixel efficiency maps for **unirradiated** MS modules (a) module V3S05 hosting 150 μm thick sensor with $25 \times 100 \mu\text{m}^2$ pixels with PT measured at 80 V, (b) module V3S13 hosting 100 μm thick sensor with $25 \times 100 \mu\text{m}^2$ pixels without PT measured at 80 V, (c) module V6S02 hosting 150 μm thick sensor with $50 \times 50 \mu\text{m}^2$ with no PT measured at 130 V, (d) module V6S04 hosting 150 μm thick sensor with $50 \times 50 \mu\text{m}^2$ with no PT measured at 130 V. The hit efficiency of the module is quoted on top.

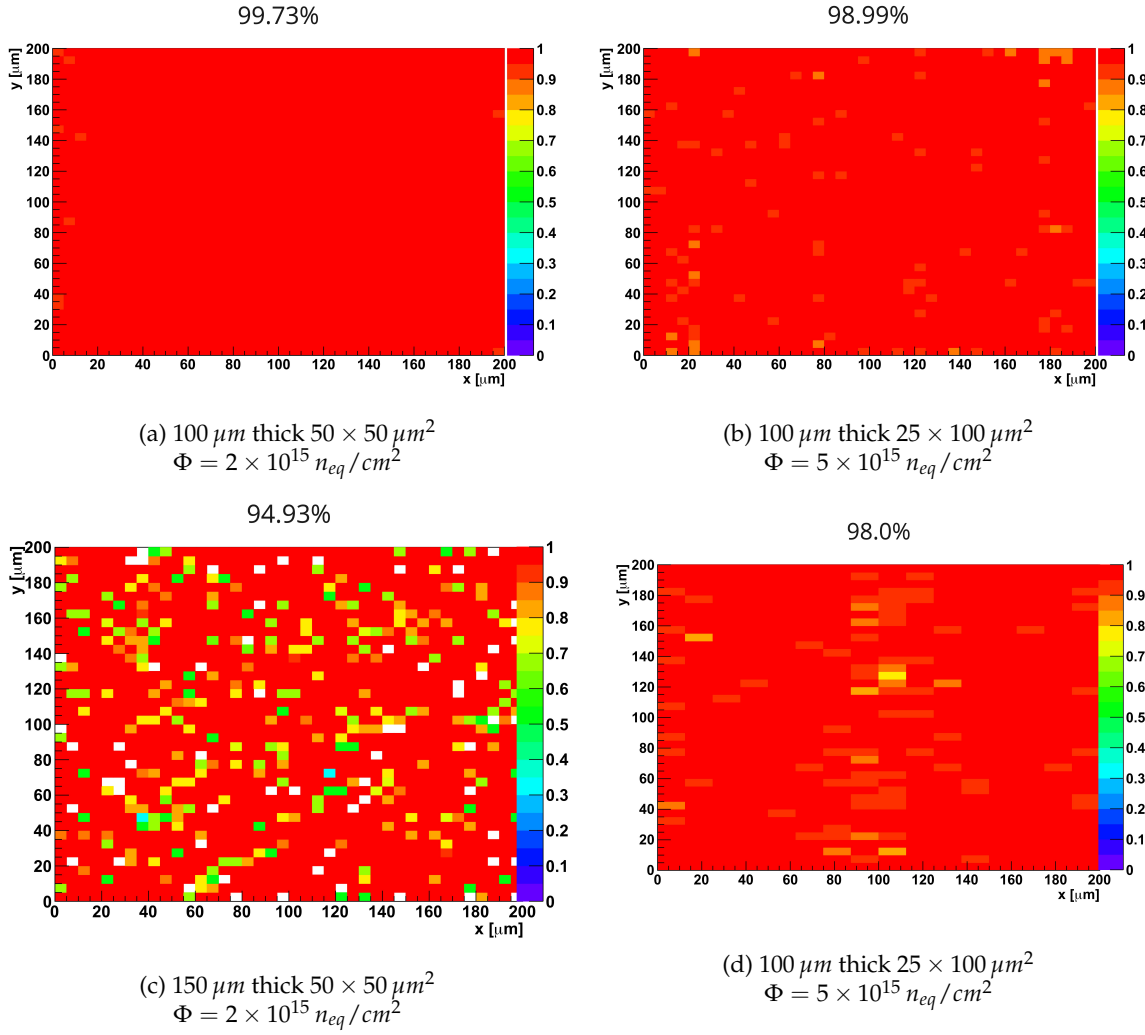


FIGURE 6.22: In-pixel efficiency map for MS **irradiated** modules measured at DESY with particle beam energy of 5 GeV showing map for (a) module V6S11 hosting 100 μm thick sensor with $50 \times 50 \mu\text{m}^2$ pixels with no PT irradiated to $\Phi = 2 \times 10^{15} n_{eq}/\text{cm}^2$ and measured at 300 V, (b) module V3S11 hosting 100 μm thick sensor with $25 \times 100 \mu\text{m}^2$ with no PT irradiated to $\Phi = 5 \times 10^{15} n_{eq}/\text{cm}^2$ and measured at 400 V, (c) module V1S01 hosting 150 μm thick sensor with $50 \times 50 \mu\text{m}^2$ irradiated to $\Phi = 2 \times 10^{15} n_{eq}/\text{cm}^2$ and measured at 400 V. (d) module V3x1026 hosting 100 μm thick sensor with $25 \times 100 \mu\text{m}^2$ irradiated to $\Phi = 5 \times 10^{15} n_{eq}/\text{cm}^2$ and measured at 300 V. The hit efficiency as depicted above the map.

using the bdaq53 board. Figure 6.22(a) shows the in-pixel efficiency map for module V6S11 hosting a $100\ \mu\text{m}$ thick sensor with $50 \times 50\ \mu\text{m}^2$ pixels irradiated to $\Phi = 2 \times 10^{15}\ n_{eq}/\text{cm}^2$ and measured at 300 V. This modules shows a hit efficiency of $99.70 \pm 0.03\%$, which shows very well performance and agrees with ITk requirements. Figure 6.22(b) shows the in-pixel efficiency map for module V3S11 hosting a $100\ \mu\text{m}$ thick sensor with $25 \times 100\ \mu\text{m}^2$ pixels irradiated to $\Phi = 5 \times 10^{15}\ n_{eq}/\text{cm}^2$ and measured at 400 V. This modules also shows good performance and achieves a hit efficiency of $98.97 \pm 0.04\%$. Figure 6.22(c) shows the in-pixel efficiency map for module V1S01 hosting a $150\ \mu\text{m}$ thick sensor with $50 \times 50\ \mu\text{m}^2$ pixels irradiated to $\Phi = 2 \times 10^{15}\ n_{eq}/\text{cm}^2$ and measured at 400 V. The module achieves a low hit efficiency of $94.93 \pm 0.29\%$, which is below the ITk requirements. Figure 6.22(d) shows the in-pixel efficiency map for module V3x1026 hosting $100\ \mu\text{m}$ thick sensor with $25 \times 100\ \mu\text{m}^2$ irradiated to $\Phi = 5 \times 10^{15}\ n_{eq}/\text{cm}^2$ and measured at 300 V achieving hit efficiency of $98.03 \pm 0.09\%$, which is in well agreement with ITk requirements.

Results from measured modules surveying the variety of thickness, biasing structures, fluences, including unirradiated modules, are summarised in table 6.5 with module and measurement details.

TABLE 6.5: Summary of the hit efficiency results from MS modules. Modules were tunes to mean threshold of $1500\ e$.

Fluence [$\times 10^{15}\ n_{eq}/\text{cm}^2$]	Name	Pixel geometry [μm^2]	Thickness [μm]	Biasing structure	Voltage [V]	Efficiency [%]
unirradiated	V3S13	50×50	100	TM	80	99.8 ± 0.1
	V6S04		150	PT	50	97.57 ± 0.03
	V3S05	25×100	150	PT	130	98.87 ± 0.1
	V3S06* ¹⁴		150	PT	80	99.94 ± 0.03
2	V6S11	50×50	100	TM	300	99.73 ± 0.03
	V1S01		150	–	400	94.93 ± 0.29
	V3S01*		150	TM	400	99.81 ± 0.03
	V4S01*		150	–	400	98.93 ± 0.03
	V2S11	25×100	100	–	300	92.03 ± 0.4
	V2S05*		150	–	400	99.43 ± 0.1
	V6S02		150	–	400	91.74 ± 0.1
5	V1S02	50×50	100	PT	400	98.9 ± 0.0
	V1S03		150	–	400	98.5 ± 0.01
	V3S02*		150	TM	400	99.91 ± 0.03
	V4S03*		150	–	600	99.86 ± 0.03
	V3S11	25×100	100	TM	300	98.97 ± 0.04
	V3x1026		100	TM	300	98.03 ± 0.09
	V6S03*		150	–	400	97.20 ± 0.04

The hit efficiency results in table 6.5 are quoted in Green if they are in well agreement with the ITk requirements, and in Red if they are below the required efficiency. The presented efficiencies are analysed with the full pixel geometry. Most of the modules in general are in well agreement especially if analysed within a fiducial region excluding the PT region from the analysis. After studying the results from all modules, and making sure they are free from systematic errors, the modules are qualified and hence the producing foundry is also qualified for the production of ITk pixel sensors. The first batch of the ITk sensor production will be assembled with the ITkPixV1 readout chip, which is the second version of the RD53A chip integrated fully with the differential analog FE (see section 3.2.3). The preproduction modules will again follow the qualification process of assembly and characterisation illustrated in section 3.3.4 in LPNHE laboratory.

6.2.3 Future thin sensors production

The planned Future Circular Collider (FCC) will be hosted in a 100 km tunnel planned to be built at CERN on the legacy of the LHC [172]. The highly ambitious integrated program of the FCC would operate on multiple center of mass energies up to 100 TeV of proton-proton collisions to achieve exhaustive understanding of the Standard Model and beyond. Detectors operating at the highest luminosity will require strategic R&D to progress the design to a highly versatile detector. Thin silicon sensors for tracking detectors are potential candidates to tolerate high levels of radiation. Thin sensors perform better at higher irradiations because they accumulate less radiation damage due to their small thickness (refer to section 2.4.1). With less radiation damage the signal of the traversing particle reaches the electrode faster. For this reason, sensors with 50 μm thickness are produced to investigate and advance their performance from current technologies as a starting point. The electrical properties of the investigated 50 μm thick sensors were discussed in section 6.1.2 before and after irradiation. In this section I discuss their performance before irradiation characterised at DESY with a particle beam at energy of 5 GeV in perpendicular incidence.

The presented modules are not planned for the ATLAS ITk and therefore they do not need to follow the ITk sensor requirements. The performance of the investigated sensors are purely R&D. All presented results in this section are obtained from unirradiated modules hosting 50 μm thick sensors with $50 \times 50 \mu\text{m}^2$ pixel geometry, produced from FBK¹⁵ and assembled with the RD53A readout chip. The analysis was carried on both linear and differential front-ends together excluding the synchronous front-end of the chip. The reconstruction of the tracks was performed in the same way as previous results using EUTelescope software (see section 5.4.1) and analysed with Tbmon2 to extract the efficiency (see section 5.4.2).

Spatial resolution

All investigated 50 μm thin sensors have the same pixel geometry of $50 \times 50 \mu\text{m}^2$. Before presenting the hit efficiency results, I discuss the spatial resolution of the modules after track reconstruction. The residuals width of 50 μm pitch is expected to be the $\sigma_{int} \simeq 15$ convoluted with the pointing resolution and multiple scattering effects. Figure 6.23 shows the residuals on x- and y-axis for the W50_17 module having residual width of $\sigma \simeq 27 \mu\text{m}$ on both axes. The residual distributions on both axes are well centered around 0, which means the modules are well aligned. The residuals show a spatial resolution about 55% larger than the intrinsic resolution of the pixel. From equation 5.6 for unbiased residuals I calculate a standard deviation of $\sigma = 22 \mu\text{m}$ as a contribution from the pointing resolution¹⁶. Setting a large residual cut in the track reconstruction, for example: accepting a track extrapolated within 500 μm of the hit, lead to accepting more tracks and hence worsen the resolution of the DUT. These residuals are achieved after 3 iteration of aligning the sensor planes for best track fit. The reconstructed tracks are filtered in the post reconstruction analysis in Tbmon2 by a χ^2 cut. A compromise on the residual cut or/and iterations between track reconstruction and analysis could be beneficial to achieve better spatial resolution, although the efficiencies remain high as will be presented in the following.

Hit efficiency studies

As previously discussed in the performance of R&D modules of ITk in section 6.2.1.2, the bias voltage and the biasing structure design of the sensors impact its overall performance. The hit efficiency as a

¹⁵<https://www.fbk.eu/en/>

¹⁶The contribution from multiple scattering is included in the pointing resolution

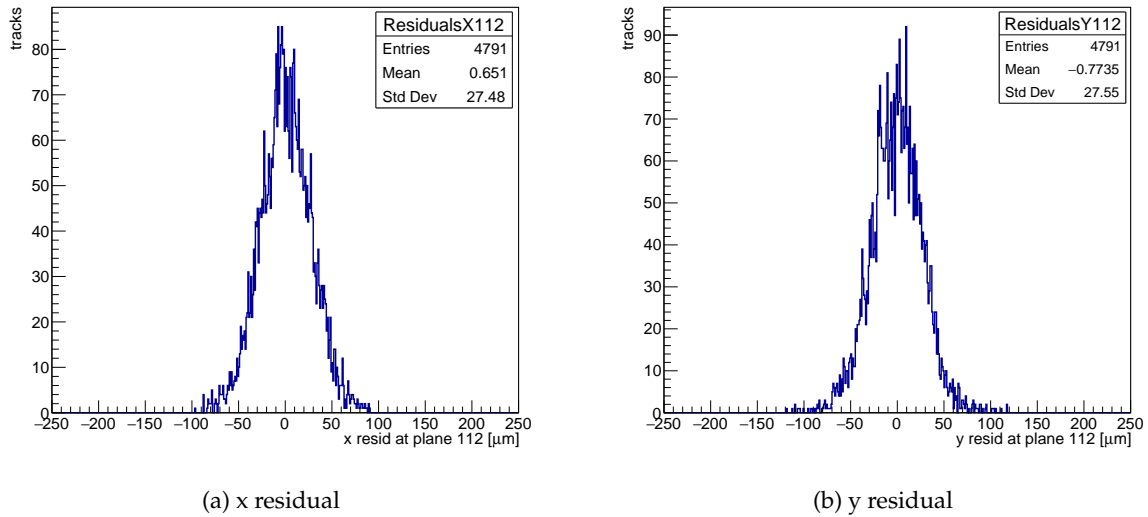


FIGURE 6.23: Residuals for a $W50_{17}$ unirradiated module hosting a $50\text{ }\mu\text{m}$ thin sensor with pixel geometry of $50 \times 50\text{ }\mu\text{m}^2$ showing (a) residual in x-axis and (b) residual in y-axis. Measurement performed at DESY with particle beam energy of 5 GeV .

function of the bias voltage for the modules hosting $50\text{ }\mu\text{m}$ thick sensors with $50 \times 50\text{ }\mu\text{m}^2$ pixel geometry are shown in figure 6.24 only before irradiation. Unfortunately, although the aim was to investigate thin modules after irradiation, the characterisation of the modules after they have been irradiated could not take its course to be included in this thesis due to the global pandemic. Figure 6.24 compares the hit efficiency performance of four modules with different biasing structure design: with wavy PT design in the biasing structure of the pixels surrounded by a $450\text{ }\mu\text{m}$ thick strip of guard rings around the pixel matrix, plotted in Red & Cyan, similar wavy PT design but surrounded by a $250\text{ }\mu\text{m}$ thick strip of guard rings around the pixel matrix, plotted in Green, and a sensor with no PT in the biasing structure using the temporary metal technique surrounded and by a $250\text{ }\mu\text{m}$ thick strip of guard rings around the pixel matrix, plotted in Blue. All the modules were tuned to a mean threshold of $1000\text{ }e$ using the bdaq53 board.

The module $W50_{61}$ with wavy PT and $450\text{ }\mu\text{m}$ thick guard rings in Red shows $95.4 \pm 0.08\%$ hit efficiency at the highest bias voltage of 120 V . The biasing structure with PT in this module induce some efficiency loss. The errors on the hit efficiency are smaller than the plotted marker to appear on graph. The hit efficiency for this module saturates at about 50 V , which is compatible with the operational characteristics indicated by the IV characteristics of the sensor shown in figure 6.3. At 20 V the sensor is about 60% depleted and hence the low efficiency. The module $W50_{17}$ with the same design in Cyan shows hit efficiency fluctuating around the average 96% achieving a hit efficiency of $94.7 \pm 0.2\%$ at 120 V . The fluctuation of the efficiency is not very clear, it could rise from unforeseen temperature fluctuation during measurement for different bias voltages.

The $W50_{105}$ module with wavy PT and $250\text{ }\mu\text{m}$ wide guard rings in Green shows $98.2 \pm 0.1\%$ hit efficiency at the highest voltage point of 120 V . For this module, as predicted from the IV characteristic of the sensor (figure 6.3) it reaches full depletion at about 100 V , hence high efficiency can be achieved at that bias voltage or beyond.

For module $W50_{11}$ with no PT surrounded by $250\text{ }\mu\text{m}$ thick guard rings in Blue shows the best performance in the highest biasing voltage step achieving a hit efficiency of $99.00 \pm 0.06\%$. The module achieves about 99% hit efficiency at all voltage steps. It shows hit efficiency saturation at 20 V as predicted from the IV characteristics of the sensor, where it is already fully depleted at that point.

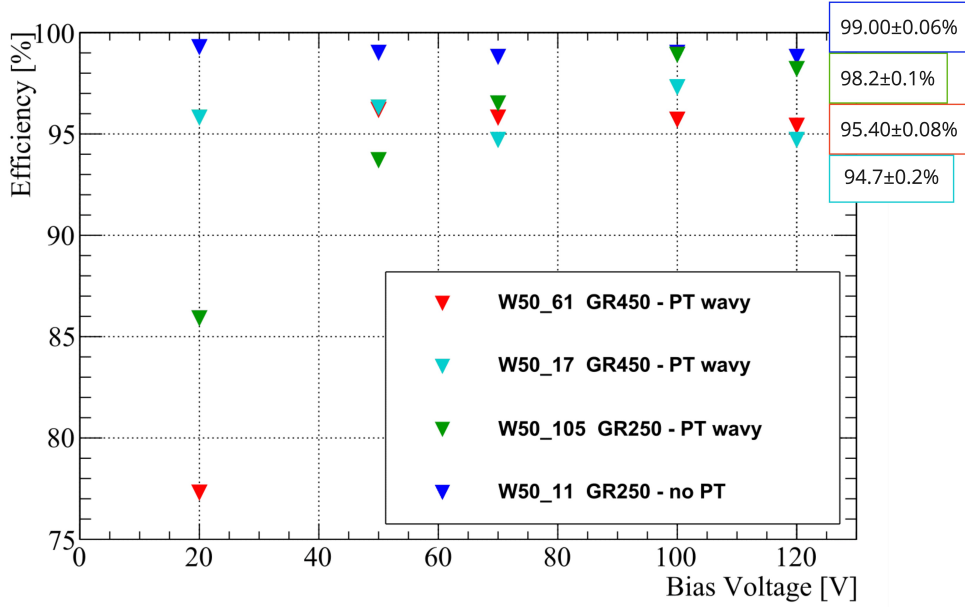


FIGURE 6.24: The hit efficiency as a function of the bias voltage for modules with 50 μm thick sensors characterised at DESY with particle beam energy of 5 GeV. Comparing sensors with different biasing structure designs with and without PT, sensor with no PT shows highest efficiency performance.

Sensors with smaller width of guard rings in their biasing structure have less controlled potential drop and hence higher leakage current. Sensors with no PT in the biasing structure achieve earlier saturation in charge collection and therefore, the highest performance on hit efficiency. The biasing structure design of the sensor shows most impact on the efficiency performance, this can also be visible from the in-pixel efficiency map (see below) where the position of efficiency loss at the PT region is visible. Moreover, the modules show general fluctuations of the hit efficiency around its average value.

For the module with no PT in the biasing structure surrounded by 250 μm thick guard rings, the in-pixel efficiency map at 120 V is shown in figure 6.25(a) folding 4×4 pixels revealing the pixel geometry of $50 \times 50 \mu\text{m}^2$ for the sensor. For a sensor without any biasing in the pixel periphery there are no regions with efficiency loss, as can be seen in the map, achieving highest hit efficiency of about 99% throughout the module. Contrary for the W50_105 module with wavy PT in the biasing structure and surrounded by 250 μm thick guard rings the in-pixel efficiency map is shown in figure 6.25(b). The figure shows four positions of efficiency loss matching the PT regions in a $50 \times 50 \mu\text{m}^2$ pitch sensor. Due to the presence of the PT, the hit efficiency decreases to about 98% for the module. The resolution on the PT position is very low due to the low particle beam energy at DESY where the module was measured. While figure 6.25(c&d) show the in-pixel efficiency for modules with wavy PT and 450 μm guard rings. The PT are also visible in the hit maps showing with low resolution due to low particle beam energy and low statistics of 100,000 events. The hit efficiencies results of this section are summarised in table 6.6.

The aim for thin sensors was to investigate their performance after irradiation. Unfortunately due to global pandemic conditions testbeams are more restricted and the modules were not characterised in due course to be included in this thesis. Overall, for all thicknesses, sensors with no PT in the biasing structure design show the best performance characterised with particle beam. Thin sensors are expected to maintain the high performance at high fluence up to $1 \times 10^{16} n_{eq}/\text{cm}^2$ and higher [178].

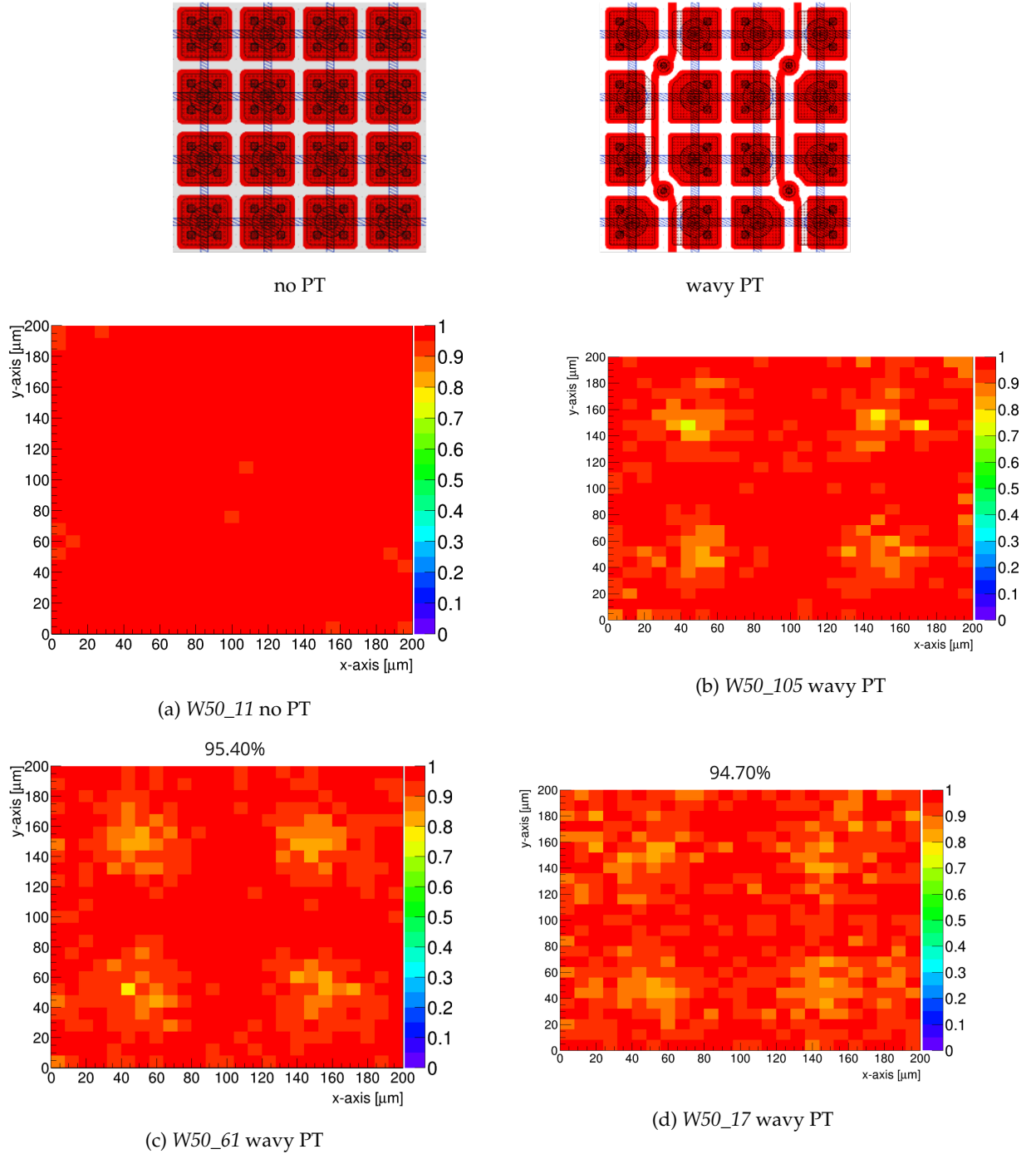
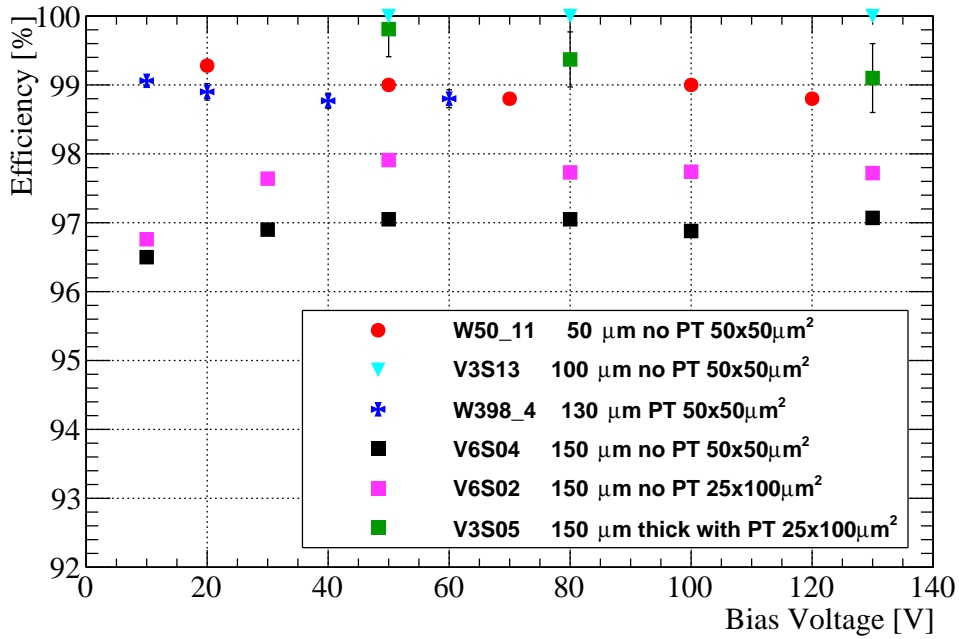


FIGURE 6.25: The in-pixel efficiency map for unirradiated modules with $50\ \mu\text{m}$ thick sensors characterised at DESY with particle beam energy of $5\ \text{GeV}$ at $120\ \text{V}$ for (a) module W50_11 with no PT, (b) module W50_105 with wavy PT, (c) module W50_61 with wavy PT and (d) module W50_17 with wavy PT in their biasing structure.

TABLE 6.6: Summary of the hit efficiencies from unirradiated modules hosting $50\ \mu\text{m}$ thick sensors at $100\ \text{V}$.

Fluence	Module	Pixel geometry [μm^2]	Thickness [μm]	Biasing structure	Voltage [V]	Mean threshold [e]	Efficiency [%]
unirradiated	W50_61	50×50	50	GR450 PT wavy	100	$1000\ e$	95.7 ± 0.1
	W50_17	50×50	50	GR450 PT wavy	100		97.3 ± 0.2
	W50_105	50×50	50	GR250 PT wavy	100		98.9 ± 0.1
	W50_11	50×50	50	GR250 no PT	100		99.00 ± 0.06

FIGURE 6.26: Hit efficiency as a function of the bias voltage for unirradiated modules comparing sensor thickness of $50\ \mu\text{m}$, $100\ \mu\text{m}$, $130\ \mu\text{m}$, and $150\ \mu\text{m}$.

6.3 Effect of thickness for planar pixel sensors

In this section I compare the hit efficiency as a function of the bias voltage for all thickness. Figure 6.26 shows the hit efficiency as a function of the bias voltage for unirradiated modules surveying thicknesses of $50\ \mu\text{m}$, $100\ \mu\text{m}$, $130\ \mu\text{m}$, and $150\ \mu\text{m}$. Presented sensors in the figure are all unirradiated and have mixed pixel geometry of $50 \times 50\ \mu\text{m}^2$ and $25 \times 100\ \mu\text{m}^2$ and mixed biasing structure to survey several samples as detailed in table 6.7. The table sums the details of the sensor thickness, pixel geometry, and biasing design of the module, the mean tuned threshold value for both linear and differential FEs, and the hit efficiency at the highest measured bias voltage.

We observe from the figure and the hit efficiency values at the highest bias voltage that all thicknesses, at least one each, achieve hit efficiency between $98 - 100\%$. For unirradiated modules this agree well with ITk requirements and all previous results for unirradiated modules. Module V3S13 shows perfect performance achieving 99.9% ¹⁷ hit efficiency at all bias voltages. Module V3S05 achieve hit efficiency above 99% , and within the uncertainty it almost matches the performance of module V3S13. While modules V6S02 & V6S04 achieve systematically lower hit efficiency this could be due to some issue during measurement or in track reconstruction as they were both measured together in the same batch. Modules W50_11 & W398_4, which are LPNHE modules produced by FBK, show similar hit efficiency

¹⁷The module shows 100% hit efficiency, but to provide the uncertainty I present the quote efficiency.

TABLE 6.7: Characteristics of the Hybrid modules plotted in figure 6.26 showing the pixel geometry of the sensor, the mean tuned threshold value for linear and differential FE, and the hit efficiency at the highest bias voltage.

Name	Pixel geometry [μm^2]	Thickness [μm]	Biasing structure	Threshold	Efficiency [%]
W50_11	50×50	50	no PT	$1000 e$	98.80 ± 0.04
V3S13	50×50	100	no PT	$1500 e$	99.9 ± 0.01
W398_4	50×50	130	PT	$1060 e$	98.80 ± 0.13
V6S04	50×50	150	no PT	$1500 e$	97.07 ± 0.05
V6S02	25×100	150	no PT	$1500 e$	97.72 ± 0.04
V3S05	25×100	150	PT	$1500 e$	99.1 ± 0.5

statistically fluctuating around 99%. In general we do not observe any systematic effect on hit efficiency specific for different thicknesses nor for different pixel geometry. It does appear that the performance of the modules is more dominant on the fabrication process of the sensor by the production batch in general ,i.e. doping concentration, and on the permanent biasing structure in particular.

Summary and conclusion

In this chapter I discussed the performance of planar pixel modules mainly for ITk prototype sensors and briefly for future thin sensors. To summarize the overall performance of planar pixel modules here I briefly present again the results and also summarize them in a grand table.

The electrical characterisation of sensors, presented in section 6.1, are typically measured before test-beam characterisation to define the operational limits and the quality of the sensor under operation. Sensors of thickness $50 - 150 \mu\text{m}$ achieve full depletion at an average of $V_b = -50 \text{ V}$ before irradiation, while after irradiation the sensor must be operated beyond $V_b = -200 \text{ V}$ to reach full depletion. Higher electric field, i.e. higher bias voltage, applied on the module after irradiation will induce the charge carriers to overcome radiation damaging effects and form the full signal at the electrodes. With higher bias voltage, also the leakage current level increases. Sensors of thickness $100 - 150 \mu\text{m}$ are expected to have leakage current below $5 \mu\text{A}$ before irradiation, while after radiation damage the leakage current level increases considerably up to $\times 10$ more depending on the fluence. Maintaining a low leakage current during measurement is an indication of low noise level to ensure a smooth operation of the module.

There are many variables that affect the hit efficiency for better or worse, the main improvement on the pixel module is the ability to characterise them without having Punch-Through dots throughout the sensor in its biasing structure. Although the biasing structure is necessary for the electrical characterisation to ensure the operation of the module, thanks to the temporary metal technique this metal connecting layer can be removed, allowing the sensor to achieve highest efficiencies at an average of 99% before irradiation and an average of 97% after irradiation. The level of fluence of the sensor does affect the performance of the sensor but at sufficiently high electric field the sensor should regain its full performance capacity. The tuning of the module before measurement could also affect its performance, a high threshold will make the collection of small signals difficult and hence decrease the overall efficiency. Measurements of modules hosting $100 - 150 \mu\text{m}$ thick sensor assembled with the RD53A differential analog front-end are able to reach a mean threshold of $1000 e$ by both YARR and BDAQ53 readout boards. From testbeam experience, tuning and operating the modules at a maximum mean threshold of $1500 e$ will ensure full signal. Tuning an irradiated module below $1500 e$ will increase the noise level. As finally discussed in section 6.3, the performance of the modules is not affected by the thickness of the sensor but rather shows the pixel design as a critical parameter for the performance of the module. With this result

we can say that the fabrication process or the production batch of the sensor has a strong impact on the pixel module performance.

The ATLAS ITk has agreed on a baseline choice of planar pixel modules hosting $100\ \mu\text{m}$ and $150\ \mu\text{m}$ thick sensors employing a pixel geometry of $50 \times 50\ \mu\text{m}^2$. The ITkPix readout chip with differential front-end will be confirmed after characterising the ITk pixels in the first production batch. The pixel geometry of $50 \times 50\ \mu\text{m}^2$ achieves a more symmetric cluster sizes of incident tracks following its symmetrical dimensions. Contrary to the pixel geometry of $25 \times 100\ \mu\text{m}^2$ where the smaller pitch of $25\ \mu\text{m}$ results in some cross talk over the sensor due to the Aluminum layers designed on top of the pixel implants. This cross talk did not show to have major implications on the hit efficiency but the phenomena was observed.

To have a final overall view of the hit efficiency, results are summarised from all production in table 6.8.

TABLE 6.8: Summary of the hit efficiency results for modules from all productions presented in this chapter. Modules are grouped by sensor thickness.

Fluence [$\times 10^{15}\ n_{eq}/\text{cm}^2$]	Name	Pixel geometry [μm^2]	Thickness [μm]	Biasing structure	Voltage [V]	Efficiency [%]
unirradiated	W360_4	25×100	130	no PT	25	97.0 ± 0.6
	W398_4	50×50	130	PT	60	98.8 ± 0.1
	V3S13	50×50	100	TM	80	99.8 ± 0.1
	V6S04		150	PT	50	97.57 ± 0.03
	V3S05	25×100	150	PT	130	98.87 ± 0.1
	V3S06		150	PT	80	99.94 ± 0.03
1.3	W398_5	25×100	130	no PT	600	98.7 ± 0.3
1.7	W398_1	50×50	130	no PT	600	97.7 ± 0.1
3.3	W398_2	50×50	130	with PT	500	95.2 ± 0.1
				no PT		98.4 ± 0.1
3.3	W398_5	25×100	130	no PT	600	98.3 ± 0.3
2	V6S11	50×50	100	TM	300	99.73 ± 0.03
	V1S01		150	–	400	94.93 ± 0.29
	V3S01		150	TM	400	99.81 ± 0.03
	V4S01		150	–	400	98.93 ± 0.03
	V2S11	25×100	100	–	300	92.03 ± 0.4
	V2S05		150	–	400	99.43 ± 0.1
	V6S02		150	–	400	91.74 ± 0.1
5	V1S02	50×50	100	PT	400	98.9 ± 0.0
	V1S03		150	–	400	98.5 ± 0.01
	V3S02		150	TM	400	99.91 ± 0.03
	V4S03		150	–	600	99.86 ± 0.03
	V3S11	25×100	100	TM	300	98.97 ± 0.04
	V3x1026		100	TM	300	98.03 ± 0.09
	V6S03		150	–	400	97.20 ± 0.04
unirradiated	W50_61	50×50	50	PT wavy	100	95.7 ± 0.1
	W50_17	50×50	50	PT wavy	100	97.3 ± 0.2
	W50_105	50×50	50	PT wavy	100	98.9 ± 0.1
	W50_11	50×50	50	no PT	100	99.00 ± 0.06

3532 *"Maybe you are searching among branches for what only appears in the roots "*

3533 Rumi

Chapter 7

Simulated performance of ITk pixel modules

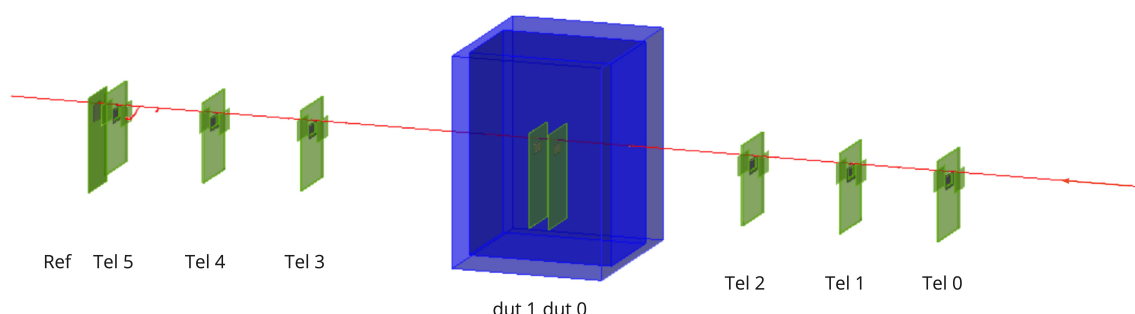


FIGURE 7.1: Simulation setup of ITk pixel modules testbeam showing six telescope planes, one reference plane, two dut planes inside a box, and a trace of the particle beam on z-direction.

This chapter presents simulation results using Allpix² software [179] to study the impact of multiple scattering effects on the ITk pixel module in a testbeam setup. The testbeam characterisation setup is simulated as shown in figure 7.1. The Allpix² simulation software is introduced in section 7.1. The simulation setup mimicking real testbeam conditions is presented in section 7.2. In section 7.3 I present the results of simulated tracks in comparison with testbeam data studying the main parameters that impact the scattering angle. In section 7.3.1 I discuss multiple scattering on the residuals for the EUDET beam telescope, in section 7.3.2 I discuss multiple scattering on the residuals for the ITk pixel sensor geometries, in section 7.3.3 I discuss multiple scattering effects and the material budget included in the setup, and in section 7.3.4 I discuss multiple scattering from particle beam energy. I conclude the chapter in section 7.4 with a summary of the presented results, some considerations on possible further developments are outlined.

7.1 Allpix²

Allpix² is a generic simulation framework for silicon tracker and vertex detectors written in modern C++ [180]. The goal of the software is to provide an easy package to simulate the performance of silicon detectors starting from the passage of ionizing particles through the sensor to the digitization of hits in the readout chip. The Allpix² framework is designed to reflect the physics through the flexibility of the simulation and the user friendly environment.

The framework is configured with text based (human readable) configuration files. Three layers of configuration files are required to run the simulation:

- **main configuration:** is the file that is passed directly to the binary. It contains the global framework and the list of the modules to instantiate together with its parameters.
- **geometry configuration:** it determines the detector setup and passive materials describing the position, orientation, and type of all detectors included.
- **model configuration:** containing the parameters describing a particular type of detector, such as an ITk (or rd53) detector.

The framework is based on the "Modules" that are dynamically loaded and instantiated. They are constructed, initialized, executed and finalized in the sequential order in which they are defined in the main configuration file. These modules include the description of the physics implemented and the parameters to configure them outside their defaults. Modules include the physics processes to propagate the charge, to interface the electric field, and to generate digital signals as will be discussed in the following. A complete, up-to-date, well documented user manual is available in reference [180] describing all available modules and their functionality.

7.2 Simulation setup

There are several simulation examples ready to use as a starting point when installing the Allpix² framework. The examples include a well defined configuration for the EUDET beam telescope with MIMOSA26 sensors (see section 5.2), which are used in the testbeam setup to characterise the pixel modules with high resolution. I contributed a new example in the Allpix² framework named *eudet_rd53a* to simulate the full testbeam setup, and the results are presented in this chapter. The goal of the *eudet_rd53a* example is to simulate the performance of RD53A modules within the testbeam characterisation setup and to study multiple scattering effects with passive and extra material. The example simulates the DESY testbeam setup that is previously discussed in chapter 5.3.2. It includes the already defined EUDET beam telescope, in addition to new defined detector model types; *rd53a_50* for $50 \times 50 \mu\text{m}^2$ pixel geometry and *rd53a_25* for $25 \times 100 \mu\text{m}^2$ pixel geometry where the dimensions, material, and the RD53A readout chip are also defined. The setup can be visualised in figure 7.1, which includes:

- six MIMOSA26 telescope sensors divided in two arms (Tel 0-5).
- one box of passive material where the DUTs are mounted.
- two RD53A modules inside the box with pixel geometry of $50 \times 50 \mu\text{m}^2$ and $25 \times 100 \mu\text{m}^2$ (DUT 0-1).
- one FE-I4B module for reference detector attached to the last telescope plane (Ref).
- a particle beam that passes through the center of the detectors.

The details of the configured modules included in the *eudet_rd53a* to instantiate the physics for this setup is discussed in the following.

Model configuration

The model configuration file is where the devices are defined. The ITk planar pixel module type is defined with both pixel geometries in `'rd53a_50.cfg'` and `'rd53a_25.cfg'`. They are defined with $150\ \mu\text{m}$ thick sensor with $\text{col} \times \text{row}$ accordingly for each geometry as was also discussed in chapter 3.2. The sensor is attached to a $400\ \mu\text{m}$ thick readout chip that is supported by $500\ \mu\text{m}$ thick Aluminum plate to hold the hybrid module to the PCB. The readout chips are produced on a $700\ \mu\text{m}$ thick wafers that were thinned to $400 - 450\ \mu\text{m}$ for the majority of the RD53A chip used in testbeams. Readout chips for the final ITk pixel detector, the ITkPixV2, are planned to be thinned down to $150\ \mu\text{m}$. More RD53A readout specifications are defined in the digitization part on the main configuration of the simulation.

Geometry configuration

The geometry configuration describes the positions and orientation of all included planes in the setup, similar to the GEAR file in EUTelescope reconstruction (see section 5.4.1). The simulation setup is very similar to the characterisation setup used for the ITk planar pixel module Market Survey campaign at DESY having the particle beam source at about $3\ \text{m}$ away from the first telescope plane on the z-direction. All planes are fixed to have perpendicular incidence of the beam. The telescope planes in one arm are separated by $10\ \text{cm}$ and have about $30\ \text{cm}$ in between the upstream and downstream arms to fit the DUTs. The telescope geometry used in the simulation results presented in this chapter are summarised in table 7.1. The FE-I4B reference plane is attached to the last telescope plane in the downstream arm. The cooling

TABLE 7.1: Positions of the telescope planes and DUTs on the z direction used in the simulation setup.

reference	Tel 5	Tel 4	Tel 3	DUT 2	DUT 1	Tel 2	Tel 1	Tel 0	plane
835	793	681	571	390	355	200	100	0	z-position [mm]

box is simulating the DoBox built by Dortmund university [155] placed in the DESY testbeam facility, which is built from PPO foam passive material. The two RD53A DUTs are positioned inside the cooling box in the simulation setup, where the positions of all planes and the thickness of the box can be modified from this file.

Main configuration

The main configuration file describe the modules that are instantiated to simulate the physics of the environment. There are four main stages to describe the physics processes in the simulation chain as shown in figure 7.2. Starting from the energy deposition from the incident beam in *stage 1*. In *stage 2* the charge will propagate the device to reach the electrode. In *stage 3* the signal is formulated and counted as the readout chip does in analog. In *stage 4* finally the signal is digitised to be readout out. Here I describe the each module added to simulate this chain for our described setup in the configured order. A complete, up-to-date, well documented user manual is available in reference [180] describing all available modules and their functionality.

7.3 Simulation-based study on ITk pixel modules

The R&D of ITk pixel module with new designs pushed forward our understanding of the module performance. There are several parameters impacting the resolution and the performance of the pixel module as discussed in the previous chapter. In this chapter I aim to breakdown the parameters contributing to the effects of multiple scattering on the residuals of the pixel modules. The Monte Carlo

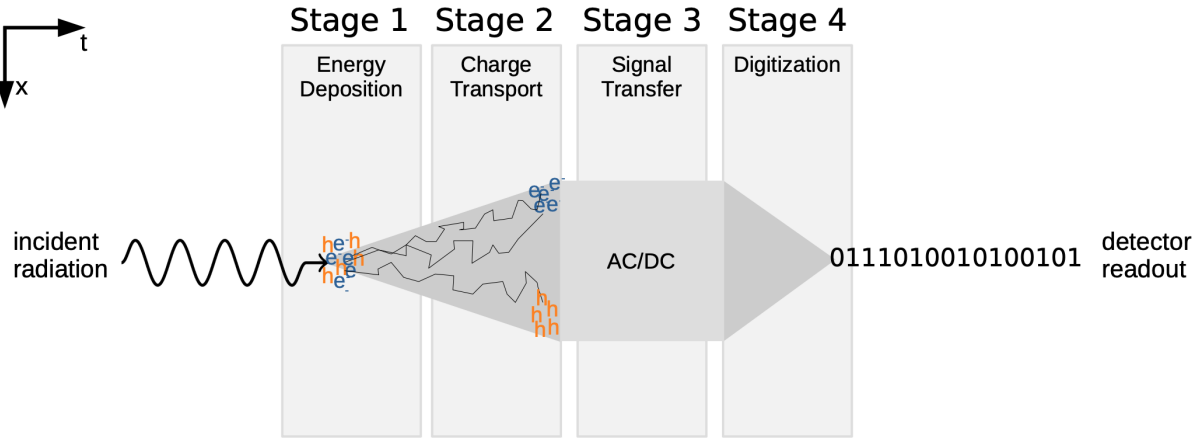


FIGURE 7.2: Allpix² simulation chain starting from the deposition of the energy from the passing particle to propagation and digitisation at the front-end side [181].

(MC) simulated tracks produced from Allpix² are reconstructed using the EUTelescope framework (see section 5.4.1). Uncertainties in track reconstruction are dominated by two sources;

- the limitation in the accuracy of track coordinates measurement, the uncertainty introduced by the alignment.
- the deviations introduced by multiple scattering effects.

The first uncertainty is mitigated when using the same residual cuts as for the testbeam data. The second uncertainty is taken into account in the GBL method in EUTelescope. Under the assumption that the simulation setup is compatible with the real testbeam setup, and in the case both uncertainties are mitigated, I expect that residuals from testbeam data agree well with residuals from simulation. so, within a consistent measurement setup and a consistent treatment for the tracks we should be able to compare results between simulation and data. From this point, I can investigate the effects of multiple scattering from different particle beam energy and different material budgets.

The standard deviation of the angular distribution increases with the increasing material budget, it demonstrates the advantage of using thin sensors. This is specially important towards low-energy beam such as the DESY II testbeam facility with maximum of 6 GeV where multiple scattering is non-negligible. There are two parameters that dominates the effects of multiple scattering in the residuals from equation 5.9

- the velocity and momentum of the particle passing through, i.e. particle beam energy and type.
- material budget, i.e. silicon sensors, support materials, and passive materials.

These parameters will be discussed in the following to set an expectation on the results for the ITk pixel modules.

7.3.1 Validation from telescope planes

The EUDET beam telescope installed in DESY and CERN testbeam facility is a main component in characterising a pixel module with a particle beam. Due to its high resolution we can determine the impact point on the measured DUT with few microns precision to construct the particle's trajectory from measured hits. Therefore, the quality of results depends also on the pointing resolution of the telescope (see

to section 5.4.3). The telescope planes host the $45\ \mu\text{m}$ thick MIMOSA26 sensors that have symmetrical pixel geometry of $18.4 \times 18.4\ \mu\text{m}^2$.

To validate the simulated telescope resolution, I compare the residuals of the simulated telescope planes to the residuals from Market Survey testbeam data in figure 7.3 for upstream planes and 7.4 for downstream planes. The figures extending in the next two pages show superimposed residual distributions between simulated tracks in **Red** and data in **Black** for all telescope planes with the simulation over data ratio plot at the bottom. The residual width σ shows almost identical resolution between x- and y-axis for all planes due to the symmetrical pixel cells of the telescope. The residual width of the simulated tracks ($\sigma_{sim} = 2.83$ for plane 0) are smaller than the binary resolution of the telescope pixel ($\sigma_{int} = 5.2\ \mu\text{m}$) due to cluster size with 2 pixels. They show systematically smaller width than data. This could be due to the perfect alignment of telescope planes in the simulation in contrary to the testbeam setup. This issue will be further investigated with Allpix² developers.

For plane 0 on the x-axis the residual width of the simulated tracks show $\sigma_{sim} = 2.83\ \mu\text{m}$ and for testbeam data $\sigma_{dat} = 3.66\ \mu\text{m}$. Even though the difference is only $0.83\ \mu\text{m}$, it is 27% underestimation from the simulation. The simulation over data ratio plot below the residuals show a peak at the center for larger number of tracks found in the simulation. The ratio plot for planes 1 & 4, which are the middle of the triplet arms, shows only 3% smaller residual widths for simulation. The residuals of the simulated tracks of planes 1 & 4 show three peaks in the distribution that is due to the good intrinsic resolution of the telescope planes and misalignment effects that are not simulated. Also, increasing uncertainties at the edges of the ratio plots distribution indicate multiple scattering effects for the smaller fraction of tracks.

There are six telescope planes arranged in two arms as shown in figure 7.1. To observe the overall behaviour on the residuals of the telescope I show the width of the residuals for all planes in figure 7.5 having the telescope number on the x-axis and the width on the y-axis. The plots in the figure show the residual width for simulated tracks setup with the DUTs between plane 2 & 3 in **Red**, without having the DUTs between plane 2 & 3 in **Blue**, and for testbeam data in **Black** including DUTs between plane 2 & 3. As shown previously the residuals from the simulation have systematically smaller widths than data. Excluding the DUTs from the setup results in lower material budget and hence smaller scattering angles. In the simulation all the telescope planes are biased. Therefore, the pointing resolution converges closer to the intrinsic resolution. The tracks are reconstructed with GBL method, the overall material budget is taken into account resulting into lower residual widths for the telescope planes. For testbeam data, planes 0 and 5 are fixed and the rest of the telescope planes are adjusted by minimization. The DUTs are unbiased in the track reconstruction. So the telescope planes close to the DUTs compensate in the deflection angle and show higher residuals. We can observe that planes 2 & 3, which are closest to the DUTs, curve up on the y-axis with increasing residual width. As discussed earlier in the GBL-fitting procedure (see section 5.2), the telescope planes are aligned in two arms and then the track is fitted through 9 planes matching the hits on the DUTs. The hits on telescope 1 & 4 benefit from precise fitting from GBL because they are the center planes of the triplets. planes 2 & 3 have largest residual widths as they benefit neither from fixed position nor precise refitting, in addition to having closer range to the DUTs and farthest distance from the biased planes. The residuals of telescope plane 3 are wider as the plane itself is downstream with respect to the DUTs convoluting the impact of multiple scattering on from the two DUTs in the middle.

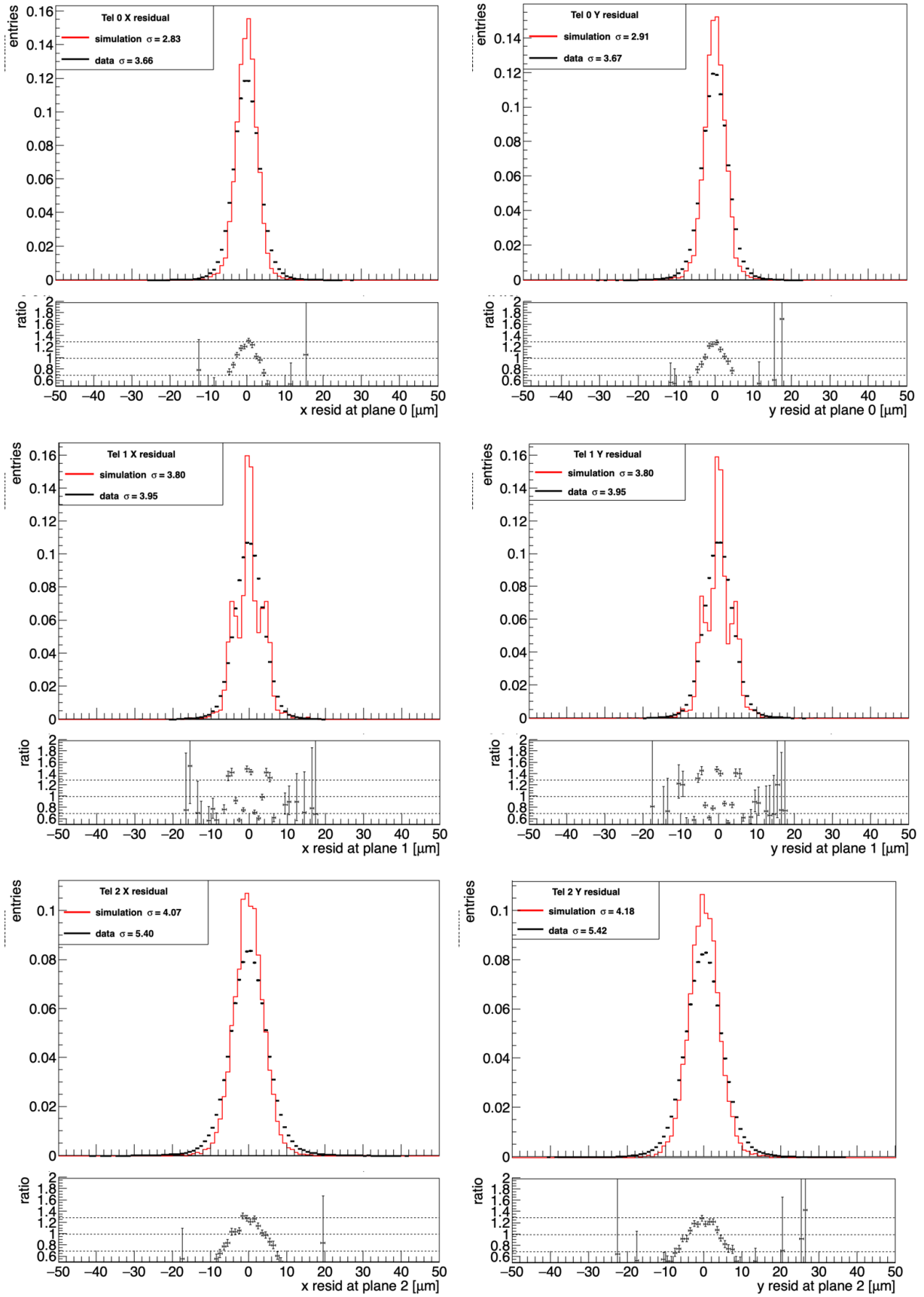


FIGURE 7.3: Comparison of residuals of MIMOSA26 sensors between simulation (Red) and testbeam data (Black) for upstream telescope planes. X residuals on the left and Y residuals on the right. Simulated tracks show systematically smaller standard deviation σ than testbeam data. The simulation over data ratio plot shows a peak with higher number of hits and increase of multiple scattering effects at the ends of the Gaussian distribution for smaller hits.

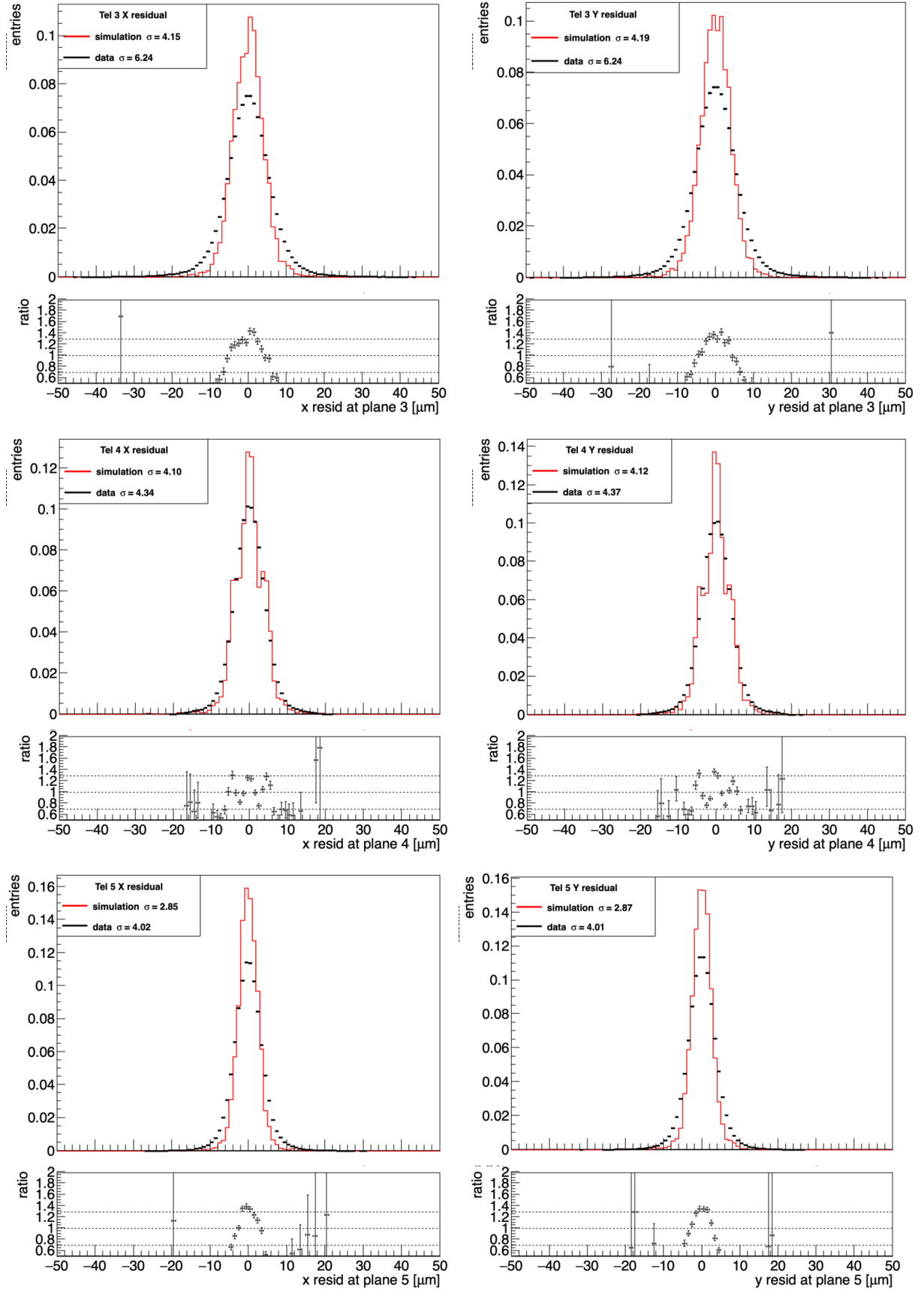


FIGURE 7.4: Comparison of residuals of MIMOSA26 sensors between simulation (Red) and testbeam data (Black) for downstream telescope planes. X residuals on the left and Y residuals on the right. Simulated tracks show systematically smaller standard deviation σ than testbeam data. The simulation over data ratio plot shows a peak with higher number of hits and increase of multiple scattering effects at the ends of the Gaussian distribution for smaller hits.

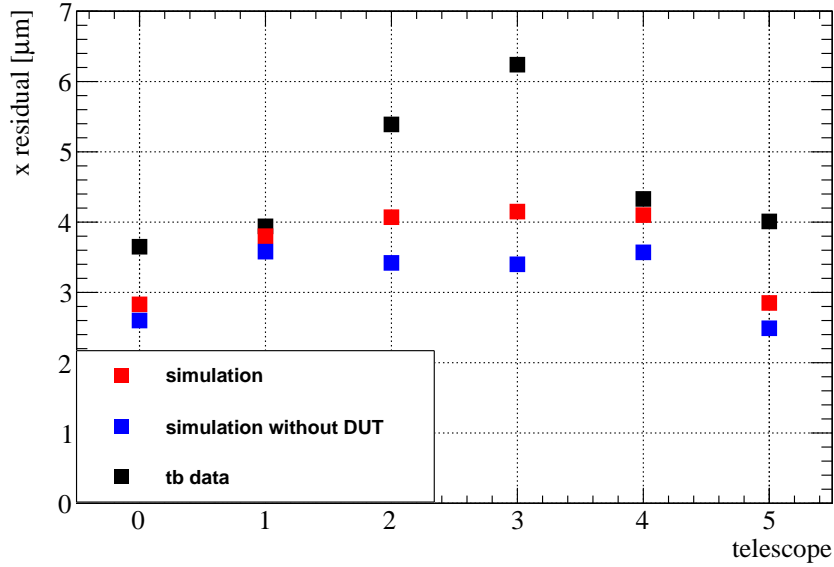


FIGURE 7.5: Residuals of the MIMOSA26 sensors from 0-5 comparing the standard deviation σ of simulated tracks in setup with DUTs included, without DUTs included, and testbeam data with DUTs included. The two planes of DUTs are positioned between telescope 2 and telescope 3.

Having almost identical x residuals for planes 1 & 4 is an indication of a first validation of the setup and reconstruction method. The scattering angles on planes 1 & 4 are corrected by using the GBL method in the alignment. Hence, the simulated tracks show better pointing resolution closer to the intrinsic resolution in comparison to data. The largest difference on residuals between simulation and data on telescope plane 3 is about 33%. This increase of residual width due to multiple scattering in data or underestimation of multiple scattering by simulation is projected on the resolution of the biased residuals of the telescope planes and on the DUTs. This is considered a non-negligible difference and is discussed with the Allpix² developers to further investigate the simulation process. From this result, I can evaluate the comparison of the residuals for multiple scattering in the following sections expecting the maximum difference in residuals between data and simulation to be within 33%.

7.3.2 Multiple scattering and pixel geometry

The goal of this section is to study the impacting parameters of multiple scattering on the ITk pixel sensor. ITk pixel sensors have two pixel geometries, $50 \times 50 \mu\text{m}^2$ and $25 \times 100 \mu\text{m}^2$. The simulated residual distribution for both geometries is discussed in the following. After validating the simulation setup from the telescope planes in comparison to testbeam data I show now the residuals of the simulated DUTs.

Figure 7.6 shows residuals of a RD53A module hosting a $150 \mu\text{m}$ thick sensor with $50 \times 50 \mu\text{m}^2$ pixel geometry. The figure compares simulated tracks and data produced from 5 GeV electron beam. Both tracks were reconstructed with EUTelescope using the same configuration cuts. The figure shows the residual distribution on both x- and y-axis with the data over simulation ratio plot at the bottom. Both x and y residuals are well centered around zero and are almost identical due to the symmetrical pixel cell having the same Gaussian shape (refer to section 5.4.3). The residuals show almost identical residual width of $\sigma \simeq 20 \mu\text{m}$ for both simulated tracks and testbeam data having 0.6% difference in width. The data over simulation ratio plot shows a compatible result between both distributions with increased uncertainties at the edges indicating multiple scattering only for small fraction of tracks. Compatible

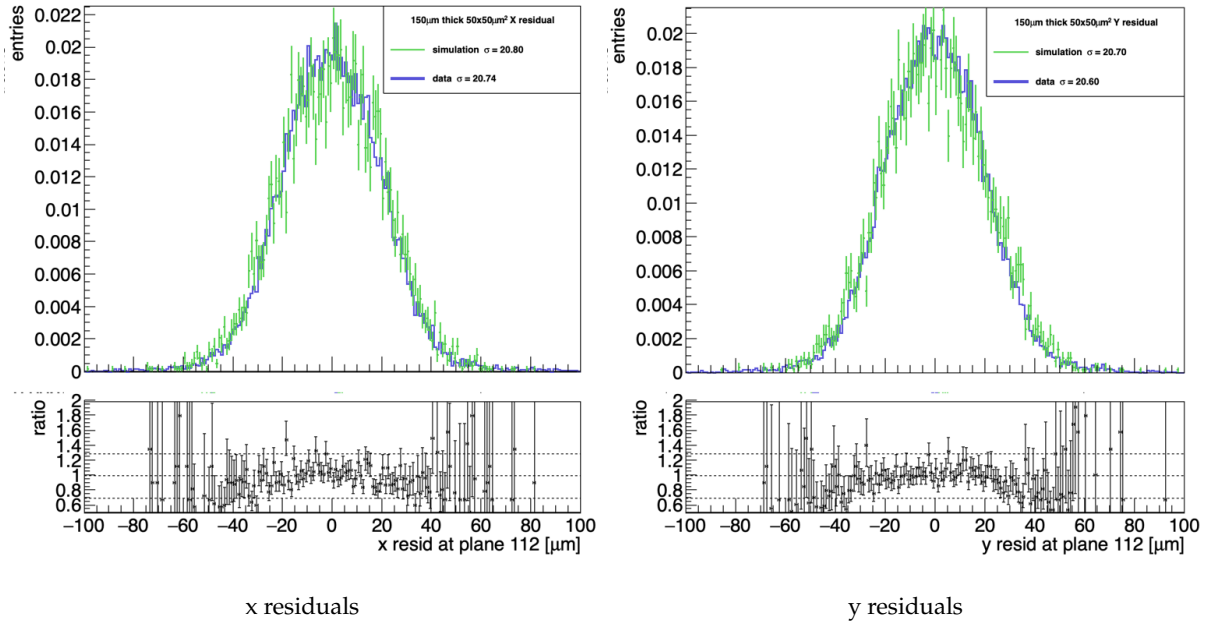


FIGURE 7.6: Residuals from simulated tracks and testbeam data of a RD53A module hosting a $150\ \mu\text{m}$ thick sensor with $50 \times 50\ \mu\text{m}^2$ pixel geometry showing compatible results on both x- and y- axis of $\sigma \simeq 20\ \mu\text{m}$. The data over simulation ratio plot shows compatible results between both residuals. The uncertainties at the edges of the distribution indicate multiple scattering for a small fraction of the tracks.

residuals would validate the used parameters in the simulation to give results close to realistic conditions as testbeam characterisation.

The same comparison for a RD53A module hosting a $150\ \mu\text{m}$ thick sensor with $25 \times 100\ \mu\text{m}^2$ pixel geometry is shown in figure 7.7. The x residuals for the $100\ \mu\text{m}$ pitch show residual width of $\sigma_{sim} = 31.69\ \mu\text{m}$ and $\sigma_{dat} = 32.34\ \mu\text{m}$. The simulation results underestimates the residuals only by 2% compared to data. Within the 25% of multiple scattering results are considered compatible. The simulated tracks show flatter distribution than data indicating better resolution, while data show more of a Gaussian distribution, which indicates the residuals are dominated by the effects of multiple scattering. The data over simulation ratio plot for the x residuals show compatible results between both distributions for most tracks and the ratio increase towards the edges indicating multiple scattering for a smaller fraction of tracks. The y residuals for the $25\ \mu\text{m}$ pitch show residual width of $\sigma_{sim} = 17.66\ \mu\text{m}$ and $\sigma_{dat} = 19.06\ \mu\text{m}$, which is about 7% increase in the standard deviation for data. I also consider this a minor difference and conclude that results are compatible between data and simulation for the $25 \times 100\ \mu\text{m}^2$ ITk pixel module.

Within the uncertainties, I consider the residuals of simulated ITk pixel module compatible with testbeam data having minor differences, less than 10% in residual width on both x- and y-axis. The residuals are well within the limit compared to the unbiased telescope planes and are as expected. The systematically larger residual width of data indicate to me that there is still some discrepancy between the testbeam and simulation setup. But within the uncertainty, compatible results would validate the simulation setup in Allpix² to further study multiple scattering for the ITk pixel module.

7.3.3 Multiple scattering and material budget

The material budget that the beam particles pass through is a dominant parameter to the size of the multiple scattering effect. High energy electrons lose energy by Bremsstrahlung proportional to the scattering

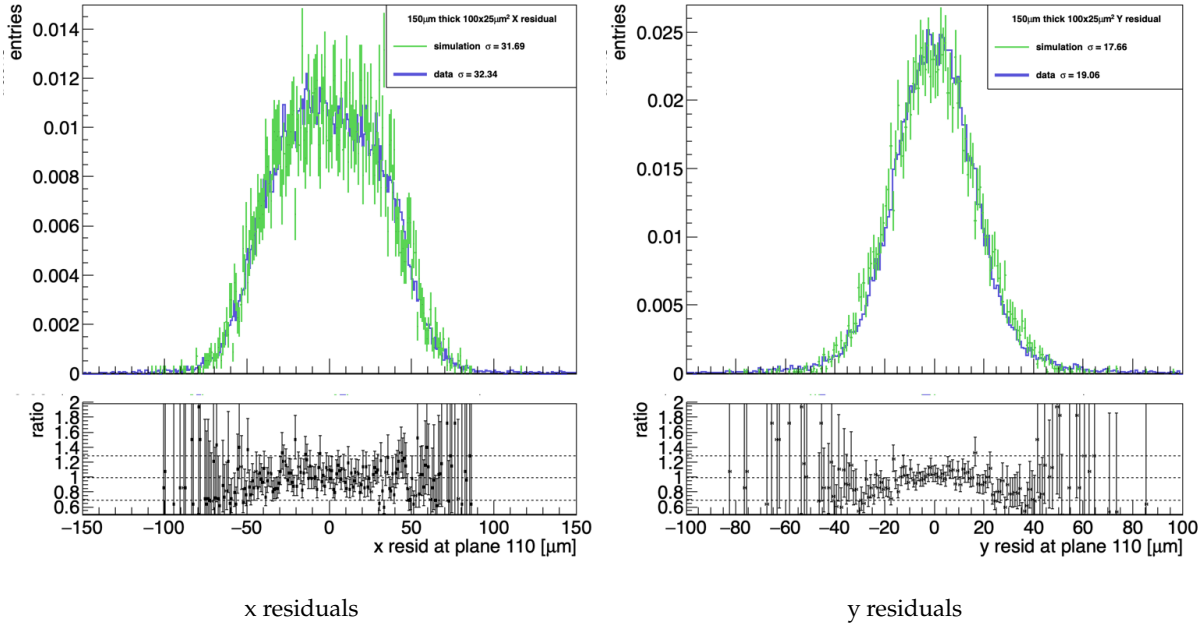


FIGURE 7.7: Residuals from simulated tracks and testbeam data of a RD53A module hosting a $150\ \mu\text{m}$ thick sensor with $25 \times 100\ \mu\text{m}^2$ pixel geometry. The residuals show smaller widths for the simulated tracks having $\sigma_{\text{sim}} = 31.69\ \mu\text{m}$ and $\sigma_{\text{dat}} = 32.34\ \mu\text{m}$ on x-axis and $\sigma_{\text{sim}} = 17.66\ \mu\text{m}$ and $\sigma_{\text{dat}} = 19.06\ \mu\text{m}$ on y-axis. The data over simulation ratio plot shows compatible results and increases at the edges of the distribution indicating multiple scattering effects for a small fraction of tracks.

medium measured in units of radiation length X_0 . As described in equation 5.9 the material thickness in radiation length plays a major role in the scattering angle. In this section I describe all the layers taken into account in the testbeam setup and study their effect independently. The testbeam setup include the telescope planes, the cooling box, the reference frame, and the DUTs inside the cooling box. The DUTs are ITk sensors attached to the RD53A chip and glued on an Aluminum plate holder to be fixed in position in the PCB. table 7.2 summarises the radiation length for each layer.

TABLE 7.2: Details of material budget in the testbeam setup for RD53A modules specifying if the budget is included in the simulation and testbeam data setup.

Layer	Material	Total thickness $x\ [\mu\text{m}]$	density $[g/cm^3]$	radiation length X_0 $[\text{cm}]$	simulation	data
MIMOSA26 sensor shield	Silicon	270	2.328	93.70	✓	✓
	Kapton	300	1.42	285.7	✓	×
ITk sensor RD53A chip support plate	Silicon	150	2.328	93.70	✓	✓
	Silicon	400	2.328	93.70	✓	✓
	Aluminum	500	2.7	88.9	✓	×
DoBox environment	PPO ¹	8000	0.05	—	✓	×
	Air	—	0.00122	30390	✓	✓

The DoBox built by Dortmund university is used to host the measured DUTs to keep them at constant temperature and to shade them from light. It is built from Poly Phenylene Oxide (PPO) foam and it has 4 cm thick walls in the beam direction, i.e. the beam traverses 8 cm of PPO foam in the setup. The PPO foam is included in the Allpix² simulation as passive material. Simulating the performance of a RD53A module hosting a $150\ \mu\text{m}$ thick sensor with $50 \times 50\ \mu\text{m}^2$ pixel geometry with and without the presence of the DoBox shows very compatible residuals as shown in figure 7.8. Due symmetrical pixel cell the x

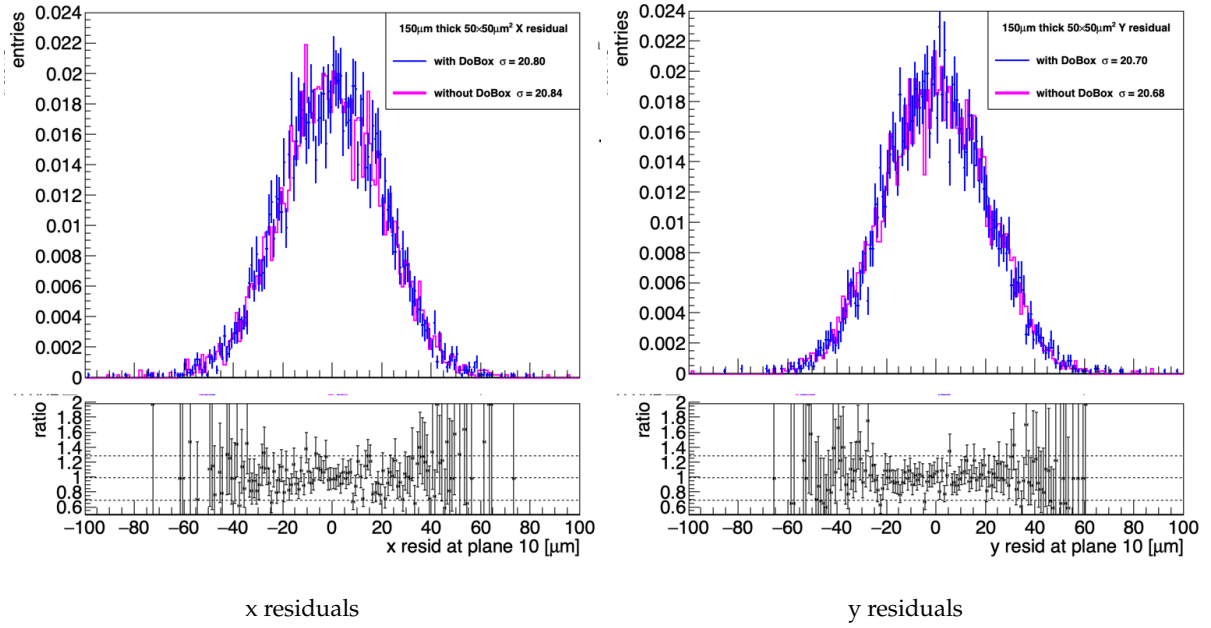


FIGURE 7.8: Residuals of simulated tracks for a $50 \times 50 \mu\text{m}^2$ ITk pixel module testbeam setup with and without the DoBox. The residuals without the DoBox over residuals with the DoBox ratio plot shows no significant difference between the two results.

and y residuals are almost identical. Both x and y residuals show residual width of $\sigma \simeq 20 \mu\text{m}$ without the DoBox. The ratio plot at the bottom for residuals including the DoBox over residuals excluding the DoBox show compatible results. Therefore we can say that the effects of multiple scattering from the DoBox is negligible.

To further investigate the effect of the DoBox several wall thicknesses were simulated. Figure 7.9 shows the residuals standard deviation σ for the modules enveloped by different thicknesses of PPO passive material. The figure shows the residual width on the y-axis and the thickness of the box on x-axis for all ITk pixel geometries $50 \mu\text{m}$, $25 \mu\text{m}$, and $100 \mu\text{m}$. The $50 \mu\text{m}$ pitch on both x and y-axis show overlapping residual width for all thicknesses at $\sigma \simeq 22 \mu\text{m}$. The $25 \mu\text{m}$ pitch shows residual width at $\sigma \simeq 18 \mu\text{m}$, and the $100 \mu\text{m}$ pitch shows residual width at $\sigma \simeq 33 \mu\text{m}$. We can observe that varying the thickness of the PPO foam material from 2 cm to 8 cm for each wall of the box has negligible effects on the width of the residuals and hence, on the scattering angles. This result confirms that the multiple scattering effects from the used DoBox at the DESY testbeam facility is negligible. The observed multiple scattering effects in the testbeam data rise from combination of several other sources such as the other layers of the material budget.

The ITk hybrid module is wire bonded into a PCB and glued on an Aluminum support layer with $500 \mu\text{m}$ thickness as shown in the image of figure 7.10 to hold the hybrid module in the open frame area on the PCB.

The Aluminum plate increases the material budget and I try to quantify it here. Figure 7.11 shows residuals of a RD53A module hosting a $150 \mu\text{m}$ thick sensor with $50 \times 50 \mu\text{m}^2$ pixel geometry with and without the Aluminum support plate holding the hybrid module. The residuals show similar results on both x- and y-axis having an average of $1 \mu\text{m}$ larger in width for the DUT with the Aluminum support. This counts as 5% increase in the residual width due to the Aluminum plate. The ratio plot below the figure showing residuals with the Aluminum plate over residuals without the Aluminum plate shows

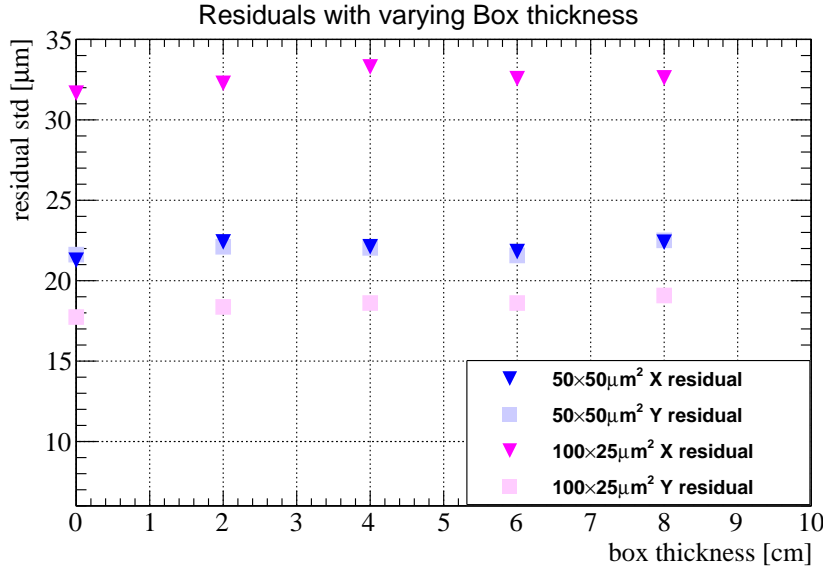


FIGURE 7.9: Residual width of ITk pixel sensors showing all pixel pitch sizes $25\ \mu\text{m}$, $50\ \mu\text{m}$, $100\ \mu\text{m}$ with varying passive material thickness of PPO foam.

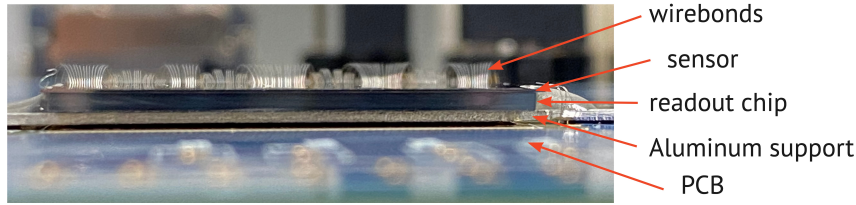


FIGURE 7.10: Cross sectional image of the hybrid module on top of the Aluminum support layer wire bonded to the PCB. Courtesy of MPP institute.

flat distribution between both residuals.

Due to the low energy beam offered at DESY testbeam facility, the setup includes a maximum of 2 DUTs at a time to be measured not to risk worse performance from multiple scattering. The simulation setup in Allpix² allows to easily test for the limits measured DUTs in one batch. Including three DUTs in the DoBox to see the effects of multiple scattering with increasing planes, figure 7.12 shows the residuals for three DUTs superimposed for both x- and y-axis. The RD53A DUTs host $150\ \mu\text{m}$ thick sensor with pixel geometry of $25 \times 100\ \mu\text{m}^2$ characterised with a particle beam of $5\ \text{GeV}$ electrons. We can observe that the residuals of the first and third DUTs for the $100\ \mu\text{m}$ pitch on the x-axis show slightly larger width at $\sigma_1 = 32.33\ \mu\text{m}$ and $\sigma_2 = 32.56\ \mu\text{m}$, while the second DUT shows residual width at $\sigma_2 = 32.87\ \mu\text{m}$. For the y residuals with $25\ \mu\text{m}$ pitch, the second DUT shows the smallest residual at $\sigma_2 = 19.13\ \mu\text{m}$ while the first and third are slightly larger at $\sigma_1 = 18.62\ \mu\text{m}$ and $\sigma_2 = 18.96\ \mu\text{m}$. The variation of the middle DUT is probably due to the compensation of the GBL alignment procedure taking into account the material budget for the included planes. From this result we can conclude that including a third DUT in the measurement at DESY might indeed increase the multiple scattering effects for the DUTs in line but reconstructing with the GBL method would recover the scattering angle by taking into account all the included material budget.

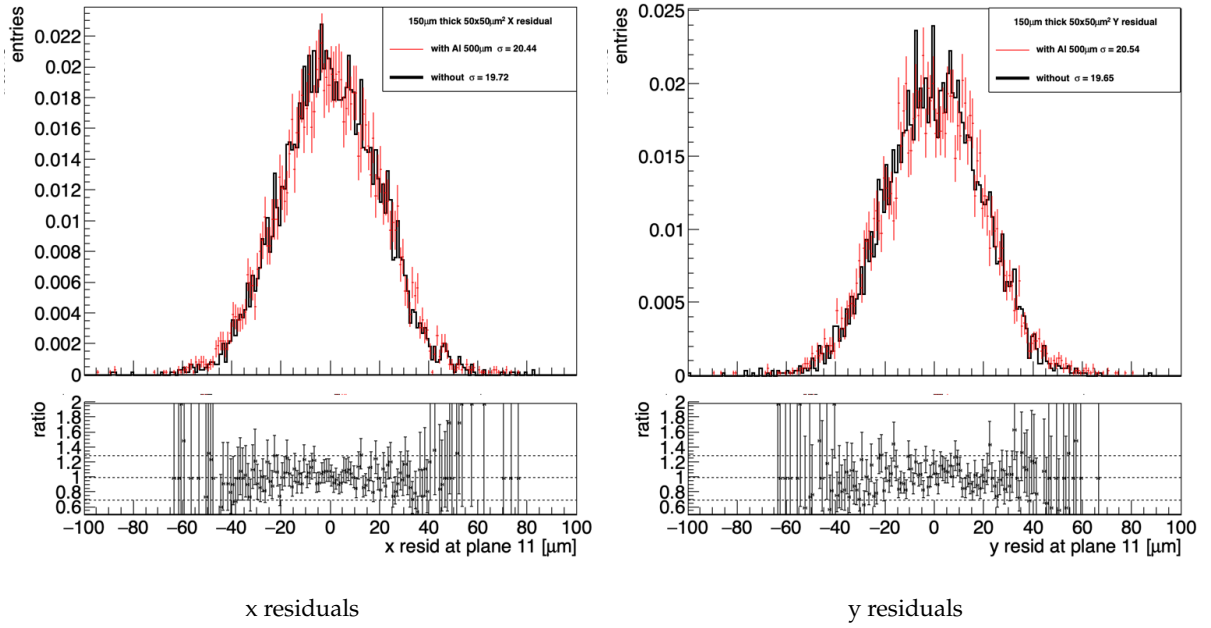


FIGURE 7.11: Residuals of an ITk pixel module including 500 μm Aluminum support plate. Residuals including the Aluminum layer show 5% increase in the residual width.

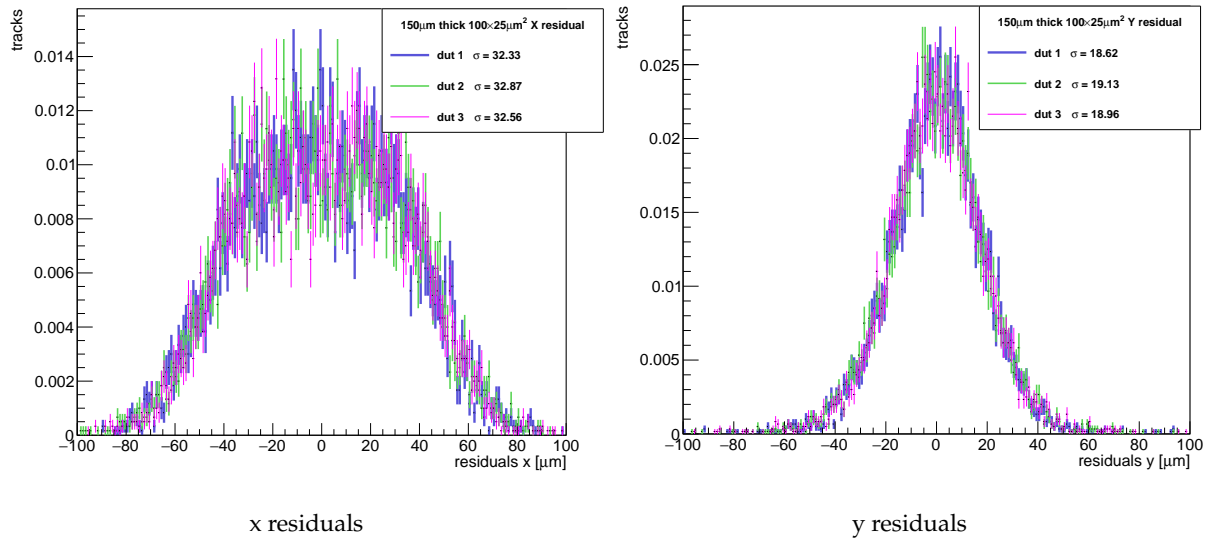


FIGURE 7.12: Multiple scattering of simulated tracks for three DUTs. Residuals reconstructed with GBL method.

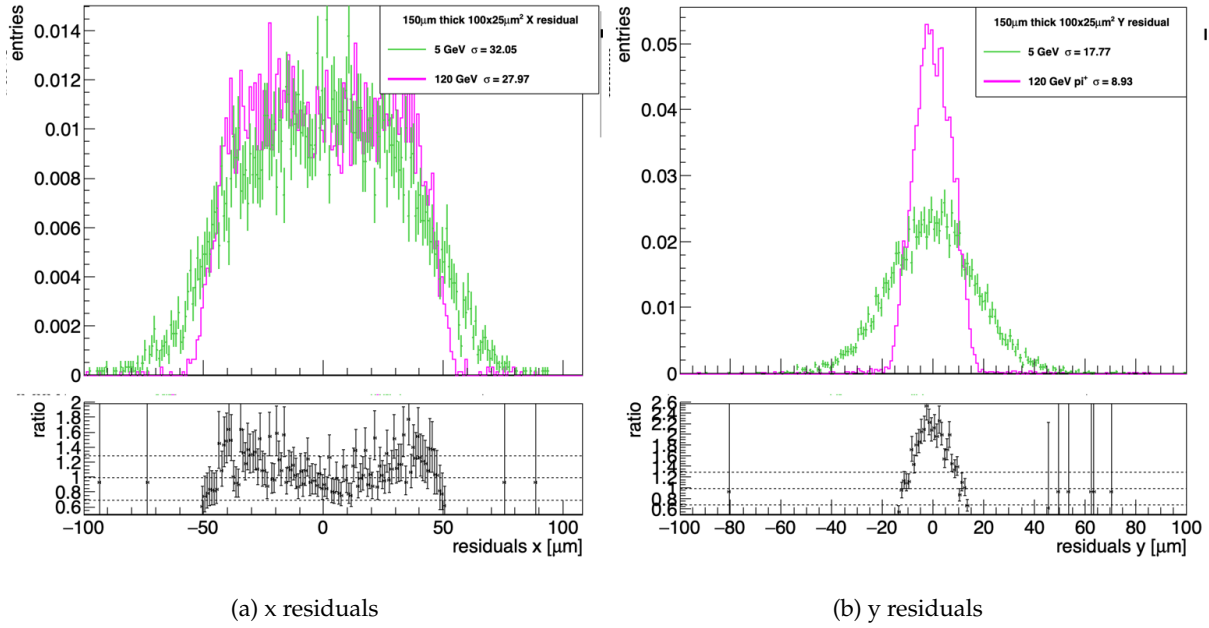


FIGURE 7.13: Ratio between residual distribution of simulated tracks for particle beam energies at 120 GeV over 5 GeV for $25 \times 100 \mu\text{m}^2$ pixel geometry.

7.3.4 Multiple scattering and beam energy

Another impacting parameter on the scattering angle is the particle energy that traverses the material. As previously described in section 5.3, in this thesis there are two testbeam facilities for characterisation with different particle beams; DESY beam line offers 5 GeV electron beam, and CERN SPS beam line offers 120 GeV pion beam. With high beam energy of 120 GeV the high resolution beam is able to resolve geometrical details in the sensor such as biasing structure or the spacing between pixel implants. Also at high resolution the residuals have flat shaped distribution indicating the width of the pixel implant. Therefore, to compare and quantify the effects from the beam energy I plot the ratio between high and low beam energies for all pitch sizes. The residuals of simulated tracks for an ITk pixel module hosting a $150 \mu\text{m}$ thick sensor with $25 \times 100 \mu\text{m}^2$ pixel geometry is shown in figure 7.13. The figure shows superimposed residuals on both axes for 5 GeV of e^- as in DESY, and 120 GeV of π^+ as in CERN with a high energy over low energy ratio plot. The width of the residuals for the $100 \mu\text{m}$ pitch are $\sigma_{5\text{GeV}} = 32.05 \mu\text{m}$ and $\sigma_{120\text{GeV}} = 27.97 \mu\text{m}$. The ratio plot in the x residuals for the $100 \mu\text{m}$ pitch shows a minimum at the center indicating the difference between the flat distribution of the residual at 120 GeV to the Gaussian residual distribution at 5 GeV. At larger residual values the ratio increases up to 1.6. While for the y residuals for the $25 \mu\text{m}$ pitch, the small pitch size increases the scattering angles showing Gaussian residuals for both energies. The width of the residuals for the $25 \mu\text{m}$ pitch are $\sigma_{5\text{GeV}} = 17.77 \mu\text{m}$ and $\sigma_{120\text{GeV}} = 8.93 \mu\text{m}$. The ratio plot shows simulated tracks from 120 GeV over 5 GeV. The residuals from 120 GeV tracks show a peak 2.6 times larger than residual with 5 GeV tracks where multiple scattering effects result into a broader distribution. The spatial resolution improves with increasing beam energy resulting into narrower residuals due to the smaller impact of multiple scattering. As expected this result agrees well with the physics and testbeam data residuals between CERN and DESY validating the used particle energy parameters in the simulation setup.

The same comparison is plotted for the $50 \times 50 \mu\text{m}^2$ pixel geometry in figure 7.14 with high energy 120 GeV over low energy 5 GeV ratio plot. The ratio plot for both x and y residuals comparing beam energy of 120 GeV over 5 GeV show the same behaviour of a flat residual distribution compared with a

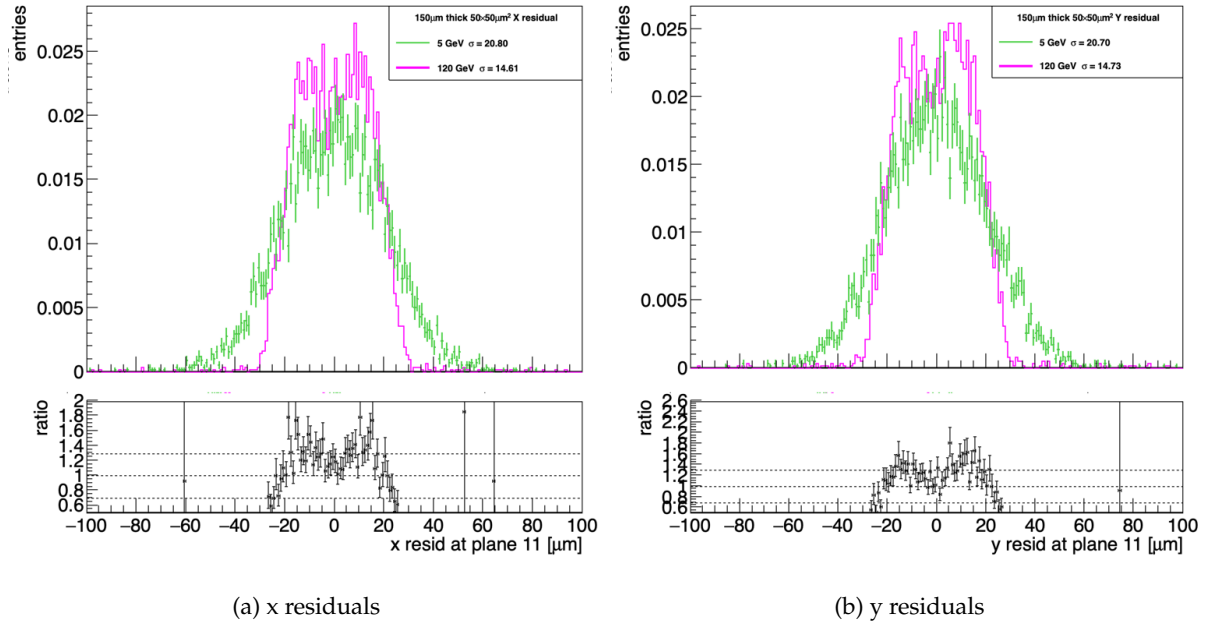


FIGURE 7.14: Ratio between residual distribution of simulated tracks for particle beam energies at 120 GeV over 5 GeV for $50 \times 50 \mu\text{m}^2$ pixel geometry.

Gaussian distribution showing two peaks around the center as the Gaussian distribution drops down. From the ratio plot we can see that the ratio of residuals from 120 GeV tracks are about 1.8 times higher than 5 GeV. The residual width for both x and y residuals are $\sigma_{5\text{GeV}} \simeq 20 \mu\text{m}$ and $\sigma_{120\text{GeV}} \simeq 14 \mu\text{m}$. As expected, the residuals show better resolution for higher beam energy.

7.4 Conclusions and outlook

In this chapter I investigated the effects of material budget and particle energy on multiple scattering within the testbeam setup thanks to Monte Carlo simulation ran using Allpix² tool. Multiple parameters play role to increase the scattering angle in simulation or data taking, but also the alignment procedure in reconstructing tracks plays a major role. From the simulated residuals of telescope planes it seems that the simulation underestimates the multiple scattering effects, or the pointing resolution of unbiased planes producing systematically narrow residuals in comparison to data. The simulated telescope planes are all biased and hence have perfect alignment contrary to the testbeam setup. Further investigation with the developers should help mitigate this discrepancy. The compatibility of telescope residuals between simulation and data is a first step to check for any discrepancy in the setup. The maximum difference shows that the simulated tracks have residual width 33% less than data. This sets a limit to the maximum discrepancy for the measured DUTs.

The ITk pixel module of both pixel geometry $50 \times 50 \mu\text{m}^2$ and $25 \times 100 \mu\text{m}^2$ show compatible results between simulated track and data with maximum difference of 7% in residual width, which validates the setup configuration in Allpix².

The multiple scattering impact from the cooling box, the DoBox, installed in the testbeam facility shows negligible effects on the residuals of the measured DUTs. Also, The ITk hybrid module is supported on a 500 μm thick Aluminum plate that does show an effect of 5% increase in the residual width.

Thanks to the GBL method, it is possible to measure several DUTs simultaneously in the DESY testbeam where the scattering angles will be correcting. The performance of the telescope planes including and excluding the DUTs in between the arms also shows an effect on the pointing resolution. The residuals the telescope planes decreases about 24% excluding the DUTs due to less counted material budget. This indicates that the difference is highly correlated to the alignment procedure not the setup. The residual cuts in the track reconstruction was consistent for data and simulation to allow the comparison even though the configuration could be optimized.

Further, the particle beam energy used for characterising the pixel modules have a major impact on the residuals as shown previously between data obtained at CERN SPS testbeam facility with 120 GeV and data obtained from DESY testbeam facility with 5 GeV. The higher the beam energy is the better the spatial resolution is achieving a narrow flat residual distribution. The decrease of the beam energy results into a fraction of the tracks with higher scattering angles which smears out the precision of the segmentation and resulting into a Gaussian convoluted residual distribution. The small pitch size shows much wider Gaussian distribution relative to the larger pitch. It shows that the 25 μm pitch has 2.6 times larger residual width when characterised with lower particle beam energy of 5 GeV. While a larger pitch of 100 μm and 50 μm show 1.6 and 1.8 times larger residual width at 5 GeV. This shows that the effects of multiple scattering is more relevant for smaller pitch sizes, i.e, small intrinsic resolution.

The complete testbeam setup that I added in the simulation framework is starting point for other users to study the performance of ITk sensors and use it in development. The study of the parameters that have an impact on the scattering angles helps to better understand the obtained results for the ITk pixel module. Both setup details and alignment procedure play major roles in the effects of scattering angles on the planes. The GBL alignment in EUTelescope allows for the measurement of more than 2 DUTs even at DESY with low particle beam energy at 5 GeV with limited impact on the residual. The Aluminum support which contributes to the material budget for the RD53A module could be replaced with a lower density material such as plexiglass in future productions to minimise the scattering angle. Finally, the impact of the DoBox on the residual width of the DUTs is found to be negligible.

3886 *"Never express yourself more clearly than you are able to think."*

3887 Niels Bohr

Conclusion

The discovery of the Higgs boson in 2012 essentially completed the predictions of the SM. But the theory still does not fully answer fundamental questions on the origin of Dark matter, Baryogenesis of the universe, the hierarchy problem, or a description on the inclusion of the gravitational force. The idea is to access rare interactions at TeV scale to access the physics beyond the SM that could potentially lead to answer some of these questions. To detect rare interactions, the LHC will undergo an upgrade schedule to increase the luminosity in 2027 about 7 times greater than its original design transforming it into HL-LHC. Consequentially, the current ATLAS detector will be prone to break under the harsh conditions of the upgrade. For this reason, among other instrumental upgrades, the current inner detector will be completely replaced with a new all-silicon Inner Tracker (ITk). In this thesis I focus on the current and future tracking detector of the ATLAS experiment. My contribution in this thesis introduced a developed tuning method for the current tracking layer, the IBL layer, to operate with better efficiency, and R&D to synthesize the optimal pixel sensor for the future ITk detector.

In chapter 4 I introduced a conclusive study on the characterisation of the readout chip for the current installed IBL sensors. To make sure we have efficient measurement of the energy deposition by the traversing particle in the tracker, the pixel modules must be operated with a well known threshold. In the analysis on Run2 data in 2015-2016 a discrepancy between the measured and the expected charge collection in the IBL modules was reported. To solve this discrepancy, a novel tuning method, the threshold baseline method, is investigated. It is found that the discrepancy of charge collection between left and right regions of the modules emerged after tuning using the charge injection circuitry. The charge injection circuit has a non-uniform behaviour (left-right bias) due to the design of the front-end chip. This bias is compensated by the tuning leading to an asymmetrical tuning in the per-pixel threshold in the module. The novel threshold baseline tuning method depends solely on counting hits, similar to a noise scan occupancy, and therefore, achieves a symmetrical tuned threshold across the pixel module. During the investigation, the charge collection is measured with external source scans to validate that the method records the same number of hits across the whole module. I observed that the threshold baseline tuning method is able to achieve low threshold values, and set a homogenous per-pixel threshold distribution over the whole pixel matrix. In Run2, the IBL detector was operating at tuned mean threshold of about $2500 e^-$. The threshold baseline tuning method is able to bring the mean threshold down to about $1000 e^-$. Having a simplified tuning method that only depends on the noise limit target and rely on counting hits makes the tuning acquire low computational demand. As the tuning algorithm is now implemented in the ATLAS pixel DAQ system, we are able to tune one module but the algorithm must be further improved to tune to the complete detector. It is one step forward towards achieving higher quality of data for Run3.

The core of this thesis revolves around the R&D and the optimization of the future ITk pixel modules to operate in the HL-LHC phase. Two main requirements the ITk pixel must satisfy in the HL-LHC regime: high granularity to maintain tracking performance at high instantaneous luminosity, and high radiation tolerance to maintain the detector's performance at high integrated luminosity. The ITk pixel

detector will be instrumented with $n^+ - in - p$ pixel sensor technology bump bonded into the ITkPixV2 readout chip. The high granular pixel sensors have pixel geometry of $50 \times 50 \mu m^2$ and $25 \times 100 \mu m^2$, which is 10 times smaller than the current pixel detector. This will allow precise tracking with the higher number of events per collision in the HL-LHC. The attached readout chip is also designed with $50 \times 50 \mu m^2$ pixel geometry to comply with the high event rate requirements. The design and assembly of the hybrid pixel module was thoroughly discussed in chapter 3. To study the performance of the hybrid pixel modules they are measured with a particle beam before and after irradiation. Efficient performance of the pixel modules will ensure precise tracking, and hence precise measurements of the physics.

The design and the operation of the hybrid pixel modules was investigated in this thesis. The investigated prototype modules were produced by FBK. The prototype modules were assembled to the first version of the readout chip, the RD53A chip. The RD53A includes linear and differential analog front-end flavours. Both front-end flavours have different tuning parameters to calibrate the chip, but they prove to produce compatible results within the same tuned threshold. The pixel sensor design for the ITk was improved from the sensor design of the IBL. The biasing structure of the sensor is essential to test the sensor before assembling it to the readout chip. Several biasing structure designs to bias the pixel sensor was tested for best performance. The biasing structure design employing a biasing dot is proven to induce efficiency loss in the sensor after assembly with the readout chip. Thanks to the new temporary metal technique, we are able to eliminate the biasing structure in the sensors and achieve full efficient performance. The temporary metal technique enables the electrical characterisation of the sensor only before module assembly and gives us the advantage of a fully operating detector throughout the complete pixel matrix without efficiency loss. The pixel module must achieve hit efficiency of at least 98% before irradiation and 97% after irradiation up to fluence of $\Phi = 5 \times 10^{15} n_{eq}/cm^2$. The radiation tolerance was studied with modules irradiated to different levels of fluences from $\Phi = 2 - 5 \times 10^{15} n_{eq}/cm^2$. Higher fluence would decrease the performance of the module due to radiation damage effects. For this reason the ITk pixel detector is planning a fully replaceable inner layer that can be replaced after integrating half of the target luminosity of the HL-LHC. The performance of the pixel module complying with the ITk requirements leads to the qualification of the module design and production foundry for the preproduction phase of the ITk pixel detector. Results show that pixel sensors from the FBK foundry agree well with the ITk requirements and hence the foundry is recommended for the ITk preproduction.

The improvement of our understanding of the performance results will lead to better operation of the pixel modules. For this reason I contributed in Allpix² software an examples to simulate the performance of ITk pixel sensors with the RD53A readout chip in the testbeam setup. The simulation results in this thesis, in this setup, were produced to study the effects of multiple scattering contributed from the testbeam setup. Residual results from the simulation show compatible performance for sensors with $50 \times 50 \mu m^2$ pixel geometry and achieves less scattering angles as expected for the $25 \times 100 \mu m^2$ pixel geometry in comparison to results from the testbeam data. The effects of passive material from the cooling box at DESY testbeam facility is considered negligible even at 5 GeV particle beam energy. The effect of the aluminum metal that holds the hybrid module with the PCB shows only 5% increase in multiple scattering effects. While the effects of measuring three DUTs in the testbeam setup shows variations the residuals width indicating it is corrected for when using the GBL alignment procedure. Also, characterising the DUTs with higher particle beam energy of 120 GeV achieves better spatial resolution as expected. While the characterisation with lower particle beam energy of 5 GeV shows that the effect of multiple scattering is dominant. The simulation setup is ready to be used by other users to simulate and predict the performance of the future ITk pixel modules.

The characterisation tools and setup that were used to produce all the results for this thesis was introduced in chapter 5. The improvement of the characterisation setup leads to better understanding of the operation of the pixel modules. The ITk planar pixel Market Survey campaign proceeded the development of the ITk detector to the preproduction phase. The development for the Market Survey campaign standardised the characterisation setup using the YARR readout system, which showed compatible results in comparison with the BDAQ53 readout system. Results from the Market Survey narrowed down specifications of the pixel modules such as the analog front-end flavour of the RD53A chip to differential, and validating the temporary metal technique. The results of the Market Survey pixel modules will qualify the production foundry, if the sensors are in good agreement with the ITk requirements. The qualification of foundries to fabricate and produce pixel sensors is parallel to the production of the ITkPixV1 readout chip with differential analog front-end to start the preproduction assembly of ITk pixel modules. Even though the time line was delayed for a global pandemic, which also lead to the delay of testbeam campaigns and results for this thesis. Thanks to the collaborative work of the ITk pixel group in the development, the ITk planar pixel Market Survey campaign was successful and the details will be propagated and documented in the Final Design Report of the ITk pixel detector.

In summary, in my thesis work I have successfully contributed to the qualification of different silicon foundries for the preproduction of ITk pixel modules. I have implemented a new tuning technique for the actual ATLAS pixel modules, which addresses a longstanding issue. The implementation of the DESY testbeam setup in the Allpix² simulation framework will help the understanding of pixel module performance and allow users to make predictions about pixel detector performance.

Appendix A

Module assembly

interconnection technology

The details of the interconnection process are being developed in collaboration with the vendors that are working with pixel upgrade during the R&D phase. An example image of chip-to-wafer interconnection

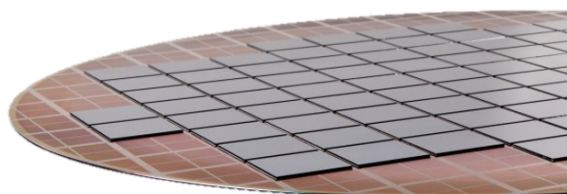


FIGURE A.1: Image of a readout chip wafer with sensors flip-chipped on top [82].

by IZM is shown in figure A.1. Interconnection is possible for chip-to-chip or chip-to-wafer based on the vendor. An example image of chip-to-wafer interconnection by IZM is shown in figure A.1. Interconnection is possible for chip-to-chip or chip-to-wafer based on the vendor. There will be no specific requirements by ITk placed on the technology used for the interconnection process but rather there will be assessment of the quality of the product via a qualification process. The present ATLAS detector using two technologies for interconnection: Indium and solder bumps. Before the bump bonding deposition, the chip wafer must be handled by a supporting wafer. Then the flip-chip bump bonding process is done in five main stages:

1. Deposition of solder metal layer, under bump metallisation (UBM), at wafer level on the pixel pads for both sensor and readout chip.
2. Deposition of the bump ball on the wafers. The bump balls are electroplated on the readout chip wafer only. The Indium process requires Indium bumps to be evaporated onto both the sensor and the readout chip wafers.
3. Wafers are diced after bump formation.
4. Front-end chip thickness below $400\ \mu\text{m}$ require specific techniques such as glass support to handle chip bow during the flip-chip process to prevent disconnected pixels.
5. Finally, the parts are assembled by the flip-chip process.

The flip-chip process requires the alignment of the two die and the application of heat and pressure to make the bond. For solder a reflow at 230°C is required, while Indium uses temperature from $30\text{-}100^\circ\text{C}$

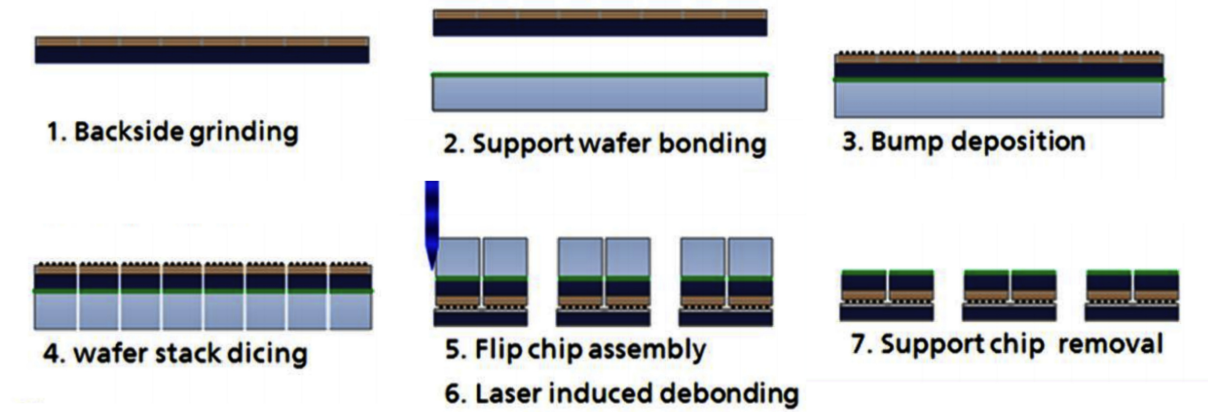


FIGURE A.2: Chip flip-chip assembly process at IZM using a transparent carrier [182]. The chip wafer is grinded and attached to a support wafer, then the bump balls are deposited on the UBM on each pixel on the chip wafer and the single chips are diced. After dicing the chip is flipped to match the single sensors on the sensor wafer and finally the support wafer is removed at the end of the process.

during the flip-chip process. The Fraunhofer institute [82], where ATLAS IBL sensors were bump bonded uses high accuracy full automatic flip chip assembly machines [182]. For ITk production, different processes have been investigated to enable thin chip flip-chip by the prospective ATLAS flip-chip vendors or manufacturers that show the challenge has been successfully met [61]. The process developed by IZM as shown in figure A.2 is the process used for all modules production presented in this thesis. The IZM process employs a temporary glass carrier wafer bonded to the backside of the thinned readout chip wafer. The deposition of UBM and bump ball are done during sensor manufacturing stage. The wafer including carrier is then diced and the chip-carrier packages are used for flip-chip to prevent the chips from bowing during the solder reflow process. The glass carrier are removed from chip backside after the flip-chip process by laser exposure. The ATLAS pixel community is working with different suppliers for manufacturing and flip-chip bump bonding technology. The vendor candidates details are summarised in reference [61].

Appendix B

Pixel DAQ infrastructure and algorithm integration

The threshold baseline tuning algorithm is intended to solve the local asymmetry issue for IBL modules, in the aim to have uniform charge collection results in LHC Run3. This section discusses the implementation of the new threshold tuning algorithm in the ATLAS Pixel DAQ system to be able to tune the complete IBL detector with the threshold baseline tuning method aiming for lower thresholds for Run3. The algorithm is being developed in the pixel detector Data Acquisition (DAQ) system to be tested and operated on IBL modules. The CERN-SR1 test facility is where all tests and calibration work takes place before applying them to the IBL modules in the ATLAS inner detector. SR1 test facility provides an identical copy of fraction of the modules, which developers can access for calibration and developments. Pixel detector developers have access to the electronics via the Detector Control system (DCS) for monitoring and interlock mechanism [183]. This section briefly introduces the pixel DAQ working environment in SR1 test facility and focuses on the implementation and the function of the threshold baseline algorithm within the test facility.

The hardware scheme of the pixel readout system shown in figure B.1 include two main parts, the Read Out Driver (ROD) card and the Back Of Crate (BOC) card. Both are placed in a VME crate dedicated for the IBL detector. In the VME Crate a Single Board Computer (SBC) controls the ROD-BOC pair. The ROD features the integrated PowerPC (PPC) that receive and send commands to run the software. The PPC integrates one master FPGA and two slave FPGAs to control the software. Data taking commands, calibration and monitoring of the detector takes place in the ROD. An external fit server PC, FitFram, is connected to analyze data during calibration [184]. The pixel DAQ infrastructure is a collection of Applications to configure and operate the pixel detector [185]. The infrastructure links the Trigger and Data Acquisition (TDAQ) with the above mentioned hardware setup. All Applications from the DAQ software communicate with the ROD and with each other to commute the commands. An Application sends a command from the host PC to the PPC to perform an action on a module.

The user interface application for the calibration is the *ConsoleApp*, which is used by experts to run scans and tunings on the modules. The *ConsoleApp* is associated in parallel operations and data base interactions for the tuning parameters. To apply the tuning on real modules, the SR1 Finite State Machine *SR1FSM* interface controls the module interlock, hardware connection and is connected to PPC and the readout chain to receive scanning commands from the *ConsoleApp* through the PPC. The command path is created from the host PC to an SR1 module. A more detailed explanation on the DAQ infrastructure can be found in [183], [184] & [108].

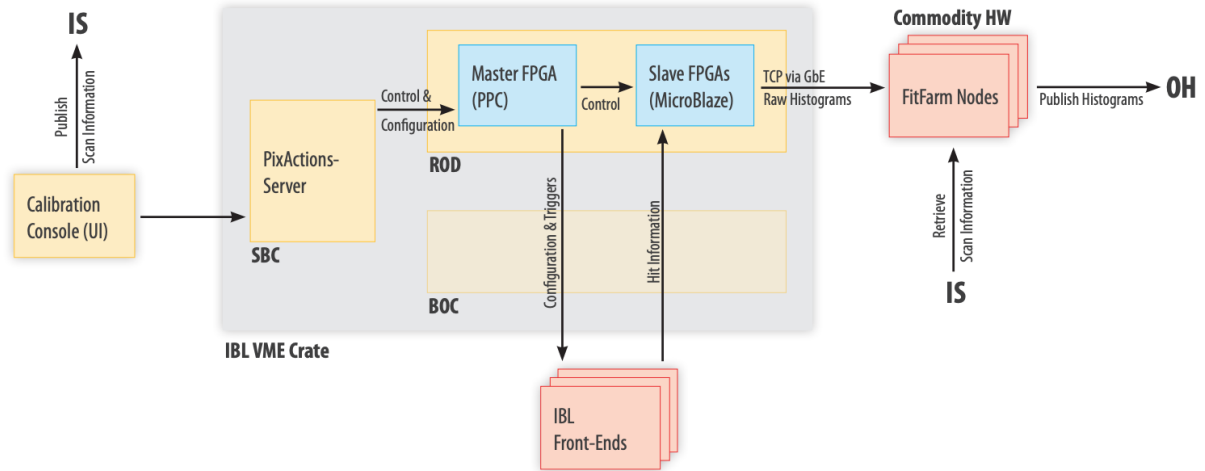


FIGURE B.1: Simplified overview scheme of pixel DAQ hardware components for test and calibration [184].

B.1 Implementation of the algorithm in PixelDAQ

The threshold baseline tuning algorithm is implemented in Pixel DAQ library PixLib/PixelModuleGroup/ with the scan name *Thr2noise_tune*¹. The scan is executed when the prepare function is called by the PixScan execution command. The PixScan application contains all functions necessary to run a scan such as; histogram server, loop indexing, loop actions, execution step, termination step, fit server. All scans in the PixLib are prepared starting from an initial loop parameter at level (loop=0) that sets the masking stages, or injection mode, for the charge injection on each pixel of the module. The masking stages for *Thr2noise_tune* is set to "mask_1", which scans each pixel independently. The *Thr2noise_tune* algorithm is implemented on free loop variables to avoid the use of standard loops, which are identified with standard settings that uses the charge injection voltage. The free loops are nested into each other by construction but they are not attached to variables such as masking stages in (loop=0) or global parameters in higher loop levels. A free loop here is identified with an arbitrary number that is set in the algorithm logic. As discussed in the algorithm description in section 4.3.2, the loops are set as, the inner loop (nloop=0) for the *TDAC*, and the outer loop (nloop=1) for the *VthinAlt*.

The *Thr2noise_tune* is based on enabling and disabling individual pixels to reach the noise floor level, the Enable/disable feature is implemented on the PPC software. As the nloop=1 (outer loop) decreases the global threshold, the occupancy map *hOcc* is updated at each *VthinAlt* increment, and the number of hits per Enabled pixels is tracked at each global configuration by:

```
hOcc = &scn->getHisto(PixScan::OCCUPANCY, this, mod,
scn->scanIndex(2), scn->scanIndex(1), scn->getLoopVarNSteps(0)-1);
```

At each global threshold, nloop=0 (inner loop) iterates over the Enabled pixels to update the per-pixel threshold setting *tdacs* with respect to the global threshold. The *tdacs* is assigned for each pixel by:

```
if (tdacs.get(col,row) > 0) {
    tdacs.set(col, row, tdacs.get(col,row)-1); }
```

The occupancy limit is based on Poisson distribution function for all Enabled pixels. It is defined as:

¹The threshold baseline tuning can be found in the Gitlab repository for Pixel DAQ(For ATLAS users): https://gitlab.cern.ch/atlaspixel/daq/atlaspixeldaq/tree/thr2noiseLinux_v1

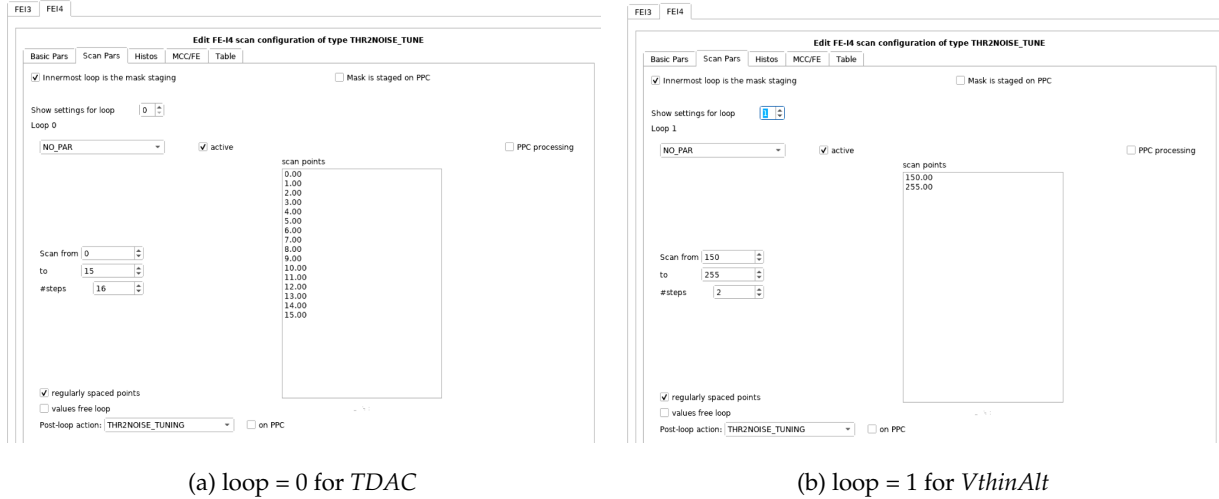


FIGURE B.2: *Thr2noise_tune* Run parameters in the ConsoleApp for FEI4 modules. a) shows parameters for loop = 0 which are set to be for the TDAC. b) shows parameters for loop = 1 which are set to be for the *VthinAlt*. Both loop are nested under "NO_PAR" loops which is the flag for the free variable loops.

```

4094 double mu = occupancy_limit*triggers*conseq_lv11;
4095 auto expected_occupancy = [] (double prb, double mu) {
4096     boost::math::poisson_distribution<> poiss(mu);
4097     return boost::math::quantile(poiss,prb);
4098 };

```

where "mu" is the mean number of Enabled pixels. The tuning converges as the global threshold decreases, and pixels that are above threshold are disabled. This iteration counts and maintains the number of disabled pixels under a certain limit by:

```

4102 pixEnable.disable(col, row);
4103 num_disabled_pixels++;

```

The scan converges in nloop=0 (inner loop) where the local threshold is constantly decreasing for enabled pixels. When the local threshold cannot be decreased any further, the pixel is disabled.

The algorithm exits the scan at three conditions:

1. When the global threshold (*VthinAlt*) have reached the lowest value possible.

```

4108 (GDAC_FE < 70)
4109

```

2. when the mean of the TDAC registers is below half of the TDAC range.

```

4111 (sumTDAC/(double)num_enabled_pixels < 14)
4112

```

3. When the number of disabled pixels reach its 1% limit.

```

4114 (num_disabled_pixels > disabled_pixels_limit*total_num_pixels)
4115

```

Only one of these conditions is sufficient for the algorithm to consider the module tuned and exits the scan, saving global configurations.

B.2 Tuning procedure in SR1

The pixel DAQ software can be compiled and deployed on an lxplus7 machine. To run a scan in SR1 testbed, a testbed and SR1 accounts are needed. To access the development Pixel DAQ PC from lxplus: ssh pix_sr1_01 or _02. For a successful scan follow steps below:

1. Book your ROD which you want to work on before hand.
2. from lxplus server ssh to pixel DAQ PC *pix-sr1-01* or *-02*
3. setup environment to link pixel Trigger and Data Acquisition software (TDAQ-09-02-01) by sourcing file *setup.sh* produced after the software deploy. Be sure to source the latest tdaq software.
4. start infrastructure by *strt_infr*.
 - *Initialize* → *config* → *start* as shown in figure B.3.
 - logs are sorted with this Run number. To monitor your infrastructure log: cd \$Pixel_LOGS and view the ActionServer logs with the same run number.

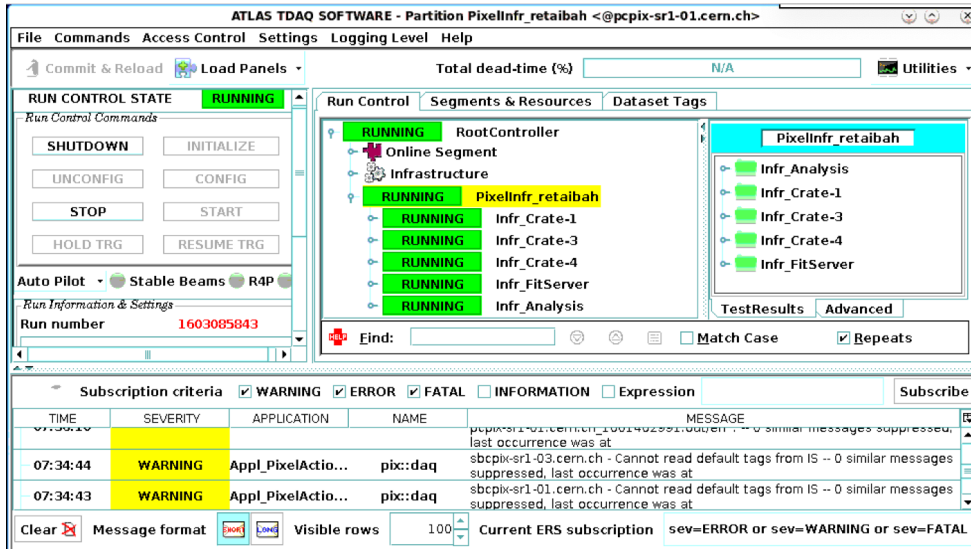


FIGURE B.3: Screenshot of a running infrastructure

5. start fsm by command *\$ sr1fsm*
 - click on IBL and choose your modules
 - activate modules with right click on 'started' status to switch ON Optoboard $\xrightarrow{\text{then}}$ LV $\xrightarrow{\text{then}}$ HV as in figure B.4.
 - to modify voltages login to expert mode.
6. start the user interface by *\$ ConsoleApp -e*
 - select and allocate your ROD.
 - the selected modules appears on the left screen in green as shown in figure B.5. You can right click on the module to deactivate or list further actions to view module data and histograms.
 - on top of the left screen you can find scan ID, and module viewing options for analysis and results.

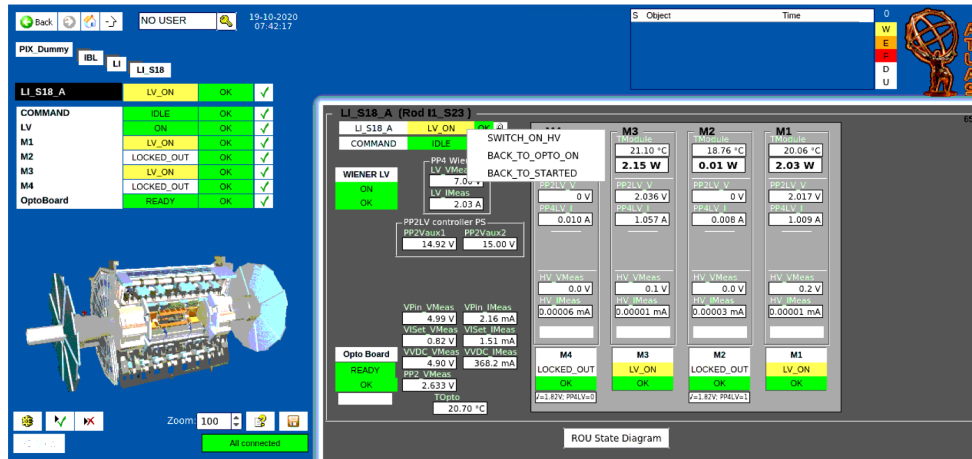


FIGURE B.4: Screenshot of IBL modules running in sr1

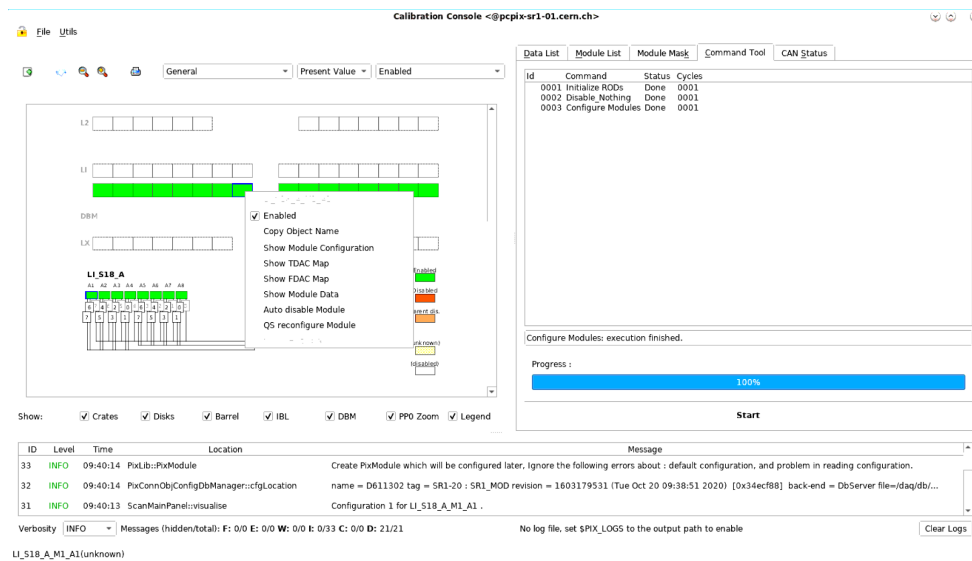


FIGURE B.5: Screenshot of IBL modules running in sr1

- to configure the modules move to 'Command Tool' tab on the left screen. Right click the empty window and first configure modules.
- to run a scan, in the 'Command Tool' tab right click and 'run scan'. A smaller window will pop up to choose the scan name. You can search for *thr2noise_tune*.
- each scan has default parameters saved in the 'presets'. You can choose an existing preset or customize one.
- to customize a preset for a scan, click on customize to find all parameters for FEI3 and FEI4 modules as shown in figure B.2. Change the name of the preset at the bottom of the window to save it as new.
- to view results, adapt your module viewing options from the drop down menu to 'results' then right click on the module and 'Show histogram'.
- In case of empty histograms, might be due to command link to PPC. This will output - ERROR Could not connect to PPC server. You can reset the slaved FPGA in the PPC from sbcpix-sr1-01 or -02 or -03 PCs based on which crate you are running on for crate 1, 2, 3 respectively. The FPGAs can be reset by the command:

```
4157     reset_ROD_FPGAs <slot-number>* all yes*
4158     *yes/no option to power cycle the PPC.
4159
4160     or flash the ROD SW by running
4161     AceProgrammer <ROD-number> /cvmfs/atlas-pixeldaq.cern/rod/rodSlave_IBL/
4162         ufficial/rodSlave_top_boot.ace
4163
4164     • In case of lost communication with the server, log will output ERROR: Client could not con-
4165       nect to server. Could be due to recent PPC or server reset, and the PPC software needs to be
4166       deployed on pix-sr1-01 machine.
4167
4167 7. to check logs
4168
4168     • infrastructure LOG $ PIXEL_LOGS/username_infr. View Action Server log file with infras-
4169       tructure run number.
4170
4170     • PPC LOG can be viewed on machine: sbcpixsr101 PC. First start the logging by $VmeUar-
4171       tReader
4172     view log from $ PIXEL_LOGS/VMEcrate/CurrentPPC
```


Appendix C

Irradiation centers

Measurements of irradiated pixel modules mimic a more realistic operating conditions in the ATLAS detector. Pixel modules are irradiated to study the irradiation hardness of the hybrid and to measure the hit efficiency at targeted fluence. There are several irradiation centers that are used to irradiate modules investigated for this thesis. The different facilities are used according to their availability or also depending on irradiation method advantages at each center. Irradiation centers available during this thesis and of interest to ITk pixel modules are summarized below.

C.1 Karlsruhe irradiation center

The irradiation facility at the Karlsruhe Institute of Technology (KIT) [186] exploits a compact cyclotron operated by ZAG Zyklotron AG [187]. The cyclotron accelerates a high intensity highly focused beam of protons of about 23 MeV [188] at proton current of about $2\mu A$. The width of the beam can be varied from 4-8 mm with a flux of approximately $9 \times 10^{12} \text{ cm}^{-2}\text{s}^{-1}$ at nominal beam current. The proton beam has an exit window to irradiate the target sample installed about 50 cm outside that window. A thermally and electrically insulated box is placed there to hold the samples as shown in the irradiation setup in figure C.1. The samples inside the box are kept at a temperature of -30°C cooled with Nitrogen. Due to the small beam spot diameter the beam has to be scanned across the area to irradiate large devices. Thus, the box is mounted on a movable stage to allow the scanning of the samples that result to a homogeneous irradiation profile. Irradiating one sensor of $20 \text{ mm} \times 20 \text{ mm}$ to $5 \times 10^{15} \text{ n}_{eq}/\text{cm}^2$ takes about 90 minutes at KIT [186]. The final fluence is extracted based on the Ni^{57} -activity measurement in Ni-foils that are attached in front of the structures and activated during irradiation. The radiation hardness factor value κ for the 23 MeV protons = 2.20 ± 0.43 [188].

C.2 University of Birmingham

The University of Birmingham hosts the MC40 proton/light-ion cyclotron [189] at the School of Physics and Astronomy to serve the fields of particle and medical physics. The cyclotron has the capability to run at kinetic energies up to 40 MeV but irradiations are performed using protons of 27 MeV. The proton beam is collimated into an area of a $10 \times 10 \text{ mm}^2$ beam spot. The irradiation beam with a current of $1 \mu A$ passing through a sample for three minutes corresponds to a proton fluence of about 10^{15} protons per cm^2 . The beam is directed onto a cooling box as shown in the irradiation setup in figure C.2 with a window for irradiation with dimensions of $140 \times 80 \text{ mm}^2$. The box is cooled to a temperature of -27°C . It is positioned on a pre-configured scanning system that can move along the horizontal axis up to 450 mm strokes (incremented distance) with $\pm 50 \mu\text{m}$ position accuracy and along the vertical axis up to 400 mm strokes with $\pm 200 \mu\text{m}$ position accuracy. Samples with dimensions that exceed the cross section of the

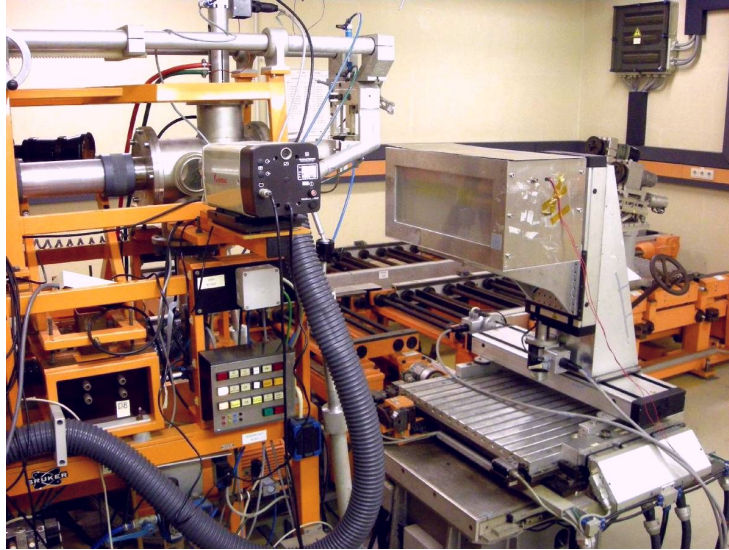


FIGURE C.1: Karlsruhe irradiation setup with cooling box [188].



FIGURE C.2: The scanning system with the cooling box attached in the Birmingham irradiation facility [189].



FIGURE C.3: Irradiation prototype table at the CERN PS Irrad facility equipped with thermostated irradiation box [190].

beam spot are scanned through the beam horizontally to reduce the beam irregularities. The uniformity of the beam is determined at the start of each run by exposing a Gafchromic film¹ to the beam. After irradiation the fluence is determined by a Ni-foil that was placed on the beam with the sample. The measurement of the foil determines the average fluence on the sample with $\pm 10\%$ uncertainty [191]. The radiation hardness factor value for 24 MeV beam of protons $\kappa = 2.11 \pm 0.49$ [188].

C.3 CERN Irrad facility

The CERN Proton Synchrotron PS Irrad1 facility [190] provides a high intensity proton irradiation beam with 24 GeV proton energy [192]. The proton beam spot size varies from $6 \times 6 \text{ mm}^2$ to $20 \times 20 \text{ mm}^2$ with a standard Gaussian profile with a FWHM spot size of $12 \times 12 \text{ mm}^2$ to irradiate samples. The beam is delivered from the Proton Synchrotron (PS) in spills of about 400 ms duration. The intensity of the beam is about 5×10^{11} protons per spill [153]. Samples are placed with a remote control system for precise positioning on the irradiation tables with $\pm 0.1 \text{ mm}$ accuracy. Irradiation tables are placed successively along the beam axis. Samples with dimensions covered by the beam spot can be irradiated up to a particle fluence of 10^{17} protons per cm^2 . The facility does not have a scanning system to move the beam spot across the sample area. Thus taking advantage of the natural beam spread, samples with dimensions larger than the beam spot are positioned with a larger distance from the beam focus point to allow the natural divergence of the Gaussian beam to cover a larger area of the sample. One of the techniques to measure the average fluence received by the sample is a thin aluminum foil that is placed in the beam in front of the sample. The measurement from the aluminum foil determines the average fluence of the sample with $\pm 7\%$ uncertainty. The radiation hardness factor determined for 23 GeV proton beam is $\kappa = 0.62 \pm 0.04$ [188].

Beam profile techniques used at the Irrad facility including Gafchromic films, OSL films and aluminum activation foils are explained in detail in reference [193]. The exact fluence for samples irradiated here require some post calculations and is determined from the details of the beam profile over the irradiated film surface. Sensors with larger dimensions as the FWHM beam spot size of $12 \times 12 \text{ mm}^2$, such as ITk modules, have a Gaussian fluence profile with the maximum fluence in the center and a decreasing fluence outward to the edges. The proton beam is monitored spill by spill by the Beam Profile Monitor (BPM) provided for each irradiation batch. The BPM measurements through the BPM system, which are provided by the facility, describe the intensity of the beam as a function of position per spill on both x- and y- axis. The result of the measurements is expressed in Volts and it is directly proportional to the beam intensity. The intensity along the x- and y- axis makes a gaussian distribution with a focal point with FWHM of $12 \times 12 \text{ mm}^2$. Then, the spatial distribution of the integrated proton-beam intensities over the duration of the irradiation gives the Gaussian beam profile in x- and y- direction as shown in figure C.4 for a RD53a sample over the complete $20 \times 20 \text{ mm}^2$ area of the module. This fluence profile is a multiplication of two dimensional Gaussian distributions of the beam. It describes the variance of the fluence over the complete area of the sample up to normalization. The normalized elliptical Gaussian function can be evaluated by

$$f(x, y) = \frac{1}{2\pi\sigma_x\sigma_y} \cdot e^{-\frac{1}{2} \left[\frac{(x-\mu_x)^2}{\sigma_x^2} + \frac{(y-\mu_y)^2}{\sigma_y^2} \right]}. \quad (\text{C.1})$$

From the average value of the fluence measured over the full module with the aluminum foil, μ_x and μ_y are determined. The integration technique is conducted to deduce the integrated fluence in any fiducial

¹<http://www.gafchromic.com/>

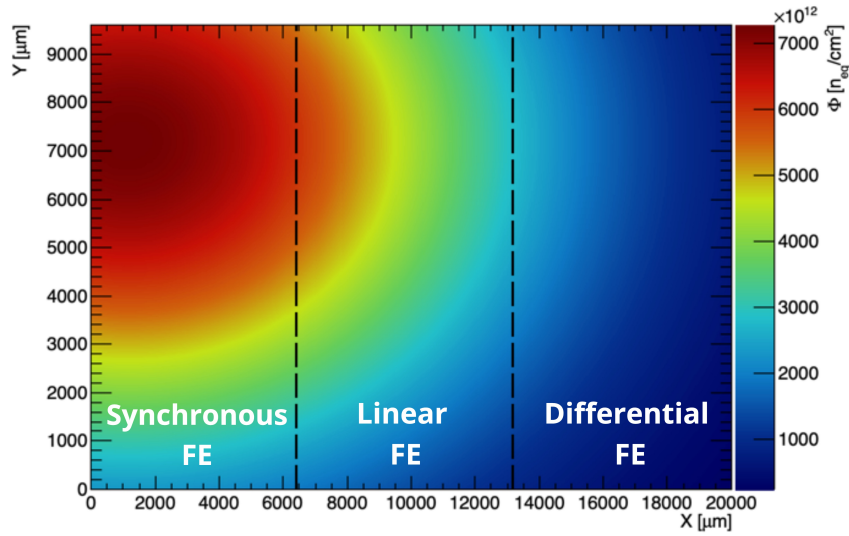


FIGURE C.4: Fluence beam profile for an RD53a module irradiated at the CERN irrads facility.

region on the module to determine the exact fluence of each front-end separately. This method is used to determine the average fluence of the modules investigated in this thesis that were irradiated at the IRRAD1 facility. The irradiation fluence for modules irradiated at CERN is quoted and discussed in the hit efficiency results of section 6.2.1.2 for the two modules that were irradiated at this facility.

C.4 CYRIC

The Cyclotron-RI Center (CYRIC) in Tohoku University in Japan [194] has an irradiation facility with proton beam of 70 MeV and beam current of about 1 μA [195]. This beam allows for 5-6 thin pixel module with back Aluminum planes to be irradiated at the same time with only 3% energy loss. The modules are kept in a cooling box and operated at temperature of −15°C with dry Nitrogen gas to keep humidity constant. The cooling box is mounted on a movable x-y stage with "push-pull" mechanism for positioning to target the beam on any pre-installed sample inside the box. Due to the movable stage, the beam is able to scan the full range of the sample area and have uniform irradiation profile. The fluence uncertainty measured after irradiation relative to the target fluence is within 10%. The radiation hardness factor determined for 70 MeV proton is about $\kappa = 1.55$

The choice of the irradiation facility to irradiate a prototype module for R&D is based on the institute preference. The choice also depend on the desired fluence, irradiation time, and hardness factor. I conclude the irradiation facility section with a summary of the main parameters in table C.1.

TABLE C.1: Summary of some parameters for the irradiation facilities.

	KIT	Birmingham	Irrad PS	CYRIC
Beam energy [GeV]	0.023	0.027	24	0.070
Beam type	protons	protons	protons	protons
Beam size [mm ²]	20 × 20	10 × 10	12 × 12	
Homogeneity	yes	yes	no	yes
hardness factor	2.20 ± 0.43	2.11 ± 0.49	0.62 ± 0.04	1.55

List of Figures

4264

4265

4266

4267

4268

4269

4270

4271

4272

4273

4274

4275

4276

4277

4278

4279

4280

4281

4282

4283

4284

4285

4286

4287

4288

4289

4290

4291

4292

4293

4294

4295

4296

4297

4298

4299

4300

4301

4302

1	An ATLAS event recording of monojets collected in 2017 with a single jet. The green bars show energy deposit in the electromagnetic calorimeter, the yellow bar in the hadronic calorimeter, and the red line is the missing transverse momentum [1].	1
1.1	Standard model of elementary particles	5
1.2	Shape of the scalar potential for $\mu^2 > 0$ (left) and $\mu^2 < 0$ (right). In the second case there is a continuous set of degenerate vacuum, corresponding to different phases θ , connected through a massless field excitation ϕ_2 [2].	7
1.3	Feynman diagrams (top) for VBF Higgs production, (bottom) trilinear and quartic Higgs coupling.	8
1.4	Contours of 68% and 95% confidence level obtained from scans of fits with fixed variable pairs M_W vs. m_t	11
1.5	Invariant mass distribution in the $H \rightarrow \gamma\gamma$ analysis	12
1.6	CERN accelerator complex	13
1.7	Upgrade schedule of the LHC for increased beam energy and luminosity. Long shut down periods of about 2 years are used to upgrade the particle detectors [40].	15
1.8	Schematics of the ATLAS detector	18
1.9	3D visualization of the structure of the barrel of the ATLAS inner detector	19
1.10	Schematics of the pixel detector and cross-section view [47].	19
1.11	Quadrant of the ITk pixel layout scheme	23
1.12	ATLAS ITk particle fluence prediction	25
2.1	Energy bands for Silicon	29
2.2	Schematics of a pn junction	32
2.3	Bethe-Bloch function for μ^+ on Cu	34
2.4	Example of 500 MeV pions incident on thin silicon detectors.	35
2.5	The MPV of the number of electron-hole pairs created per micron for various particles and energies as a function of the sensor thickness	35
2.6	Possible doping combinations for pixel sensors highlighting advantages and disadvantages	37
2.7	Illustration of pixel sensor fabrication layout	38
2.8	Reduced schematic layout of segmented planar $n^+ - in - p$ sensor	39
2.9	Image of 6" wafer produced by FBK	40
2.10	Schematics of an IBL sensor showing guard ring structure	40
2.11	Schematics of a sensor structure	41
2.12	Image of a sensor employing a temporary metal layer	42
2.13	Schematic layout of a 3D sensor	42
2.14	Difference between Hybrid and CMOS processes	43
2.15	Interstitial impurities in silicon lattice showing types of defects [67].	44
2.16	NIEL cross section normalized to 95 MeVmb.	45
2.17	Radiation induced leakage current increase as a function of particle fluence	46

4303	2.18 Evolution of the effective doping concentration to type inversion as a function of annealing	
4304	time.	47
4305	2.19 Evolution of the inverse trapping time as function of annealing time at 60°C [93].	49
4306	3.1 Picture of a FE-I4B planar hybrid pixel module on printed circuit board.	53
4307	3.2 Picture for FE-I4a chip in comparison to FE-I3	54
4308	3.3 Schematics of an IBL sensor with pitch size $50 \times 250 \mu m^2$	55
4309	3.4 IBL hybrid prototype modules.	55
4310	3.5 Layout of the ATLAS IBL	56
4311	3.6 Schematics of the IBL stave [108].	56
4312	3.7 Edge region of IBL planar pixel sensor	57
4313	3.8 Schematic overview of the FEI4 readout electronics	58
4314	3.9 Analog pixel cell of the ATLAS FE-I4B front-end chip	59
4315	3.10 ITk pixel sensor geometries	61
4316	3.11 ITk pixel sensors without biasing structure	62
4317	3.12 Schematics of the RD53A chip showing analog and digital parts	63
4318	3.13 RD53A synchronous analog front-end scheme	65
4319	3.14 RD53A differential analog front-end scheme	66
4320	3.15 RD53A linear analog front-end scheme	67
4321	3.16 Schematics of the ITkPixV1 chip in comparison to the RD53A chip.	68
4322	3.17 Cross section schematic view of a complete module on PCB	69
4323	3.18 Pictures of single, triplet, and quad flexes for RD53A module.	70
4324	3.19 Procedure of gluing the hybrid module to a PCB at LPNHE.	71
4325	3.20 Organization map of bottom of RD53A chip pad frame.	72
4326	3.21 Module assembly work plan for Paris group	73
4327	4.1 Schematics of tuning and charge collection measurement setup	77
4328	4.2 Image of the MMC3 readout board.	79
4329	4.3 Image of the bdaq53 readout board	79
4330	4.4 Image of the readout board board supported by YARR firmware	80
4331	4.5 Schematics of FE-I4B charge injection circuitry and PulserDAC	81
4332	4.6 Charge injection circuitry output pulse amplitude as a function of the corresponding DAC	
4333	for FE-I4B	82
4334	4.7 Nonlinearity of the PulserDAC circuitry in FE-I4B	82
4335	4.8 Measurement of the injection capacitance slope for FE-I4B chip	83
4336	4.9 Charge injection voltage generation in the RD53 readout chip [115]. $V_{cal-high}$ and V_{cal-}	
4337	med are generated in the ACB.	84
4338	4.10 Analog and digital occupancy maps	86
4339	4.11 S-curve and threshold distribution for a FE-I4B module tuned using PyBAR	87
4340	4.12 S-curve and threshold distribution for a RD53A module tuned using bdaq53	87
4341	4.13 ToT distribution fitted with a Gaussian convoluted with a Landau showing MPV at about	
4342	7 ToT per bunch-crossing.	89
4343	4.14 The ToT as a function of the injected charge measured in VCAL shows non-linear relation .	90
4344	4.15 Hit occupancy map for a FE-I4B module showing local threshold asymmetry between left	
4345	and right region.	91
4346	4.16 Measurement of local threshold asymmetry for a FE-I4B module	91
4347	4.17 Threshold baseline tuning algorithm	92

4348	4.18 Visual representation in 2D map for TDAC values across an IBL module after tuning. . . .	94
4349	4.19 Average TDAC per column comparison for double module	95
4350	4.20 Average TDAC per column comparison for single module	95
4351	4.21 Average TDAC per column comparison for quad-0 module	95
4352	4.22 Average TDAC per column comparison for quad-1 module	95
4353	4.23 Average TDAC per column comparison for quad-2 module	96
4354	4.24 Average TDAC per column comparison for 3D module	96
4355	4.25 Average TDAC value per column showing the effect of tuning parameter $TDACVbp$ with	
4356	standard tuning method	97
4357	4.26 Average TDAC value per column shows no effect to the $TDACVbp$ parameter when tuning	
4358	with the threshold baseline	97
4359	4.27 TDAC at different noise occupancy target values	97
4360	4.28 The evolution of hit maps per tuned threshold from source scans with ^{109}Cd after tuning	
4361	for standard tuning. Tuned threshold value quoted on top.	98
4362	4.29 The evolution of hit maps per tuned threshold from source scans with ^{109}Cd after tuning	
4363	for baseline tuning. Tuned threshold value quoted on top.	98
4364	4.30 Left and right fiducial regions for source scan analysis	99
4365	4.31 An image of a FE-I4B module with a 3D printed source holder fixing ^{109}Cd source on top. .	99
4366	4.32 No. of hits Vs. $VthinAlt$ for quad module	99
4367	4.33 No. of hits Vs. $VthinAlt$ for IBL module	100
4368	5.1 RD53a modules mounted in testbeam to be characterised with a particle beam source. . . .	105
4369	5.2 Coordinate system	107
4370	5.3 Picture of testbeam setup with EUDET telescope at DESY	108
4371	5.4 Data Acquisition software EUDAQ scheme for EUDET beam telescope [147].	109
4372	5.5 Beam tests facilities provided at CERN SPS and at DESY	110
4373	5.6 Cooling boxes installed for testbeams (a) at DESY [155] (b) at CERN.	112
4374	5.7 Scheme of testbeam data reconstruction in EU Telescope framework.	113
4375	5.8 Example scheme of sparse clustering logic in EU Telescope software	114
4376	5.9 Mean cluster size in x-axis for a $50\text{ }\mu\text{m}$ thick sensor with pixel pitch of $50 \times 50\text{ }\mu\text{m}^2$	114
4377	5.10 The pre-aligner and correlator histograms of the Hitmaker step	115
4378	5.11 Schematics of trajectory reconstruction with general broken lines model [165].	116
4379	5.12 Residuals of GBL-align step for a module with $50 \times 50\text{ }\mu\text{m}^2$ pixel geometry.	117
4380	5.13 Fitted residuals of GBL-fit step for a module with $50 \times 50\text{ }\mu\text{m}^2$ pixel geometry.	118
4381	5.14 Example Tbmon2 in-pixel hit efficiency maps	119
4382	5.15 Definition of hit position x_{hit} , track position x_{trk} , and residual r in a segmented detector	
4383	with segmentation width w	120
4384	5.16 Example of segmentation width w shows hit formed in case of (a) single readout channel	
4385	hit, (b) two neighboring readout channels firing.	121
4386	5.17 Example residual distributions for cluster sizes 1 and 2	122
4387	6.1 Mounting modules in DESY testbeam facility to be characterised with 5 GeV electron beam	125
4388	6.2 IV curve for RD53A modules without PT before and after irradiation	127
4389	6.3 IV characteristics for unirradiated modules hosting $50\text{ }\mu\text{m}$ thick sensors with two different	
4390	guard ring widths and biasing structure designs	128
4391	6.4 IV characteristics of RD53A modules hosting $50\text{ }\mu\text{m}$ thick sensors Irradiated to $\Phi = 5.3 \times$	
4392	$10^{15}\text{ }n_{eq}/\text{cm}^2$	130

4393	6.5	Residuals of fitted tracks for EUDET beam telescope plane 1 measured at CERN and DESY	131
4394	6.6	Residuals for EUDET telescope planes from ITk pixel module MS campaign	132
4395	6.7	Residual of fitted tracks for the FE-I4B reference plane measured at CERN and DESY	133
4396	6.8	Residuals of fitted tracks for an ITk module with $50 \times 50 \mu m^2$ pixel geometry measured at	
4397		DESY	134
4398	6.9	Residuals of fitted tracks for an ITk module with $25 \times 100 \mu m^2$ pixel geometry measured	
4399		at CERN	135
4400	6.10	Hit efficiency for an unirradiated ITk module with $100 \mu m$ thick sensor measured at DESY	136
4401	6.11	Hit efficiency as a function of bias voltage for unirradiated module W398_4 hosting $130 \mu m$	
4402		thick sensor. Module tuned to mean threshold of $1060 \pm 88e$ and achieved hit efficiency	
4403		$98.8 \pm 0.1\%$ at $60 V$.	137
4404	6.12	Irradiation beam profile at CERN PS Irrad facility for a RD53A module	137
4405	6.13	Efficiency as a function of bias voltage for different irradiation level from CERN SPS and	
4406		Birmingham facility	138
4407	6.14	Evolution of the hit efficiency map for an irradiated module with $130 \mu m$ thick sensor	
4408		irradiated to average fluence $\Phi = 5 \times 10^{15} n_{eq}/cm^2$ measured at CERN	139
4409	6.15	Hit efficiency as a function of bias voltage for an irradiated module with $130 \mu m$ thick	
4410		sensor measured at CERN	140
4411	6.16	Evolution of the hit efficiency map for an irradiated module with $130 \mu m$ thick sensor	
4412		irradiated to $3.6 \times 10^{15} n_{eq}/cm^2$ measure at CERN	141
4413	6.17	Cluster size map for an irradiated module with pixel geometry $25 \times 100 \mu m^2$ folding 2×4	
4414		pixels with $cs=1$ and $cs=2$	143
4415	6.18	Hit efficiency as a function of the tuned threshold for unirradiated and irradiated modules	
4416		measured at DESY	144
4417	6.19	Residuals for unirradiated ITk pixel modules hosting $50 \times 50 \mu m^2$ and $25 \times 100 \mu m^2$	148
4418	6.20	In-pixel efficiency maps for unirradiated MS modules measured at DESY	149
4419	6.21	In-pixel efficiency maps for unirradiated MS modules measured at DESY	151
4420	6.22	In-pixel efficiency map for MS irradiated modules measured at DESY	152
4421	6.23	Residuals for unirradiated modules hosting $50 \mu m$ thick sensors	154
4422	6.24	The hit efficiency as a function of the bias voltage for modules with $50 \mu m$ thick sensors	155
4423	6.25	The in-pixel efficiency map for unirradiated modules with $50 \mu m$ thick sensors measured	
4424		at DESY	157
4425	6.26	Hit efficiency as a function of the bias voltage for unirradiated modules comparing sensor	
4426		thickness	158
4427	7.1	Simulation setup of ITk pixel modules testbeam	163
4428	7.2	Allpix ² simulation chain	166
4429	7.3	Comparison of residuals of MIMOSA26 sensors between simulation and testbeam data for	
4430		upstream planes	168
4431	7.4	Comparison of residuals of MIMOSA26 sensors between simulation and testbeam data for	
4432		downstream planes	169
4433	7.5	Residuals of MIMOSA26 sensors from 0-5 comparing simulated tracks and testbeam data	170
4434	7.6	Residuals from simulated tracks and testbeam data for a RD53A module with $50 \times 50 \mu m^2$	
4435		pixel geometry	171
4436	7.7	Residuals from simulated tracks and testbeam data for a RD53A module with $25 \times 100 \mu m^2$	
4437		pixel geometry	172

4438	7.8	Residuals of simulated tracks for a $50 \times 50 \mu m^2$ ITk pixel module with and without the cooling box included in the setup	173
4439			
4440	7.9	Residual width of ITk pixel sensors showing all pixel pitch sizes $25 \mu m$, $50 \mu m$, $100 \mu m$ with varying passive material thickness of PPO foam.	174
4441			
4442	7.10	Cross sectional image of the hybrid module on top of the Aluminum support layer wire bonded to the PCB	174
4443			
4444	7.11	Residuals of an ITk pixel module including $500 \mu m$ Aluminum support plate	175
4445	7.12	Multiple scattering of simulated tracks for three DUTs in testbeam	175
4446	7.13	Ratio of particle beam energy for $25 \times 100 \mu m^2$ pixel geometry at $5 GeV$ and $120 GeV$	176
4447	7.14	Ratio of particle beam energy for $50 \times 50 \mu m^2$ pixel geometry $5 GeV$ and $120 GeV$	177
4448	A.1	Image of flip-chip on wafer	185
4449	A.2	Chip flip-chip assembly process at IZM using a transparent carrier	186
4450	B.1	Overview scheme of pixel DAQ hardware components	188
4451	B.2	ConsoleApp run paramters for FEI4	189
4452	B.3	Infrastructure view	190
4453	B.4	sr1fsm view	191
4454	B.5	ConsoleApp interface	191
4455	C.1	Karlsruhe irradiation setup with cooling box [188].	194
4456	C.2	The scanning system with the cooling box attached in the Birmingham irradiation facility [189].	194
4457			
4458	C.3	Irradiation prototype table at the CERN PS Irrad facility equipped with thermostatzed irradiation box [190].	194
4459			
4460	C.4	Fluence beam profile for an RD53a module irradiated at the CERN irrad facility.	196

List of Tables

4461

4462	1.1	Measurements of mass and charge for fermions. Adapted from [27].	10
4463	1.2	Measurements of mass and charge for bosons. Adapted from [27].	10
4464	1.3	Fit results for the observables used in the global electroweak fit including all experimental	
4465		data. Adapted from [31].	11
4466	1.4	Beam parameters for LHC and High Luminosity LHC	16
4467	1.5	Parameters for the ITk coupled rings for layers 0 and 1 [60].	24
4468	1.6	Parameters for the ITk pixel flat barrel [60].	24
4469	1.7	Parameters for the ITk outer inclined pixel barrel [60].	24
4470	1.8	1 MeV neutron equivalent fluences for each layer in ITk layout.	26
4471	2.1	parameter definition for Bethe-Bloch equation	34
4472	3.1	Basic specifications for FE-I4B readout electronics [84].	60
4473	3.2	Basic parameters of the pixel modules for the ITk pixel system. Parameters updated from	
4474		[61, 74].	62
4475	3.3	RD53A analog front-end flavors.	64
4476	3.4	Basic specifications for the ITkPixV1 readout electronics [120].	69
4477	4.1	The injected charge to tune the ToT varies with the thickness of the module, the MPV of	
4478		injected charge from MIPs based on sensor thickness.	89
4479	4.2	summary of the investigated IBL modules	94
4480	4.3	Time performance of the threshold baseline tuning at different noise rate levels	96
4481	5.1	An example of the positions of the beam telescope and DUTs on the z direction for mea-	
4482		surement at DESY testbeam facility in June 2020.	114
4483	5.2	Details of radiation length for silicon.	114
4484	6.1	Summary of the binary resolution values for each pitch for ITk sensors. Values calculated	
4485		from equation 5.4.	134
4486	6.2	Summary of the average fluence achieved for each analog front-end region for a RD53A	
4487		module irradiated at the CERN Irrad facility to an average fluence of $3.36 \times 10^{15} n_{eq}/cm^2$	137
4488	6.3	Mean value of tuned threshold and tuning dispersion corresponding to the tuned modules	
4489		shown in figure 6.18. Modules were tuned using bdaq53 board.	144
4490	6.4	Summary of the results from ITk prototype modules. Efficiencies quoted in green are	
4491		in agreement with ITk requirements for a pixel sensor and efficiencies quoted in red are	
4492		below the requirement limit.	145
4493	6.5	Summary of the hit efficiency results from MS modules. Modules were tunes to mean	
4494		threshold of $1500 e$	153
4495	6.6	Summary of the hit efficiencies from unirradiated modules hosting $50 \mu m$ thick sensors at	
4496		100 V.	156

4497	6.7	Characteristics of the Hybrid modules plotted in figure 6.26 showing the pixel geometry	
4498		of the sensor, the mean tuned threshold value for linear and differential FE, and the hit	
4499		efficiency at the highest bias voltage.	158
4500	6.8	Summary of the hit efficiency results for modules from all productions presented in this	
4501		chapter. Modules are grouped by sensor thickness.	160
4502	7.1	Positions of the telescope planes and DUTs on the z direction used in the simulation setup.	165
4503	7.2	Details of material budget in the testbeam setup for RD53A modules specifying if the	
4504		budget is included in the simulation and testbeam data setup.	172
4505	C.1	Summary of some parameters for the irradiation facilities.	196

Bibliography

- [1] CERN. URL: <https://home.cern/> (visited on 11/11/2020) (pages 1, 12).
- [2] Antonio Pich. *The Standard Model of Electroweak Interactions*. 2012. arXiv: 1201.0537 [hep-ph] (pages 1, 5–7).
- [3] “Observation and study of the Higgs boson candidate in the two photon decay channel with the ATLAS detector at the LHC”. In: (Dec. 2012) (page 1).
- [4] “Observation of a new particle in the search for the Standard Model Higgs boson with the ATLAS detector at the LHC”. In: *Physics Letters B* 716.1 (2012), pp. 1–29. ISSN: 0370-2693. DOI: <https://doi.org/10.1016/j.physletb.2012.08.020>. URL: <http://www.sciencedirect.com/science/article/pii/S037026931200857X> (page 1).
- [5] Stephen P. Martin. “A Supersymmetry primer”. In: *Adv. Ser. Direct. High Energy Phys.* 21 (2010). Ed. by Gordon L. Kane, pp. 1–153. DOI: 10.1142/9789812839657_0001. arXiv: hep-ph/9709356 (pages 1, 9).
- [6] P.A.R. Ade et al. “Planck 2015 results. XIII. Cosmological parameters”. In: *Astron. Astrophys.* 594 (2016), A13. DOI: 10.1051/0004-6361/201525830. arXiv: 1502.01589 [astro-ph.CO] (page 1).
- [7] WikiMedia. *File:Standard Model of Elementary Particles*. revised 15 June 2017. URL: https://commons.wikimedia.org/w/index.php?title=File:Standard_Model_of_Elementary_Particles.svg&oldid=247917323 (visited on 10/04/2020) (page 5).
- [8] Ashok Das. *Lectures on quantum field theory; 2nd ed.* Singapore: World Scientific, 2020. URL: <https://cds.cern.ch/record/2743407> (page 5).
- [9] Michele Maggiore. *A modern introduction to quantum field theory*. Oxford master series in statistical, computational, and theoretical physics. Oxford: Oxford Univ., 2005. URL: <https://cds.cern.ch/record/845116> (page 6).
- [10] D. Hanneke, S. Fogwell, and G. Gabrielse. “New Measurement of the Electron Magnetic Moment and the Fine Structure Constant”. In: *Phys. Rev. Lett.* 100 (2008), p. 120801. DOI: 10.1103/PhysRevLett.100.120801. arXiv: 0801.1134 [physics.atom-ph] (page 6).
- [11] G.W. Bennett et al. “Final Report of the Muon E821 Anomalous Magnetic Moment Measurement at BNL”. In: *Phys. Rev. D* 73 (2006), p. 072003. DOI: 10.1103/PhysRevD.73.072003. arXiv: hep-ex/0602035 (page 6).
- [12] B. Abi, T. Albahri, and S. et al. Al-Kilani. “Measurement of the Positive Muon Anomalous Magnetic Moment to 0.46 ppm”. In: *Phys. Rev. Lett.* 126 (14 2021), p. 141801. DOI: 10.1103/PhysRevLett.126.141801. URL: <https://link.aps.org/doi/10.1103/PhysRevLett.126.141801> (page 6).
- [13] Luis A. Anchordoqui et al. “Muon Discrepancy Within D-brane String Compactifications”. In: *Fortschritte der Physik* (2021), p. 2100084. ISSN: 1521-3978. DOI: 10.1002/prop.202100084. URL: <http://dx.doi.org/10.1002/prop.202100084> (page 6).

- [14] Andrzej Buras. *Gauge theory of weak decays: the standard model and the expedition to new physics summits. Gauge theories of weak decays*. Cambridge: Cambridge University Press, 2020. DOI: [10.1017/9781139524100](https://cds.cern.ch/record/2722969). URL: <https://cds.cern.ch/record/2722969> (page 6).
- [15] Peter Ware Higgs. “Broken symmetries, massless particles and gauge fields”. In: *Phys. Lett.* 12 (1964), pp. 132–133. DOI: [10.1016/0031-9163\(64\)91136-9](https://cds.cern.ch/record/641590). URL: <http://cds.cern.ch/record/641590> (page 6).
- [16] *Measurement prospects of the pair production and self-coupling of the Higgs boson with the ATLAS experiment at the HL-LHC*. Tech. rep. Geneva: CERN, 2018. URL: <https://cds.cern.ch/record/2652727> (pages 6, 10).
- [17] J. Goldstone. “Field Theories with Superconductor Solutions”. In: *Nuovo Cim.* 19 (1961), pp. 154–164. DOI: [10.1007/BF02812722](https://cds.cern.ch/record/2812722) (page 7).
- [18] G. Aad et al. “Combined Measurement of the Higgs Boson Mass in p-p Collisions at $\sqrt{s} = 7\text{ TeV}$ and $\sqrt{s} = 8\text{ TeV}$ with the ATLAS and CMS Experiments”. In: *Physical Review Letters* 114.19 (2015). ISSN: 1079-7114. DOI: [10.1103/physrevlett.114.191803](https://doi.org/10.1103/PhysRevLett.114.191803). URL: <http://dx.doi.org/10.1103/PhysRevLett.114.191803> (pages 8, 10).
- [19] S. Borowka et al. “Higgs Boson Pair Production in Gluon Fusion at Next-to-Leading Order with Full Top-Quark Mass Dependence”. In: *Physical Review Letters* 117.1 (2016). ISSN: 1079-7114. DOI: [10.1103/physrevlett.117.012001](https://doi.org/10.1103/PhysRevLett.117.012001). URL: <http://dx.doi.org/10.1103/PhysRevLett.117.012001> (page 9).
- [20] Andrea Dainese et al. “Report on the Physics at the HL-LHC, and Perspectives for the HE-LHC”. In: (2019). DOI: [10.23731/CYRM-2019-007](https://cds.cern.ch/record/2703572). URL: <https://cds.cern.ch/record/2703572> (pages 9, 15, 16).
- [21] Björn Penning. “The pursuit of dark matter at colliders - an overview”. In: *J. Phys. G* 45.6 (2018), p. 063001. DOI: [10.1088/1361-6471/aabea7](https://arxiv.org/abs/1712.01391). arXiv: 1712.01391 [hep-ex] (page 9).
- [22] “Measurement of matter–antimatter differences in beauty baryon decays”. In: *Nature Physics* 13.4 (2017), 391–396. ISSN: 1745-2481. DOI: [10.1038/nphys4021](https://doi.org/10.1038/nphys4021). URL: <http://dx.doi.org/10.1038/nphys4021> (page 9).
- [23] John Ellis et al. *Low-Energy Probes of No-Scale SU(5) Super-GUTs*. Tech. rep. arXiv:2011.03554. 45 pages, 38 figures. 2020. URL: <https://cds.cern.ch/record/2744089> (page 9).
- [24] Ellis Kay. “Exploring the Dark Sector with the ATLAS Detector”. In: (2021). URL: <https://cds.cern.ch/record/2773484> (page 9).
- [25] Monika Blanke. *Flavour Physics Beyond the Standard Model: Recent Developments and Future Perspectives*. Tech. rep. 2014. arXiv: 1412.1003. URL: <https://cds.cern.ch/record/1973867> (page 9).
- [26] Jared Barron and David Curtin. “On the origin of long-lived particles”. In: *Journal of High Energy Physics* 2020.12 (2020). ISSN: 1029-8479. DOI: [10.1007/jhep12\(2020\)061](https://doi.org/10.1007/jhep12(2020)061). URL: [http://dx.doi.org/10.1007/JHEP12\(2020\)061](http://dx.doi.org/10.1007/JHEP12(2020)061) (page 9).
- [27] C Patrignani et al. “Review of Particle Physics, 2016-2017”. In: *Chin. Phys. C* 40.10 (2016), 100001. 1808 p. DOI: [10.1088/1674-1137/40/10/100001](https://cds.cern.ch/record/2241948). URL: <https://cds.cern.ch/record/2241948> (page 10).
- [28] Marco Ciuchini et al. “Electroweak precision observables, new physics and the nature of a 126 GeV Higgs boson”. In: *Journal of High Energy Physics* 2013.8 (2013). ISSN: 1029-8479. DOI: [10.1007/jhep08\(2013\)106](https://doi.org/10.1007/jhep08(2013)106). URL: [http://dx.doi.org/10.1007/JHEP08\(2013\)106](http://dx.doi.org/10.1007/JHEP08(2013)106) (page 10).

- [29] M. Aaboud et al. "Observation of $H \rightarrow b\bar{b}$ decays and VH production with the ATLAS detector". In: *Physics Letters B* 786 (2018), 59–86. ISSN: 0370-2693. DOI: [10.1016/j.physletb.2018.09.013](https://doi.org/10.1016/j.physletb.2018.09.013). URL: <http://dx.doi.org/10.1016/j.physletb.2018.09.013> (page 10).
- [30] M. Baak et al. "The global electroweak fit at NNLO and prospects for the LHC and ILC". In: *Eur. Phys. J. C* 74 (2014). Comments: 26 pages, 9 figures, 3046. 14 p. DOI: [10.1140/epjc/s10052-014-3046-5](https://doi.org/10.1140/epjc/s10052-014-3046-5). arXiv: [1407.3792](https://arxiv.org/abs/1407.3792). URL: <http://cds.cern.ch/record/1743339> (pages 10, 11).
- [31] Johannes Haller et al. "Update of the global electroweak fit and constraints on two-Higgs-doublet models". In: *Eur. Phys. J. C* 78 (2018). 33 pages, 13 figures, submitted to EPJC, 675. 33 p. DOI: [10.1140/epjc/s10052-018-6131-3](https://doi.org/10.1140/epjc/s10052-018-6131-3). arXiv: [1803.01853](https://arxiv.org/abs/1803.01853). URL: <https://cds.cern.ch/record/2309961> (page 11).
- [32] *Results for the Global Electroweak Standard Model Fit*. URL: http://project-gfitter.web.cern.ch/project-gfitter/Standard_Model/ (page 11).
- [33] G. et al Aad. "Measurement of the Higgs boson mass from the $H \rightarrow \gamma\gamma$ and $H \rightarrow ZZ^* \rightarrow 4\ell$ channels in pp collisions at center-of-mass energies of 7 and 8 TeV with the ATLAS detector". In: *Phys. Rev. D* 90 (5 2014), p. 052004. DOI: [10.1103/PhysRevD.90.052004](https://doi.org/10.1103/PhysRevD.90.052004). URL: <https://link.aps.org/doi/10.1103/PhysRevD.90.052004> (pages 11, 12).
- [34] Michael Benedikt et al. *LHC Design Report*. CERN Yellow Reports: Monographs. Geneva: CERN, 2004. DOI: [10.5170/CERN-2004-003-V-3](https://doi.org/10.5170/CERN-2004-003-V-3). URL: <http://cds.cern.ch/record/823808> (page 12).
- [35] In: (2008). DOI: [10.1088/1748-0221/3/08/s08003](https://doi.org/10.1088/1748-0221/3/08/s08003). URL: <https://doi.org/10.1088/1748-0221/3/08/s08003> (pages 13, 17).
- [36] *CMS experiment*. URL: <https://cms.cern/> (visited on 11/11/2020) (page 13).
- [37] *ALICE experiment*. URL: <http://aliceinfo.cern.ch/Public/Welcome.html> (visited on 11/11/2020) (page 13).
- [38] *LHCb experiment*. URL: <http://lhcb.web.cern.ch/> (visited on 11/11/2020) (page 13).
- [39] Julie Haffner. "The CERN accelerator complex. Complexe des accélérateurs du CERN". In: (2013). General Photo. URL: <https://cds.cern.ch/record/1621894> (page 13).
- [40] *HL-LHC Plan*. URL: <https://project-hl-lhc-industry.web.cern.ch/content/project-schedule> (visited on 11/11/2020) (page 15).
- [41] G Apollinari et al. *High-Luminosity Large Hadron Collider (HL-LHC): Preliminary Design Report*. CERN Yellow Reports: Monographs. Geneva: CERN, 2015. DOI: [10.5170/CERN-2015-005](https://doi.org/10.5170/CERN-2015-005). URL: <https://cds.cern.ch/record/2116337> (pages 14, 16).
- [42] "Measurement of the effective leptonic weak mixing angle using electron and muon pairs from Z boson decay in the ATLAS experiment at $\sqrt{s} = 8 \text{ TeV}$, reportNumber = ATLAS-CONF-2018-037, month = 7, year = 2018". In: () (page 16).
- [43] M. Woods. "Electroweak results from the SLD experiment". In: *14th Lake Louise Winter Institute: Electroweak Physics*. May 1999. arXiv: [hep-ex/9905015](https://arxiv.org/abs/hep-ex/9905015) (page 16).
- [44] A. et al Cerri. *Report from Working Group 4: Opportunities in Flavour Physics at the HL-LHC and HE-LHC. Flavour Physics at the HL-LHC and HE-LHC*. Tech. rep. Report from Working Group 4 on the Physics of the HL-LHC, and Perspectives at the HE-LHC, 292 pages. Geneva: CERN, 2018. DOI: [10.23731/CYRM-2019-007.867](https://doi.org/10.23731/CYRM-2019-007.867). arXiv: [1812.07638](https://arxiv.org/abs/1812.07638). URL: <https://cds.cern.ch/record/2650175> (page 16).
- [45] *ATLAS experiment Multimedia*. URL: <https://atlas.cern/discover/detector> (visited on 11/11/2020) (pages 18, 19).

- [46] G. Aad et al. “The ATLAS Inner Detector commissioning and calibration”. In: *Eur. Phys. J. C* 70 (2010), pp. 787–821. DOI: [10.1140/epjc/s10052-010-1366-7](https://doi.org/10.1140/epjc/s10052-010-1366-7). arXiv: 1004.5293 [physics.ins-det] (page 17).
- [47] M. Capeans et al. *ATLAS Insertable B-Layer Technical Design Report*. Tech. rep. CERN-LHCC-2010-013. ATLAS-TDR-19. 2010. URL: <https://cds.cern.ch/record/1291633> (pages 18, 19, 55, 57, 94).
- [48] M. Backhaus. “The upgraded Pixel Detector of the ATLAS Experiment for Run 2 at the Large Hadron Collider”. In: *Nucl. Instrum. Meth. A* 831 (2016). Ed. by Yoshinobu Unno et al., pp. 65–70. DOI: [10.1016/j.nima.2016.05.018](https://doi.org/10.1016/j.nima.2016.05.018) (pages 18, 54).
- [49] M. Garcia-Sciveres et al. “The FE-I4 pixel readout integrated circuit”. In: *Nucl. Instrum. Meth. A* 636 (2011). Ed. by Takashi Ohsugi, Hartmut Sadrozinski, and Yoshinobu Unno, S155–S159. DOI: [10.1016/j.nima.2010.04.101](https://doi.org/10.1016/j.nima.2010.04.101) (page 18).
- [50] I. Peric et al. “The FEI3 readout chip for the ATLAS pixel detector”. In: *Nucl. Instrum. Meth. A* 565 (2006). Ed. by J. Grosse-Knetter, H. Krueger, and N. Wermes, pp. 178–187. DOI: [10.1016/j.nima.2006.05.032](https://doi.org/10.1016/j.nima.2006.05.032) (pages 20, 54).
- [51] The ATLAS collaboration. “Operation and performance of the ATLAS semiconductor tracker”. In: *Journal of Instrumentation* 9.08 (2014), P08009–P08009. DOI: [10.1088/1748-0221/9/08/p08009](https://doi.org/10.1088/1748-0221/9/08/p08009). URL: <https://doi.org/10.1088/1748-0221/9/08/p08009> (page 20).
- [52] The ATLAS TRT collaboration. “The ATLAS Transition Radiation Tracker (TRT) proportional drift tube: design and performance”. In: *Journal of Instrumentation* 3.02 (2008), P02013–P02013. DOI: [10.1088/1748-0221/3/02/p02013](https://doi.org/10.1088/1748-0221/3/02/p02013). URL: <https://doi.org/10.1088/1748-0221/3/02/p02013> (page 20).
- [53] V. A. MITSOU. “THE ATLAS TRANSITION RADIATION TRACKER”. In: *Astroparticle, Particle and Space Physics, Detectors and Medical Physics Applications* (2004). DOI: [10.1142/9789812702708_0073](https://doi.org/10.1142/9789812702708_0073). URL: http://dx.doi.org/10.1142/9789812702708_0073 (page 20).
- [54] *ATLAS magnet system: Technical Design Report, 1*. Technical Design Report ATLAS. Geneva: CERN, 1997. URL: <https://cds.cern.ch/record/338080> (page 20).
- [55] *ATLAS liquid-argon calorimeter: Technical Design Report*. Technical Design Report ATLAS. Geneva: CERN, 1996. URL: <http://cds.cern.ch/record/331061> (page 21).
- [56] *ATLAS calorimeter performance: Technical Design Report*. Technical Design Report ATLAS. Geneva: CERN, 1996. URL: <https://cds.cern.ch/record/331059> (page 21).
- [57] Mark Thomson. *Modern particle physics*. New York: Cambridge University Press, 2013. ISBN: 978-1-107-03426-6 (page 21).
- [58] *ATLAS muon spectrometer: Technical Design Report*. Technical Design Report ATLAS. Geneva: CERN, 1997. URL: <https://cds.cern.ch/record/331068> (page 21).
- [59] ATLAS Collaboration. *Technical Proposal: A High-Granularity Timing Detector for the ATLAS Phase-II Upgrade*. Tech. rep. ATL-COM-LARG-2018-008. Draft of Technical Proposal for circulation to ATLAS. Geneva: CERN, 2018. URL: <https://cds.cern.ch/record/2310228> (page 22).
- [60] *Expected Tracking Performance of the ATLAS Inner Tracker at the HL-LHC*. Tech. rep. ATL-PHYS-PUB-2019-014. Geneva: CERN, 2019. URL: <http://cds.cern.ch/record/2669540> (pages 23, 24, 61).
- [61] ATLAS Collaboration. *Technical Design Report for the ATLAS ITk Pixel Detector*. Tech. rep. ATL-COM-ITK-2018-019. Geneva: CERN, 2018. URL: <https://cds.cern.ch/record/2310230> (pages 24, 25, 61, 62, 69, 70, 145, 186).

- [62] Stefano Terzo. “ATLAS ITk Pixel Detector Overview”. In: (2020). URL: <https://cds.cern.ch/record/2725538> (pages 25, 68).
- [63] Torbjörn Sjöstrand, Stephen Mrenna, and Peter Skands. “A brief introduction to PYTHIA 8.1”. In: *Computer Physics Communications* 178.11 (2008), 852–867. ISSN: 0010-4655. DOI: [10.1016/j.cpc.2008.01.036](https://doi.org/10.1016/j.cpc.2008.01.036). URL: <http://dx.doi.org/10.1016/j.cpc.2008.01.036> (page 25).
- [64] A Ferrari et al. *FLUKA: A multi-particle transport code (program version 2005)*. CERN Yellow Reports: Monographs. Geneva: CERN, 2005. DOI: [10.5170/CERN-2005-010](https://cds.cern.ch/record/898301). URL: <https://cds.cern.ch/record/898301> (page 25).
- [65] *ATLAS experiments public results*. URL: <https://twiki.cern.ch/twiki/bin/view/AtlasPublic/RadiationSimulationPublicResults> (visited on 10/22/2020) (page 25).
- [66] ATLAS experiment-public results. *Number of Interactions per Crossing*. URL: https://atlas.web.cern.ch/Atlas/GROUPS/DATAPREPARATION/PublicPlots/2018/DataSummary/figs/mu_2015_2018.png (page 26).
- [67] Simon Sze and Ming-Kwei Lee. *Semiconductor devices: physics and technology; 3rd ed.* Hoboken, NJ: Wiley, 2012. URL: <https://cds.cern.ch/record/1632394> (pages 30, 31, 33, 44, 45).
- [68] Gerhard Lutz. *Semiconductor radiation detectors: device physics*. Berlin: Springer, 1999. URL: <https://cds.cern.ch/record/411172> (pages 30, 41).
- [69] A Chilingarov. “Temperature dependence of the current generated in Si bulk”. In: *Journal of Instrumentation* 8.10 (2013), P10003–P10003. DOI: [10.1088/1748-0221/8/10/p10003](https://doi.org/10.1088/1748-0221/8/10/p10003). URL: <https://doi.org/10.1088/1748-0221/8/10/p10003> (pages 31, 33).
- [70] Frank Hartmann Manfred Krammer. *Silicon Detectors*. URL: <https://indico.cern.ch/event/124392/contributions/1339904/attachments/74582/106976/IntroSilicon.pdf> (visited on 03/05/2021) (page 32).
- [71] Colinge C.A. Colinge J.-P. *Physics of Semiconductor Devices*. Springer, 2002. URL: <https://www.springer.com/gp/book/9781402070181> (pages 32, 33, 45).
- [72] P.A. Zyla et al. “Review of Particle Physics”. In: *PTEP* 2020.8 (2020), p. 083C01. DOI: [10.1093/ptep/ptaa104](https://doi.org/10.1093/ptep/ptaa104) (pages 33–35, 122).
- [73] Lev Davidovich Landau. “On the energy loss of fast particles by ionization”. In: *J. Phys.* 8.4 (1944), pp. 201–205. URL: <https://cds.cern.ch/record/216256> (page 34).
- [74] Stefano Terzo. “Development of radiation hard pixel modules employing planar n-in-p silicon sensors with active edges for the ATLAS detector at HL-LHC”. 2015. URL: <https://cds.cern.ch/record/2676574> (pages 35, 42, 62, 83, 122).
- [75] C. Canali et al. In: () (page 36).
- [76] Zhong He. “Review of the Shockley–Ramo theorem and its application in semiconductor gamma-ray detectors”. In: *Nuclear Instruments and Methods in Physics Research Section A: Accelerators, Spectrometers, Detectors and Associated Equipment* 463.1 (2001), pp. 250–267. ISSN: 0168-9002. DOI: [https://doi.org/10.1016/S0168-9002\(01\)00223-6](https://doi.org/10.1016/S0168-9002(01)00223-6). URL: <http://www.sciencedirect.com/science/article/pii/S0168900201002236> (page 36).
- [77] Simon Ramo. “Currents induced by electron motion”. In: *Proc. Ire.* 27 (1939), pp. 584–585. DOI: [10.1109/JRPROC.1939.228757](https://doi.org/10.1109/JRPROC.1939.228757) (page 36).
- [78] Werner Riegler. “Electric fields, weighting fields, signals and charge diffusion in detectors including resistive materials”. In: *JINST* 11.11 (2016), P11002. DOI: [10.1088/1748-0221/11/11/P11002](https://doi.org/10.1088/1748-0221/11/11/P11002). arXiv: [1602.07949](https://arxiv.org/abs/1602.07949) [[physics.ins-det](https://arxiv.org/abs/1602.07949)] (page 36).

- [79] Fuyue Wang, Benjamin Nachman, and Maurice Garcia-Sciveres. “Ultimate position resolution of pixel clusters with binary readout for particle tracking”. In: *Nucl. Instrum. Meth. A* 899 (2018), pp. 10–15. DOI: [10.1016/j.nima.2018.04.053](https://doi.org/10.1016/j.nima.2018.04.053). arXiv: 1711.00590 [physics.ins-det] (page 37).
- [80] G.-F. Dalla Betta et al. “The INFN–FBK “Phase-2” R&D program”. In: *Nuclear Instruments and Methods in Physics Research Section A: Accelerators, Spectrometers, Detectors and Associated Equipment* 824 (2016). Frontier Detectors for Frontier Physics: Proceedings of the 13th Pisa Meeting on Advanced Detectors, pp. 388–391. ISSN: 0168-9002. DOI: <https://doi.org/10.1016/j.nima.2015.08.074>. URL: <https://www.sciencedirect.com/science/article/pii/S0168900215010463> (page 38).
- [81] *Foundation Bruno Kessler*. URL: <https://www.fbk.eu/> (visited on 12/08/2020) (page 38).
- [82] *Fraunhofer Institute für Zuverlässigkeit und Mikrointegration (IZM)*. URL: <https://www.izm.fraunhofer.de/> (visited on 12/08/2020) (pages 38, 185, 186).
- [83] E. Vianello et al. In: (pages 39, 41).
- [84] The ATLAS IBL collaboration. “Prototype ATLAS IBL modules using the FE-I4A front-end read-out chip”. In: *Journal of Instrumentation* 7.11 (2012), P11010–P11010. DOI: [10.1088/1748-0221/7/11/p11010](https://doi.org/10.1088/1748-0221/7/11/p11010). URL: <https://doi.org/10.1088/1748-0221/7/11/p11010> (pages 40, 54, 56, 57, 59, 60).
- [85] Audrey Ducourthial. “Upgrade of the ATLAS experiment Inner Tracker and related physics perspectives of the Higgs boson decay into two b quarks. Amélioration du trajectographe de l’expérience ATLAS et impact sur l’étude de la désintégration du boson de Higgs en deux quarks b”. Presented 26 Oct 2018. 2018. URL: <https://cds.cern.ch/record/2652024> (pages 40, 56).
- [86] Stephan Meschter Sungwon Han Michael Osterman and journal =Journal of Electronic Materials keywords =Tin whisker, conformal coating, coating coverage year =2012 month =sep volume =41 number =9-pages =2508-2518 doi =10.1007/s11664-012-2179-2 adsurl =https://ui.adsabs.harvard.edu/abs/2012JEM...41..2508M adsnote =Provided by the SAO/NASA Astrophysics Data System Michael Pecht title =Evaluation of Effectiveness of Conformal Coatings as Tin Whisker Mitigation. In: () (page 40).
- [87] M. Bomben et al. In: (pages 42, 140).
- [88] A. Micelli et al. “3D-FBK pixel sensors: Recent beam tests results with irradiated devices”. In: *Nucl. Instrum. Meth. A* 650 (2011). Ed. by Roland Horisberger, Danek Kotlinski, and Andrey Starodumov, pp. 150–157. DOI: [10.1016/j.nima.2010.12.209](https://doi.org/10.1016/j.nima.2010.12.209) (page 42).
- [89] Andrea Schilp Franz Laermer. *Process for anisotropic etching of silicon*. German patent (1992) DE4241045C1 (page 42).
- [90] C. DaVia and S.J. Watts. “The geometrical dependence of radiation hardness in planar and 3D silicon detectors”. In: *Nuclear Instruments and Methods in Physics Research Section A: Accelerators, Spectrometers, Detectors and Associated Equipment* 603.3 (2009), pp. 319–324. ISSN: 0168-9002. DOI: <https://doi.org/10.1016/j.nima.2009.02.030>. URL: <http://www.sciencedirect.com/science/article/pii/S0168900209003994> (page 42).
- [91] M. Backhaus et al. “Development of a versatile and modular test system for ATLAS hybrid pixel detectors”. In: *Nucl. Instrum. Meth. A* 650 (2011). Ed. by Roland Horisberger, Danek Kotlinski, and Andrey Starodumov, pp. 37–40. DOI: [10.1016/j.nima.2010.12.087](https://doi.org/10.1016/j.nima.2010.12.087) (page 43).
- [92] Johannes Wüthrich. “First results with novel pixel detectors based on wafer-wafer bonding”. In: (2020). URL: https://indico.cern.ch/event/813597/contributions/3727951/attachments/1989372/3316084/20200218_WaferWaferBonding_TREDI2020_JWuethrich.pdf (page 43).

- [93] Michael Moll. "Displacement damage in silicon detectors for high energy physics. Displacement Damage in Silicon Detectors for High Energy Physics". In: *IEEE Trans. Nucl. Sci.* 65.8 (2018), 1561–1582. 22 p. DOI: [10.1109/TNS.2018.2819506](https://doi.org/10.1109/TNS.2018.2819506). URL: <https://cds.cern.ch/record/2640820> (pages 44–49).
- [94] A Ruzin et al. "Comparison of radiation damage in silicon induced by proton and neutron irradiation". In: *IEEE Trans. Nucl. Sci.* 46.5 (1999), pp. 1310–13. DOI: [10.1109/23.795808](https://doi.org/10.1109/23.795808). URL: <https://cds.cern.ch/record/410789> (page 44).
- [95] C. Inguibert et al. In: () (page 45).
- [96] C. Inguibert and title=Equivalent Displacement Damage Dose for On-Orbit Space Applications year=2012 volume=59 number=6 pages=3117-3125 doi=10.1109/TNS.2012.2221477 S. Messenger journal=IEEE Transactions on Nuclear Science. In: () (page 45).
- [97] S. R. Messenger et al. In: () (page 45).
- [98] Michael Moll. "Radiation damage in silicon particle detectors: microscopic defects and macroscopic properties". Presented on 30 Nov 1999. 1999. URL: <http://cds.cern.ch/record/425274> (pages 46, 48, 49).
- [99] *The RD-48 (ROSE) Collaboration*. URL: <http://rd48.web.cern.ch/> (visited on 01/07/2021) (page 47).
- [100] *The RD-50 Collaboration*. URL: <https://rd50.web.cern.ch/> (visited on 01/01/2021) (page 47).
- [101] O. Krasel et al. In: () (page 48).
- [102] W. Adam et al. "Trapping in proton irradiated p^+ - n - n^+ silicon sensors at fluences anticipated at the HL-LHC outer tracker". In: *JINST* 11.04 (2016), P04023. DOI: [10.1088/1748-0221/11/04/P04023](https://doi.org/10.1088/1748-0221/11/04/P04023). arXiv: [1505.01824](https://arxiv.org/abs/1505.01824) [[physics.ins-det](https://arxiv.org/archive/physics)] (page 48).
- [103] Michael Moll, E Fretwurst, and G Lindström. "Investigation on the improved radiation hardness of silicon detectors with high oxygen concentration". In: *Nucl. Instrum. Methods Phys. Res., A* 439.2-3 (2000), pp. 282–92. DOI: [10.1016/S0168-9002\(99\)00842-6](https://doi.org/10.1016/S0168-9002(99)00842-6). URL: <http://cds.cern.ch/record/427352> (page 49).
- [104] F. Moscatelli et al. "Combined Bulk and Surface Radiation Damage Effects at Very High Fluences in Silicon Detectors: Measurements and TCAD Simulations". In: *IEEE Trans. Nucl. Sci.* 63 (2016), pp. 2716–2723. DOI: [10.1109/TNS.2016.2599560](https://doi.org/10.1109/TNS.2016.2599560). arXiv: [1611.10138](https://arxiv.org/abs/1611.10138) [[physics.ins-det](https://arxiv.org/archive/physics)] (page 50).
- [105] FE-I4 Collaboration. "The FE-I4B Integrated Circuit Guide". Version 2.3. In: (2012) (pages 54, 57, 58, 81, 83, 96).
- [106] C. Nellist. "Achievements of the ATLAS Upgrade Planar Pixel Sensors R&D Project". In: *JINST* 10.PSD10. PSD10 (2014). Comments: 10 pages, 9 figures, PSD10: 10th International Conference on Position Sensitive Detectors, C01027. 10 p. DOI: [10.1088/1748-0221/10/01/C01027](https://doi.org/10.1088/1748-0221/10/01/C01027). URL: <https://cds.cern.ch/record/1955726> (page 54).
- [107] G Aad et al. "ATLAS pixel detector electronics and sensors". In: *Journal of Instrumentation* 3.07 (2008), P07007–P07007. DOI: [10.1088/1748-0221/3/07/p07007](https://doi.org/10.1088/1748-0221/3/07/p07007). URL: <https://doi.org/10.1088/1748-0221/3/07/p07007> (page 56).
- [108] G Balbi et al. "The Read-Out Driver ROD card for the Insertable B-layer IBL detector of the ATLAS experiment: commissioning and upgrade studies for the Pixel Layers 1 and 2". In: *Journal of Instrumentation* 9.01 (2014), pp. C01044–C01044. DOI: [10.1088/1748-0221/9/01/c01044](https://doi.org/10.1088/1748-0221/9/01/c01044). URL: <https://doi.org/10.1088/1748-0221/9/01/c01044> (pages 56, 187).

- [109] S Altenheiner et al. "Planar slim-edge pixel sensors for the ATLAS upgrades". In: *Journal of Instrumentation* 7.02 (2012), pp. C02051–C02051. DOI: [10.1088/1748-0221/7/02/c02051](https://doi.org/10.1088/1748-0221/7/02/c02051). URL: <https://doi.org/10.1088/1748-0221/7/02/c02051> (page 56).
- [110] David-Leon Pohl. "3D-Silicon and Passive CMOS Sensors for Pixel Detectors in High Radiation Environments". In: (2020). URL: <http://hdl.handle.net/20.500.11811/8743> (pages 56, 90, 91, 101).
- [111] Andrew James Blue. "Edgeless & Slim-edge Detectors for RD50". In: *PoS Vertex2014* (2015), p. 042. DOI: [10.22323/1.227.0042](https://cds.cern.ch/record/2159161). URL: <https://cds.cern.ch/record/2159161> (page 56).
- [112] Ivan Perić et al. "The FEI3 readout chip for the ATLAS pixel detector". In: *Nuclear Instruments and Methods in Physics Research Section A: Accelerators, Spectrometers, Detectors and Associated Equipment* 565.1 (2006). Proceedings of the International Workshop on Semiconductor Pixel Detectors for Particles and Imaging, pp. 178–187. ISSN: 0168-9002. DOI: <https://doi.org/10.1016/j.nima.2006.05.032>. URL: <http://www.sciencedirect.com/science/article/pii/S0168900206007649> (page 57).
- [113] Marlon Barbero et al. "FE-I4 ATLAS pixel chip design". In: *PoS VERTEX2009* (2010), 027. 10 p. DOI: [10.22323/1.095.0027](https://cds.cern.ch/record/1319298). URL: <https://cds.cern.ch/record/1319298> (page 57).
- [114] *The RD-53 Collaboration*. URL: <https://rd53.web.cern.ch/> (visited on 11/19/2020) (pages 63, 78).
- [115] Maurice Garcia-Sciveres. *The RD53A Integrated Circuit*. Tech. rep. CERN-RD53-PUB-17-001. Geneva: CERN, 2017. URL: <https://cds.cern.ch/record/2287593> (pages 63–67, 72, 84).
- [116] Mark Standke. "Characterization of the Joined ATLAS and CMS RD53A Pixel Chip". Presented 28 Feb 2019. 2019. URL: <https://cds.cern.ch/record/2717863> (pages 63, 64, 78).
- [117] Maurice Garcia-Sciveres. *RD53B Design Requirements*. Tech. rep. CERN-RD53-PUB-19-001. Geneva: CERN, 2019. URL: <https://cds.cern.ch/record/2663161> (pages 64, 68).
- [118] *RD53B users guide*. Tech. rep. Geneva: CERN, 2020. URL: <https://cds.cern.ch/record/2754251> (pages 65, 67, 68).
- [119] Niharika Mittal. "Development of an FPGA emulator for the RD53B chip". Presented 05 Jun 2020. 2020. URL: <https://cds.cern.ch/record/2720510> (page 65).
- [120] Lingxin Meng. *ATLAS ITk Pixel Detector Overview*. 2021. arXiv: [2105.10367](https://arxiv.org/abs/2105.10367) [physics.ins-det] (page 69).
- [121] Lingxin Meng. "Module and System Test Development for the Phase-II ATLAS ITk Pixel Upgrade". In: (2020). URL: <https://cds.cern.ch/record/2708062> (pages 70, 72).
- [122] B. Abbott et al. "Production and Integration of the ATLAS Insertable B-Layer". In: *JINST* 13.05 (2018), T05008. DOI: [10.1088/1748-0221/13/05/T05008](https://doi.org/10.1088/1748-0221/13/05/T05008). arXiv: [1803.00844](https://arxiv.org/abs/1803.00844) [physics.ins-det] (page 69).
- [123] Aneliya Karadzhinova et al. "Characterization of Ni/SnPb-TiW/Pt Flip Chip Interconnections in Silicon Pixel Detector Modules". In: *PoS TIPP2014* (2014), p. 092. DOI: [10.22323/1.213.0092](https://cds.cern.ch/record/2025936). URL: <https://cds.cern.ch/record/2025936> (page 70).
- [124] *Araldite 2011 epoxy adhesive*. URL: https://samaro.fr/pdf/FT/Araldite_FT_2011_EN.pdf (visited on 01/06/2020) (page 71).
- [125] Joe Muse Marija Marjanovic Jessica Metcalfe. *RD53A Quad Module Assembly (internal)*. URL: https://indico.cern.ch/event/949229/contributions/3988103/attachments/2091110/3513727/RD53A_module_assembly.pdf (page 71).

- [126] Lingxin Meng. *RD53A Module Testing Document*. Tech. rep. ATL-COM-ITK-2019-045. Geneva: CERN, 2019. URL: <https://cds.cern.ch/record/2702738> (page 71).
- [127] D Alvarez Feito, A Honma, and B Mandelli. *Studies of IBL wire bonds operation in a ATLAS-like magnetic field*. Tech. rep. PH-EP-Tech-Note-2015-002. Geneva: CERN, 2015. URL: <https://cds.cern.ch/record/2010249> (page 72).
- [128] Jessica Metcalfe. *Plans to the FDR - ATLAS ITk pixel module Preliminary review*. URL: https://indico.cern.ch/event/843905/contributions/3609013/attachments/1929327/3195088/ModulePDR_PlansToFDR_Oct22_2019.pdf (visited on 05/01/2021) (page 72).
- [129] SiLab-Bonn PyBAR. URL: <https://github.com/SiLab-Bonn/pyBAR> (visited on 01/12/2021) (page 78).
- [130] Basil firmware release 3.1.0. URL: <https://basil.readthedocs.io/en/latest/> (visited on 01/12/2021) (page 78).
- [131] Viacheslav Filimonov. “Development of a serial powering scheme and a versatile characterization system for the ATLAS pixel detector upgrade”. PhD thesis. Bonn U., 2017 (page 78).
- [132] Rd53a collaboration. *Bdaq53*. URL: <https://gitlab.cern.ch/silab/bdaq53> (visited on 12/03/2021) (page 79).
- [133] M. Daas et al. “BDAQ53, a versatile pixel detector readout and test system for the ATLAS and CMS HL-LHC upgrades”. In: *Nuclear Instruments and Methods in Physics Research Section A: Accelerators, Spectrometers, Detectors and Associated Equipment* 986 (2021), p. 164721. ISSN: 0168-9002. DOI: 10.1016/j.nima.2020.164721. URL: <http://dx.doi.org/10.1016/j.nima.2020.164721> (page 79).
- [134] Timon Heim. “Performance of the Insertable B-Layer for the ATLAS Pixel Detector during Quality Assurance and a Novel Pixel Detector Readout Concept based on PCIe”. Presented 28 Aug 2015. 2016. URL: <https://cds.cern.ch/record/2206274> (page 80).
- [135] Nikola Lazar Whallon et al. “Upgrade of the YARR DAQ system for the ATLAS Phase-II pixel detector readout chip”. In: *PoS TWEPP-17* (2018), 076. 5 p. DOI: 10.22323/1.313.0076. URL: <https://cds.cern.ch/record/2312402> (page 80).
- [136] T. Hemperek T. Heim J. Jansen H. Krüger D. Pohl M. Garcia-Sciveres M. Standke M. Vogt M. Daas Y. Dieter. *Readout system comparison & injection timing measurement*. 2018. URL: https://indico.physics.lbl.gov/event/783/contributions/2763/attachments/1678/2025/2018_08_28-RD53A.pdf (page 80).
- [137] Malte Backhaus. “High bandwidth pixel detector modules for the ATLAS Insertable B-Layer”. Presented 30 Oct 2014. 2014. URL: <https://cds.cern.ch/record/1696901> (pages 81–83).
- [138] Jens Weingarten. “System Test and Noise Performance Studies at The ATLAS Pixel Detector”. Presented on 19 Sep 2007. 2007. URL: <http://cds.cern.ch/record/1099748> (page 90).
- [139] Paolo Sabatini, Jorn Grosse-Knetter, and Arnulf Quadt. *Charge calibration for the FEI4 chip in the Insertable B-Layer*. Tech. rep. ATL-COM-INDET-2018-052. Geneva: CERN, 2018. URL: <https://cds.cern.ch/record/2636167> (pages 90, 91).
- [140] J. Janssen. “Test beam results of ATLAS DBM pCVD diamond detectors using a novel threshold tuning method”. In: *Journal of Instrumentation* 12.03 (2017), pp. C03072–C03072. DOI: 10.1088/1748-0221/12/03/c03072. URL: <https://doi.org/10.1088/1748-0221/12/03/c03072> (page 92).

- [141] Poisson distribution. URL: https://en.wikipedia.org/wiki/Poisson_distribution (visited on 07/05/2021) (page 93).
- [142] Natascha Savic Anna Macchiolo Richard Nisius Reem Taibah Julien Beyer. *Investigation of the threshold shift using modules with FE-I4 chips*. 2017. URL: https://indico.cern.ch/event/683834/contributions/2802802/attachments/1565517/2466779/Investigation-of-threshold-shift_V2.pdf (visited on 11/17/2020) (page 101).
- [143] WP10: Beam test facilities. 2020. URL: <https://aida2020.web.cern.ch/aida2020/node/241.html> (page 106).
- [144] Hendrik Jansen et al. "Performance of the EUDET-type beam telescopes". In: *EPJ Techniques and Instrumentation* 3.1 (2016). ISSN: 2195-7045. DOI: 10.1140/epjti/s40485-016-0033-2. URL: <http://dx.doi.org/10.1140/epjti/s40485-016-0033-2> (pages 106–109).
- [145] C. Hu-Guo et al. "First reticule size MAPS with digital output and integrated zero suppression for the EUDET-JRA1 beam telescope". In: *Nucl. Instrum. Meth. A* 623 (2010). Ed. by Hiroyuki Iwasaki, Takeshi K. Komatsubara, and Yasuhiro Sugimoto, pp. 480–482. DOI: 10.1016/j.nima.2010.03.043 (page 107).
- [146] P. Baesso, D. Cussans, and J. Goldstein. "The AIDA-2020 TLU: a flexible trigger logic unit for test beam facilities". In: *JINST* 14.09 (2019), P09019. DOI: 10.1088/1748-0221/14/09/P09019. arXiv: 2005.00310 [physics.ins-det] (page 107).
- [147] I. Rubinskiy. "An EUDET/AIDA Pixel Beam Telescope for Detector Development". In: *Phys. Procedia* 37 (2012). Ed. by Ted Liu, pp. 923–931. DOI: 10.1016/j.phpro.2012.02.434 (pages 107–109).
- [148] EUDAQ2 development team. "EUDAQ2 User Manual". Version 2.0.0. In: (2017). Ed. by Yi Liu (pages 108, 109).
- [149] Tobias Bisanz et al. "EUTelescope: A modular reconstruction framework for beam telescope data". In: *JINST* 15.09 (2020), P09020. DOI: 10.1088/1748-0221/15/09/P09020. arXiv: 2011.10356 [physics.ins-det] (pages 109, 113).
- [150] EUDAQ2 github repository. URL: <https://github.com/eudaq/eudaq> (page 109).
- [151] Bastien Raë. *Overview over CERN test beam facilities and LS2 modifications*. URL: https://indico.cern.ch/event/813822/contributions/3648315/attachments/1975530/3291392/BTTB_8th_Overview_over_CERN_test_beam_facilities_and_LS2.pdf (page 110).
- [152] R. Diener et al. "The DESY II test beam facility". In: *Nuclear Instruments and Methods in Physics Research Section A: Accelerators, Spectrometers, Detectors and Associated Equipment* 922 (2019), pp. 265–286. ISSN: 0168-9002. DOI: <https://doi.org/10.1016/j.nima.2018.11.133>. URL: <https://www.sciencedirect.com/science/article/pii/S0168900218317868> (pages 110, 111).
- [153] Niels Doble et al. "The Super Proton Synchrotron (SPS): A Tale of Two Lives". In: *Adv. Ser. Direct. High Energy Phys.* 27 (2017). Ed. by Christian Fabjan et al., pp. 135–177. DOI: 10.1142/9789814749145_0005 (pages 110, 195).
- [154] Julien-Christopher Beyer. "Optimisation of pixel modules for the ATLAS inner tracker at the high-luminosity LHC". PhD thesis. Munich U., 2019. DOI: 10.5282/edoc.23939 (pages 111, 142).
- [155] Georg Troska. "Development and operation of a testbeam setup for qualification studies of ATLAS pixel sensors". PhD thesis. Tech. U., Dortmund (main), Feb. 2012. DOI: 10.17877/DE290R-3375 (pages 112, 165).

- [156] The EUTelescope developers. *EUTelescope*. URL: <https://github.com/eutelescope/eutelescope> (page 112).
- [157] Tobias Bisanz et al. "EUTelescope: A modular reconstruction framework for beam telescope data". In: *JINST* 15.09 (2020), P09020. DOI: 10.1088/1748-0221/15/09/P09020. arXiv: 2011.10356 [physics.ins-det] (page 112).
- [158] *tbmon2*. URL: <https://gitlab.cern.ch/tbmon2/tbmon2> (pages 112, 118).
- [159] *iLCsoft*. URL: https://ilcsoft.desy.de/portal/software_packages/marlin/ (page 112).
- [160] T Bisanz, A Morton, and I Rubinskiy. "EUTelescope 1.0: Reconstruction Software for the AIDA Testbeam Telescope". In: (2015). URL: <https://cds.cern.ch/record/2000969> (pages 112, 114).
- [161] Claus Kleinwort. "General broken lines as advanced track fitting method". In: *Nuclear Instruments and Methods in Physics Research Section A: Accelerators, Spectrometers, Detectors and Associated Equipment* 673 (2012), 107–110. ISSN: 0168-9002. DOI: 10.1016/j.nima.2012.01.024. URL: <http://dx.doi.org/10.1016/j.nima.2012.01.024> (page 113).
- [162] Matthias George. "Testbeam measurements with pixel sensors for the ATLAS Insertable b-Layer project". Presented 07 May 2014. 2014. DOI: 11858/00-1735-0000-0022-5F07-A. URL: <https://cds.cern.ch/record/1742531> (pages 113, 118, 119, 140).
- [163] Claus Kleinwort. "Track fitting and alignment for a TPC with General Broken Lines". In: *DESY notes* (2014). URL: <http://www-flc.desy.de/lcnotes> (page 113).
- [164] R. Fruhwirth. "Application of Kalman filtering to track and vertex fitting". In: *Nucl. Instrum. Meth. A* 262 (1987), pp. 444–450. DOI: 10.1016/0168-9002(87)90887-4 (page 116).
- [165] *DESY - general broken lines*. URL: <https://belle2.desy.de/e101530/e111982/@@siteview> (visited on 01/03/2021) (page 116).
- [166] Dominik Dannheim et al. "Corryvreckan: A Modular 4D Track Reconstruction and Analysis Software for Test Beam Data". In: *JINST* 16 (2020), P03008. 23 p. DOI: 10.1088/1748-0221/16/03/P03008. arXiv: 2011.12730. URL: <https://cds.cern.ch/record/2745788> (page 118).
- [167] *Reconstruction and analysis of test-beam data from ATLAS ITk pixel modules with the Corryvreckan package*. URL: <https://indico.cern.ch/event/945675/contributions/4159742/> (visited on 10/05/2021) (page 118).
- [168] H A Bethe. "MOLIERE'S THEORY OF MULTIPLE SCATTERING". In: *Physical Review (U.S.) Superseded in part by Phys. Rev. A, Phys. Rev. B: Solid State, Phys. Rev. C, and Phys. Rev. D* Vol: 89 (Mar. 1953). DOI: 10.1103/PhysRev.89.1256. URL: <https://www.osti.gov/biblio/4390169> (page 123).
- [169] G. Calderini et al. In: 14.07 (2019), pp. C07001–C07001. DOI: 10.1088/1748-0221/14/07/c07001. URL: <https://doi.org/10.1088/1748-0221/14/07/c07001> (pages 126, 135, 140).
- [170] Marco Bomben. *LPNHE - FBK thin n-on-p pixels for HL-LHC upgrades and beyond*. URL: <https://indico.cern.ch/event/813597/contributions/3727772/> (page 127).
- [171] Giovanni Calderini. *LPNHE - FBK thin n-on-p pixels for HL-LHC upgrades and beyond*. URL: <https://indico.cern.ch/event/895924/contributions/3993230/> (page 127).
- [172] Michael Benedikt et al. *Future Circular Collider - European Strategy Update Documents*. Tech. rep. CERN-ACC-2019-0007. Geneva: CERN, 2019. URL: <https://cds.cern.ch/record/2653673> (pages 127, 153).

- [173] A. Macchiolo et al. "Performance of n-in-p pixel detectors irradiated at fluences up to $5 \times 10^{15} n_{eq}/cm^2$ for the future ATLAS upgrades". In: *Phys. Procedia* 37 (2012). Ed. by Ted Liu, pp. 1024–1031. DOI: 10.1016/j.phpro.2012.02.447. arXiv: 1110.4468 [physics.ins-det] (page 140).
- [174] J. Weingarten et al. "Planar Pixel Sensors for the ATLAS Upgrade: Beam Tests results". In: *JINST* 7 (2012), P10028. DOI: 10.1088/1748-0221/7/10/P10028. arXiv: 1204.1266 [physics.ins-det] (page 140).
- [175] ATLAS ITk project. *Technical Specification Supply of Planar Pixel Sensors for the ATLAS Inner Tracker upgrade project (internal)*. URL: https://indico.cern.ch/event/1015557/contributions/4262170/attachments/2203094/3727611/IT-4339_Technical_Specification_Technical_Auditing_V3.pdf (page 145).
- [176] Tobias Fitschen. *ITk Planar Pixel Sensor Market Survey (internal)*. URL: <https://indico.cern.ch/event/871479/contributions/3740679/attachments/1989981/3317292/Fitschen-LHCC-2020-02-19.pdf> (page 146).
- [177] Mareike Wagner. "Investigations of Planar n+-in-n ATLAS Silicon Sensors with Modified Pixel Implantations". In: *TU Dortmund* (2020). URL: <https://www.e4.physik.tu-dortmund.de/cms/de/AG-Kroeninger/Publikationen/Abschlussarbeiten/Abschlussarbeiten-ATLAS-Upgrade/index.html> (page 147).
- [178] Francisca Munoz Sanchez. *ATLAS ITk Pixel Detector Overview*. Tech. rep. Geneva: CERN, 2021. URL: <https://cds.cern.ch/record/2773697> (page 156).
- [179] *Allpix Squared, Generic Pixel Detector Simulation framework*. URL: <https://project-allpix-squared.web.cern.ch/project-allpix-squared/> (page 163).
- [180] *Allpix²* (pages 163–165).
- [181] Paul Schütze. *The Allpix2 Framework, Silicon Detector Monte Carlo Simulations*. URL: <https://indico.cern.ch/event/984049/contributions/4146598/attachments/2163621/3651169/AllpixSquared.pdf> (page 166).
- [182] "Bump Bonding and Electronic Packaging". In: (). URL: https://indico.cern.ch/event/324785/contributions/1705687/attachments/629587/866507/2014-06-23_Fraunhofer_IZM_Bump_Bonding_and_future_trends_v1.pdf (page 186).
- [183] Nicholas David Dreyer. "An Introduction to ATLAS Pixel Detector DAQ and Calibration Software Based on a Year's Work at CERN for the Upgrade from 8 to 13 TeV". Presented 15 Dec 2016. 2016. URL: <https://cds.cern.ch/record/2266060> (page 187).
- [184] Moritz Kretz and ATLAS Collaboration. *Performance Evaluation of the ATLAS IBL Calibration*. Tech. rep. ATL-COM-INDET-2015-020. Proceedings deadline May 17th. Geneva: CERN, 2015. URL: <https://cds.cern.ch/record/2014123> (pages 187, 188).
- [185] Maria Elena Stramaglia. *DAQ hardware and software development for the ATLAS Pixel Detector*. Tech. rep. ATL-COM-INDET-2015-044. 13th Pisa Meeting - Frontier Detectors for Frontier Physics 24-06-2015. Geneva: CERN, 2015. URL: <https://cds.cern.ch/record/2025511> (page 187).
- [186] *Irradiation Center Karlsruhe*. URL: <https://www.kit.edu/english/> (page 193).
- [187] ZAG Zyklotron AG. URL: <http://www.zyklotron-ag.de/en/> (page 193).
- [188] P. Allport et al. "Experimental Determination of Proton Hardness Factors at Several Irradiation Facilities". In: *JINST* 14.12 (2019), P12004. DOI: 10.1088/1748-0221/14/12/P12004. arXiv: 1908.03049 [physics.ins-det] (pages 193–195).

- [189] P. Dervan et al. "The Birmingham Irradiation Facility". In: *Nuclear Instruments and Methods in Physics Research Section A: Accelerators, Spectrometers, Detectors and Associated Equipment* 730 (2013). Proceedings of the 9th International Conference on Radiation Effects on Semiconductor Materials Detectors and Devices, pp. 101–104. ISSN: 0168-9002. DOI: <https://doi.org/10.1016/j.nima.2013.05.156>. URL: <https://www.sciencedirect.com/science/article/pii/S0168900213007675> (pages 193, 194).
- [190] *PS Irrad Proton facility*. URL: <https://ps-irrad.web.cern.ch/ps-irrad/> (pages 194, 195).
- [191] P. Dervan et al. "Upgrade to the Birmingham Irradiation Facility". In: *Nucl. Instrum. Meth. A* 796 (2015). Ed. by Mara Bruzzi et al., pp. 80–84. DOI: [10.1016/j.nima.2015.02.005](https://doi.org/10.1016/j.nima.2015.02.005) (page 195).
- [192] F Ravotti et al. "The Beam Profile Monitoring System for the CERN IRRAD Proton Facility". In: AIDA-2020-CONF-2016-005 (2016), p. 4. DOI: [10.18429/JACoW-IBIC2016-WEPG75](https://doi.org/10.18429/JACoW-IBIC2016-WEPG75). URL: <https://cds.cern.ch/record/2235850> (page 195).
- [193] Federico Ravotti. "Development and characterisation of radiation monitoring sensors for the high energy physics experiments of the CERN LHC accelerator". PhD thesis. Montpellier U., 2006 (page 195).
- [194] *CYRIC, Tohoku university*. URL: <https://www.cyric.tohoku.ac.jp/> (visited on 01/03/2021) (page 196).
- [195] Koji Nakamura. "Proton Irradiation in Japan". In: (CERN internal) (2018). URL: <https://indico.cern.ch/event/756872/contributions/3196472/> (page 196).